A STUDY OF THE IMAGING OF ATOMIC ELEMENTS

BY COMPUTERISED AXIAL TOMOGRAPHY

A thesis for the degree of

PHILOSOPHIAE DOCTOR

Presented to

DUBLIN CITY UNIVERSITY

By

KIERAN JOSEPH McCARTHY B.Sc.

THE SCHOOL OF PHYSICAL SCIENCES

DUBLIN CITY UNIVERSITY

Research Supervisor

JOSEPH FRYAR B.Sc. Ph.D.

May 1989

THIS THESIS IS DEDICATED TO

MY PARENTS KIERAN AND MARY AND TO MY BROTHER LIAM

IN APPRECIATION FOR THEIR CONTINUED SUPPORT AND ENCOURAGEMENT.

DECLARATION

This thesis is based on my own work.

i

PLATE INDEX

TABLE INDEX.

ABSTRACT

Conventional computerized axial tomography images show the
spatial variation in the linear attenuation coefficient in a
cross-section of a specimen. However, no information is present to
enable one to predict the location nor concentration of an atomic
element in the image. Differential X-ray absorptiometry is a well
established analytic technique for determining the concentration of
an atomic element in a specimen. In this thesis, it is shown that
by applying differential X-ray absorptiometry to computerized axial
tomography, element specific images of a cross-section of a
specimen can be produced using either radioisotope or tube sources.

Differential X-ray absorptiometry involves the measurement of
incident and transmitted photon fluxes, in narrow energy bands
which straddle an absorption edge of the atomic element of
interest, for a collimated beam through a specimen. At an
absorption edge there is a sudden jump in the element's attenuation
coefficient. It is this phenomenon that is the basis of
differential X-ray absorptiometry. From the measured photon counts,
the equivalent thickness (kg/m^2) of an element along a path length
can be determined. Two technique are developed here. The first is
for the case when radioisotopes are used. It involves two
measurements, i.e. with and without the element of interest
present. The second is for the case when an X-ray tube source is
used. In this case, the equivalent thickness is found by
extrapolation of the count data to the absorption edge of the
absorption edge. Using this technique, several elements can be
imaged simultaneously. By measuring the equivalent thickness at
many different orientations to the specimen, enough data can be
collected so that an image of the cross-section, showing elemental
concentration, can be produced. Special mathematial algorithms,
called reconstruction algorithms are required. The computer programs
written to generate reconstructed images are outlined.

The sensitivities of the techniques developed for imaging atomic
elements are studied both experimentally and theoretically.
Equations are derived herein to calculate the minimum concentration
of an element that can be imaged in a specimen. Using these

equations, the most sensitive X-ray energy to an element in a chosen specimen can be determined. In addition, some example calculations are given and these are compared with experimentally obtained values to verify the equations.

Finally, descriptions of the experimental apparatus setup and the experiments undertaken are given. The elements which are imaged include palladium, silver, cadmium, indium and caesium. In all cases the concentrations are of the order of several kilogrammes per cubic metre. Finally, possible future developments are considered.

TABLE OF IMPORTANT SYMBOLS.

N_0, N incident and transmitted photon counts.

U   linear attenuation coefficient.

y   beam path.

E   photon energy.

R   number of rotation steps per linear scan.

S   number of steps per linear scan.

u   mass absorption coefficient $m^2\ kg^{-1}$.

t   equivalent thickness $kg\ m^{-2}$.

p density.

w   weight fraction.

a,m   analyte, matrix.

l,h   low, high energy sides of absorption edge.

a+m   analyte plus matrix.

E_k K-absorption edge energy.

Y_h, Y_l extrapolated projection values.

t_a, t_m analyte, matrix equivalent thickness.

Z, z   dead-time correction factors for MCA.

E_l, E_h low, high energy side of absorption edge.

$K\alpha$, $K\beta$ characteristic K-lines of an element.

dy   small path length.

C_a analyte concentration.

r, ϕ polar co-ordinates system.

$f(r,\phi)$ analyte concentration or linear attenuation coefficient.

O   origin of (r,ϕ) co-ordinate system

B   baseline of (r,ϕ) co-ordinate system.

l, θ radon transform co-ordinate system.

L beam path length in (r,ϕ) system.

R^{-1} inverse radon transform.

D_z partial derivative with respect to first variable.

H_z Hilbert transform.

B back-projection.

s,r   step and rotation co-ordinates.

C_{jk} concentration in pixel j,k.

W_{jk}^{sr} overlap of beam s,r with pixel j,k.

t_{ai}, t_{ao} image, object ray-sums.

λ_{jk}^{sr} fractional overlap area of beam s,r with pixel j,k.

χ^{sr} beam correction factor for ART.

τ relaxation constant for ART.

σ^q standard deviation of an image after the qth iteration.

D matrix diameter

x   the number of mean free paths in a matrix diameter.

N_t total transmitted count for a linear scan.

N_T total transmitted count for all rotations.

U+dU   linear attenuation coefficient for matrix plus analyte.

dN   the difference in total counts for matrix scan and matrix plus analyte scan

B   multiplication factor to account for noise amplification in an image.

Q   machine dependent factor.

V_a, V_m analyte, matrix volume.

f factor to include the effect of the projection of the Poisson distributions during extrapolation.

I.1   Introduction.

For three quarters of a century after Röntgen had discovered X-rays in 1895, and showed that bones could be seen when he X-rayed his wife's hand, X-rays were linked to photographic film. Despite its high spatial resolution, a conventional X-ray transmission photograph is a two-dimensional image of a three-dimensional structure, where many layers are imaged on the film giving rise to overlap and poor contrast. See figure I.1.

In the twenties, the French surgeon Bocage [1], suggested a method to isolate a single layer of a three-dimensional object. See figure I.2. This involves displacing any two of the three participating components, i.e. (X-ray-tube, patient and photographic plate) in parallel planes, while leaving the third one fixed during the taking of the photograph. In this way, only one layer produces a sharp image on the film, while the other layers are smeared over the whole film. This is known as focal plane tomography. However such images have poor contrast and there is a penumbra effect around the images of the objects that are in focus.

More recently, the development of Computerized Axial Tomography, (CAT), led to a totally different approach to extracting cross sections of interest. No longer were X-rays linked to photographic film. It was Cormack [2], who laid the foundations of computerized tomography when he reconstructed an image of some simple aluminium and wood phantoms which he had manually scanned with collimated gamma rays. In the late sixties and early seventies, Hounsfield [3] developed the first operational medical X-ray CAT scanner for high contrast reconstruction of cross-sections of the human brain. This involved taking a large

1
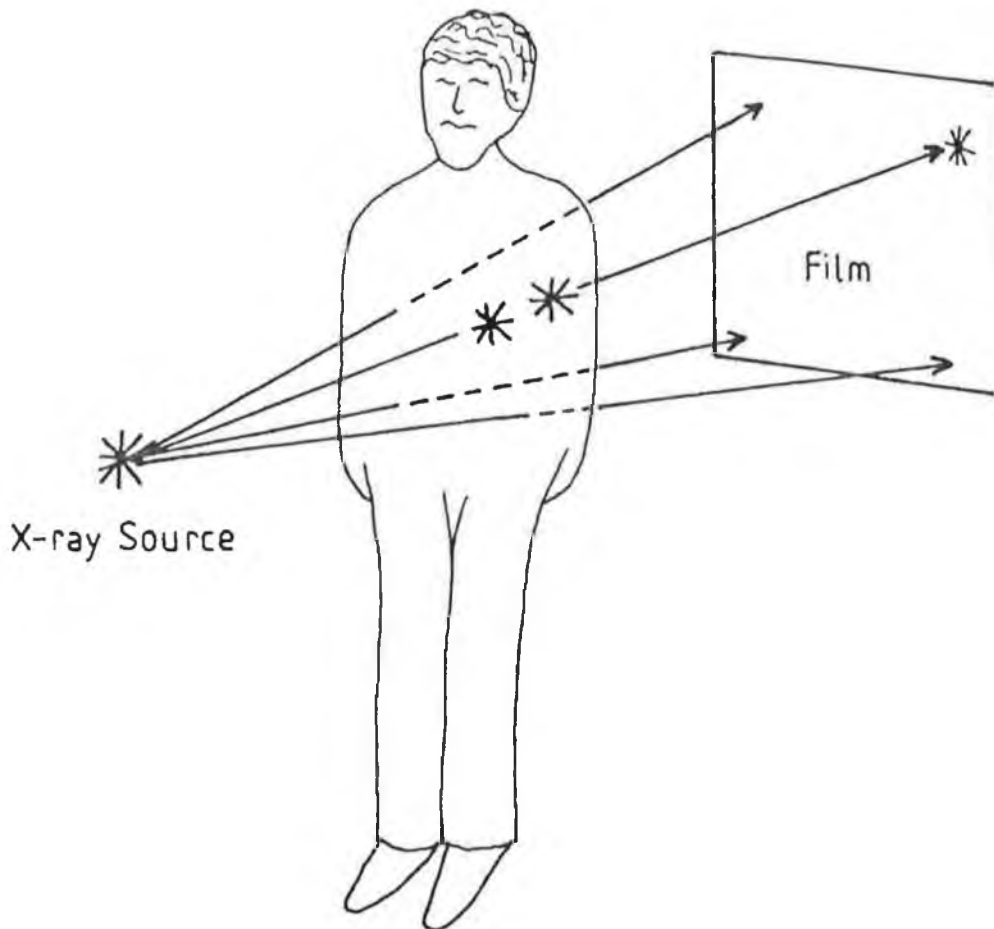
Fig I.1
 Schematic diagram of a conventional X-ray transmission
photograph. The two objects "*" are overlapped on the film
plane.
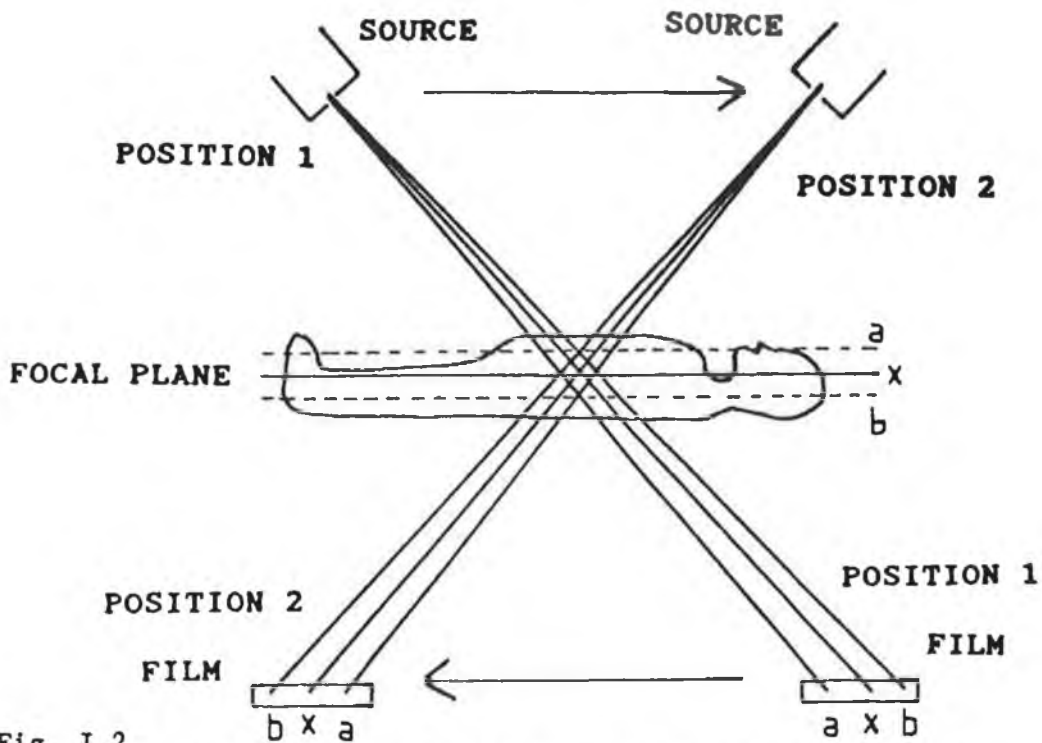
Fig. I.2
 Schematic diagram of classical tomography. The X-ray source
and film are displaced in parallel planes. Only the "x" plane
of the patient produces a sharp image. The "a" and "b" planes
are smeared over the whole film plane.

number of one-dimensional views of a two-dimensional transverse axial slice through the patient and then mathematically reconstructing the structure within the slice. The X-rays used for imaging only traversed the plane under examination so unwanted planes were completely omitted. X-ray computerized tomography is now a widely used medical diagnostic technique with CAT systems operating in most developed countries. As a result of the revolutionary advances in medical radiography due to computerized axial tomography, both Cormack and Hounsfield were awarded the Nobel prize for Medicine in 1979.

A conventional CAT image shows the spatial variation in linear attenuation coefficient, i.e. "density", through the cross-section of interest. In such an image it is possible to differentiate between density variations of less than 1% in water like objects. However, there is no information present in conventional CAT images to identify the atomic elements present nor to distinguish between elements close in atomic number. In recent years, several researchers have investigated techniques to image individual elements for both medical and non-destructive testing applications.

One approach using the broad continous energy spectrum from an X-ray tube source has been investigated by several researchers. Several methods based on this have been developed. In one such method, by Van Riet et al. [4], calcium and water like components can be imaged separately by switching the X-ray tube voltage while scanning. In a second method using an X-ray tube source, by Riederer and Mistretta [5], a contrast agent like iodine is imaged by scanning the object with three beams whose mean energies straddle the contrast agent absorption edge. However, these methods are limited in the number of elements that can be imaged simultaneously and also they are not capable of distinguishing between elements which are close in atomic number. These methods are outlined in more detail in section I.3.1.

Another technique developed, which is based on differential absorption across an element absorption edge, requires two or more monochromatic X-ray energy beams which straddle the K- or L- absorption edge of the atomic element of interest (*the analyte*). When using energies close to the analyte absorption edge, the

3

effect of the other atomic elements present (*the matrix*) is removed. In this way element specific CAT images can be produced. Grodzin [6] has investigated the suitability of a synchrotron as a source for imaging elements in this way. The high intensity, nearly monochromatic and well collimated X-ray beam, which can be obtained from a synchrotron is particularly suited to imaging elements in small samples, for example in water like samples. Several researchers have used synchrotron radiation to produce element specific images. Flannery et al. [8] have produced three-dimensional copper specific images in a sample less than 1mm in diameter with micrometre spatial resolution. Thompson and Llacer [9] using a synchrotron, have produced iodine specific images of an excised pig heart, whose chambers had been filled with iodine as the contrast agent, by scanning just above and below the iodine K-absorption edge (33.17keV). However, as shown by Grodzin [7], synchrotrons are not particularly suited for imaging human subjects. Also, their main use has been in research since synchrotrons are not very numerous. These techniques are described in more detail in section I.3.1.

There are several other imaging techniques, other than X-ray imaging techniques, which are now well established. These include gamma computed tomography, ultrasound scanning, neutron computed tomography and nuclear magnetic resonance (NMR). To date, element imaging techniques based on gamma computed tomography or ultrasound scanning have not been developed. In the case of neutron computed tomography, it is possible to image some low atomic number elements in high atomic number specimens. In NMR the density variation of hydrogeon and some isotopes of other elements can be imaged individually. In both cases the number of elements than can be imaged is limited. These techniques are outlined in more detail in section I.3.1.

In this thesis, X-ray energies which straddle the analyte absorption edge are monitored in order to produce element specific images. In the first method developed, nearly monochromatic radiation produced either by fluorescence from a suitable target or by electron capture within a suitable radioactive isotope is used. However, this method is limited to samples where the analyte can be added to the matrix specimen. In the second of the methods

4

developed, an energy dispersive detector allows several elements to be imaged simultaneously in a single scan. In this case the continous spectrum from an X-ray tube is used. In both methods, the differential absorption of X-ray beams which straddle the analyte absorption edges is monitored. Thus in theory, if suitable sources can be found, all elements with an absorption edge energy which lies within the energy range of the detector used can be imaged.

Computerized axial tomography has been sucessfully used in non-desructive testing, by Gilboy [10] and Kinney et al. [11], using both X-rays and gamma rays. In my thesis it is applied to imaging atomic elements in small non-living samples. Mid-periodic table elements such as palladium, silver and cadmium are imaged. The constraints which apply to living samples do not apply here. These include dose considerations; a medical scan gives a maximum surface dose of approximately 2 rads. to a patient's head [12], but such considerations do not apply to non-living samples. Similarily, artifacts due to patient motion and long scan times are not a problem.

Some work [7] has also been done to investigate the sensitivity of elemental imaging in CAT. However, no easy method to calculate the minimum analyte concentration detectable in a matrix specimen has been developed. In my thesis equations to calculate the minimum analyte concentration detectable in a CAT image have been derived and experiments done to verify the theory. These equations are applied to the two possible situations, namely the case when analyte is added to the matrix and the case when analyte is already present in the matrix.

In the rest of this chapter, the principles of computerized axial tomography are outlined and the factors influencing image contrast, spatial resolution, etc. are described. The other techniques for elemental imaging, which were mentioned earlier, are described in more detail. In the next chapter, the principles of differential X-ray absorption and the techniques developed to produce element specific images are described. In the same chapter, the reconstruction algoritmhms used and their application to image reconstruction are also described. In subsequent chapters, the equations to calculate element sensitivities are derived and the experimental work undertaken is outlined.

I.2.1 Principles of Computerized Axial Tomography.

The aim of computerized axial tomography is to construct an image of a cross-section through an object without interference from other planes. The basic principles of CAT are based on well accepted physics principles, which are outlined here. Computerized axial tomography systems can be divided into three sections. These include the data collection system, the data processing section and the image display system. The first, the data collection, is now considered. Consider a monochromatic pencil beam of X-rays incident on a homogenous object. In practice, the X-ray beam is normally, but not necessarily, polychromatic. For simplicity it is considered to be monochromatic. If the incident beam flux is N_0, then the transmitted flux through an object is given by

$$N = N_0 \exp \left\{ - U_1 \, y_1 \right\} \quad \ldots \ldots \; 1.1$$

where U_1 is the linear attenuation coefficient of the material in the object and y_1 is the path length through the object. The transmitted flux is always less than the incident flux due to attenuation of the X-rays in the object. If a second homogenous object, with linear attenuation coefficient U_2 and thickness y_2, is placed in the beam path then the exponential term of equation 1.1 is given by the sum of the values for both objects. This is given by

$$N = N_0 \exp \left\{ -\left(U_1 \, y_1 + U_2 \, y_2 \right) \right\} \ldots \ldots \; 1.2$$

If more homogenous objects are put in the beam path the exponential term becomes the sum of the attenuation and thickness values.

For the range of energies used in diagnostic applications, typically from a few keV to several hundred keV, photoelectric absorption and Compton scattering are the main processes contributing to the X-ray attenuation. Photoelectric absorption predominates over Compton scattering in materials at these energies except for the very lightest elements at high energies. See figure I.3. Thus, different elements attenuate an X-ray beam of a fixed energy by differing amounts. In fact, the attenuation cross section for X-ray photons increases with the atomic number. Also, as the X-ray energy is increased the X-rays become more penetrating, except at discontinuties called absorption edges. It is these

absorption edges which are important in differential X-ray absorption.

If N_0, N, y and the photon energy E are known for the pencil beam incident on the homogenous object, the linear attenuation U can be determined from equation 1.1 and hence the material present in the homogenous object. On the other hand, if the object is a heterogenous mixture of many elements, the transmitted flux is given by

$$N = N_0 \exp \left\{ - \int U \, dy \right\} \quad \ldots \ldots \quad 1.3$$

where dy is a small path length. Equation 1.3 can be rearranged as

$$\boxed{\ln \left\{ \frac{N_0}{N} \right\} = \int U \, dy} \quad \ldots \ldots \quad 1.4$$

which is the fundamental equation in computerized axial tomography The left-hand side of equation 1.4 is called the projection value. In the case of the hetrogenous object, it is not possible to determine the localized U values along the path length from a single measurements as there are too many unknowns in equation 1.4. Thus more measurements, taken at different directions through the specimen are required. The techniques commonly used to collect the data are described in the following section.

I.2.2 Scan Geometry.

In medical and non-destructive applications, it is required to image a cross-section through the patient or sample. In order to collect the data, the specimen is scanned by a collimated pencil or fan beam of X-rays in synchrony with a detector, or detectors, on the opposite side of the specimen. In the first generation of CAT scanners, the scan geometry consisted of linear scans interspersed by rotations of the source and detector. See figure I.4. In Hounsfield's scanner the linear scan consisted of two hundred and forty 1mm steps. Then, at the end of each linear scan the X-ray tube source and the scintillation detector were rotated about the specimen by a small angle and the linear scan was repeated. In total, one hundred and eighty angular rotations were made to cover a complete rotation of 180 degrees. Further rotations would have resulted in measurements being repeated. At each step position, the
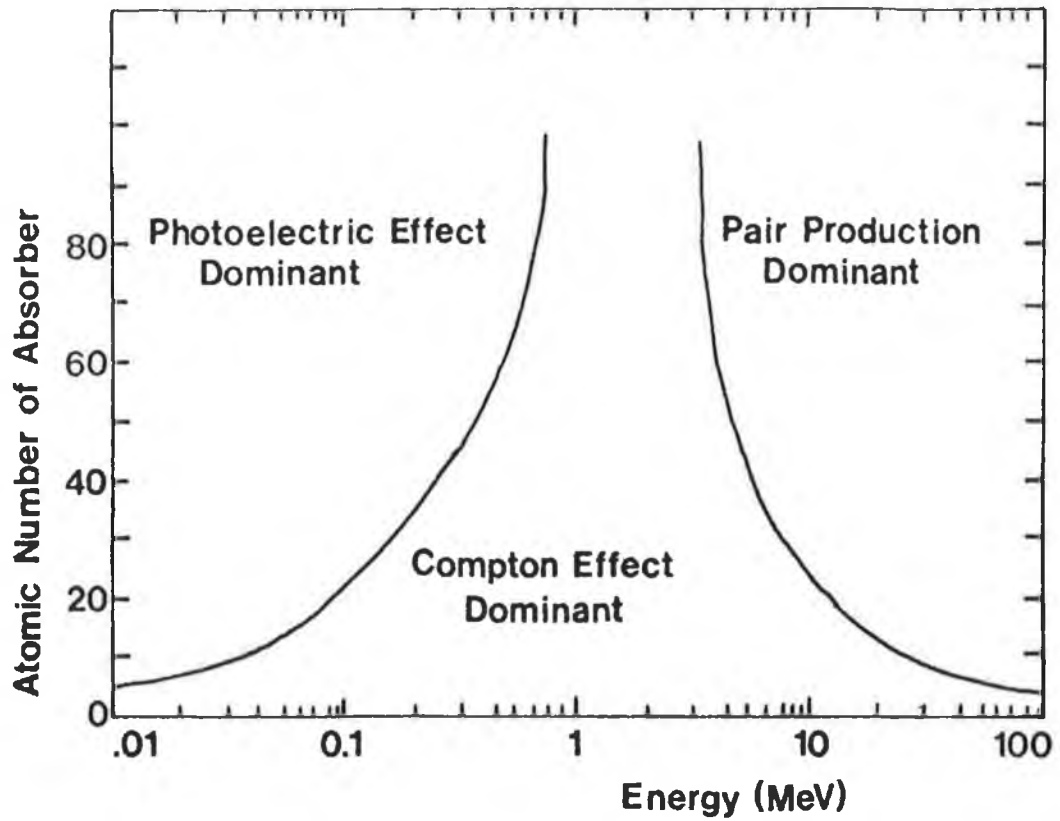
Fig. I.3
The relative importance of the three principal interactions
of X- and γ-rays as a function of photon energy. In this work,
photons of energy less than 0.1MeV are of most interest.

transmitted photon flux was measured and stored. Typically, in these first generation scanners a complete scan took several minutes to complete. In later generations of CAT scanners, see figure I.5, the scan times were decreased to a few seconds by increasing the number of detectors and by using a fan beam of X-rays. The principles are the same as for the first generation scanners and the resultant images are the same.

In all scanners, it is required that R rotations should be made, where R is given by

$$R \simeq \left(\frac{S\pi}{4} \right) \quad \ldots \ldots 1.5$$

and where S is the total number of step positions per linear scan. This number of rotation positions is required in order to ensure that an adequate number of measurements is made. If insufficient measurements were made, this would give rise to streak artifacts in the reconstructed image [13]. Also, in order to ensure that the scan area is covered as uniformly as possible, so as to provide an accurate representation of the cross-section of the body, the step rotation angle must be constant.

The scan geometry used for this thesis is based on that used in the first generation CAT scanners. It is used because of the simplicity and ease of implementation of the method. Also, scan times are not important with non-living samples. There is a slight difference in the motions however, which does not affect the resultant images. In the apparatus built for this work, the source and detector are stationary due to their bulk. Instead, the specimen is stepped and rotated. Stepping the specimen through the X-ray beam and then rotating it at the end of each linear scan is exactly analagous to the normal scan motions previously described. Figure I.7 shows a schematic diagram of the scan motions. A typical scan of a specimen several centimetres in diameter, consisted of forty 1 millimetre steps and forty 4.5 degree rotations.

When all the data has been collected, the problem is then to reconstruct an image of the cross-section of interest from this data. This is done by computers using computer programs which are based on special reconstruction algorithms.

9
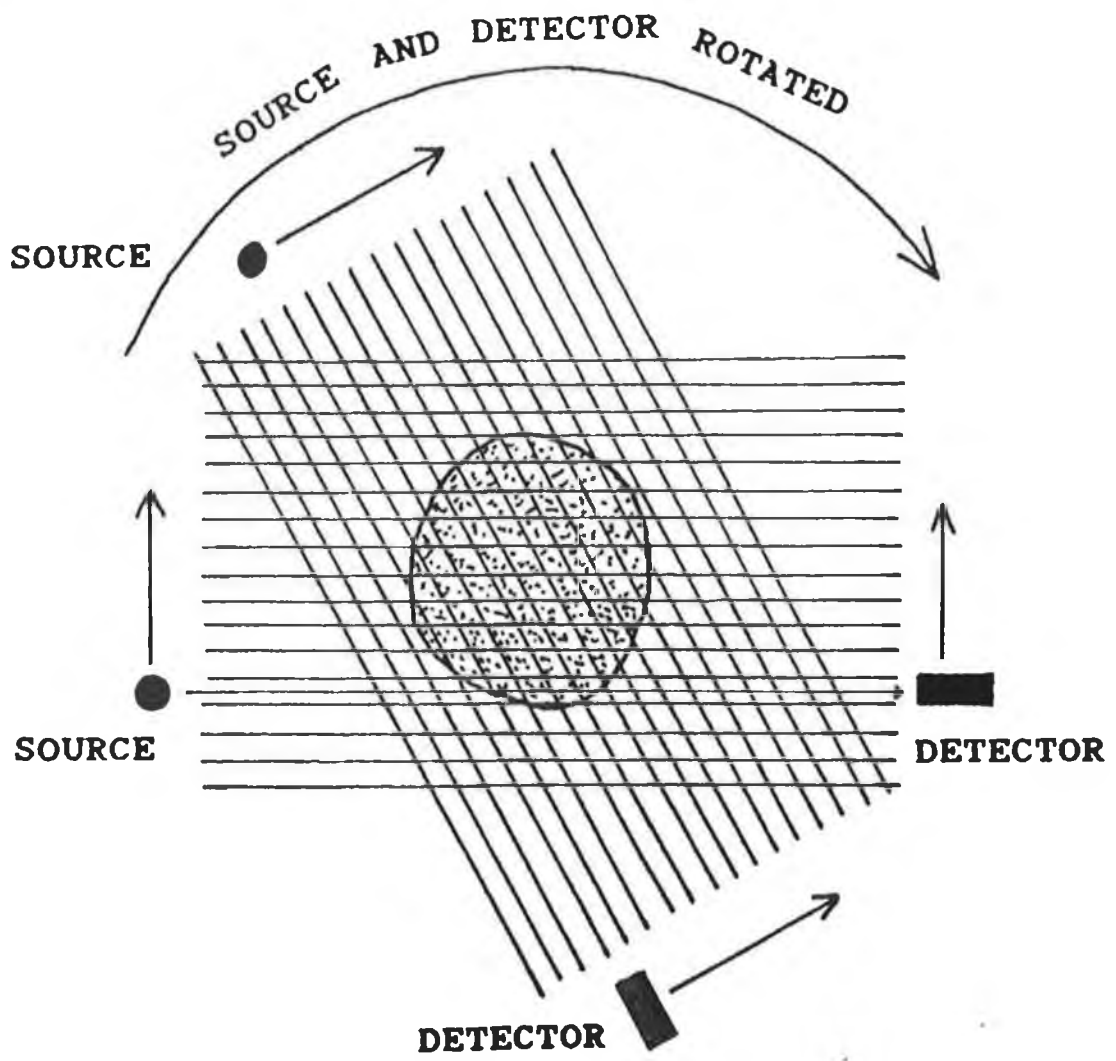
Fig. I.4
A schematic diagram of the scan motions of a first generation CAT scanner. The source and detector are stepped in linear steps and rotations about the sample. In this work, the source and detector were stationary while the sample was stepped and rotated through the beam.
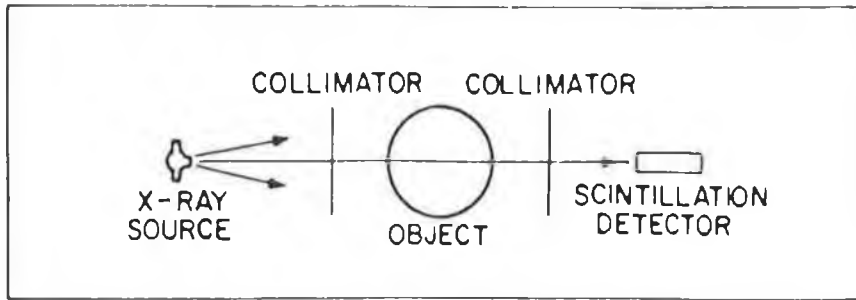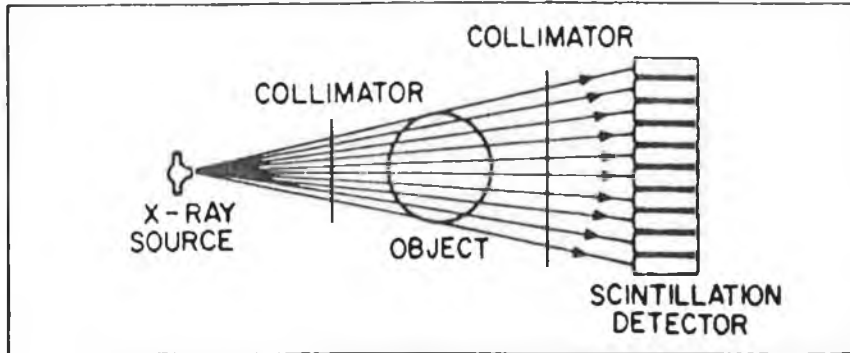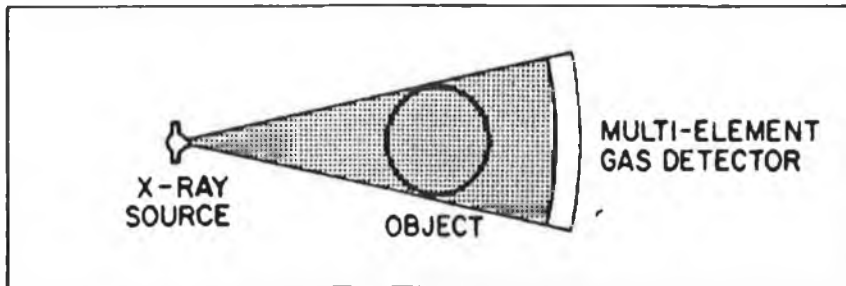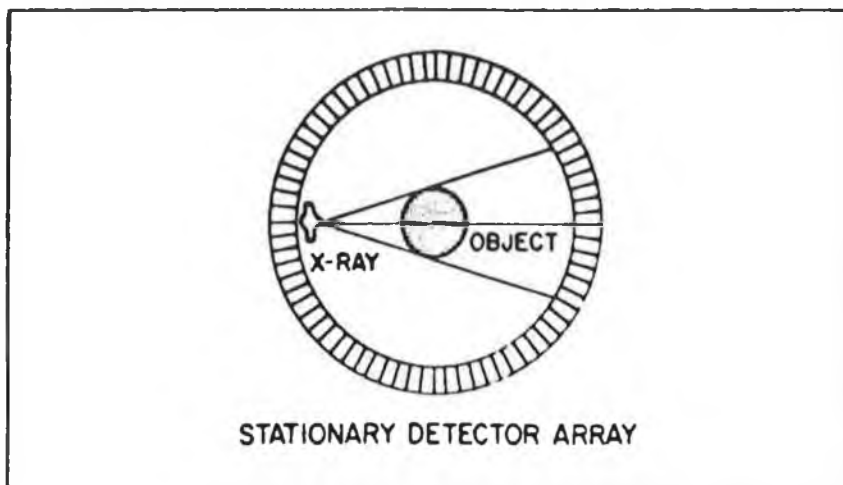
Fig. I.5
Schematic diagrams of the A) 1st, B) 2nd, C) 3rd, and D) 4th generation CAT scanners.

I.2.3 Image Reconstruction.

As previously noted, the attenuation coefficients at each point in the object cannot be determined from a single projection measurement. Instead many measurements are needed. The problem now is to produce an image of the spatial distribution of the linear attenuations in the slice through the object from the projection values calculated using equation 1.4. A mathematical routine called a reconstruction algorithm, which is implemented on a computer, is required for this. Prior to reconstruction, an area in the image plane called a reconstruction grid, is defined by the computer. This grid is divided into small areas, called pixels. In the reconstruction process, the attenuation coefficient in each pixel is determined from the projection data. The value in each pixel is the average attenuation value of all points covered by that pixel. It is not possible to determine the attenuation coefficient of all individual points because of the finite nature of the data. The resultant reconstructed image is a representation of the slice through the specimen.

Several different types of algorithms have been developed most notably the iterative solutions, as used by Hounsfield [3] in the first CAT scanners and the analytic solutions, such as the filtered back-projections and fourier methods. The fourier methods are now favoured in modern machines. The iterative solutions require that all the projection data has been obtained before the reconstruction can begin. The process begins with an initial guess at the image. This is then corrected by comparing the object and image projections. However, this method is slow as it involves much computation. On the other hand, the filtered back-projection methods can be implemented as the data is collected. These methods involve filtering the projection data with a suitable filter function prior to back-projecting the filtered data across the image plane. This is a much faster method. Also, a suitable filter can be chosen to suit the situation. In both cases, high speed computers are required due to the large amount of data and computations involved. Both methods are used in this work and in Chapter II the algorithms and their implementation are explained in more detail.

I.2.4 Image Display.

The reconstructed image is stored as a matrix of numbers, each of which represents the attenuation coefficient in a pixel. A viewing system converts this numeric matrix into a picture. In order to facilitate the displaying of images in conventional computerized axial tomography, an arbitary scale of CAT numbers was devised by Zatz and Alvarez [14] to represent attenuation coefficient in each pixel. These CAT numbers are calculated using the formula

$$\text{CT number} = \frac{\hat{U}_{material} - \hat{U}_{water}}{\left(\hat{U}_{water}/ 1000 \right)} \quad \ldots \ldots \ 1.6$$

where ^ indicates the average linear attenuation coefficient value in the pixel. The usual background material is water so the CT number of water is zero. The scale is adjusted so that the CT numbers range from -1000 for air, 0 for water, to several thousand for bone. The normalized CT numbers are called Hounsfield units. They are useful as they provide a range of several CT numbers for a 1% change in attenuation coefficient. Figure I.6 shows the range of CT numbers for various materials normally encountered in a medical CAT scan. Normally, the CT numbers are displayed as a grey scale on a visual display unit and the full range of shades can be used for different ranges of the CT numbers. This contrast enhancement feature is essential when trying to distinguish between tissues since the X-ray attenuation coefficient for most tissues are similar.

CT numbers are a convenience for displaying rather than a necessity. In this work, pixels contain either the voxel concentration or the attenuation coefficient. Computer programs have been written, so that, as in conventional CAT images the images can be displayed using either grey shades or false colours. Also, the pixels within any range of interest can be enhanced as above and printouts of the reconstructed image can be produced. This is discussed in more detail in Chapter II.

I.2.4.1 Image Resolution.

The two most important contributions of computerized axial tomography are the greatly improved abilities to distinguish

13
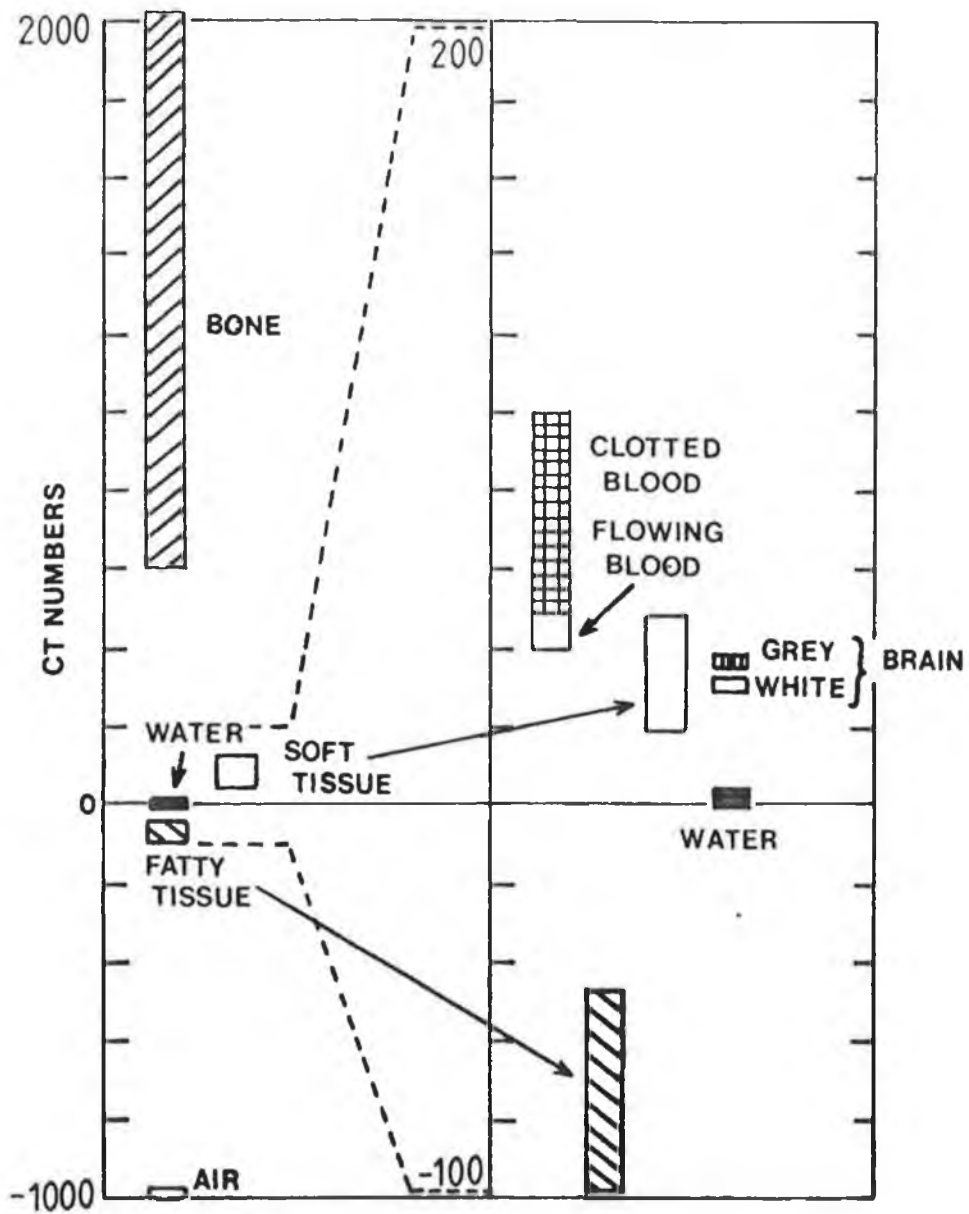
Fig. I.6
The range of CAT display values used for body components in conventional scanners in which water is 0 and air is -1000 at 120kV.

structures with different transmittance and also to separate overlying structures. Compared to conventional diagnostic radiology images, which have a contrast resolution of a few percent, the contrast resolution in CAT images can be better then one percent. However, the spatial resolution in computerized axial tomography images is much poorer than in radiograph pictures. Many factors influence the contrast and spatial resolutions of a CAT image and these are outlined here. Some of these do not affect the images produced for this work, for instance beam hardening due to a polychromatic X-ray beam, but none the less they are included.

I.2.4.2 Contrast Resolution.

Contrast resolution in an image can be defined as the ability to detect and distinguish between small contrast differences in adjacent regions. Quantitatively, it is given by the formula

$$\% \text{ contrast} = \frac{U_{(signal)} - U_{(background)}}{U_{(background)}} \times 100 \quad \ldots . \ 1.7$$

which can be defined as the minimum contrast of a signal of a specified size or shape which can just be discriminated. Thus the ability to detect or perceive a low contrast signal within an image depends on the contrast of the signal as compared to the amplitude of the background signal.

The factors which influence the contrast resolution in a CAT image can be divided into two groups. These include the group which is influenced by the object that is being scanned and the group which is influenced by the inherent background noise in the data. In both cases, many factors contribute and these include

A) Object Contrast

    i) Attenuation of the X-rays in the object relative to that in the background at the effective energy used.

    The closer the X-ray attenuation of the object to that of the background or the lower the analyte concentration, the more difficult it is to distinguish between the two in an image.

    ii) Scatter of the X-ray photons in the beam

    Scatter of photons is a major problem in conventional radiographs and results in a fuzziness in the image. In

comparison, scatter is not such a major problem in CAT when well collimated X-ray beams are used when scanning. It can however be a problem with fan beam scanners.

iii) Partial volume effects

Since the slice thickness is not infinitely thin, the attenuation value in the pixel is the average for all the material in the the full thickness of the slice. Because of this, perception of low contrast features may be diminished. Typically, the slice thickness is between 1.5mm and 15mm in commercial machines. Making the slice thinner increases the exposure to the tissue being imaged. Alternatively, keeping the exposure constant when reducing the slice thickness reduces the number of incident X-rays on the detector which increases the statistical noise in the image. In this work the beam diameter is 1mm so partial volume effects are not negligible

B) Background Noise

i) Photon statistical noise

If a uniform cylindrical object is imaged, the resultant imaged will have a speckled apperance due to the Poisson noise on the detected photon count. Typically, the noise power spectrum, which is the plot vs. spatial frequency of the average power (square of the amplitude) of the noise is uniform over all spatial frequencies. However, the lower spatial frequencies are removed by the filter function in the reconstruction process. Also, increasing the number of incident photons by a factor of four decreases the noise by a factor of two. Statistical noise is an important factor when determining the minimum analyte concentration detectable in chapter III.

ii) Polychromatic X-rays

If the X-ray beam is polychromatic, beam hardening effects as well as the variation of detector efficency with X-ray energy may affect the resultant image. This does not occur with monochromatic X-rays.

iii) Mechanical and electrical noise

Noise due to mechanical or electrical defects usually give

rise to structural noise in the image. This type of noise is usually system dependent and can be reduced by good design.

iv) Filter function

The choice of filter function used in filtered back-projection can have an important effect on the contrast resolution. If large low contrast features are of interest then the Hann filter is preferred, while the Ram-Lak filter enhances detectability for small high contrast features [12].

v) Artifacts

Some common artifacts which affect contrast resolution include beam hardening , misalignment artifacts, specimen motion artifacts and streaking due to an insufficient number of projections.

a) beam hardening

Because of the polychromatic nature of X-rays beams, lower energy photons are more readily absorbed in the first few layers of the object. This gives rise to cupping artifacts in the centre of the image. This does not occur with monochromatic X-ray beams.

b) misalignment

If the centre of rotation of the machine is misaligned, even by a few millimetres, then positive streaks arise on one side of the image while negative streaks arise on the other side of the image. In this work, computer programs are used to align the centre of rotation prior to starting a scan and thus remove misalignment artifacts.

c) streaking

Streaks radiating from a dense object may be due to an insufficient number of angular rotations. In this work, equation 1.5 is applied when determining the number of rotation angles.

d) patient motion

In older CAT scanners, patient motions was a major problem due to the long scan times required. Nowadays, it is not a major problem due to very fast scanners. It is not a problem in this work where only non-living samples are imaged.

As stated, the contrast resolution or the perception of an

object is dependent on the percentage contrast between the object and the background, as well as on the noise. For instance, the signal in a single pixel should be at least ten times the amplitude of the pixel noise in order to distinguish the pixel from the background. In a good scanner, the noise level is about 0.5%. Thus the lowest signal that can be observed in one pixel is about 5% contrast. This is poorer than that for a photographic film which is about 2% [12]. Thus, only small structures with high contrast can be distinguished in an image. On the other hand, if the pixel size is 1mm^2 and the feature of interest covers 10 by 10 pixels in area, the noise is now 0.5% / $\sqrt{100}$ or 0.05%. which gives a contrast of 0.5%. Thus if the feature is big enough, the contrast resolution available in CAT is much better than that for a photographic image.

In summary, it can be said that for small high contrast objects, the detectability is dependent on the spatial resolution of the system whereas, the low contrast detectability is relatively independent of the spatial resolution but depends on factors relating to image noise.

I.2.4.3 Spatial Resolution.

The spatial resolution of a CAT image can be defined both qualitatively as well as quantitatively. Qualitatively, it is the ability to distinguish between two small high contrast objects located a small distance apart. Quantitatively, it is commonly related to the full-width half-maximum (fwhm) of the point spread function (PSF) of a small high contrast object. Many factors influence the spatial resolution of a CAT system and these can be divided into two groups [14]. The first group includes those factors which are inherent in the CAT scanner, while the second group includes such factors as the spacing considerations, the filter function used and the grid matrix used. These factors are listed and outlined in more detail here.

A) Inherent limitations

    i) Focal spot size

    ii) Detector aperture size

    iii) Effective detection area

The inherent spatial resolution, as shown, is determined by factors

which are related to the data collection system. In order to maximize the spatial resolution, in relation to these factors, it is required that the X-ray tube produce a uniformly distributed beam, that the detector has uniform sensitivity over the detection area and that the X-ray beam is well collimated. In the system built for this work a well collimated beam of X-rays, $1mm^2$ in area, is produced using lead collimators. See chapter IV. The Si(Li) detector used has a uniformly sensitive area of $28mm^2$. In addition, the lower collimator was adjustable and was positioned so that the photon count was uniform across the beam area.

B) Other factors

    i) Step size

The beam profile of the incident beam places a fundamental constraint on the spatial resolution. For instance, two small features separated by less than the full-width at half-maximum (fwhm) of the beam at the centre of rotation cannot be distinguished from a single large feature no matter how frequently the projections are sampled. Applying the Nyquist theorem [15], the projections should be sampled at least twice the fwhm. Sampling at a greater spatial frequency does not enhance the image. In this work, the step size was equal to the beam width in order to reduce the scan times. Improved spatial resolution could have been achieved by increasing the sampling frequency but it was not of paramount importance.

    ii) Rotation step size

Provided that there is an adequate number of rotation step positions, as stipulated by equation 1.5, neither the contrast resolution nor the spatial resolution depend on the number of rotation steps, [13]. However, insufficient rotations result in streaking artifacts in the image, which results in a reduction in the spatial resolution.

    iii) Mechanical accuracy of the scanner

Inaccurate positioning of the centre of rotation of the scan system results in artifacts, called tuning fork artifacts, which may reduce the spatial resolution of the image. Such artifacts can be suppressed by including rotations between

19

180 and 360 degrees. However, this results in poorer spatial resolution although the contrast resolution is unaffected.

iv) Filter function

Once the data has been collected, the spatial resolution can be altered by the filter function chosen in the back-projection reconstruction process. For instance, the Ram-Lak [13] filter is a high spatial resolution filter function while the Hann filter reduces the spatial resolution.

v) Reconstruction matrix

When the reconstruction grid pixel size is equal to the linear step size, the image resolution is optimum. Smaller pixels will not improve the resolution but may make the image more pleasing to the eye. On the other hand, larger pixels will decrease the spatial resolution, while reducing the pixel noise [12].

vi) Display matrix

The spatial resolution of a CAT image can be no greater than that provided by the display matrix. Making the display pixels smaller than the reconstruction pixels does not contribute to the information available while increasing the display pixel size may cause information to be lost.

As previously stated, many of the factors listed do not affect the quality of the images produced. In this thesis, however, some factors including partial volume effects, statistical noise and mechanical and electrical noise are inherent to all systems and affect the images produced.

It should also be noted that the minimum size of object that can be resolved is not equal to the minimum size of object that can be detected. For example, an object which is smaller than the pixel size and contained within the pixel may have high enough attenuation to raise the average attenuation value of the pixel. Also, when compared to a conventional radiograph, the spatial resolution in a CAT image is much poorer.

So far in this discussion, the X-ray beam has been assumed to

be monochromatic but in comercial scanners the X-ray tube generates a broad spectrum of X-rays. This gives rise to the beam hardening artifact, which is due to the lower energy X-rays being more rapidly attenuated and so changing the shape of the energy spectrum. Because of this, the CT values vary from those which would be expected using a monochromatic source. Some scanners reduce this by correction of the measured data using a reference phantom or by prior filtering of the X-ray beam to remove the lower X-ray energies. Also, since a structure in the slice may be composed of many atomic elements, the individual effect of a single element cannot be distinguished from the whole. However several techniques have been developed to overcome these problems. Some of these have been successful but are limited in some way. These are described below.

I.3 Techniques to Image Atomic Elements.

In recent years much work had been done to investigate ways to image the spatial distribution of individual atomic elements in a cross-section for both medical and non-destructive testing applications. In conventional computerized tomography, the CAT image is a map of the spatial variation in the linear attenuation coefficient through the cross-section. However, it gives no information about the elements present nor of the distribution of these elements. The reason for this can be understood by considering an object which contains two separate structures within the cross-section of interest. Typically, such structures contain a mixture of several different atomic elements. If these structures have the same total attenuation then it is not possible to determine the distribution nor the concentration of the atomic elements for a conventional CAT image. This is true if the shape of the spectrum is not recorded when the object is scanned with a single polychromatic X-ray beam. Even if the total attenuations were different it still might not be possible to determine the attenuation due to each element when scanning at a single tube voltage. However, several methods have been developed to enable elemental specific images to be produced.

One such method is based on the use of a contrast medium as used in conventional radiographs. Iodine is commonly used as a contrast agent. If the attenuation of the iodine is high enough, it

21

may be clearly seen in a single image. If not, it may be necessary for images with and without the contrast agent to be subtracted. The resultant subtracted image shows the spatial distribution of the contrast agent. This technique is limited to situations where a contrast agent can be added to the object.

One such technique, based on this idea, was developed by Riederer and Mistretta, [5], and enables quantitative selective images of the iodine concentration in a cross-section of a patient to be made by switching the tube voltage. The method employs scans using three heavily filtered polychromatic X-ray beams, two having mean energies which straddle the iodine K-absorption edge at 33.17keV and another at a slightly higher energy. By choosing energies which straddle the iodine K-edge, the sensitivity to iodine is maximised. Two energies are sufficient if only iodine and tissue like materials are present. If the slice contains any other materials, such as bone, then three beams are necessary. This is because, for X-ray energies up to several hundred keV, the attenuation properties of all the materials present in the slice can be characterised by only two components, photoelectric and Compton. In fact, they can be expressed as linear combinations of the bone and tissue coefficients. Thus, three energies are sufficient, provided that the mean beam energies do not straddle the K-edges of any other elements present. Using this method for a simulated phantom, selective iodine images with sensitivity and precision of 1 ± 0.25 kg/m^3 and spatial resolution of 3×10^{-3}m were obtained for slices with diameters 0.3m using doses comparable to conventional CAT [3].

A second technique, called 'Dual-energy scanning', has been developed by Van Riet et al, [4], where the attenuation due to a succession of materials along an X-ray beam path is expressed as resulting from equivalent contributions of two base materials. Typically, in diagnostic cases, these consist of a water like part (tissue) and a calcium like part (bone). Knowing the incident spectrum, the attenuations corresponding to different combinations of thicknesses of water and calcium can be calculated for each tube voltage, and inversely, the combinations of thicknesses which give rise to the same attenuation. In figure I.8, iso-attenuation curves for two different tube voltages are shown. Each curve represents
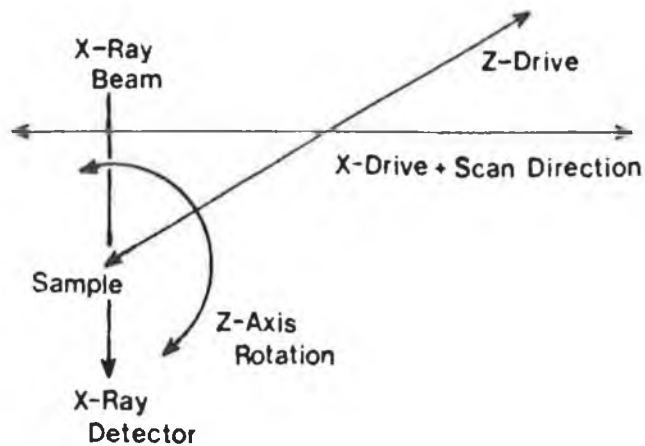
Fig. I.7
A schematic diagram of the scan table scan motions. The
sample was stepped through the beam along the X-direction and
was rotated about the Z-axis. The sample was also moved in the
Z-direction when choosing the cross-section of interest.
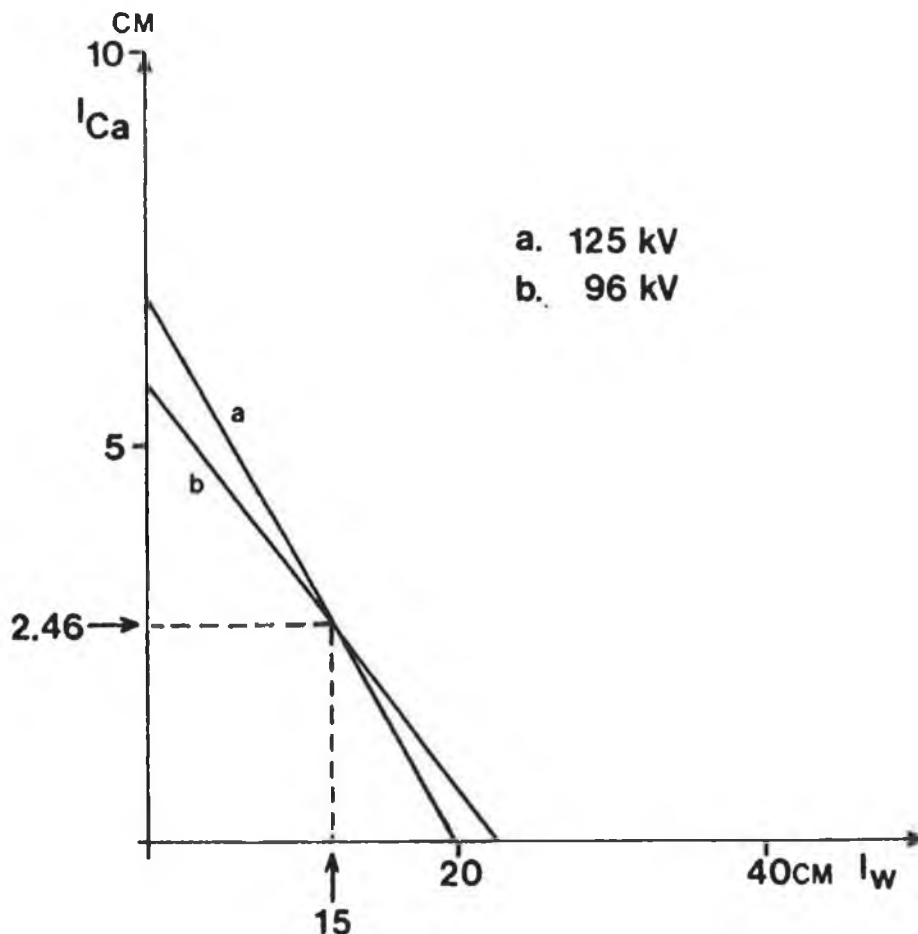
Fig. I.8
Iso-attenuation curves for two different tube voltages (125
and 96kV) for the "dual-energy scanning" technique. These
represent the combinations of thicknesses of water and calcium
yielding the observed attenuation.The crossing point represents
the unique combinations of thicknesses (1.4cm of calcium and
15cm of water) yielding the measured attenuations at both
voltages.

23

the combinations of thicknesses of water and calcium which yield the observed attenuation for that tube voltage. The crossing point of the curves represents the unique combination of thicknesses which yields the measured attenuation at both voltages. By repeating such measurements for all step positions and rotation angles, it is possible to construct separate images of the two components.

In both methods, the radiation dose is comparable to ordinary CAT scans and the errors due to beam hardening and multicomponent mixing are considerably reduced. However, these techniques are not capable of imaging elements which are close in atomic number. In fact, the method described by Mistretta and Riederer [5] requires that no other elements with similar atomic numbers are present in the slice. These problems can be overcome by scanning the object with at least two monochromatic beams which straddle the K-absorption edge or L-absorption edge of the analyte element of interest. The radiation required might come from a synchrotron, from fluorescence of a suitable target or from electron capture within a suitable radioactive source.

Grodzin, [6] and [7], has theoretically studied the application of synchrotron radiation to computerized tomography and has shown it to be especially suitable to the study of small samples. In [6], Grodzin shows that there is an optimum X-ray energy for a given sample size and material which minimizes the time for obtaining a given resolution/sensitivity. At the optimum energy, the resolution/sensitivity is determined by the total number of photons per scan. This optimum energy is quite sharp, for instance for a 1mm sample of tissue it is 6-7keV and the effectiveness at 4keV or at 12keV is an order of magnitude worse.

In the second paper, [7], Grodzin suggests taking successive tomographs, one at an energy above and another at an energy below an absorption edge of the element to be imaged. Then by making a comparison between the reconstructed images the spatial variation in the element of interest could be determined. A synchrotron is especially suited to this technique as it provides high intensity collimated beams of nearly monochromatic photons whose mean energy can be tuned across the absorption edge of the elements. For

24

instance, the National Synchrotron Light Source at Brookhaven Laboratory provides fluxes of 10^{15} photons/sec·mrad·$\Delta E/E$=1%, at energies below 25keV, [7]. Due to dose considerations, the method is only suited to imaging heavier elements (Z>50) in medical subjects. The imaging of lighter elements in humans would require incident fluxes in excess of permitted radiation dose limits because of the higher absorption at low energies. Thus light elements can only be imaged in small non human samples.

Grodzin, [7], also investigated the sensitivity to an element in a single picture element for this technique. Since the scan energies in this case are determined by the element absorption edge, a sample of a given diameter cannot always be scanned at the optimum energy which maximizes the sensitivity/resolution for that sample. Thus only for a sample diameter where the element absorption edge energy corresponds to the optimum energy will the resolution/sensitivity be maximized. With this in mind, Grodzin calculated the sensitivity, in terms of the minimum fraction of critical atoms detectible in a pixel, for all elements in samples whose diameters are optimum for the energy of the element absorption edge. Note, however that the sensitivity in terms of the minimum concentration of an element was not determined by Grodzin, [7]. As an example, see figure I.9, for a scan of a water like medium using 4×10^{10} incident photons, 100 steps per linear scan and requiring a 1% accuracy in each pixel. In this case, the sensitivity in a pixel falls rapidly from Z=40 to Z=20 by a factor of 10 and a further factor of 10 to Z=13. Furthermore, a factor of 100 increase in the incident photon flux only increases the sensitivity in a pixel by one order of magnitude. Also, as seen in figure I.9, the sensitivity to trace elements worsens as the matrix gets heavier. For example, for elements above lead the sensitivity in silicon is about the same as in water but in iron the sensitivity falls by an order of magnitude. For elements around Z=50 the sensitivity deteriorates again by a factor of ten in silicon and by a further order of magnitude in iron. The corresponding values for the L-absorption edges are not shown as the sensitivities are much poorer.

Thompson and Llacer, [9], have studied the application of synchrotron radiation to elemental imaging by scanning an excised

pig heart, in which the cardiac chambers were filled with iodinated vaseline. By making use of the sharp increase in the iodine absorption at the iodine K-absorption edge at 33.17keV, the difference in the photon transmission for monochromatic X-ray beams below and above this edge is due to the iodine only. This is because, across the iodine K-absorption edge there is no change in the attenuation coefficients of all the other elements present, i.e. the matrix. In the experimental work, a tomograph was taken at 25eV below the iodine K-edge and a second one was taken at 25eV above the K-edge. An iodine specific image was obtained by logarithmically subtracting the lower energy data from the higher energy data and then reconstructing the data. The resultant images showed the spatial distribution of the iodine in the slices through the pig heart. However no quantative evaluations were made. Beam hardening artifacts were not present as the photons were almost monochromatic. Also the background signal due to scattered photons was reduced since the beam has a divergence of only several mrad.

Flannery et al, [8], describe a system that they have developed to construct three-dimensional maps of density and elemental distribution in submillimetre samples by scanning above and below the elemental K-absorption edge with synchrotron generated X-radiation. One aspect of their work involved the development of a digital imaging X-ray detector system capable of submicrometre resolution and very high count rates. Because of the vast amount of data generated, very fast computers were required to reconstruct images in reasonable times. Experiments were done, using nearly monochromatic beams at energies just above and below the copper K-absorption edge (8.99keV), to produce three-dimensional images of a nested set of thin walled glass tubes filled with copper sulphate solutions of known concentrations. Two sets of images were reconstructed corresponding to the lower and higher energy data. Although the images were not subtracted the location of the copper was clearly visible [8]. The experiment showed that images with 10^{-6}m resolution and showing the distribution of an element can be made using synchrotrons.

As stated previously, the sensitivity to the low atomic number elements in large samples when using X-ray techniques is very poor. This is because of the high attenuation in all materials for X-ray energies of a few keV. However, alternative techniques allow such
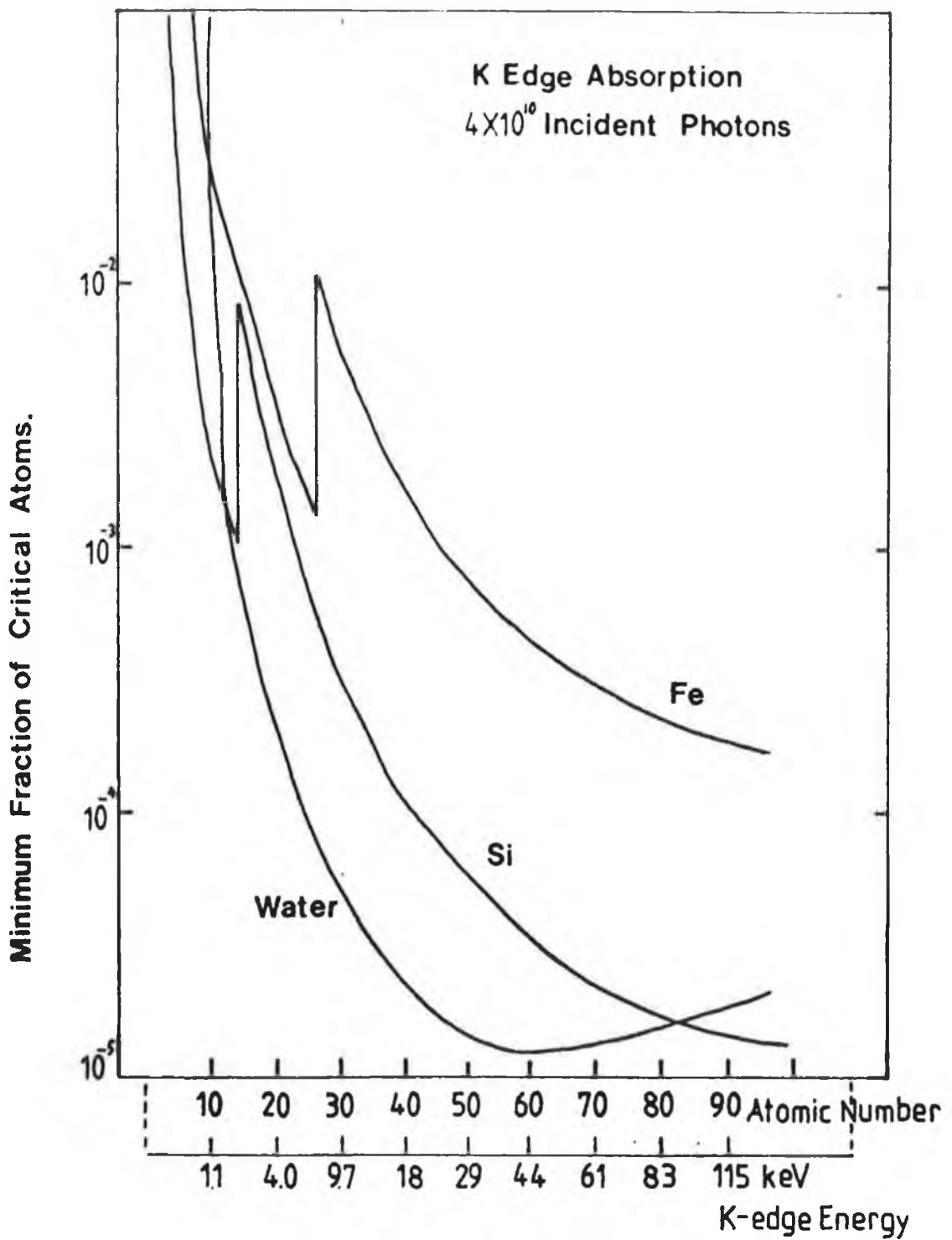
Fig. I.9
The minimum fraction of atoms detectible in water, silicon and
iron matrices as a function of atomic number and K-edge energy.
For all cases the sample size is optimum for the analyte K-edge
energy.
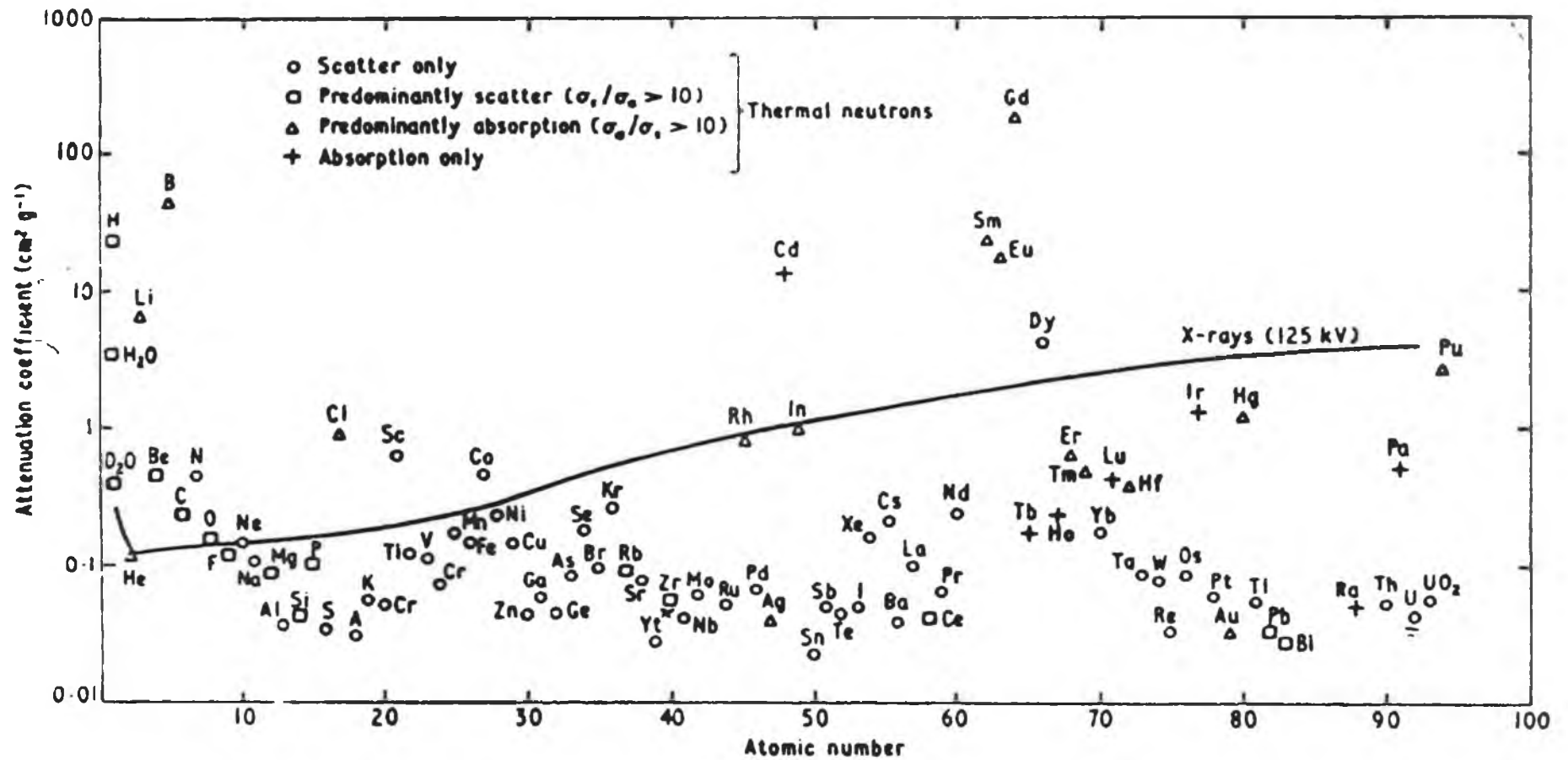
Fig. I.10
Neutron and X-ray mass attenuation coefficients
for the elements. [17]

elements to be imaged. These include neutron computerized tomography and Nuclear Magnetic Resonance. With these methods, it is possible to image some of the low atomic number elements even in high atomic number specimens.

In the first case, neutrons are uncharged and are thus highly penetrating. They interact with the nuclei in a material to an extent that depends on the existence of stable configurations of protons and neutrons in the nuclei. For a few types of nuclei, the addition of a neutron forms a particularily stable configuration so that the probability of interation is very high. As seen in figure I.10, hydrogen, boron, lithium and cadmium have much higher attenuation coefficients for neutrons than most elements and so can be readily imaged. On the other hand lead, natural uranium and aluminim have high transparencies. The principles used in neutron CAT for data collection and image reconstruction are similar to those in conventional CAT. However the neutron sources and detectors differ considerably [16]. Neutron CAT images have been sucessfully produced by G. Pfister et al. [17] and by G. Matsumoto and S. Krata [18]. However, the nature of the sources required i.e. nuclear reactors, accelerators and Van der Graff generators, limit the widespread use of the technique, especially as a medical diagnostic tool. Also, as shown, the number of elements that can be imaged is limited.

Another imaging technique which is now widely used in medical applications is Nuclear Magnetic Resonance, [19]. This method is based on the magnetic moment that is present in a wide variety of organic and inorganic materials. To possess a magnetic moment the nuclei must contain an odd number of protons and neutrons. The usual atoms of many elements do not show this effect eg, ^{12}C and ^{16}O but most elements involved in biological systems have a useful isotope such as ^{23}Na, ^{14}N, ^{31}P, ^{19}F, ^{13}C, ^{17}O and ^{1}H. In the presence of an external magnetic field the magnetic moments tend to align with the field. These can be caused to precess by an externally applied radio-frequency signal. When excitation ceases, the magnetic moment decays to it equilibrium state and emits a signal at its resonant frequency. This resonant frequency is characteristic of the element. Hydrogen provides by far the most intense signal and is thus most commonly imaged. From these signals a spatial image of the distribution of hydrogeon can be produced.

Other elements can be distinguished by their characteristic procession frequencies but unlike hydrogen they require very long data acquisition times. In fact only a few elements have been sucessfully imaged to date, most notably, fluorine in the form of a tracer, by Holland et al. [20], sodium-23 by De Layre et al. [21] and phosphorous-31 by Haselgrove et al. [22]. To date, NMR has been mainly used in medical applications.

In all of the techniques described, the number of elements and the range of atomic numbers that can be imaged is limited. In the presence of other elements of similar atomic number some of these techniques fail, [4] and [5]. Also, in all the methods so far described only one element can be imaged in a single scan. Even though synchrotrons are well suited to producing elemental specific images when using differential absorption across the element K-absorption edge, they are not very common. There are only 25 synchrotrons worldwide. In this thesis, element specific images are produced using both radioisotopes and X-ray tube sources. An energy despersive Si(Li) detector is used, so that, in principle, all elements whose absorption edges lie within the energy range of the detector can be imaged. In fact, by doing a pulse-height analysis of the tube spectrum using a multi-channel analyser, several elements close in atomic number can be imaged simultaneously. In addition, theory is developed so that quantative images can be produced for the cases when the analyte element is added to the matrix and when the anlyte element is already present.

In previous works on sensitivity, no easy method has been developed to calculate the minimum detectable concentration of an element in a given matrix sample. In this work, equations to calculate the minimum concentration of an element in any matrix are derived for the cases when analyte can be added to the matrix and when it is already present. This is described in detail in chapter II. Finally, comparisons of calculated concentrations are made with experimentally determined minimum detectable concentrations.

Chapter II

II.1 <u>Introduction to Differential X-ray Absorptiometry.</u>

After the discovery of X-rays by Roentgen [23], one of their first properties noted was that the X-ray photons are absorbed by differing amounts by different materials of the same thickness. Within a year of their discovery, the absorption properties of X-rays was widely applied in medical and industrial radiography. In 1901, Roentgen received the first Nobel Prize for his discovery and his pioneering work with X-rays. In 1909, Barkla [24] noted evidence of the presence of absorption edges. However, it was Glocker and Frohnmoyer [25], who in 1925 first used these absorption edges, in X-ray absorptiometry, to determine elemental concentration in specimens. This involved passing one or more X-ray energies on both sides of analyte element absorption edge through a cell, containing both the analyte and matrix solution. The process was then repeated for a cell containing matrix only. Knowing the absorption coefficients of the analyte element at the bracketing energies and the cell thickness, the analyte equivalent thickness along the path length, as well as the analyte element concentration, could be calculated. Since then, the procedure has been refined and is now used to measure the concentration of analyte elements in solutions, solids, briquets and even gases.

In this thesis, differential X-ray absorptiometry is applied to Computerized Axial Tomography (CAT) to determine the analyte concentration distribution through a slice in a specimen. In a typical CAT scan, the analyte equivalent thickness is determined for many path lengths through the cross-section and these are then used to construct an image of the slice. In this section, the equations to calculate the equivalent thickness for the case when

31

analyte can be added to the matrix specimen and for the cases when the analyte is already present are derived.

II.2.1 Principles of X-ray Absorptiometry.

Consider a pencil beam of X-rays directed onto a homogenous specimen of uniform thickness "P" (metres) and density "p" (kilogrammes/metre^3). The resultant transmitted X-ray beam has flux N, which is always less than N_0, the incident beam flux, because of absorption. The transmitted beam flux is given by

$$N = N_0 \exp (-U\ P) \quad \dots \quad 2.1$$

where U (metres^{-1}) is the linear attenuation coefficient. Alternatively, this equation can be rewritten as

$$N = N_0 \exp (-u\ t) \quad \dots \quad 2.2$$

where u is the mass absorption coefficient of the material (m^2/kg) and t is the equivalent thickness (kg/m^2) along the beam path. The mass absorption coefficient (m^2/kg) is defined as the linear attenuation coefficient (m^{-1}) divided by the density p (kg/m^3). The equivalent thickness can be written in terms of the specimen thickness and the specimen density as t=pP. From now on, the variables t and u are used.

The mass absorption coefficient u is a property of an element and it is independent, for practical purposes, of the chemical or physical state. It varies only with atomic number and X-ray energy. If a specimen consists of several elements, then for any X-ray energy, the total mass absorption coefficient at any point in the specimen is given by

$$u = \sum w_n\ u_n \quad \dots \quad 2.3$$

which is the sum of the weight fraction w of each element times its mass absorption coefficient. For the case where a specimen consists of one element of interest, called the analyte, in a matrix of other elements, equation 2.3 can be given by

$$u = w_a\ u_a + w_m\ u_m \quad \dots \quad 2.4$$

where subscripts a and m refer to analyte and matrix respectively.

Substituting for u in equation 2.2 with equation 2.4, it becomes

$$N = N_0 \exp \left\{ - \left(w_a u_a + w_m u_m \right) t \right\} \quad \ldots \ 2.5$$

The mass absorption coefficient of an element is the result of several phenomena. These include photoelectric absorption, which is dominant at low energies, Compton scattering which is dominant at energies greater than several hundred keV and pair production which occurs at energies greater than 1MeV. See figure II.1 which shows the relative contributions of each effect as a function of X-ray energy for some atomic elements. In general, for a given X-ray energy, the mass absorption coefficient increases with atomic number since the "heavier" the element the greater its stopping power for X-rays. Similarily, for a given element, the mass absorption coefficient should decrease with increasing X-ray energy as X-ray penetration increases with energy.

However, there are abrupt discontinuties in the absorption coefficients, first noted by Barka [24]. It is these discontinuties, called absorption edge jumps, which are significant in differential X-ray absorptiometry. See figure II.2. At low X-ray energies, less than 100keV, the photo-electric effect dominates over Compton scatter and pair-production. In the photoelectric effect, the minimum X-ray energy required to expel an electron from a given level in an atom is called the absorption edge energy. This gives rise to the abrupt increase in the mass absorption coefficient on the high energy side of the absorption edge. Each element has as many absorption edges as it has excitation potentials, one K, three L, five M etc. In general, only K and LIII absorption edges have absorption edge differences (uh-ul) large enough to be useful for differential absorptiometry. For most elements the K-edge difference is greater. For heavier elements the LIII edge difference is greater but the overall absorption may be higher due to their low energy. It is for this reason that the K-absorption edges are prefered in this work. The absorption curves of the chemical elements showing the K-absorption edges are shown in figure II.3.

Differential X-ray absorptiometry was first applied by Glocker and Frohnmeyer [25], for the determination of the quantity of an

33
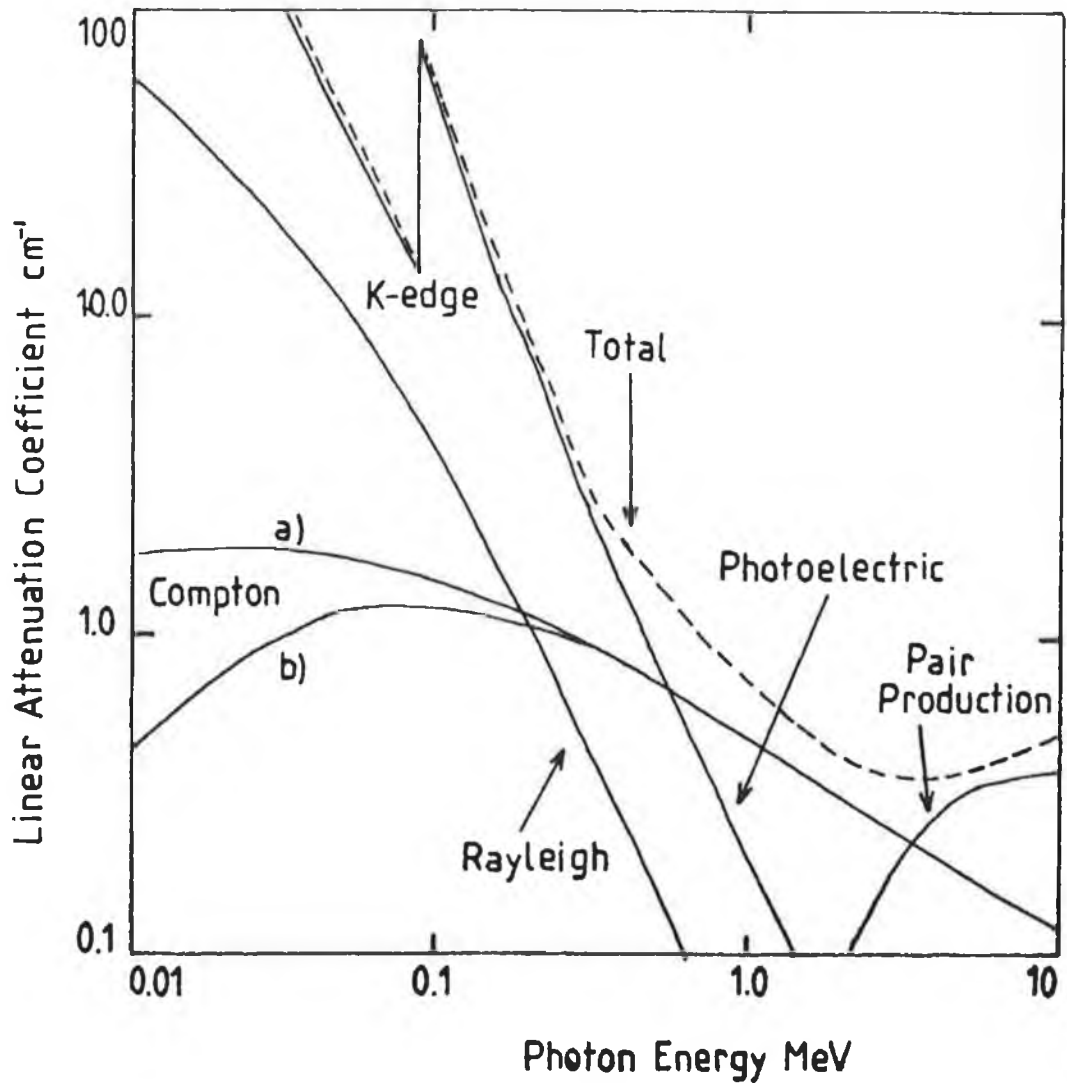
Fig. II.1
Linear attenuation coefficients as a function of photon energy for a collimated monochromatic beam in lead. The relative contributions of photoelectric, Compton effect, Rayleigh and pair production are shown. The Compton (a) and (b) curves are those pertaining to free and bound electrons.
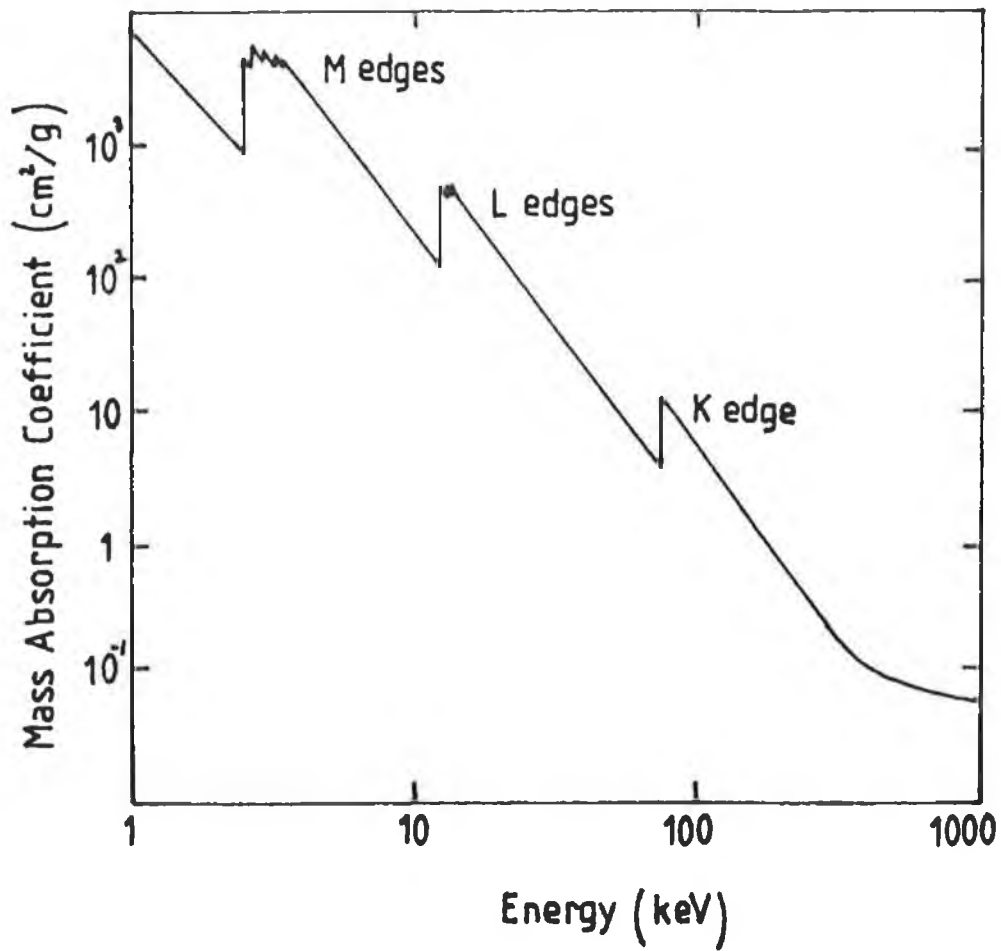
Fig. II.2
The mass absorption coefficient of lead as a function of photon energy. It shows one K-edge, three L edges and five M edges.

element in a homogenous specimen. In differential X-ray absorptiometry, one or more X-ray energies, which straddle the analyte absorption edge, are passed through the homogenous specimen. Knowing the beam path length, the analyte concentration in the specimen can be calculated using the measured transmitted intensities if the analyte absorption coefficients are known. In this work, analyte elements are distributed unevenly in non-homogenous specimens. Applying differential X-ray absorptiometry to CAT the elemental distribution in a slice through the specimen and their concentrations can be determined for such specimens. In the next section, the mathematical background for differential X-ray absorptiometry is given. In section II.4 the methods for producing the images are described.

II.2.2 Mathematics of Differential X-ray Absorptiometry.

Consider two monochromatic co-linear X-ray beams, one on either side of the analyte K-absorption edge, see figure II.4, being incident on a specimen. The emergent fluxes are given by

$$N_1 = N_{01} \exp\left\{ -\left(W_a \, U_{al} + W_m \, U_{ml} \right) t \right\} \quad \dots \quad 2.6$$

and

$$N_h = N_{0h} \exp\left\{ -\left(W_a \, U_{ah} + W_m \, U_{mh} \right) t \right\} \quad \dots \quad 2.7$$

where the subscripts 1 and h refer to the low energy beam E_l and the high energy beam E_h respectively. Division of equation 2.6 by equation 2.7 gives

$$\frac{N_1}{N_h} = \left(\frac{N_{01}}{N_{0h}} \right) \exp\left\{ W_a \left(U_{ah} - U_{al} \right) t \right\} \exp\left\{ W_m \left(U_{mh} - U_{ml} \right) t \right\} \dots 2.8$$

Rearrangement of equation 2.8 gives

$$W_a \, t = \left\{ \ln\left(\frac{N_1 \, N_{0h}}{N_h \, N_{01}} \right) \right\} \left(U_{ah} - U_{al} \right)^{-1} + W_m \, t \left\{ \frac{(U_{mh} - U_{ml})}{(U_{ah} - U_{al})} \right\} \quad \dots \quad 2.9$$

Since the composition of the matrix may be unknown it is desirable to remove the matrix term on the right hand side of this equation. Hence, the bracketing X-ray beam energies should be close enough together in energy and therefore also close to the

Fig. II.3
 The mass absorption coefficients of the elements as a
function of photon wavelength showing the K-absorption edges.
The conversion factor to photon energy is Ekev= 12.396/λ.
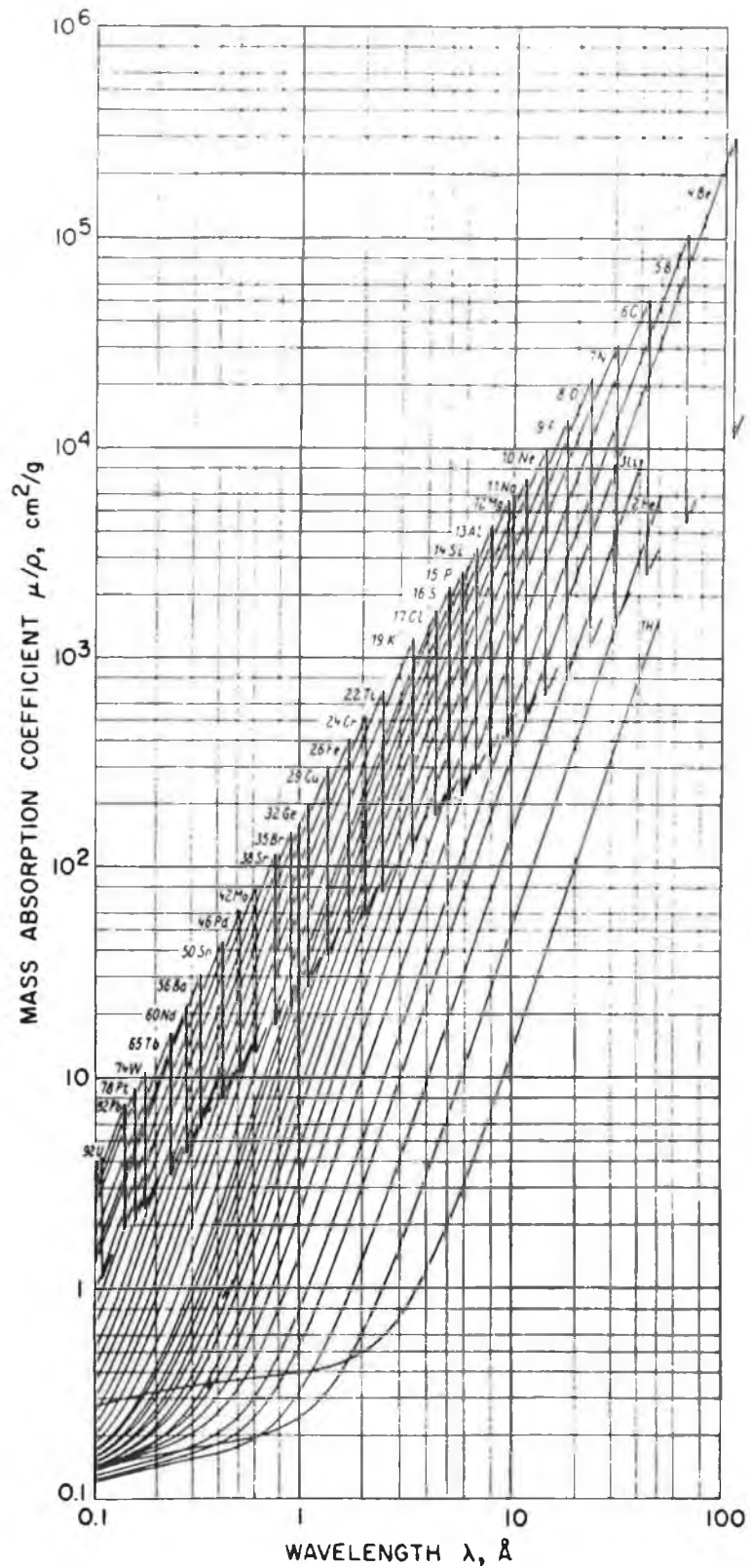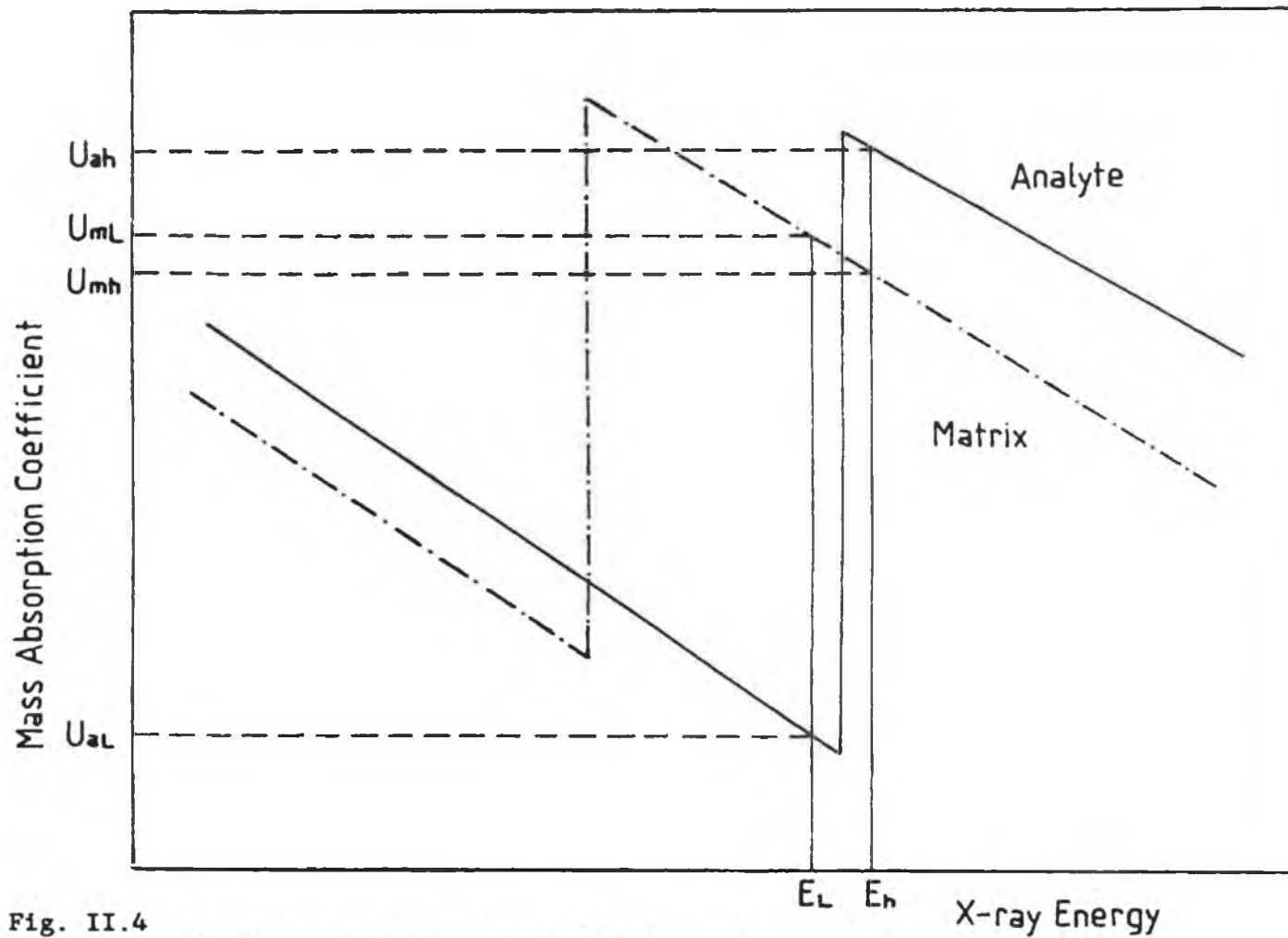
Fig. II.4

The variation of **mass absorption coefficient** of analyte and matrix elements near the K-absorption edge of the analyte. The difference in the analyte **mass** absorption coefficient at energies E_l and E_h is much greater for the analyte than the matrix. Note, $U_{ah}-U_{al}$ is positive while $U_{mh}-U_{ml}$ is negative.

K-absorption edge in order to minimise the effect of the matrix absorption. However, both energies should be far enough from the absorption edge, especially on the high energy side, to avoid the absorption edge fine structure. In general fine structure is confined to within 200eV of the absorption edge, [26]. If the matrix undergoes little change in its absorption coefficient between the bracketing X-ray energies, i.e. $u_{mh}=u_{ml}$, then equation 2.9 becomes

$$t_a = \left\{ \ln \left(\frac{N_l \, N_{Oh}}{N_h \, N_{Ol}} \right) \right\} \left(u_{ah}-u_{al} \right)^{-1} \quad \ldots \ldots 2.10$$

where $t_a = w_a \, t$ is the analyte equivalent thickness along the beam path.

Without the use of a synchrotron it is unlikely that available X-ray energies will be close enough to the analyte K-absorption edge in order that the matrix term can be dropped from equation 2.10. Near the K-edge of the analyte, the term $(u_{ah}-u_{al})$ is positive while the term $(u_{mh}-u_{ml})$ is negative. See figure II.4. Thus the effect of the matrix term on equation 2.9 is to reduce the measured analyte equivalent thickness. Since, the composition of the matrix is unknown in most cases, a technique to correct for the matrix effect is required. Here, two such techniques are described.

II.3.   Correction Techniques for Matrix Effect.

II.3.1   Technique to Correct for Matrix Effect when the Analyte
          can be Added to the Matrix.

The technique of determining analyte equivalent thickness using the transmitted X-ray fluxes through specimens when the anaylte can be added to the matrix specimen are well established. Such techniques are described by Bertin [27], where the Kα and Kβ lines of a suitable element which straddle the analyte K-absorption edge are used. Since the energies of the K-lines may lie at several keV from the analyte K-edge, it is first necessary to make measurements on a matrix, before making measurements on the matrix plus analyte, so that the effect of the matrix on the analyte equivalent thickness can be removed. An equation, for this technique, to calculate the corrected analyte equivalent thickness has been formulated by J. Fryar and K.J.McCarthy [28] and it is described in

39

detail here.

The transmitted fluxes for a monochromatic pencil beam of X-rays through the matrix only specimen are given by

$$N_{ml} = N_{Oml} \exp\left\{-\left(w_m \, u_{ml}\right)t\right\} \quad \ldots \, 2.11$$

on the low energy side of the analyte K-edge

$$N_{mh} = N_{Omh} \exp\left\{-\left(w_m \, u_{mh}\right)t\right\} \quad \ldots \, 2.12$$

on the high energy side of the absorption edge. Dividing equation 2.11 by equation 2.12 gives

$$\left(\frac{N_{ml}}{N_{mh}}\right) = \left(\frac{N_{Oml}}{N_{Omh}}\right) \exp\left\{\left(u_{mh}-u_{ml}\right)t_m\right\} \quad \ldots \, 2.13$$

where $t_m = w_m t$ is the matrix equivalent thickness along the path length. Cross multiplying the N_0 terms, equation 2.13 becomes

$$\exp\left\{\left(u_{mh}-u_{ml}\right)t_m\right\} = \left(\frac{N_{ml}}{N_{mh}}\right)\left(\frac{N_{Omh}}{N_{Oml}}\right). \quad \ldots \, 2.14$$

Similarily for the specimen containing both the analyte and the matrix, the transmitted fluxes are given by

$$N_{(a+m)l} = N_{O(a+m)l} \exp\left\{-\left(w_a \, u_{al} + w_m \, u_{ml}\right)t\right\} \quad \ldots \, 2.15$$

and by

$$N_{(a+m)h} = N_{O(a+m)h} \exp\left\{-\left(w_a \, u_{ah} + w_m \, u_{mh}\right)t\right\} \quad \ldots \, 2.16$$

for the same X-ray energies. Division of equation 2.15 by equation 2.16 gives

$$\left(\frac{N_{(a+m)l}}{N_{(a+m)h}}\right) = \left(\frac{N_{O(a+m)l}}{N_{O(a+m)h}}\right)\exp\left\{\left(u_{mh}-u_{ml}\right)t_m\right\}\exp\left\{\left(u_{ah}-u_{al}\right)t_a\right\}. \quad .2.17$$

Substitution of the matrix exponential term of equation 2.17 with equation 2.14 gives

$$\left(\frac{N_{(a+m)l}}{N_{(a+m)h}}\right) = \left(\frac{N_{O(a+m)l}}{N_{O(a+m)h}}\right)\left(\frac{N_{ml}}{N_{mh}}\right)\left(\frac{N_{Omh}}{N_{Oml}}\right)\exp\left\{\left(u_{ah}-u_{al}\right)t_a\right\}. \quad .. \, 2.18$$

If the same source of X-rays is used in both cases then the ratios of the incident low and high X-ray energies are the same i.e.

$$\left(\frac{N_{O(a+m)l}}{N_{O(a+m)h}}\right) = \left(\frac{N_{Oml}}{N_{Omh}}\right) \quad \ldots \ 2.19$$

so these cancel each other in equation 2.18. This leaves equations 2.18 as

$$\left(\frac{N_{(a+m)l}}{N_{(a+m)h}}\right) = \left(\frac{N_{ml}}{N_{mh}}\right) \exp\left\{\left[u_{ah}-u_{al}\right]t_a\right\} \quad \ldots \ 2.20$$

By cross-multiplying the N_m terms and then taking the natural logarithms of both sides of equation 2.20, an equation for the analyte equivalent thickness along the beam path between the source and detector results. It is given by

$$t_a = \ln\left\{\left(\frac{N_{(a+m)l}}{N_{(a+m)h}}\right)\left(\frac{N_{mh}}{N_{ml}}\right)\right\}\left(u_{ah}-u_{al}\right)^{-1} \quad \ldots \ 2.21$$

Using equation 2.21, the analyte equivalent thickness, t_a, along any beam path through a specimen can be calculated. In this case, the effect of the matrix, which was previously present in equation 2.10, has been removed. To calculate t_a, the transmitted fluxes through the matrix, N_m , are measured initially. Then, when the analyte has been added, the matrix plus analyte transmitted fluxes, $N_{(a+m)}$, are measured for the same path. As stipulated in equation 2.19, the same source of X-rays should be used for both measurements. Finally, the values of mass absorption coefficients, u_{ah} and u_{al}, can be found in published tables [29].

When applied to Computerized Axial Tomography, this technique requires that two scans of the specimen be made. The first scan is made of the matrix only. When completed, an identical scan is made of the matrix plus analyte. In this work, a scan consists of linear and rotational steps. At each step position, when all the data has been collected, the analyte equivalent thickness along each beam path between the source and detector is calculated using equation 2.21. These analyte equivalent thicknesses are then stored and used in the reconstruction of a slice through the specimen. The resultant reconstructed image shows the distribution of the analyte in the slice and also the concentration values. See section II.4.

As described, the distribution of analyte in a slice through a specimen can be obtained using this technique. However, there are several drawbacks to this method. The first is that it is limited to samples where the analyte can be added to or removed from the matrix. Secondly, the technique requires two identical scans. This means that the specimens must be aligned exactly for both scans. Finally, a complete scan using the K-lines form a radioisotope takes much longer than an ordinary CAT scan. The reason for this, is that the radioisotope sources used have low photon fluxes thus requiring longer count times. In order to overcome these drawbacks, a second technique was developed which made it possible to collect, in a single complete scan, the data required to image multiple analyte elements.

II.3.2 Technique to Correct for Matrix Effect by Extrapolation to The Analyte Absorption Edge.

Since it may not always be possible to add analyte to the matrix, a second technique for matrix correction was developed by J. Fryar, K.J. McCarthy and A. Fenelon [30]. In this method the analyte equivalent thickness along a path length can be determined in a single measurement. This involves measuring the transmitted beam fluxes through the specimen at two or more energies on both sides of the analyte absorption edge. Then, by extrapolating the photon counts to the analyte absorption edge, the effect of the matrix is removed to give analyte equivalent thickness only.

For the case where two energies on both sides of the analyte absorption edge are considered, see figure II.5, the transmitted fluxes are given by the equations

$$N_{l1} = N_{Ol1} \exp \left\{ -\left(Wa\ Ual1 + Wm\ Uml1 \right) t \right\} \quad \ldots\ 2.22$$

$$N_{l2} = N_{Ol2} \exp \left\{ -\left(Wa\ Ual2 + Wm\ Uml2 \right) t \right\} \quad \ldots\ 2.23$$

$$N_{h1} = N_{Oh1} \exp \left\{ -\left(Wa\ Uah1 + Wm\ Umh1 \right) t \right\} \quad \ldots\ 2.24$$

$$N_{h2} = N_{Oh2} \exp \left\{ -\left(Wa\ Uah2 + Wm\ Umh2 \right) t \right\} \quad \ldots\ 2.25$$
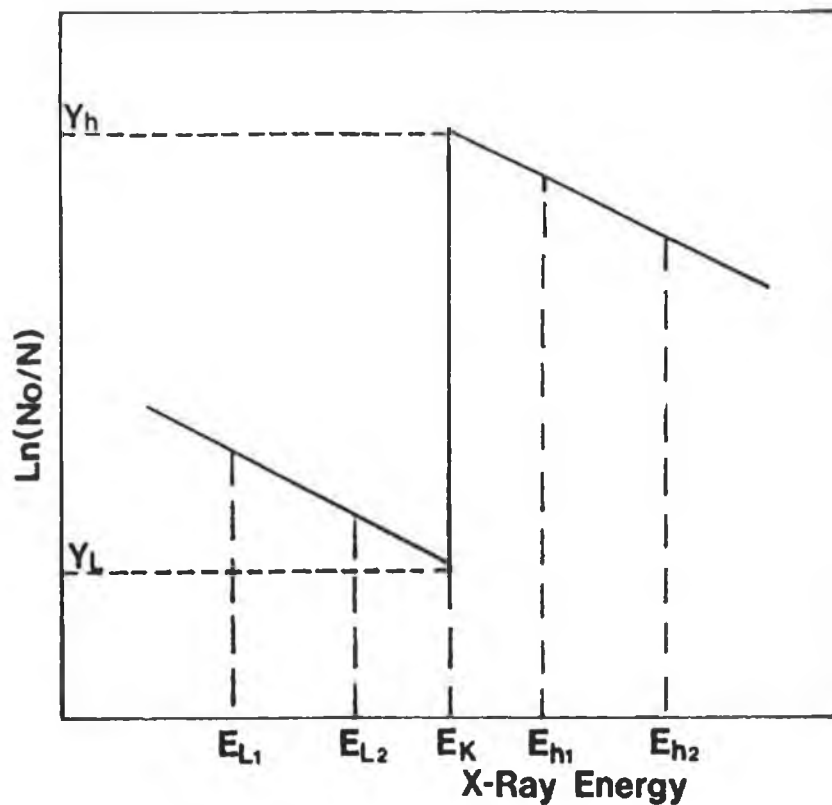
Fig. II.5
Schematic diagram to illustrate the extrapolation of
projection data, taken at two X-ray energies on both sides
of the analyte K-edge energy. Y_h and Y_l are the extrapolated
values of ln (N_0/N)

for X-ray energies $E_{l1} < E_{l2} < E_K$ and for $E_K < E_{h1} < E_{h2}$, where E_K is the analyte absorption edge energy. Cross multiplying by the N_o term in each equation above and then taking the natural logarithm of both sides of the resultant equation gives

$$\ln \left(\frac{N_{ol1}}{N_{l1}} \right) = t_a \, u_{al1} + t_m \, u_{ml1} \quad \ldots \ 2.26$$

$$\ln \left(\frac{N_{ol2}}{N_{l2}} \right) = t_a \, u_{al2} + t_m \, u_{ml2} \quad \ldots \ 2.27$$

$$\ln \left(\frac{N_{oh1}}{N_{h1}} \right) = t_a \, u_{ah1} + t_m \, u_{mh1} \quad \ldots \ 2.28$$

$$\ln \left(\frac{N_{oh2}}{N_{h2}} \right) = t_a \, u_{ah2} + t_m \, u_{mh2} \quad \ldots \ 2.29$$

where $t_a = w_a \, t$ and $t_m = w_m \, t$. Since $u_{a1} > u_{a2}$ and $u_{m1} > u_{m2}$ for energies both above and below the absorption edge, it is clear that

$$\ln \left(\frac{N_{ol1}}{N_{l1}} \right) \rangle \ln \left(\frac{N_{ol2}}{N_{l2}} \right) \quad \ldots \ 2.30$$

and

$$\ln \left(\frac{N_{oh1}}{N_{h1}} \right) \rangle \ln \left(\frac{N_{oh2}}{N_{h2}} \right) \quad \ldots \ 2.31$$

A plot of $\ln(No/N)$ against X-ray energy is shown in figure II.5. Extrapolation to the analyte absorption edge E_K on the low and high energy sides gives the values of $\ln(No/N)$ at the low and high energy sides of the K-absorption edge as Y_l and Y_h respectively, where

$$Y_l = u_{al} \, t_a + u_{ml} \, t_m \quad \ldots \ 2.32$$

and

$$Y_h = u_{ah} \, t_a + u_{mh} \, t_m. \quad \ldots \ 2.33$$

The difference in the $\ln(No/N)$ terms at the absorption edge is $Y_h - Y_l$ which is given by

$$Y_h - Y_l = \left(u_{ah} - u_{al} \right) t_a. \quad \ldots \ 2.34$$

The u_m term disappears since $u_{ml}=u_{mh}$ across the analyte absorption edge while the difference in the analyte absorption is $(u_{ah}-u_{al})$. Rearrangement of equation 2.34 gives the analyte equivalent thickness along the beam path as

$$t_a = \left(Y_h - Y_l \right)\left(u_{ah} - u_{al} \right)^{-1} \quad \ldots\ldots 2.35$$

which becomes

$$t_a = \frac{\ln\left(\dfrac{N_{oh}}{N_h}\right)_e - \ln\left(\dfrac{N_{ol}}{N_l}\right)_e}{\left(u_{ah} - u_{al} \right)} \quad \ldots\ldots 2.36$$

when the Y's are replaced by the $\ln(N_o/N)$ terms. The term e indicates the extrapolated values. Now, if the number of photons per unit energy interval is the same just above and below the analyte absorption edge then the N_o terms in equation 2.36 cancel. Thus equation 2.36 becomes

$$t_a = \frac{\ln\left(\dfrac{N_l}{N_h} \right)_e}{\left(u_{ah} - u_{al} \right)} \quad \ldots\ldots 2.37$$

In both equation 2.36 and 2.37 the effect of the matrix has been removed by extrapolation to the absorption edge. Thus if two or more monochromatic co-linear X-ray energies on both sides of the analyte absorption edge are available, the analyte equivalent thickness can be determined in a single measurement.

The energies required can be easily obtained if a continuous spectrum of X-rays is used. Narrow energy bands can be defined on a multi-channel analyser if an energy dispersive detector is used. See chapter IV for the experimental setup.

During a CAT scan of a specimen, which contains both analyte and matrix, the transmitted fluxes through the specimen are measured for each narrow energy band at each step position. The $\ln(N_o/N)$ values for each energy band are then calculated and extrapolated to the analyte absorption edge. Then the analyte equivalent thickness along the beam path can be calculated using

equation 2.36. The mass absorption coefficients are obtained from published tables [29]. In this way, the required data to reconstruct an image showing the analyte distribution and its concentration in a slice through the specimen, containing both analyte and matrix, can be collected in a single scan.

This technique also allows the analyte equivalent thicknesses of several elements which are close in atomic number, to be determined simultaneously. For two elements, six energy bands are required, since the data taken between two absorption edges is extrapolated to both edges. Similarily, for n analyte elements, 2n+2 energy bands are required. See figure II.6. In chapter IV, several elements in a specimen are scanned and imaged in a single scan.

It is reasonable to assume that corrections for dead-time in the pulse counting apparatus, especially for high count rates, and for source fluctuations may be important. Consider the case where the dead-times in the incident flux N_0 and transmitted flux N are different. In this case, if ZN_0 and zN are the corrected values for N_0 and N for each energy band, then the resultant equations are $\ln(ZN_0/zN)$ or $\ln(Z/z)+\ln(N_0/N)$. Thus the effect of dead-time correction is an equal displacement along the ordinate axis for each point in figure II.7. In effect, the extrapolated value of Y_h-Y_l is unaffected. However, high dead-times are undesirable as they gives rise to to poorer counting statistics. In order to reduce dead-time, the beam from the X-ray tube source is filtered. The filtering reduces the flux and also removes unwanted energies, thus reducing the dead-time. See section IV.3.3.1c Similarily, equation 2.36 is unaffected by changes in the intensity of the source. This is because the photon counts appear as ratios within the logarithms, so fluctuations in the source between recording the incident and transmitted spectra are eliminated upon subtraction of the logarithms. In equation 2.37, fluctuations in the source between measuring the incident and transmitted fluxes are insignificant since the term N_0 does not appear in the equation.
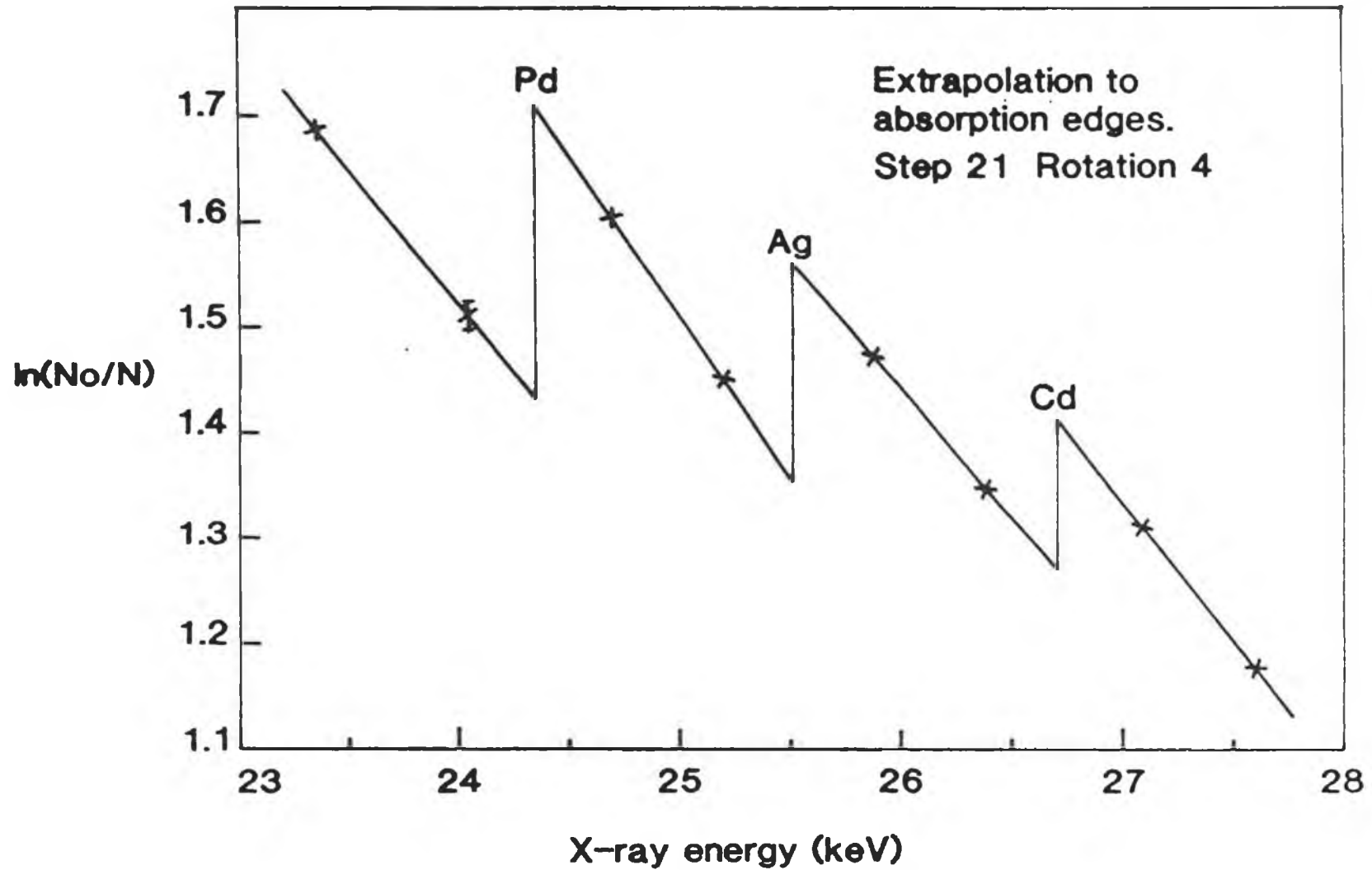
Fig. II.6
 Extrapolation to the Pd, Ag and Cd K-absorption edges of the
ln(No/ N) values in narrow energy bands. This data is taken
from the expereiment described in section IV.3.3.4.
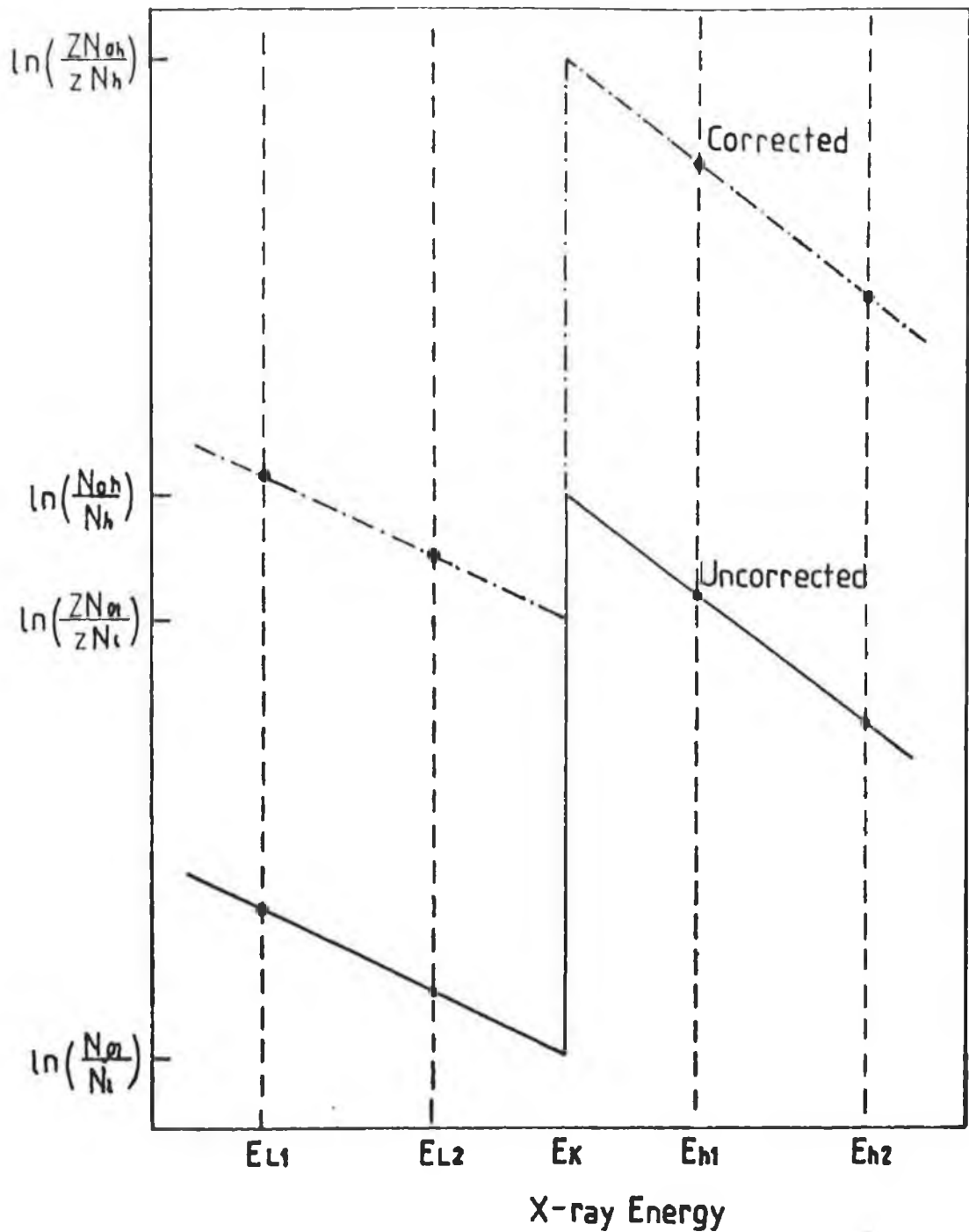
Fig. II.7
The effect of dead-time corrections to the $\ln(N_0/N)$ data is shown here to be an equal displacement along the ordinate axis on both sides of the analyte K-edge. In this case Z and z are the correction factors to the incident beam N_0 and transmitted beams N respectively.

II.4 Reconstruction Algorithms.

II.4.1 Introduction to Reconstruction Algorithms.

The problem of reconstructing a two dimensional section of an object from a set of one dimensional projections arose and found solution independently and more or less simultaneously in the fields of electron microscopy (Crowther et al. [31]), radio-astronomy (Bracewell and Riddle. [32]) and X-ray computerized tomography (Gordon et al. [33]). The process of image reconstruction has been defined by Herman [34]; *"image reconstruction from projections is the process of producing an image of a two dimensional distribution from estimates of the line integrals along a finite number of lines of known locations"*. Historically, the solution to the problem of image reconstruction in CAT has polarised into two distinct and mathematically dissimilar classes of algorithms. These include

1) Analytic Solutions.

These reconstruction techniques, which are used in many commercial CAT machines because of their speed, include the filtered back-projection methods. With these algorithms, the reconstruction process can be implemented as the data is collected and the image can be produced in a single iteration. Without prior filtering of the projection scan data, simple back-projection produces a blurred image. See figure II.8. Filtration was introduced to eliminate this blurring but it is not without side effects. Some filters commonly used include the Shepp-Logan filter [35], the Ramachandran-Lakshminarayanan (Ram-Lak) [36], which is used in this work and the Hann filter.

2) Iterative Solutions

In the first commercial EMI scanner, by Hounsfield [3], the reconstruction technique used was one form of a general class called iterative solutions. In its simplest form, the iterative technique is essentially a mathematical trial and error procedure that gradually approaches the best estimate of the object. It is no longer favoured by commercial manufactures for several reasons. For instance, before starting the reconstruction, all the projection data is required. The technique is also slower than the now
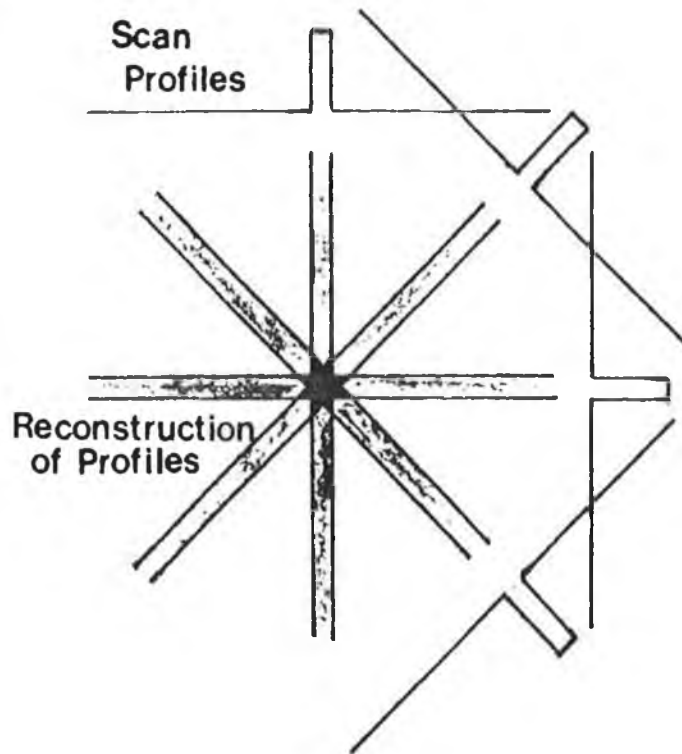
Fig. II.8
A schematic diagram to illustrate how simple back-projection
of the scan profiles of a small cylindrical object produces a
blurred image.
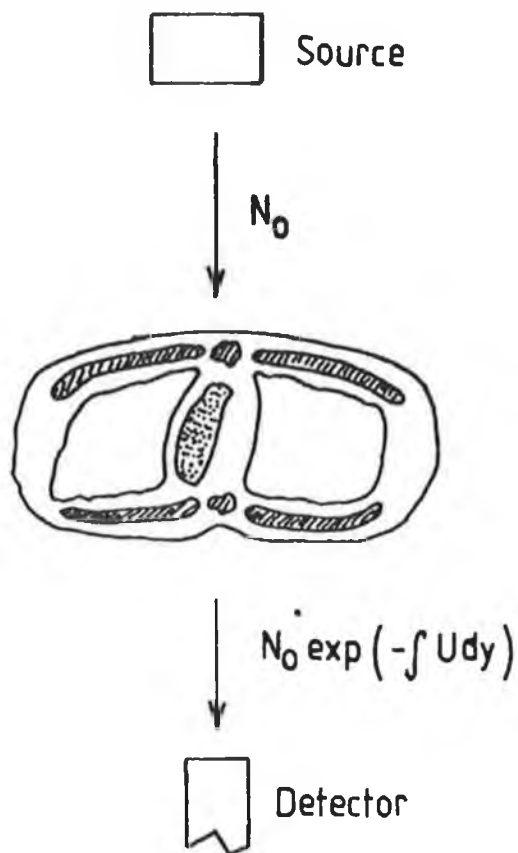
Fig. II.9
A schamatic diagram to illustrate the transmiitted beam flux
N for a well collimated monochromatic X-ray beam No incident on
a nonhomogenous body.

favoured analytic technique. This is because several iterations are normally required before an acceptable image is produced. In this work, the Algebraic Reconstruction Technique, ART, is one of the two reconstruction techniques used. Although slower, the resultant concentrations were found to be closer to the expected values.

These algoritms are described in more detail further on in this chapter. Before that, the scanning method employed and the idea of ray-sums are described.

II.4.2 Parallel Mode of Data Collection.

In the parallel mode of data collection, one X-ray source and one X-ray detector are used. See figure I.4. Two motions are required. First, the source and detector are stepped in parallel along a direction which is perpendicular to the line connecting the source and detector. At each step position, for a set period of time, the detected transmitted photons are counted, and the source and detector are then moved to the next position. After a set number of linear steps, the source and detector are rotated about the object by a few degrees and the linear stepping procedure is repeated.

In first generation medical scanners, the source and detector were stepped and rotated as described above, but in this work the specimen was stepped and rotated while the source and detector were stationary. This is because the preamplifier of the Si(Li) detector was immersed in a liquid nitrogen dewar. The two methods are geometrically analogous and the resultant projections are the same. This method of scanning has been used with synchrotron sources by Suzuki et al. [45].

II.4.3 Ray-Sums.

Consider a monochromatic collimated X-ray beam as it passes through a specimen. See figure II.9. Since the specimen is inhomogenous, the attenuation of the X-ray beam is given by Beer's law as

$$N = N_0 \exp\left(-\int U(y) \, dy \right) \quad \ldots \ldots 2.38$$

where N and N_0 are the transmitted and incident photon counts, $U(y)$

51

is the linear attenuation coefficient at a point y along the line
joining the source and detector and dy is the differential of path
length along the beam. The ray-sum for the corresponding beam, i.e.
the total attenuation of the beam between the source and detector,
is defined as

$$\text{ray-sum} = \ln\left(\frac{N_o}{N}\right) = \int U(y)\, dy \quad \ldots \ 2.39$$

Using such ray-sums as the one dimensional projections, the
resultant reconstructed image shows the spatial variation in linear
attenuation coefficient through the slice of the specimen.

Similarily, for differential X-ray absorptiometry applied to
CAT, where the projection data is analyte equivalent thickness, t_a,
the ray-sum is defined as

$$\text{ray-sum} = t_a = \int C_a(y)\, dy \quad \ldots \ 2.40$$

where the right-hand side of the equation is the integral along the
line joining the source and detector of the analyte concentration,
$C_a(y)$, at the point y. In section II.3, the analyte equivalent
thickness was defined in equations 2.21 and 2.36. When equation
2.36 is substituted for t_a in equation 2.40 it gives

$$\frac{\ln\left(\frac{N_{oh}}{N_h}\right)_e - \ln\left(\frac{N_{ol}}{N_l}\right)_e}{(u_{ah} - u_{al})} = \int C_a(y)\, \delta y \quad \ldots \ 2.41$$

The resultant reconstructed image, using such ray-sums shows the
spatial distribution of analyte concentration in the cross section
through the specimen. The resultant image is the same when equation
2.21 is substituted into equation 2.40.

In conventional medical CAT, the images are usually
reconstructed using the ART and filtered back-projection
algorithms. These images normally show the spatial variation of
linear attenuation coefficient through the patient. It is proposed
to use the same algorithms to reconstruct images showing analyte
concentration from the ray-sums of analyte equivalent thickness. In
some cases these algorithms are used to reconstruct images showing
linear attenuation coefficients. Such images act as a useful

reference to show the relative coefficient of the analyte within the object.

II.4.4 Filtered Back-projection.

II.4.4.1 Introduction to Convolution Methods.

In this section the theory of the convolution or filtered back-projection method is described. In II.4.1, it was stated that back-projection of the projection data can never give a proper "unblurred" image. However, if the scan projections, i.e. ray-sums, are modified appropiately prior to back-projection then an accurate reconstruction image can be achieved. For this, negative values are introduced into the projection data before back-projection is performed. These negative values cancel contributions to the images except at the appropiate positions. This is the basis of the convolution reconstruction method.

In this section, the theory of Radon transforms and transform methods, the determination of the convolution function and the implementation of the resultant algorithm are described.

II.4.4.2 Radon Transforms.

Before describing the theory of the reconstruction algorithms, it is first necessary to describe the co-ordinate systems used and the mathematical way in which the ray-sums and the reconstructed images are represented. The problems of reconstructing an image from discrete measurements can then be defined. In the sections following this, the theory of the filtered back-projection and ART methods are described in more detail.

A polar co-ordinate system is used to describe the location of any point within the cross section of interest of the object. See figure II.10. The point O in figure II.10 is the origin and the line B is defined as the baseline. Any point p in the cross section can be described by two variables, r its distance from the origin and ϕ the counter clockwise angle between the baseline and the line joining Op. For now, the analyte concentration or the linear attenuation coefficient at any point is given by $f(r,\phi)$.

Similarily, beam paths through a cross section can also be described by two co-ordinates. The line L, i.e. the beam path, in

53

figure II.10 is described by $(\imath, \theta)$ where $\imath$ is the perpendicular distance from the origin O to the point Q on the line L. θ is the angle the line $\imath$ makes with the baseline. The analyte equivalent thickness or the total linear attenuation, i.e. the ray-sum, along this line is denoted by $[Rf](\imath, \theta)$. This function depends on f, the linear attenuation coefficient or the analyte concentration at the point (r, ϕ), and is called the Radon Transform.

The function $[Rf]$ can be plotted on a two dimensional rectangular co-ordinate system. See figure II.11. A single point in this $(\imath, \theta)$ space can be thought of as corresponding to a ray-sum, or line, in (r, ϕ) space. Figure II.10 further emphasises the relationship between the (r, ϕ) and $(\imath, \theta)$ spaces. First, consider the line Ψ, which is perpendicular to the beam path L and makes an angle θ' with the baseline. Any other beam path which is perpendicular to Ψ has an orientation θ' so that the ray-sums, corresponding to the beam paths correspond to the points along the straight line $\theta = \theta'$ in figure II.11.

Similarily, for a point (r, ϕ) in the (r, ϕ) space. The locus of the set of points $(\imath, \theta)$, which correspond to lines passing through the point (r, ϕ) is given by the equation

$$\imath = r \, \text{Cos} \left(\theta - \phi \right) \quad \dots \quad 2.42$$

The locus is a cosine wave on the $(\imath, \theta)$ plane of amplitude r and phase $-\phi$. This can be seen in figure II.11. However, in practice the ray-sums are measured at discrete step positions and rotations. Thus the set of discrete points in $(\imath, \theta)$ space in figure II.12 correspond to measurements at these discrete step and rotation positions. The points form a rectangular grid with horizontal spacing s which is the linear step size and vertical spacing $d\theta$ which is the angular step size. The problem of reconstruction can now be stated, that given the data $Rf[\imath, \theta]$ estimate the image of the object in the (r, ϕ) plane. In conventional CAT, this representation of ray-sums is called a sinograph. Although not essential to this work, it is useful in showing the difference in the representations of the functions f and $[Rf]$.

With this in mind, the reconstruction problem can now be stated;
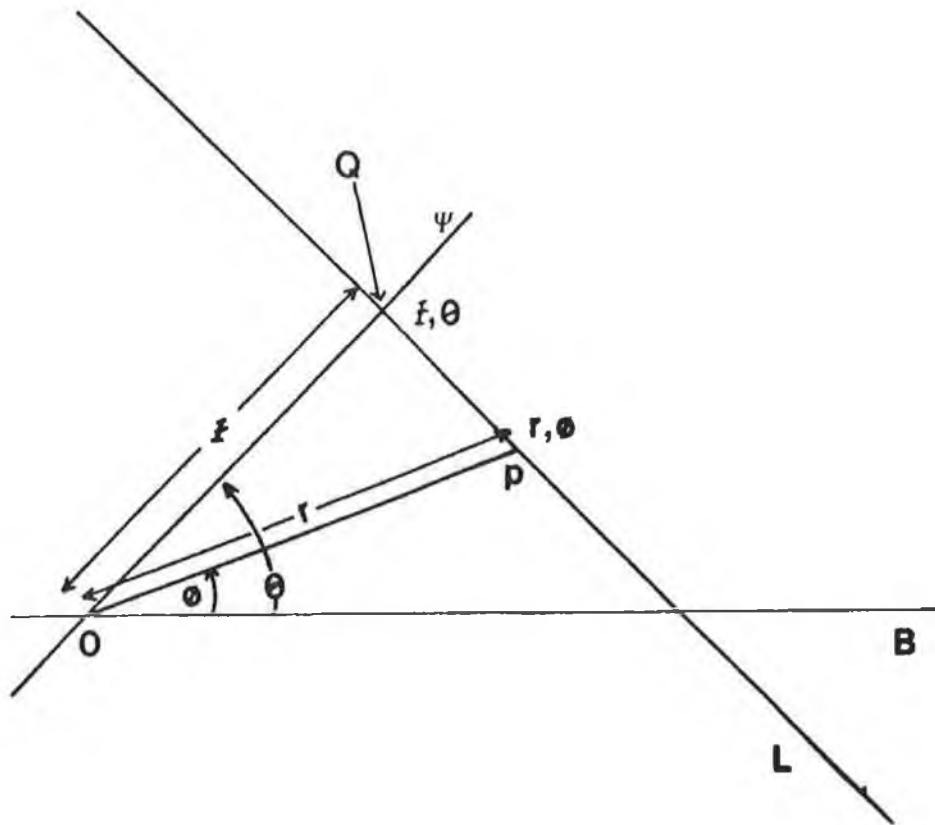
Fig. II.10
The polar co-ordinate system to describe the location of a
point p in the plane of interest. This is the r,ϕ space. Here,
O is the origin, B is the baseline, r is the distance from O to
p, ϕ is the counter clockwise angle between the baseline B and
the line ψ joining O and p, L is the beam path, l is the
perpendicular distance from O to Q and θ is the angle between
the line L and B.
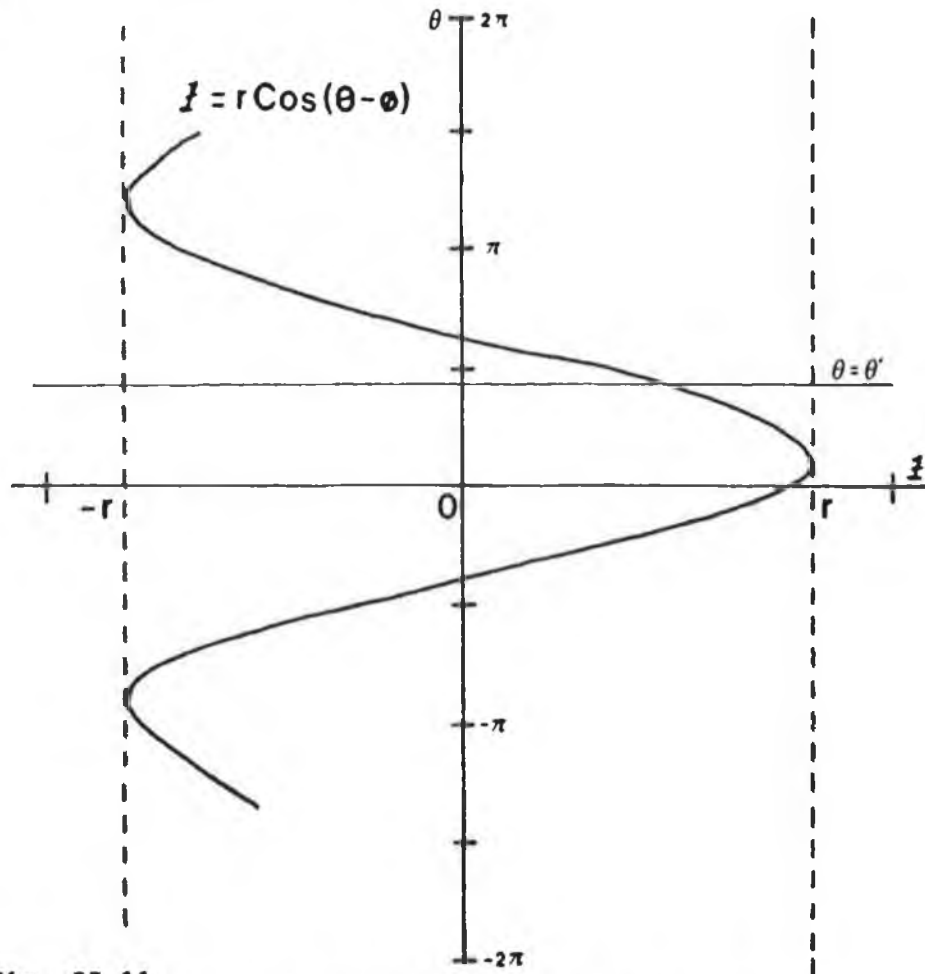
Fig. II.11
The two dimensional co-ordinate system in l,θ space. A point in l,θ space corresponds to a ray-sum in r,ϕ space. The line $\theta = \theta'$ corresponds to all rays-sums which are parallel to the line L in r,ϕ space. The locus of the set of ray-sums l,θ which pass through a point r,ϕ in r,ϕ space is described by the equation shown. This is known as a sinograph.
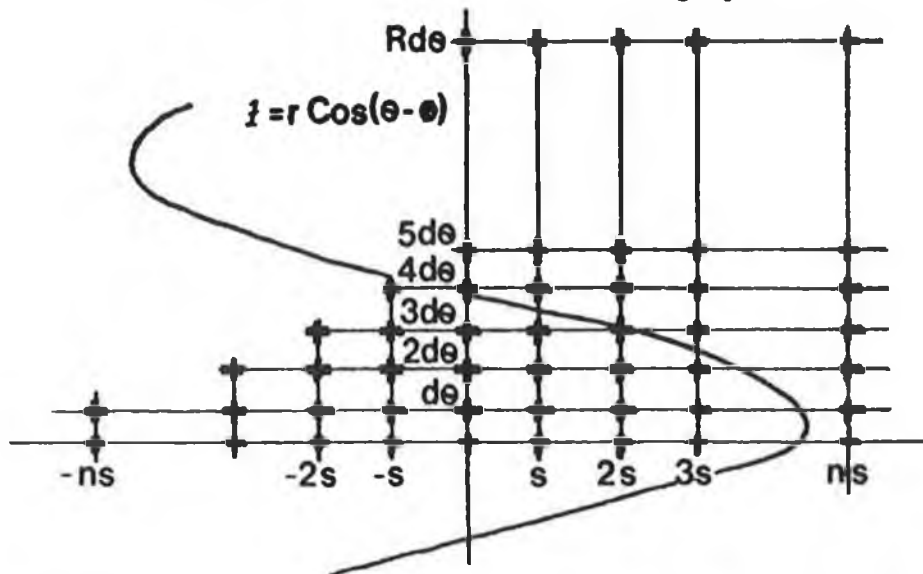
Fig. II.12
The discrete form of the sinograph described in figure II.11.. Each discrete point corresponds to a ray-sums in r,ϕ space. The variable s is the linear step size while $d\theta$ is the rotation step angle.

56

given $[Rf](l,\theta)$ for a large number of ray-sums, find an algorithm that provides $f(r,\phi)$ at points of interest (r,ϕ). This problem was first solved by Radon [37], but there are some difficulties in applying it to the reconstruction of CAT images.

1) In CAT, measurements of $[Rf](l,\theta)$ are made along a finite number of beam paths, while the Radon formula assumes the availability of $[Rf](l,\theta)$ for all lines (l,θ).

2) Radon's formula is sensitive to inaccuracies in the ray-sum data such as noise, width of the X-ray beam etc.

3) Radon gives a mathematical formula, but an effective algorithm that can be evaluated on a computer is required.

II.4.4.3 Transform Methods.

The Radon transform of the function f, i.e. the ray-sum, can be defined as

$$[Rf](l,\theta) = \int_{-\infty}^{\infty} f\left[(l^2 + y^2)^{1/2}, \; \theta + \tan^{-1}\left(\frac{y}{l}\right)\right] \; dy \; \dots \; 2.43$$

and

$$[Rf](0,\theta) = \int_{-\infty}^{\infty} f[\; y, \; \theta + \frac{\pi}{2} \;] \; dy \qquad \dots \; 2.44$$

where the variables are as defined previously. In equation 2.43, $r^2 = (l^2 + y^2)$ by Pythagoras' theorem and $\phi = \theta + \tan^{-1}\left(\frac{y}{l}\right)$. The zero of this integral on the line L is the point Q. See figure II.10. Now, the Radon transform associates a function $[Rf]$ of two variables, with a function f of two polar variables. An operator R^{-1}, called an inverse Radon transfrom, is now sought such that $[R^{-1}Rf]$ is equal to f, (i.e. R^{-1} associates the function f with the function $[Rf]$). If such an operator can be found, then as proved by Radon [37], for any function of two polar variables, $[R^{-1}Rf]$ equals f for all points (r,ϕ) such that

$$[R^{-1}R \; f](r,\phi) = f(r,\phi) \; \dots \; 2.45$$

Thus, if a suitable R^{-1} can be found, it is possible to reconstruct a slice through the object showing $f(r,\phi)$, the spatial distribution of the linear attenuation coefficient or the analyte concentration, from $[Rf](l,\theta)$, the ray-sums of total attenuation coefficient or analyte equivalent thickness respectively.

The operator R^{-1} can be expressed as a sequence of simple operators. Herman [34], shows how these operators are derived, see Appendix A, and expresses R^{-1} as

$$R^{-1} = - \frac{1}{2\pi} B \ Hz \ Dz \quad \ldots . \ 2.46$$

where

1) Dz is the partial derivative of $[Rf](l,\theta)$ with respect to its first variable to obtain a function $q(l',\theta)$

2) Hz is a Hilbert transform of the function $q(l',\theta)$ with respect to its first variable to obtain the function $t(l',\theta)$ The Hilbert transform is given by

$$[Hq](l',\theta) = - \frac{1}{\pi} \int_{-\infty}^{\infty} \frac{q(l,\theta)}{l' - l} \ dl \ \ldots . \ 2.47$$

3) B is the back-projection of the function $t(l,\theta)$ which results in a function of two polar variables $[Bt](r,\phi)$ which is given by the equation.

$$[Bt](r,\phi) = \int_{0}^{\pi} t \ (r\cos(\theta-\phi),\theta) \ d\theta \quad \ldots . \ 2.48$$

and

4) the resultant function is then multiplied by the function $-\frac{1}{2\pi}$ which is called normalization.

Such a process assumes that the values of $[Rf](l,\theta)$ are known for all l and θ, i.e. for all ray-sums, and that the required operations can be carried out precisely. The former of these requirements cannot be satisfied in practice since the projection data is measured at a finite number of step positions and rotation angles. The latter assumes perfect data, but in pratice the data contains errors due to noise etc. However, such operators are in fact integrals and are difficult to implement on computers. None the less, the transform method can be approximated by a convolution function which can be easily implemented on a computer.

The first two stages of evaluating the inverse Radon transform, namely differentation of the projection data with respect to its first variable and then taking its Hilbert transform can be approximated by a single convolution of the data with a fixed convolution function. This is done because the numeric evaluation

58

of the Hilbert transform may be far from straight forward, Herman [34]. Having found such a convolution function, an estimate of f can be made. It is given by

$$f^* = B \; (p * q) \quad \ldots \ldots \; 2.49$$

where (p * q) is the convolution of the projection data p, i.e. $[Rf](l,\theta)$, with respect to l along a scan projection, when θ is fixed, with a function q (the convolving function). Having convolved p with q, the resultant is then back-projected onto the (r,ϕ) plane to give the estimate $f^*(r,\phi)$.

Mathmetically the convolution of any two functions, say ω and φ, can be given by

$$[\omega * \varphi] = \int_{-\infty}^{\infty} \omega(\mu) \; \varphi(v-\mu) \; \delta\mu. \quad \ldots \ldots \; 2.50$$

where v and μ are variables associated with ω and φ. Some examples of convolution functions are shown in figure II.13 as smoothly varying curves. The negative side lobes of the convolution functions introduce negative values into the scan profiles. In this way the blurring in the back-projected images is removed. In summary, the convolution method approximates to the inverse Radon transform in two steps

1) a convolution with respect to step position of the projection ray-sums

2) a back-projection,

In what follows, the application of the convolution function or filter function, as it may now be called, for discrete steps and rotations is described. An algorithm, based on equation 2.49, that can be implemented on a computer for filtering and back-projection is also described.

II.4.4.4 Implementation of Convolution Methods.

In practice, the projection data is collected at many discrete steps positions at a similar number of discrete rotation angles. Thus a discrete form of the convolution function is required. Since most of the images reconstructed in the course of this work show the spatial distribution of analyte concentration, only analyte
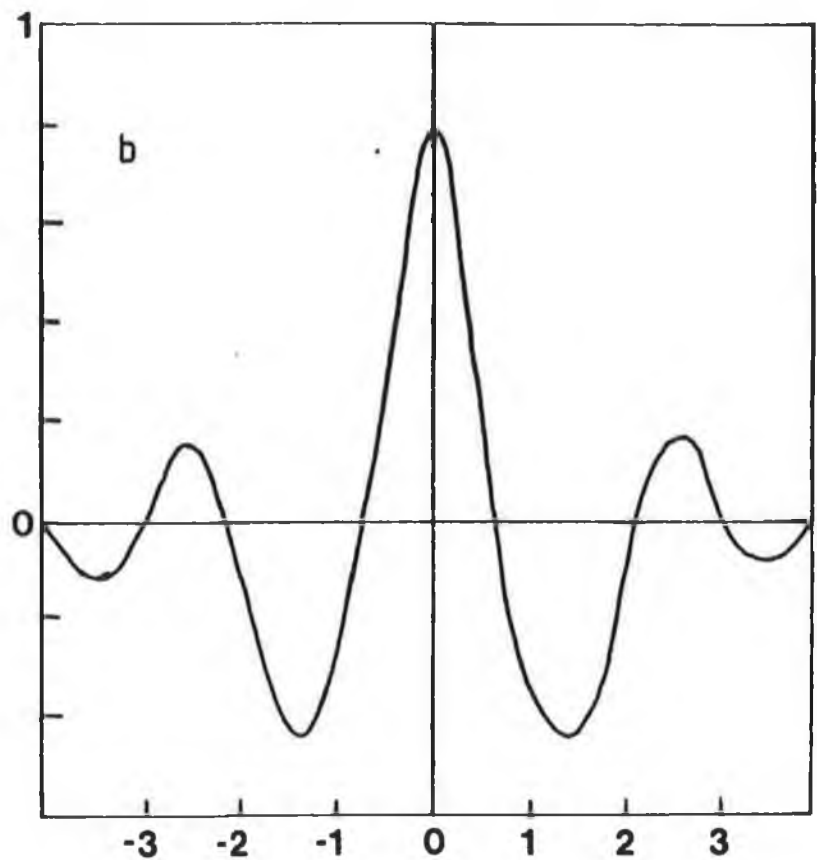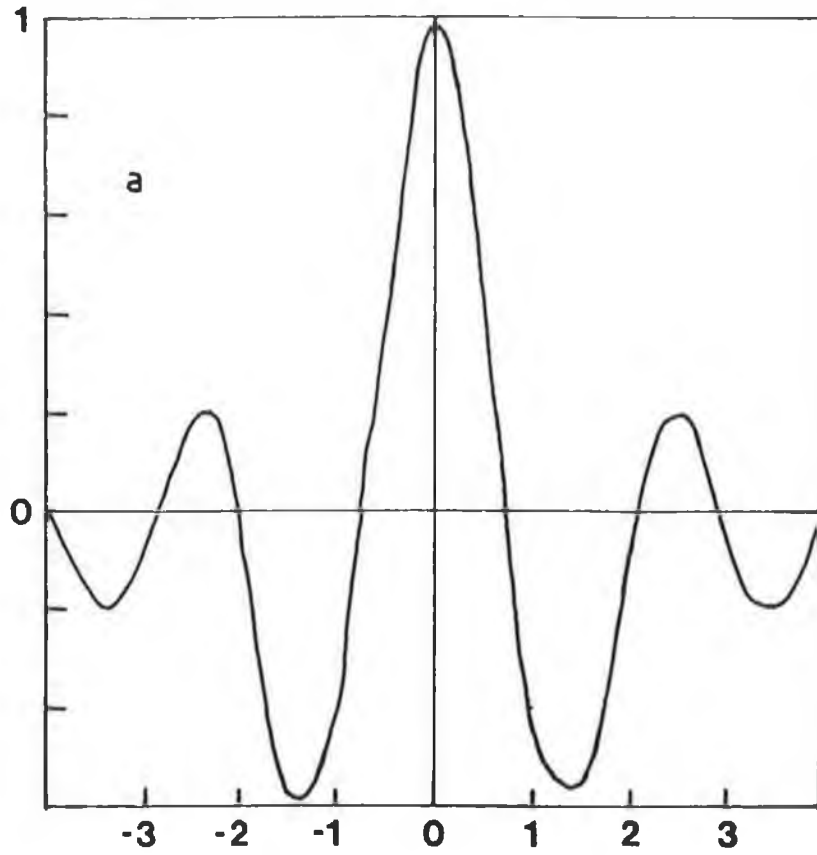
Fig. II.13
a) The continous form of the Ramachandran-Lakshminarayanan
   filter function.

b) The continous form of the Shepp-Logan filter function.

equivalent thickness and concentration will be considered. The algorithms to determine the linear attenuation coefficients from projections of total attenuation are in fact very similar. In the discrete form, the analyte equivalent thickness is given by $t_a^{s,r}$ where s is step position and r is rotation step position. Also, since a computer is used for the calculations, the reconstruction space is limited to a finite area. This area is divided into pixels which form the reconstruction grid. See figure II.14. When reconstructing an image the pixel values C_{jk} are first set to zero.

When the projection data has been collected at all step positions at some rotation step position and the ray-sums have been calculated, filtering of that profile can commence. The resultant filtered analyte equivalent thickness, $\underline{t}_a^{s,r}$, when $t_a^{s,r}$ is filtered with the filter function q(s-s') centred on the step position (s,r) is given by

$$\underline{t}_a^{s,r} = \sum_{-S'/2}^{S'/2} t_a^{s,r} \, q(s-s') \quad \ldots 2.51$$

where q(s-s') is the spread of the filter function along the scan profile and S' is the width in step positions of the filter function. The discrete form [36] of the Ramachandran and Lakshminarayanan (Ram-Lak) filter function used is given by

$$q(s') = \frac{1}{4(d)}2 \qquad s' = 0$$

$$q(s') = -\frac{1}{(\pi \, d \, s')}2 \qquad s' = \pm1, \, \pm3, \, \pm5\ldots \qquad \ldots 2.52$$

$$q(s') = 0 \qquad s' = \pm2, \, \pm4, \, \pm6\ldots$$

where d is the sampling spacing and s' is the filter step position relative to the step position s. This is the discrete form of the convolution function curve in figure II.13 sampled at positions of spacing "d" apart. See figure II.15. The discrete form of the convolution function is entirely equivalent to the continous form once the sampling spacing is less than or equal to the step size [15]. The filter function introduces negative values into the equivalent thickness profile which cancels the contributions to the image except at the appropriate locations. As an example, the filter function is applied to a profile of a scan of a cylindrical object in figure II.16.

61

k 1 2 3 4 5 6 7 8 9 10 11 12 13 14 15 16 17 18 19 20 21 22 23 24

1
2
3
4
5
6
7
8
9
10
11
12
13
14
15
16
17
18
19
20
21
22
23
24
j

X-ray Beam (s,r)
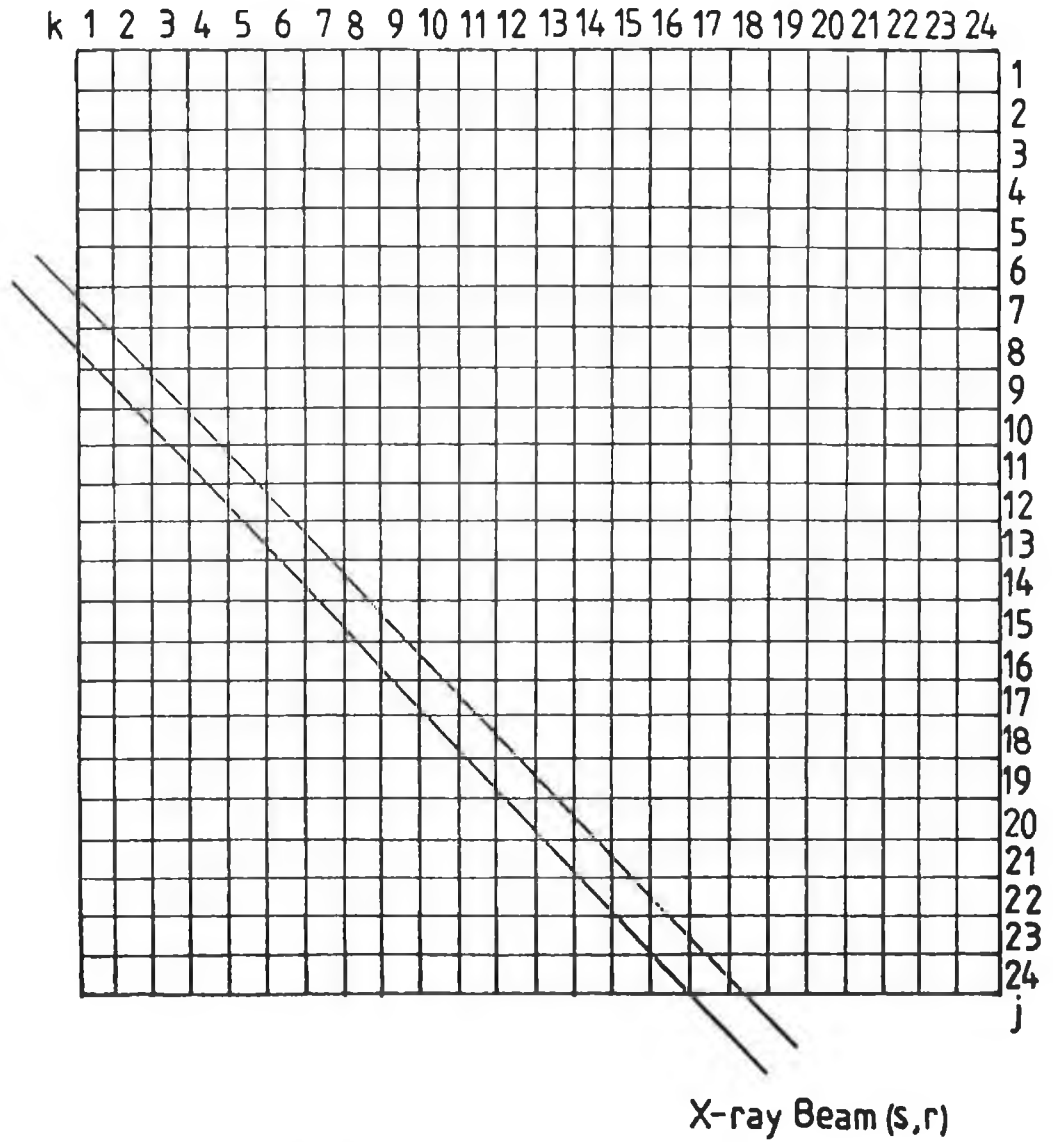
Fig. II.14
A schematic diagram of the reconstruction grid used in reconstruction. The pixels are labelled j,k and the beams are labelled s,r. The value of a pixel is given by $C_{j,k}$.

In figure II.16, the Ram-Lak filter function is just below the scan profile. Starting with the first rotation step position, the filter function is applied sequentially to the ray-sums at each step position, i.e. starting with s=1 and then to s=2 and so on, along the scan profile. The sequence is shown in figure II.16. The same procedure is applied to each subsequent rotation.

When each scan profile is completely filtered it is back-projected across the reconstruction grid along a line which is perpendicular to the scan profile, i.e. the rotation angle. The discrete back-projection procedure is described by

$$C_{jk} = \sum_{sr} t_a^{sr} W_{jk}^{sr} \quad \ldots \ldots 2.53$$

where $W_{jk}^{sr} = 1$ if the centre of the X-ray beam s,r crosses the pixel j,k else $W_{jk}^{sr} = 0$. As subsequent scan profiles are filtered and back-projected, the image of the slice through the object is built up. Thus the concentration value in a pixel j,k is equal to the sum of all the modified ray-sums that pass through that pixel. The reconstructed image of the cylindrical object using the ray-sums modified by equation 2.51 is shown in figure II.17. When compared with figure II.18, showing the unfiltered back-projected image of the same object, it can be seen that the blurring that is present in figure II.18 has been removed in figure II.17 by the effect of the negative values. See also figure II.8.

Figure II.19 shows reconstructed images of some dummy data. The phantom object consisted of two 3X3 pixel sized solids. In figure II.19a, it is difficult to distinguish between the two objects. This was reconstructed using unfiltered data. In figure II.19b, the two objects can be clearly distinguished. The data was filtered using the Ram-Lak filter function prior to back-projection. The improvement in the reconstructed image when the data is filtered is clearly seen from these images.

It should be noted that the final pixel values in the reconstructed image are not the expected concentration values. This is due to the error introduced by not taking into account the fractional overlap area of the pixel and the X-ray beam. However, the ratios of the pixel to pixel values are similar to those produced by the more accurate ART method. Also, filtered

63
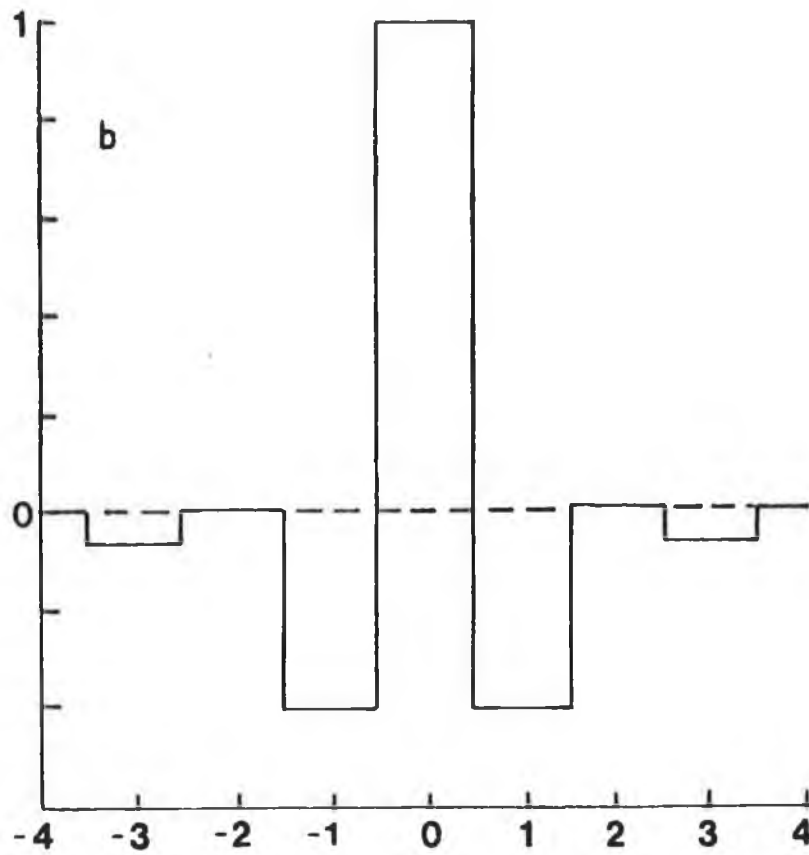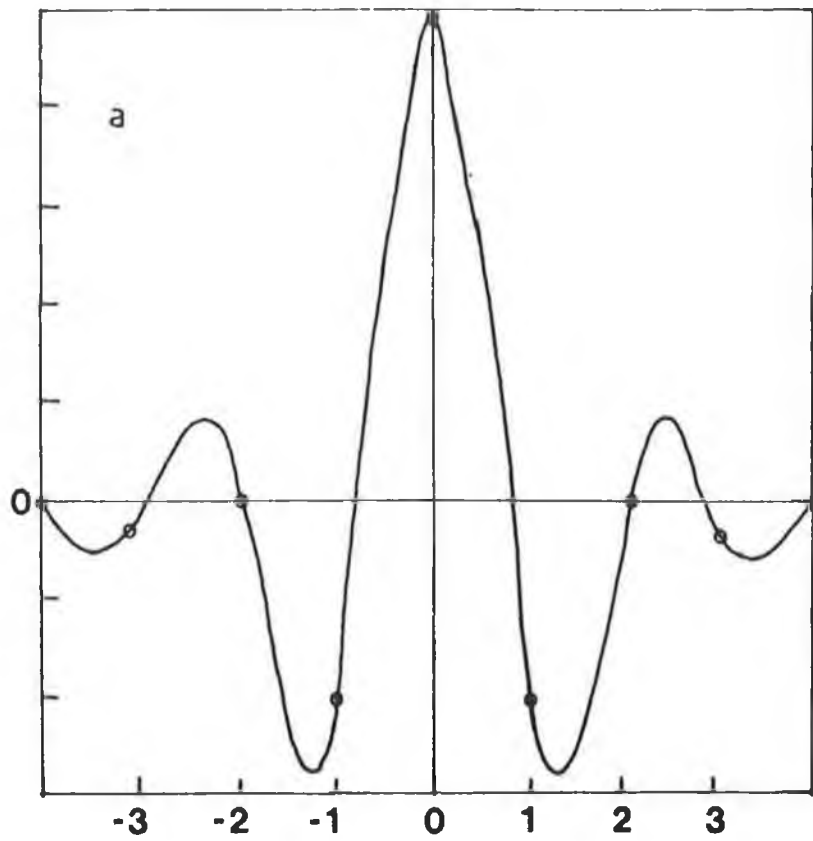
Fig. II.15
a) The continous form of the Ramachandran-Lakshminarayanan
   filter function.
b) The discrete form of the Ramachandran-Lakshminarayanan
   filter function.
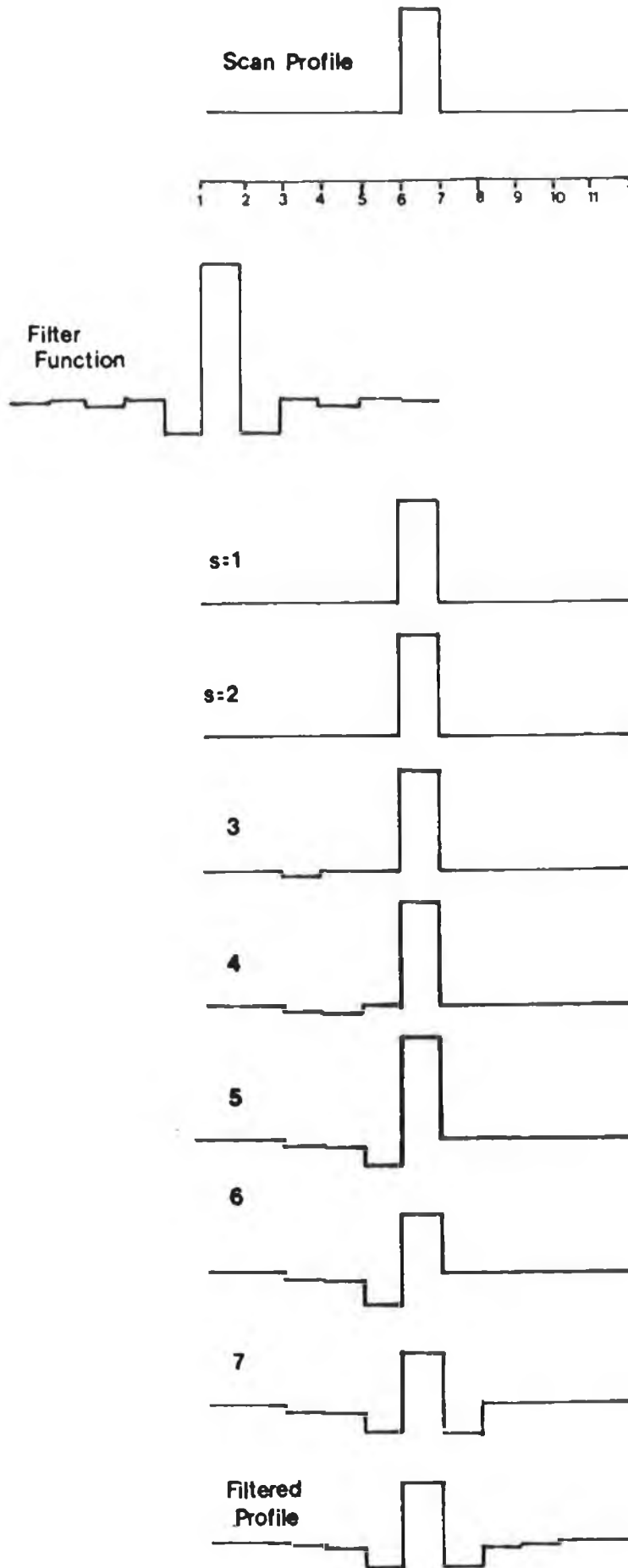
Fig. II.16
A schematic diagram of the the discrete form of the Ram-Lak
filter function being applied to a typical scan profile of a
cylindrical object. The diagrams shows how the filter function
is applied sequentially to each step position.

65

FILTERED BACK-PROJECTION

(FILTERED PROJECTIONS)
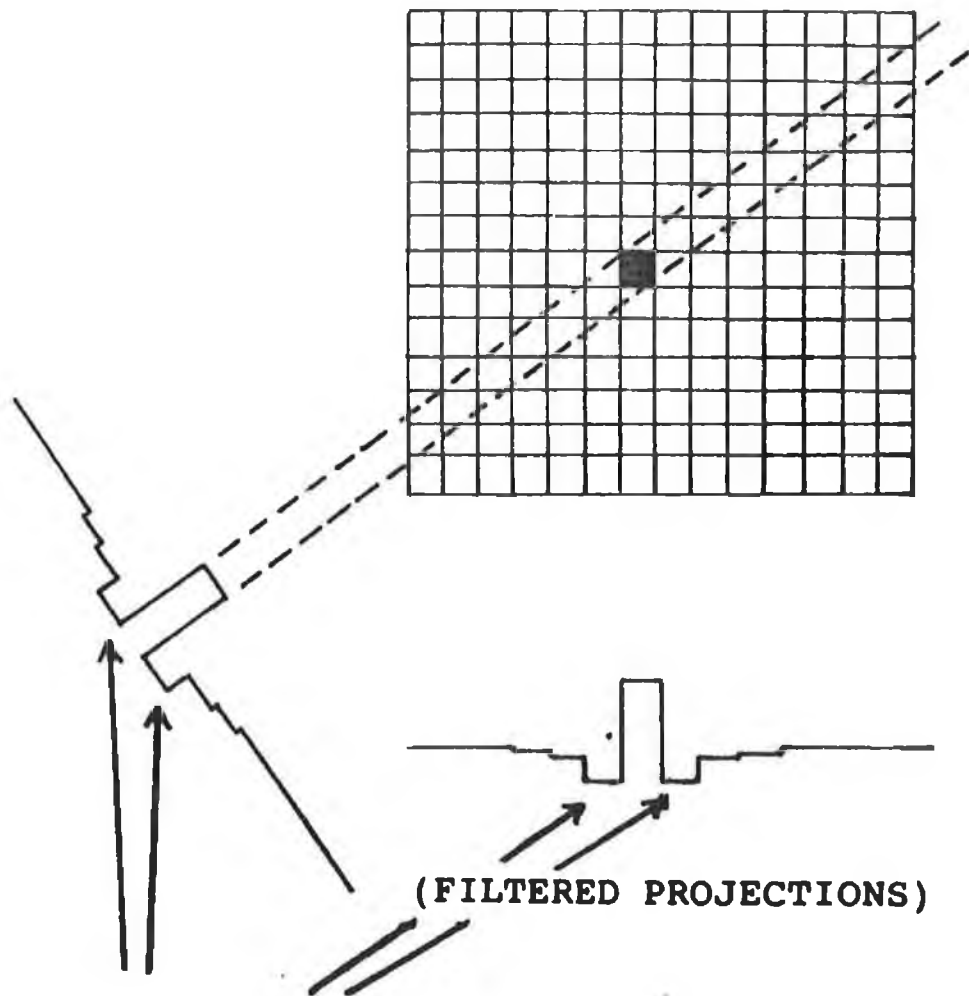
NOTE: NEGATIVE LOBES

Fig. II.17
A schematic diagram which illustrates the back-projection
across the reconstruction grid of filtered scan profiles.
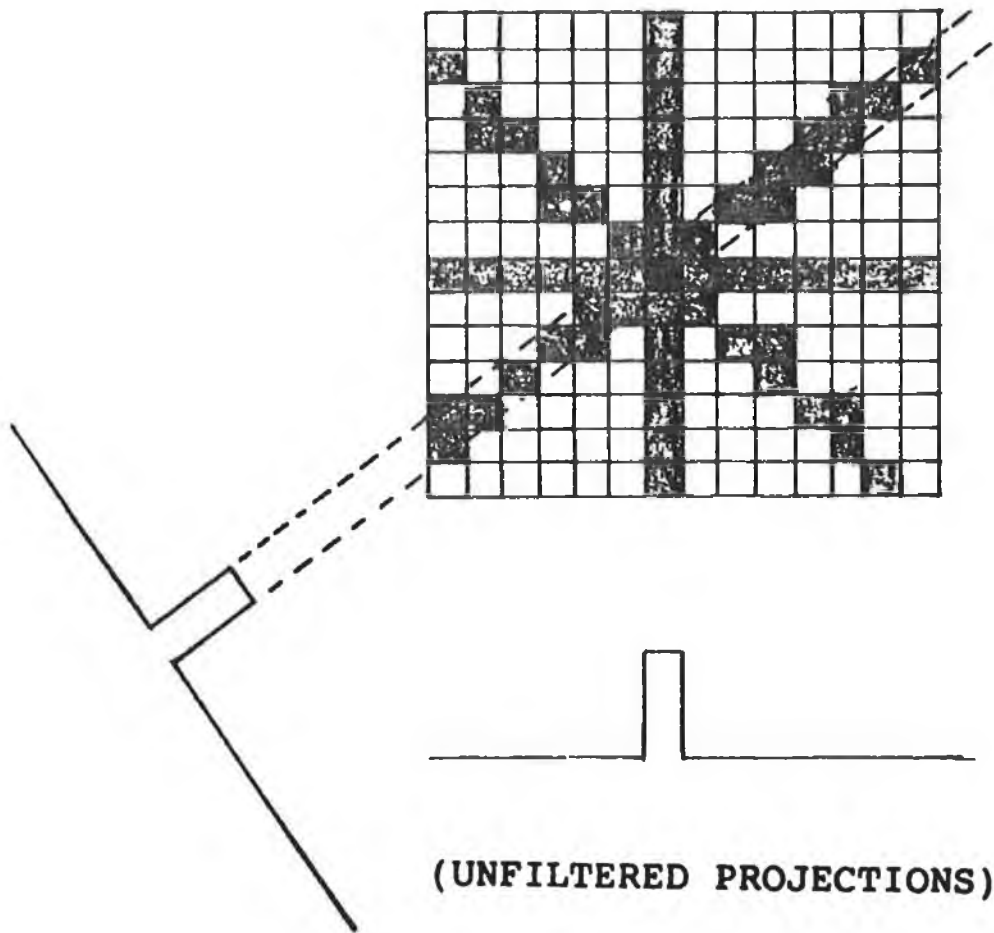
BACK-PROJECTION

(UNFILTERED PROJECTIONS)

NOTE: IMAGE IS SMEARED

Fig. II.18
A schematic diagram which illustrates the back-projection
across the reconstruction grid of unfiltered scan profiles.

back-projection is a fast and easily implemented reconstruction method. Only one iteration is required to produce a good image. This makes it a fast reconstruction method as further iterations do not improve the image.

II.4.4.5 Computer Programs for Filtered Back-projection.

A BASIC computer program for the VAX 11/785 to reconstruct images, using the Ram-Lak filter, from the data collected by experiment is shown in Appendix B. This program was written for scans using 40 step positions and 40 rotation positions. The ray-sums which form the basic data for this program are calculated and stored on file. It was found that an improved image is formed if the pixels are divided into quarters and the beam into halves (mathematically speaking) for back-projection.

Lines 110 to 310

The reconstruction program starts by inputing the ray-sums from a file and storing this data in an array, "stp(T)". Side lobes, five step positions wide, containing zero are added to both ends of each profile. This is done to facilate the filtering process.

Lines 320 to 430

Starting with the first profile, "R=0", each profile is modified in turn using the discrete form of the Ram-Lak filter function, as given by equation 2.52. Since the filter function value is insignificant beyond five step positions from its centre, the filter function is limited in width to five steps on either side of its centre. It is for this reason that the sides lobes are required. The filter is applied to each step position along the profile starting at the first ray-sum. When the filtering is completed, the sides lodes are removed, leaving 40 steps per profile. The back-projection process can then begin.

Lines 450 to 830 and 910 to 1010.

The back-projection process starts with the first rotation. Firstly its angle with respect to the zero angle and its slope with respect to the reconstruction grid are determined. Knowing this, the pixel quarters inside the reconstruction grid which are intersected by either half of the beam can be determined. If a pixel quarter is intersected, i.e. if the centre line of the beam
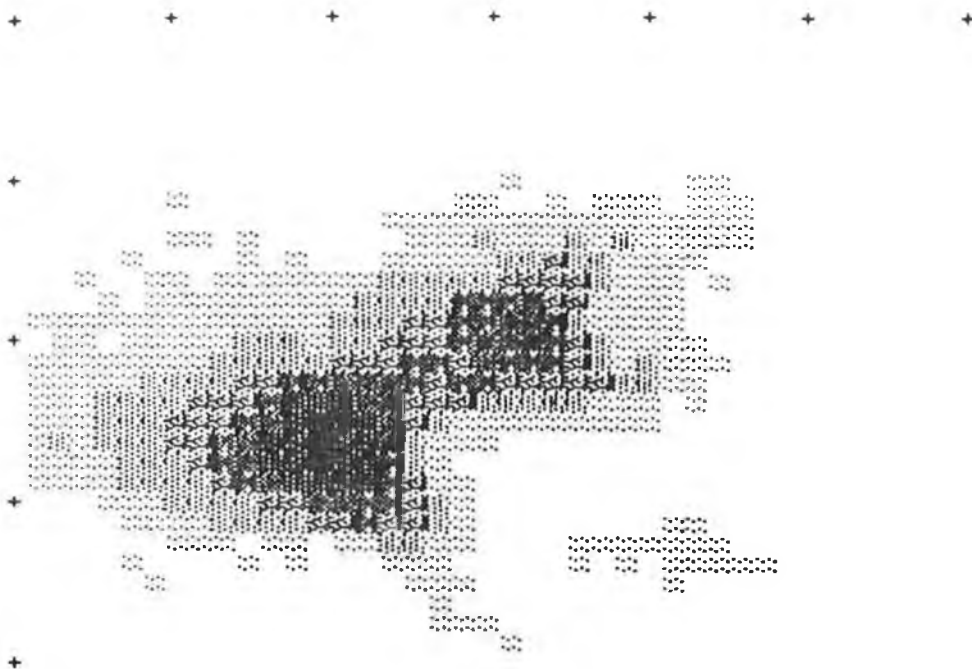
a)
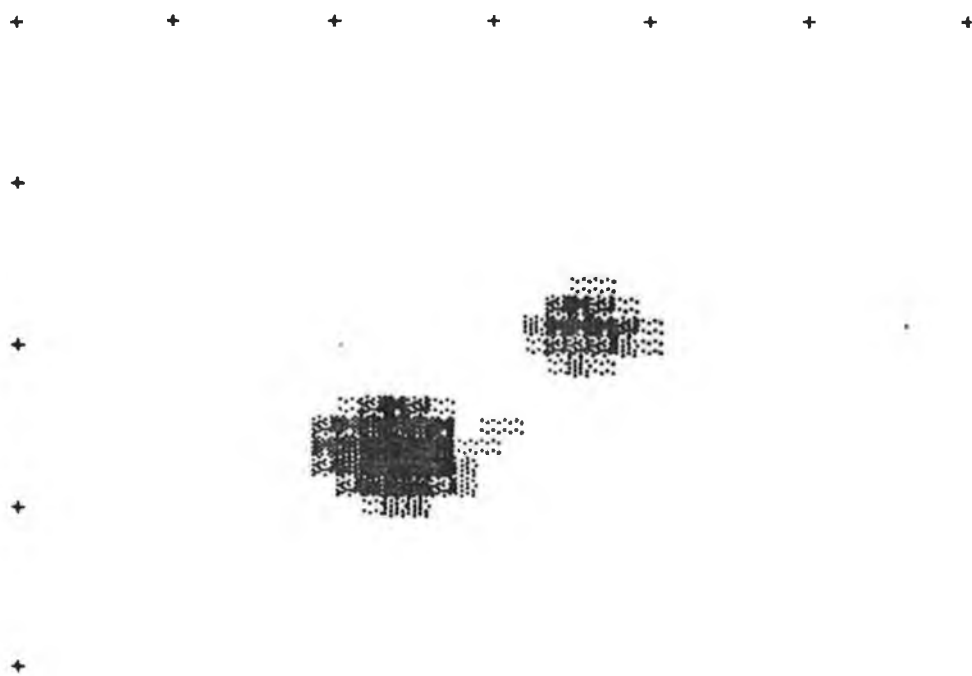
b)

Fig. II.19
Reconstructed images of a phantom containing two 3X3 pixel
cylinders.
 a) Using unfiltered scan profiles,
 b) using Ram-Lak. filtered scan profiles.

half passes through the pixel quarter, then the filtered ray-sum of that beam is added to that pixel quarter. This is repeated for all intersected pixel quarters and then in turn for each beam. This is back-projection. There is a special case when the beam is at right angles to the first rotation. Here the program jumps to lines 910 to 1010, does the back-projection and then returns to the normal process.

Lines 840 to 900.
Having completed the back-projection, the final image is stored in a file on the VAX 11/785.

Only one iteration is required as this is adequate to produce a satisfactory image. Typically, an image is reconstructed in less than 30 seconds CPU time. Such images were used to check the image before starting the ART reconstruction program which normally takes 35 minutes per iteration. In order to display these images the data is transfered as ASCII code from the VAX file to a BBC microcomputer using a Termulator ROM, by Acornsoft. Once successfully transferred, the ASCII code is decoded and saved as bit characters in a Random Access File. In this way the file can be read and displayed in a few seconds on the BBC. The program used to display the images is shown in Appendix D.

II.4.4.6 Other Filters for Back-projection.

The Ramachandran-Lakshminarayanan filter is essentially a filter for removing the blurring which is inherent in back-projection. The filter is best when high spatial resolution is required and it also enhances the detectibility for small high contrast features. Many of the specimens used in the experiments have small high contrast features, eg. small test tubes containing analyte in a large cork bung. The Ram-Lak filter is especially suited for such objects. A second filter commonly used for CAT is the Hann filter [13]. It is preferable when large low contrast features are of interest. A third filter, which is a compromise between the previous two, is the Shepp-Logan filter [35]. This filter is useful when a compromise between high spatial resolution and high contrast is required. The three filters can be implemented in the same way as described.

70

II.4.5 Algebraic Reconstruction Techniques.

II.4.5.1 Introduction to Algebraic Reconstruction Technique.

A second and quite different approach to the reconstruction problem is the use of an iterative process, in which a series of successive approximations to the slice through the object finally converge on a solution. The method differs from the filtered back-projection method in several ways. Firstly, the problem is discretized at the very beginning by defining the reconstruction domain as a grid. Then having made an initial guess at the object, the process continues by refining the image of the object until its projections satisfactorily match the measured object projections.

One such, technique, called the Algebraic Reconstruction Technique (ART), which was developed by Gordan [33], was used by Hounsfield [3] in the original CAT scanner. The version used in this work, is based on the unconstrained ART, which was modified by Herman [40]. A computer program based on this algorithm was written for the VAX 11/785 and this was used to reconstruct all the images showing analyte concentration.

II.4.5.2 Theory of ART.

Consider an object with an unknown two-dimensional distribution of linear attenuation coefficient or analyte concentration, and a limited set of ray-sums, of total attenuation or analyte equivalent thickness, calculated using experimentally obtained data. The problem is to construct the best representation of the object from these ray-sums. This is called the best estimate of the object or the image.

As in the previous case, the parallel mode of data collection is used to scan the object. See figure I.4. While scanning the object, the X-ray source and detector are stepped in parallel across the object and then rotated. At each of the R rotation angle positions, the photon beam is measured at S linear step positions. The individual step positions and rotation angle positions are denoted s and r respectively.

In ART, it is necessary to define a reconstruction grid before

starting to reconstruct the object. See figure II.14. The grid is composed of picture elements called pixels which are labelled as j,k. During reconstruction, the value attributed to a pixel is distributed evenly over the whole pixel. This produces a digitized image of the object. Also, because there are a limited number of projections, the image can only be a representation of the real object. Thus, in order to be able to produce a good estimate of the object, it is necessary to have an adequate number of projections. Taylor [13], argues that the number of independent measurements must at least equal the number of pixels in the image and that the number of rotation angle positions must be at least $\pi/4$ times the number of step positions per rotation angle position. If this is satisfied then, providing that the data is good, a good estimate of the object can be determined.

In order to reconstruct the object, it is first necessary to decide on an initial image for the reconstruction grid, i.e. an initial guess at the object. There are an infinite number of possible initial guesses. For example, all pixels could be set to zero or to some other finite value. Alternatively, the image reconstructed by the filtered back-projection method could be used. Having decided on an initial image, ray-sums of the image, which are analagous to the calculated ray-sums, are calculated from the image in the reconstruction grid. Figure II.14 shows a typical beam path through the reconstruction grid.

With these points in mind, the problem of reconstruction can now be stated; given a set of object projections, an image is sought such that the image ray-sums most closely resemble the object ray-sums. For this, a criterion, which is described later, is needed. In fact, several iterations may be required before this can be satisfied. Then, when such an image has been found, it is regarded as the best estimate to the object. However, due to noise in the object projections there can never be an exact agreement between the object and the image ray-sums.

II.4.5.3 Implementation of ART.

The ART method is easily implemented on a computer since it is a discrete problem. Here the steps followed and the algorithm used

72

are described. Since most of the images reconstructed using this method show analyte concentration, only analyte equivalent thickness, t_a and analyte concentration, C_{jk}, will be considered. As before, reconstructions showing linear attenuation coefficient can be produced using the same steps and algorithm.

The ART method can be described by the following set of operations

i) Assume an initial image C^1_{jk}

ii) Compute the image ray-sum t^{sr}_{ai}

iii) Compare to the corresponding object ray-sum t^{sr}_{a0}

iv) Compute a correction factor and update the C^1_{jk} values which lie along the projection

v) Repeat from ii) for all projections and then keep repeating from ii) with new iterations until a satisfactory image is produced that satisfies the set criterion.

There are several ways in which the comparisons can be made and several ways in which the corrections can be applied. In this work the direct additive algebraic reconstruction technique, by Herman [15], is used. The operations stated above are described in more detail below. The computer program written for the VAX 11/785 to reconstruct images follows the operations above and is shown in in Appendix B. It is described in II.4.5.5.

The first operation undertaken is an initial guess at the concentration distribution in the object. In order to have a reasonable guess at the concentration in the object the average of all the measured ray-sums is calculated. This is a reasonable guess since the effect of the total analyte present is distributed evenly among all pixels. This initial value is calculated using

$$C^1_{jk} = \frac{\sum t^{sr}_{a0}}{JK\ d} \quad \ldots. \ 2.54$$

where JK is the total number of pixels and d is the pixel size. All pixels in the reconstruction grid are given this value.

The next operation is the process of computing image ray-sums. It begins with the first projection, i.e. s=1 and r=0. The image

73

ray-sum for the first projection is calculated by summing the contribution of the concentration in each of the pixels in the reconstruction grid overlapped by the projection beam s=1, r=0. The contribution of each pixel is weighted according to how much of the overlapped pixel is intersected by the X-ray beam. The calculated ray-sum is given by

$$t^{sr}_{a1} = \sum \lambda^{sr}_{jk} C^i_{jk} \, d \, \ldots \ldots 2.55$$

where λ^{sr}_{jk} is the fractional overlap area of beam s,r with pixel j,k, and d is the pixel width. The fractional overlap areas are calculated using the computer program in Appendix F1. The factor d is included in order to compensate for the fact that the reconstruction grid is a two-dimensional structure which contains concentration values, i.e. kilogrammes per cubic metre.

The next two steps of the procedure involve the comparison of the image and object ray-sums and the calculation of the correction factor for the beam of interest. The comparison involves a simple subtraction of the two ray-sums and their difference is then used to calculate the correction factor χ for the s,r beam. The correction factor is given by

$$\chi^{sr} = \left(\frac{t^{sr}_{a0} - t^{sr}_{a1}}{\sum\limits_{jk} (\lambda^{sr}_{jk})^2} \right) \ldots \ldots 2.56$$

This correction factor is then applied to all the pixels along the s,r beam according to

$$C^i_{jk}(\text{new}) = C^i_{jk}(\text{old}) + \tau \, \chi^{sr} \lambda^{sr}_{jk} \ldots \ldots 2.57$$

where τ is a relaxation constant whose value is open to choice. The correction to the concentration value in a pixel is applied according to the fractional overlap of the pixel and the X-ray beam. The choice of relaxation constant in the equation has a large significance on the final image. This will be discussed in more detail later. For now it is enough to say that choosing a low value (0.1 to 0.5) for τ suppresses the oscillations in pixel concentration with successive iterations which occurs when higher values of τ are chosen. See II.4.5.4.

When all the corrections to the pixels along the s,r beam path

have been completed, the comparison and correction procedures are repeated for the next beam and then in turn, continued for all beams. When this has been done for all step positions and rotation angles the first iteration is completed and an estimate of the object results.

Having generated an estimate of the object it is then necessary to determine the nearness of this image to the object. To do this, the standard deviation of the initial guess and of the image after the first iteration are calculated and compared. The standard deviation of the image is calculated using

$$\sigma^q = \frac{1}{JK} \left[\sum_{jk} \left(C_{jk}^q - \overline{C}_{jk}^{q} \right)^2 \right]^{1/2} \quad \ldots \quad 2.58$$

where q is the iteration number and $\overline{C}$ is the average of the pixel values. The estimate of the object is said to be the best if the following criterion is satisfied; that the difference in standard deviations of the images between successive iterations is less than one hundredth of the standard deviation of the qth iteration image. If this criterion is satisfied then the process is terminated and the resultant image after the qth iteration is taken to be the best estimate of the object. Mathematically the criterion is given by

$$\sigma^{q+1} - \sigma^q < \frac{\sigma^q}{100} \quad \ldots \quad 2.59$$

It is unlikely that the image after the first iteration will satisfy this criterion. In this case, operations ii) to v) are repeated until a best estimate of the object is obtained. If one was to continue with more iterations after the best estimate was found, then the image would gradually start to deteriorate.

The resultant image is displayed on a VDU monitor. The image is the best approximation to the distribution of analyte concentration in the object slice but not a perfect image. This is because it is not possible to generate image ray-sums which are in exact agreement with the object ray-sums, which contain noise due to statistics in the measured photon counts. With high levels of noise more iterations are needed to produce a best estimate. See Webb [39]. Also, the value of the relaxation constant τ used has an important bearing on the pixel concentration values. The effect of

this constant is described below.

II.4.5.4 Relaxation Constant.

The choice of relaxation constant τ in equation 2.57 is critical in determining the final pixel values and the number of iterations required. In order to see its effect, consider a phantom, a solid with sides of length equal to three step sizes and having a uniform concentration equal to one, being scanned by a pencil beam of X-rays. The phantom is scanned in the parallel mode. Dummy data for such a phantom was calculated on the VAX 11/785 using the computer program in Appendix E.

Reconstruction of the phantom with $\tau = 1$ produces an image which is 3X3 pixels in size. With $\tau = 1$ the pixel values oscillate with each iteration before converging. See figure II.20. The centre pixel value converges to a value which is well above 1 while the average pixel value is below 1. This shows that there is a smearing of the concentration values in neighbouring pixels. Using values between 1.0 and 0.1 in equation 2.57, the oscillations are removed and the pixel concentrations converge to a final value which nears 1 as τ is decreased. See figure IV.14.

Figure II.21 shows the variation in σ with iteration number for the same relaxation constant values as before. With $\tau=1$ the standard deviation oscillates to a final value which satisfies the criterion in equation 2.59 after 9 iterations. As τ is decreased, the number of iterations required to obtain the best estimate of the object increases while σ rises monotonically to its final value. For $\tau=0.1$ the number of iterations required is 18. This makes reconstruction by ART a very slow method. These observations are in agreement with the observations made by Webb [39]. However, the reason ART is used in reconstructing the analyte concentrations is that the pixel concentration values have a small error, for example the error is less than 5% for $\tau=0.1$. This is because the fractional overlap areas are calculated to within an error of 2%.

II.4.5.5 Computer Programs for ART.

The computer programs used to generate the images of the object slice by the ART additive method described above are shown in
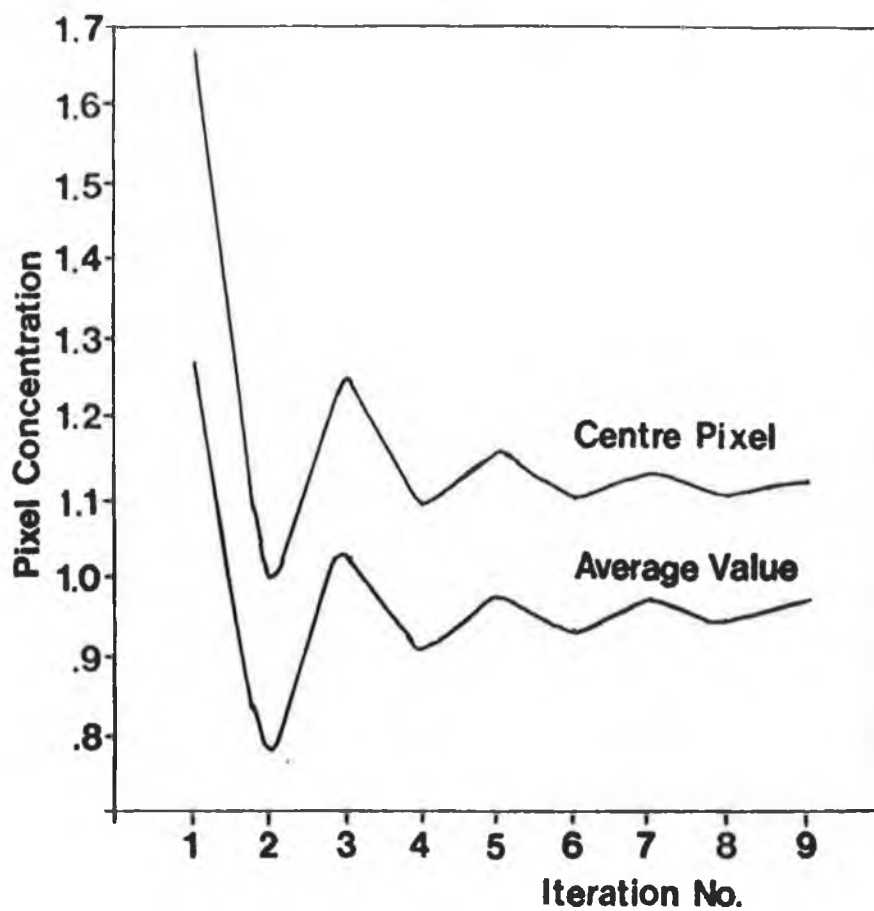
Fig. II.20
The variation in the pixel concentration as a function of the
iteration number. This is for a 3X3 pixel sized phantom. The
variation in the centre pixel and in the average over the 9
pixels are shown.

77

Appendices F1 & F2. The programs are written in BASIC computer language. An attempt was made later to write the program in C. The first program generates the pixel and beam fractional overlap areas. The second program produces a CAT image which is the best estimate of the object. Both were written for the VAX 11/785. A third computer program, written in BASIC for a BBC microcomputer, is used to display the images. Programs were written for scans using 20 steps at 24 rotation postions and for scans with 40 steps and 40 rotation positions. The programs for both cases are similar and the programs for the case of 40 steps and rotations are described here.

a) Program to calculate the fractional overlap areas.

The program in Appendix F1 was used to calculate the fractional overlap areas of each beam r,s with each pixel j,k of the reconstruction grid. These fractional overlap areas are required for ART in order to calculate the image ray-sums, equation 2.55, the correction factor, equation 2.56, and then to correct the pixel concentrations, equation 2.57. The values are stored in a file on the VAX 11/785.

Lines 100 to 220.
The program starts by calculating the angle, "THETA" and the slope "SLOPE" of each rotation position with respect to the first rotation. Then, for the beam corresponding to each step position of a rotation, "S%","R%", the distances from the top, "CEPTA", and from the bottom, "CEPTB", of the beam path to the centre of the grid along the Y-axis is calculated. These distances, "CEPTA", and "CEPTB", are shown in figure II.22.

Lines 230 to 280,
Starting with pixel, J%=1, K%=1, the program firstly calculates the X and Y positions, "XP" and "YP" respectively. The program then determines whether the beam path S%, R% overlaps this pixel knowing the slope and Y intercept of the beam.

Lines 290 to 600,
If the beam overlaps a certain pixel, then the pixel is divided into fifty narrow vertical strips. The fractional overlap of the beam with each strip is summed to give the total fractional overlap area of the beam and pixel. This fractional overlap area, together
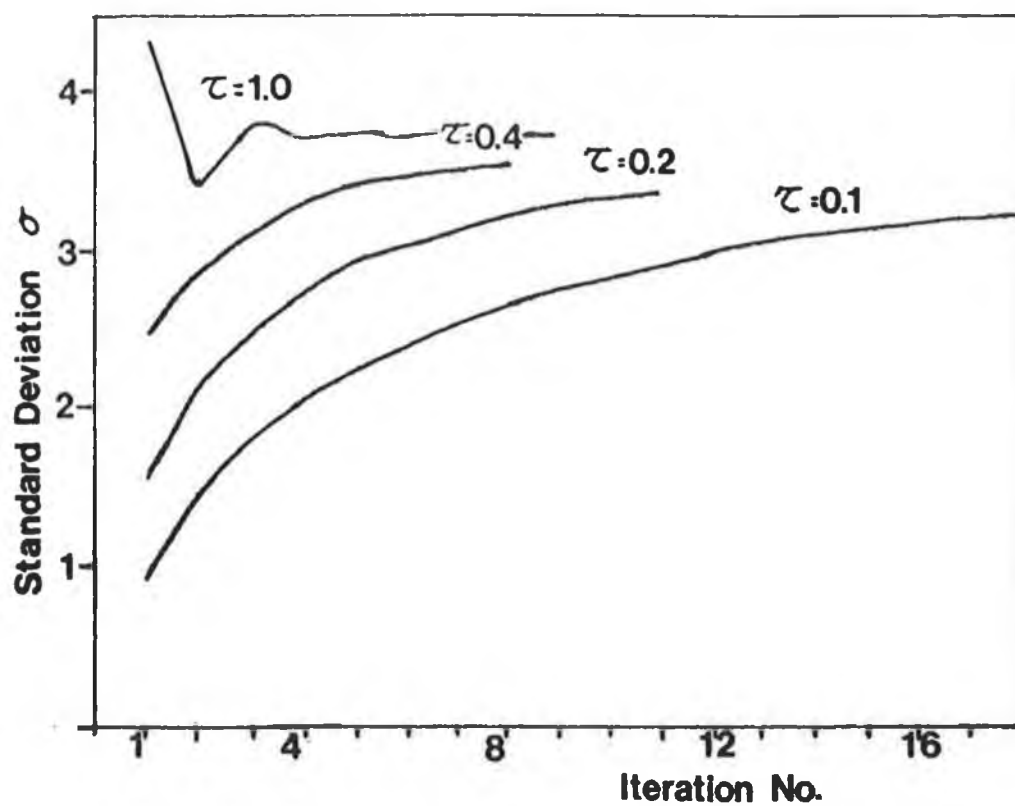
Fig. II.21
The variation in the standard deviation between sequential images, as calculated using equation 2.56, as a function of relaxation constant τ and iteration number.

with the beam and pixel coordinates are saved on file string variables code. The sequence is

Overlap area, Pixel, Beam,

AREA , K , J , S , R

This procedues is continued for each pixel in the grid. The procedure is repeated for all the step positions at that rotation and then moves on to the next rotation. When the procedure reaches the beam slope equal to 90 degrees the whole procedue begins again. In this case, the fractional overlap areas, the pixel coordinates and the r beam coordinate plus 20 is saved. The file is closed with a code which is easily recognisable. Storing these overlap areas and the co-ordinates consumes a large quantity of computer memory, approximately 5000 blocks in VAX 11/785 for 40 steps by 40 rotations. However, the values need only be calculated and stored once and can be used repeately.

b) ART Program

This program, written in BASIC on the VAX 11/785, generates reconstructed image of an object by the additive ART method. The program requires a file containing the analyte equivalent thickness and another containing the fractional overlap areas. The program shown in Appendix F2 is for scans using 40 steps and 40 rotations.

Lines 110 to 280
The analyte equivalent thickness values are read from a file and stored in the array "lambda(s,r)". Using these, an initial guess is made at the object according to equation 2.54 and all the reconstruction pixel variables "$f(k,j)$" are given this value.

Lines 290 to 390
This is the main control section of the program. It is here that the fractional overlap areas "v,k,j,s,r" are read individually from file and sent to be interpretted, lines 620 to 790. The two running summations required in equation 2.56 are made in the subroutine at lines 800 and 830 so that once the overlap area is interpreted for a particular beam and pixel, the summation of the ray-sum "sum1" and the overlap area squared "sum2" is incremented. Starting with the first step position of the first rotation angle, the program continues to interpret and store the overlap areas

80

"area$(a)" until the next step position is reached.

At this point, the program jumps to the subroutine which applies the correction as given by equation 2.57 to each pixel along the beam path, lines 840 to 900. The program then returns to interpreting and storing the overlap areas for the next step position and so on to the next rotation angle position.

At the end of a complete iteration, the program calculates the standard deviation of the image "standev", as in equation 2.58, and compares this values with the value for the previous iteration "oldstandev". If the criterion of equation 2.59 is not satsifed, then the latest image is saved on file, lines 1020 to 1190, and the programs starts on another iteration. If the criterion is satisfied the program is stopped and the image from the previous iteration is taken to be the best estimate of the object.

It now can be clearly seen why this method is much slower that the filter back-projection method. The reason is that the overlap areas and their co-ordinates need to be read and interpreted many times. A single iteration takes thirty five minutes CPU time to run for the case of 40 steps by 40 rotations. For each reconstruction many iterations are required so that it normally takes several hours to produce an image.

As with the filtered back-projected images, the resultant analyte concentrations are transfered as ASCII code to a BBC microcomputer using a Termulator ROM, by Acornsoft. Once successfully transferred, the ASCCI code is decoded and saved as bit characters in a Random Access File. In this way the file can be read and displayed in a few seconds on the BBC. The maximum concentration is also noted so when the image is displayed on a VDU, the pixel concentrations can be displayed as chosen. The program used to display the images is shown in Appendix D.
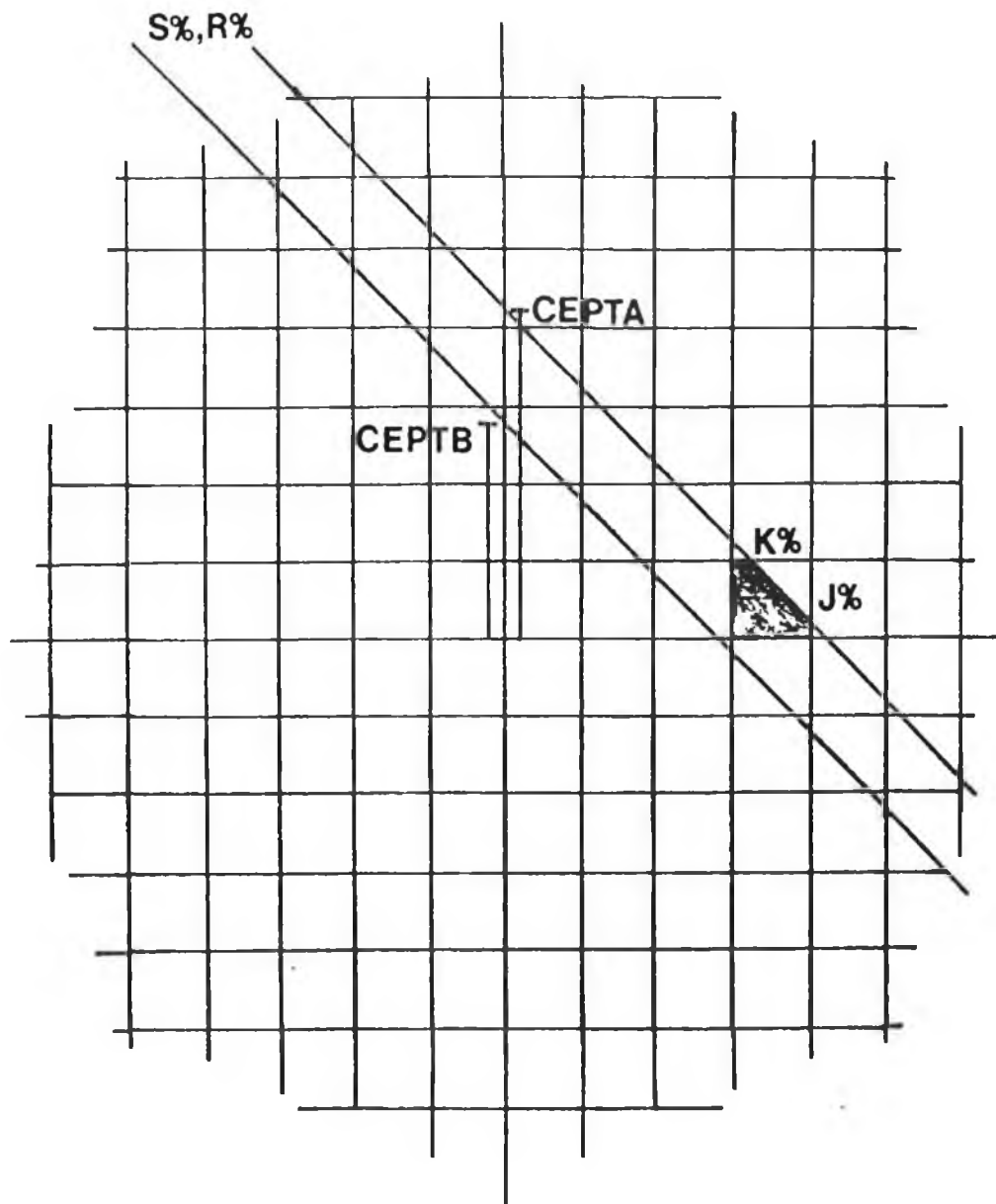
Fig. II.22
A schematic diagram showing the overlap of pixel J%, K% with
the ray S%, R%. The variables CEPTA and CEPTB are the
distances from the centre of the grid to the top and bottom
of the ray respectively.

Chapter III.

III.1   Introduction to Sensitivity for Elemental Imaging.

In previous works, [7] and [8], the authors have investigated the sensitivity of CAT to elemental imaging but neither provide an easy method to determine the minimum detectable concentration of a chosen analyte element in a particulat matrix. In this chapter, the factors which influence the detectibility of an element are investigated for two common situations and easily implemented equations are formulated. The first, is the case when the analyte element is added to the matrix and the second is when the analyte element is already present in the matrix. In both cases the analyte is uniformly distributed in a homogenous cylindrical matrix and the object is assumed to be scanned with monochromatic X-ray beams. Having formulated equations, calculations are made for a range of elements whose absorption edges lie within the detection range of the high resolution energy dispersive detector.

As might be expected, synchrotron sources provide the highest sensitivity to elements due to the high intensities available. In the two previously referenced works, the authors consider synchrotron sources, in particular Grodzin [7] who has investigated the suitability of using such sources for elemental imaging. Grodzin investigates the minimum elemental concentration detectable in a single image pixel in terms of the minimum fraction of analyte "critical" elements. In pratice, it is difficult to verify this experimentally for a single image pixel. In this work, a conventional X-ray tube source is used and the calculated results using the equations formulated for both situations are investigated experimentally.

83

III.2 The Influence of Noise on the Image.

In chapter I, it was stated that noise in the measured data reduces the ability to distinguish low contrast objects in a conventional CAT image by causing fluctuations in the reconstructed attenuation coefficient values. In the same way, noise in X-ray differential CAT images causes fluctuations in the values of the analyte concentration and thus limits the sensitivity of the method to analyte elements .

The noise in a CAT image arises from two sources [41],

   i) noise in the projection data

and

   ii) noise amplification introduced in the reconstruction.

For the first case, i.e. noise in the projection data, two types of noise are considered. The first type is statistical noise, i.e. Poisson noise in the detected counts, while the second is systematic noise which is machine dependent. Statistical noise in the projection data causes images to display a mottled appearance with random pixel to pixel variations from the true image. This is due to the amplification of the statistical noise when the image is reconstructed [41] and [42]. Ideally, there should be no amplification of the noise when reconstructing an image. On the other hand, systematic noise, which may be due to scattering of photons, insufficent projections or misalignment of the detector, gives rise to artifacts in the images such as streaking or tuning-fork artifacts. The overall effect of the noise in CAT is to reduce the quality of the image and limit the elemental concentration that can be detected.

In this analysis, only statistical noise and its amplification due to reconstruction are considered. Noise due to poor alignment of source and detector or due to insufficent projections are machine dependent and are difficult to quantify. These were outlined in Chapter I. In this chapter, the equations to calculate minimum analyte concentrations based on statistical noise and its amplification due to reconstruction are derived.

84

III.3.1 Introduction.

A scan of a slice through a homogenous cylindrical object by a pencil beam of X-rays, with linear and rotational steps, produces scan profiles which are similar for all rotation angles. A cylinder is considered in order to simplfy the mathematics. It is also a good approximation to many of the objects scanned. Since the object is homogenous, it is possible to calculate the transmitted beam flux for any path length knowing the linear attenuation coefficient of the object. In this way, the transmitted beam fluxes for all step positions can be calculated and by summing these, since the projections for all rotations are similar, an equation for the total transmitted beam flux for the whole scan can be found. Finally, a simplified equation which approximates to this is determined. For simplicity, the detector width and the linear scan step size are assumed to be equal.

III.3.2 Calculation of Fractional Transmission for Uniform Matrix.

Consider a homogenous cylindrical matrix of diameter D. A monochromatic X-ray beam in narrow beam geometry (a pencil beam) is incident on the specimen. The transmitted X-ray beam flux after passing through a path length P of the matrix, in the absence of scattering, is given by Beer's law as

$$N = N_0 \exp\left(-U\,P \right) \quad \dots \quad 3.1$$

where U is the linear attenuation coefficient of the uniform specimen and N_0 is the incident flux. A complete scan of the specimen consists of S linear steps of step size dx, at each of R rotation angle positions. See Figure III.1. For any rotation angle and any step position, the beam path length P through the matrix can be given by Pythagoras' theorem as

$$P = 2\left[r^2 - ((s-0.5)dx)^2 \right]^{1/2} \quad \dots \quad 3.2$$

where s is the step position with respect to the centre of rotation. Substituting for P in equation 3.1 gives

$$N = N_0 \exp\left(-2U\left[r^2 - ((s-0.5)dx)^2 \right]^{1/2}\right) \quad \dots \quad 3.3$$
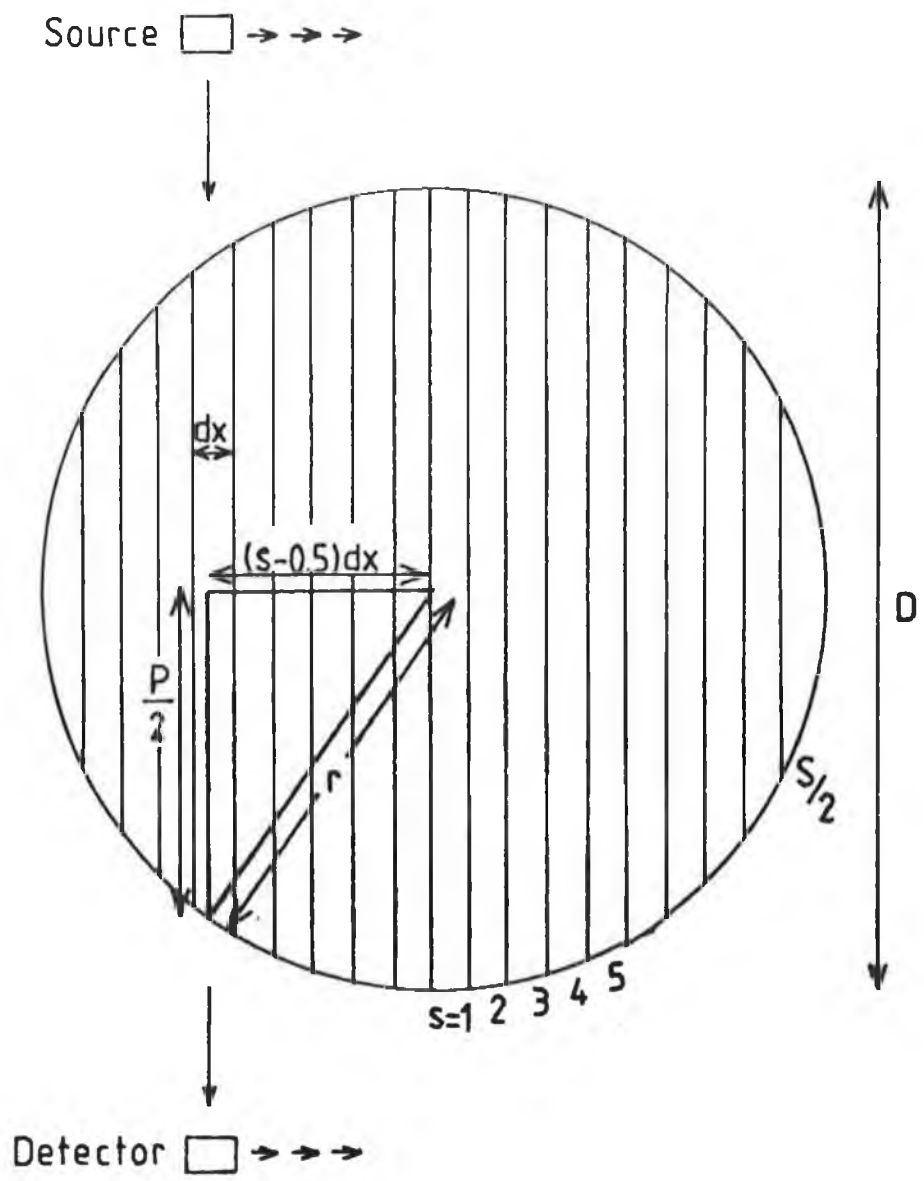
Fig. III.1
The scan geometry as used in the theory for sensitivity.
The sample diameter is D, the radius is r, the path length is
P, step position is s and the beam width is dx.

transmitted photon counts for all step positions for any rotation angle position, the total transmitted count N_t for that profile is

$$N_t = 2 \sum_{s=1}^{S} N_0 \exp\left(-2U\left[r^2-((s-0.5)dx)^2\right]^{1/2}\right) \quad \ldots \ 3.4$$

There are R rotations, so the total number of transmitted photons for a complete scan is

$$N_T = 2R \sum_{s=1}^{S/2} N_0 \exp\left(-2U\left[r^2-((s-0.5)dx)^2\right]^{1/2}\right) \quad \ldots \ 3.5$$

Now, bringing the U term of this equation inside the [] brackets it becomes

$$N_T = 2R \sum_{s=1}^{S/2} N_0 \exp\left(-2\left[r^2U^2-(s-0.5)^2dx^2U^2\right]^{1/2}\right) \quad \ldots \ 3.6$$

Now, the mean free path L for a pencil beam of X-rays is defined as

$$L = 1/U \quad \ldots \ 3.7$$

so the matrix diameter D can be rewritten in terms of x, the number of mean free paths in the specimen diameter. Since D=2r=xL and the step size dx=(D/S)=(xL/S), equation 3.6 becomes

$$N_T = 2R \sum_{s=1}^{S/2} N_0 \exp\left(-2\left[\frac{x^2L^2}{4}\frac{1}{L^2} - (s-0.5)^2\frac{x^2L^2}{S^2}\frac{1}{L^2}\right]^{1/2}\right) \quad \ldots \ 3.8$$

The L terms cancel, so when rearranged equation 3.8 becomes,

$$N_T = \frac{2}{S} N_{OT}\sum_{s=1}^{S/2} \exp\left(-x\left[1 - \frac{4(s-0.5)^2}{S^2}\right]^{1/2}\right) \quad \ldots \ 3.9$$

where N_{OT} = R . N_0. S is the total number of incident photons in a scan. A plot of N_T/N_{OT} (the fractional transmission) vs. x (the specimen diameter in mean free paths) is shown in figure III.3. The fraction N_T/N_{OT} is for the purpose of this work, independent of S if S>20. The curve in figure III.3 can be approximated, for x =0.1 to 10, by the expression

$$N_T = N_{OT}\exp\left\{-\left(0.0275+0.762x-0.0279x^2\right)\right\} \quad \ldots \ 3.10$$

In this way it is quite easy to determine the total number of transmitted photons, N_T, knowing the object diameter in mean free paths.

FRACTION TRANSMISSION VS BEAM POSITION

FOR CYLINDRICAL MATRIX
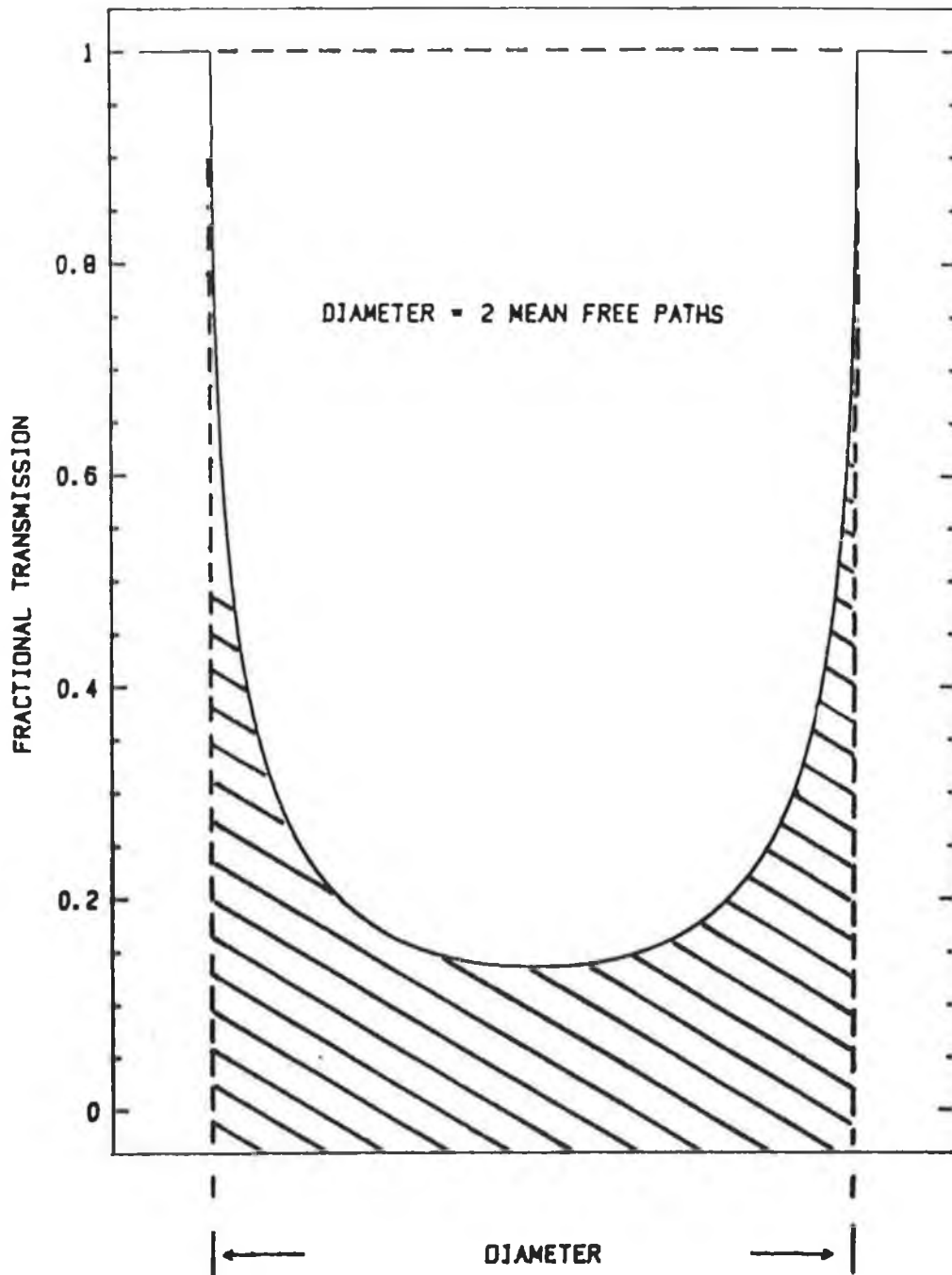
Fig. III.2
The X-ray beam transmission as a function of step position
for a sample diameter of two mean free paths. The shaded area
divided by the total enclosed area is the total fractional
transmission for two mean free paths, i.e. N_T/N_{0T} = 0.21.

TRANSMISSION —:

$Nt/Not = EXP(-(0.0275+0.762X-0.0279X^2))$

X (DIAMETER IN MEAN FREE PATHS)
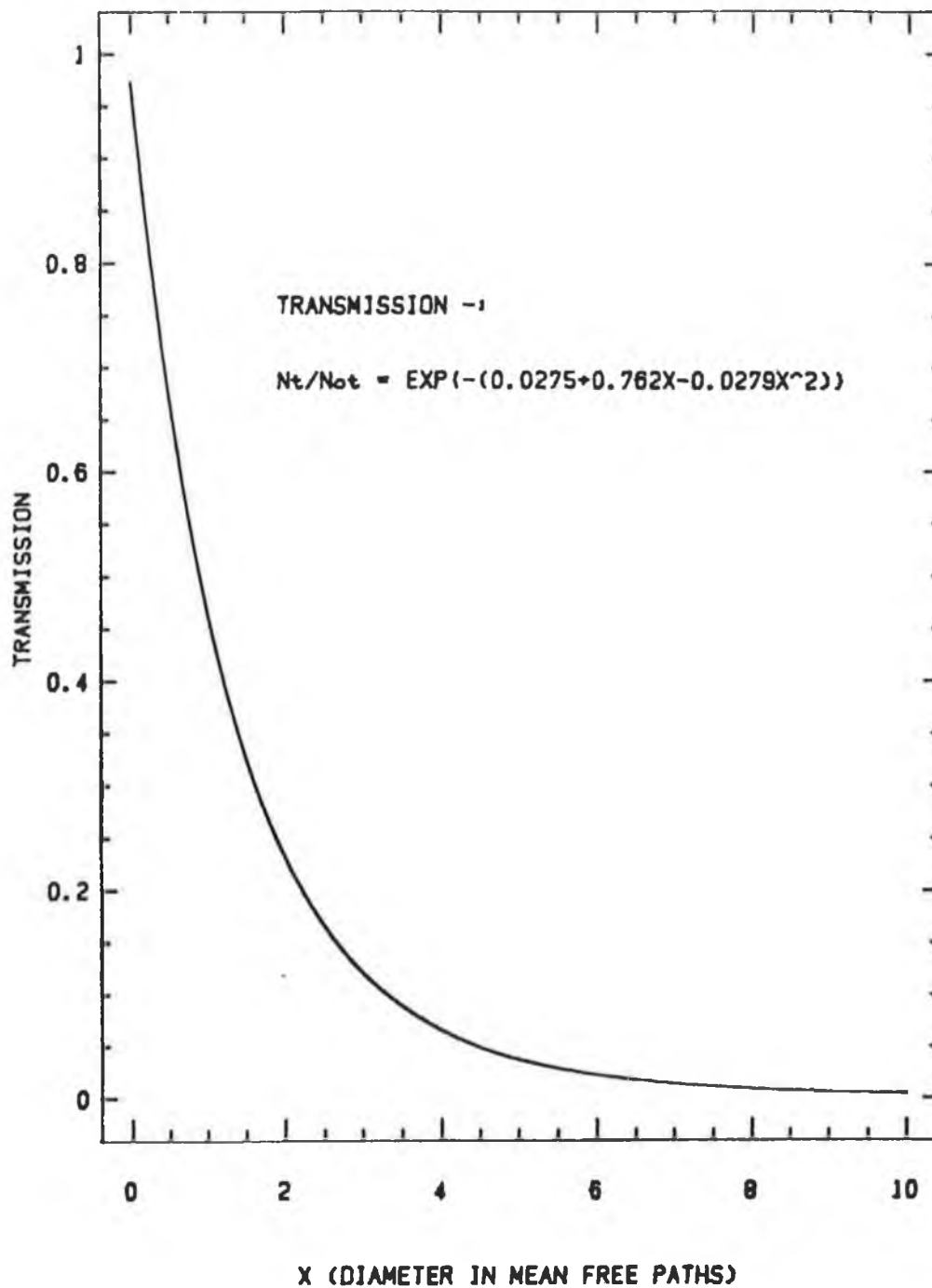
Fig. III.3
The transmission Nt/Not through a cylindrical matrix as a function of the diameter in mean free paths. The curve is approximated by the equation shown for x - 0.1 to 10.

III.4 Calculation of the minimum analyte concentration detectable in a homogenous cylindrical matrix for the first case when analyte can be added to the matrix.

III.4.1 Introduction.

For this first case, an expression is formulated to calculate the minimum analyte concentration detectable in a homogenous cylindrical matrix when the analyte material can be added to the matrix specimen. The specimen is scanned, as previously described, by X-ray beams of the same energy both before and after the analyte is added. After reconstructing the images, the matrix image is subtracted from the analyte plus matrix image to leave an image showing the analyte only. The equation formulated here is used to determine the minimum analyte concentration detectable above the noise in the subtracted image. This equation takes account of the statistical noise in the detected photon count, its amplification due to reconstruction and also includes parameters which are machine dependent. However, before such an expression can be derived, an expression is required to determine the minimum change in the specimen linear attenuation coefficient that can detected when the analyte is added to the matrix. This expression is derived below.

III.4.2 The minimum detectable fractional change in the linear attenuation coefficient.

Consider the case where the specimen, a homogenous cylindrical matrix, is scanned by an X-ray beam in narrow beam geometry. The total number of detected X-ray photons N_T at any energy E, is given by equation 3.10 as

$$N_T = N_{OT}\exp\left\{-\left(0.0275+0.762x-0.0279x^2\right)\right\} \dots 3.10.$$

While keeping the specimen diameter constant, a small concentration of analyte is added to the specimen. In doing so, the mean free path, L, for X-rays of energy E, becomes L'. Similarily there are now x' new mean free paths along the diameter so that

$$\text{diameter} = D = xL = x'L'. \quad \dots 3.11$$

When the analyte plus matrix specimen is now scanned at the same

90

X-ray energy, the total detected X-ray count is given by

$$N'_T = N'_{0T} \exp\left\{-\left[0.0275+0.762x'-0.0279x'^2\right]\right\} \quad \ldots \text{ 3.12}$$

Recalling equation 3.7, where $L=1/U$ and rearranging equation 3.11, gives x' as

$$x' = \frac{xL}{L'} = x\left(\frac{U+dU}{U}\right) \quad \ldots \text{ 3.13}$$

where U is the linear attenuation coefficient of the matrix and U+dU is that for the matrix plus analyte. Substituting for x' in equation 3.12 with equation 3.13, the total detected X-ray count for the analyte plus matrix specimen is now given by

$$N'_T = N'_{0T} \exp\left\{-\left[0.0275+0.762x\left(\frac{1+dU}{U}\right)-0.0279x^2\left(\frac{1+dU}{U}\right)^2\right]\right\} \quad \ldots \text{ 3.14}$$

Having determined equations for the transmitted photon counts for the scans before and after analyte is added, a criterion for the detectibility of the analyte can now be stated; that the analyte is statistically detectable if the difference in the total detected X-ray counts of the two scans is greater than or equal to ρ standard deviations, where ρ has yet to be determined. One standard deviation is equal to the square root of N_T and it is assumed for small analyte concentrations that $\sqrt{N_T}$ is equal to $\sqrt{N'_T}$. Mathematically the criterion is satisfied at the limit of detection if the difference dN in the total count is given by

$$dN = \rho\left(N_T\right)^{1/2} = N_T - N'_T. \quad \ldots \text{ 3.15.}$$

Unfortunately, amplification of the statistical noise occurs during reconstruction so equation 3.15 needs further modification to take account of this. Since a typical image consists of KxK pixels, then on average the number of photons which pass through a pixel is N_T/K and N'_T/K for the two beams. Taking this into account, the analyte is detectable in the subtracted image if

$$\frac{N_T}{K} - \frac{N'_T}{K} \geq \rho\, B \sqrt{\frac{N_T}{K}} \quad \ldots \text{ 3.16}$$

or when rearranged

$$N_T - N'_T \geq \rho\, B\, K^{1/2}\, N_T^{1/2} \quad \ldots \text{ 3.17}$$

where B is a factor (≈ 2) introduced in the reconstruction algorithm by Chesler [41]. The factor B is dependent on the reconstruction algorithm used and is approximately equal to 2 for filtered back-projection. It is introduced as a multiplication factor which amplifies the statistical noise in the detected photon count. The factor $N_T^{1/2}$ is a measure of the statistical noise, i.e. Poisson noise, present in the total detected photon count [41]. Equation 3.17 can be rewritten as

$$N_T - N'_T \geq Q \, N_T^{1/2} \quad \dots \, 3.18$$

where $Q = \rho \, B \, K^{1/2}$. Substituting for N_T and N'_T with equations 3.10 and 3.14 in equation 3.18, it becomes at the limit of detection,

$$Q(N_{OT})^{1/2} \, \exp\left\{-0.5\left(0.0275+0.762x-0.0279x^2\right)\right\} =$$
$$N_{OT}\left[\exp\left\{-\left(0.0275+0.762x-0.0279x^2\right)\right\} \qquad \dots \, 3.19\right.$$
$$\left. - \exp\left\{-\left(0.0275+0.762x\left(\frac{1+dU}{U}\right)-0.0279x^2\left(\frac{1+dU}{U}\right)^2\right)\right\}\right]$$

Expansion and rearrangement of the terms on the right hand side of equation 3.19 gives

$$Q(N_{OT})^{1/2} \, \exp\left\{-0.5\left(0.0275+0.762x-0.0279x^2\right)\right\} =$$
$$N_{OT}\left[\exp\left\{-\left(0.0275+0.762x-0.0279x^2\right)\right\} \qquad \dots \, 3.20\right.$$
$$\left.\left(1-\exp\left\{-\left(0.762xdU/U-0.0558x^2dU/U-0.0279x^2dU^2/U^2\right)\right\}\right)\right]$$

Multiplying both sides of equation 3.20 by the term

$$-\exp\left\{\left(0.0275+0.762x-0.0279x^2\right)\right\} \quad \dots \, 3.21$$

and then rearranging the result gives

$$\exp\left\{-\left(0.762xdU/U-0.0558x^2dU/U-0.0279x^2dU^2/U^2\right)\right\} =$$
$$\qquad\qquad\qquad \dots \, 3.22$$
$$1-Q\left[\exp\left\{0.5\left(0.0275+0.762x-0.0279x^2\right)\right\}\right]\Big/ N_{OT}^{1/2}$$

After taking the natural logarithm of both sides of equation 3.22, the dU^2/U^2 term can be dropped as it is insignificant for small

analyte concentrations, i.e., $dU/U \gg dU^2/U^2$, when $dU \ll U$. This leaves

$$\left(0.0558x^2 - 0.762x\right) dU/U =$$

$$\ln\left[1 - Q\left[\exp\left\{0.5\left(0.0275 + 0.762x - 0.0279x^2\right)\right\}\right]\right] \Big/ N_{OT}^{1/2} \qquad \qquad \ldots. \ 3.23$$

which becomes, when both sides of this equation are divided by the term $(0.0588x^2 - 0.762x)$,

$$\frac{dU}{U} = \frac{\ln\left[1 - Q\left[\exp\left\{0.5\left(0.0275 + 0.762x - 0.0279x^2\right)\right\}\right]\right] \Big/ N_{OT}^{1/2}}{\left(0.0558x^2 - 0.762x\right)} \qquad \ldots. \ 3.24$$

where dU/U is the minimum fractional change in the linear attenuation coefficient that can be distinguished in a subtracted image. Since the term $\ln[1-Z]$ can be approximated by $-Z$ when Z is small, equation 3.24 can be approximated to

$$\boxed{\frac{dU}{U} = \frac{Q\,F}{N_{OT}^{1/2}}} \qquad \ldots. \ 3.25$$

provided $N_{OT} > 10^6$ and $0.1 < x < 10$. The function F is given by

$$F = \frac{\left(\exp\left\{0.5\left(0.0275 + 0.762x - 0.0279x^2\right)\right\}\right)}{\left(0.762x - 0.0558x^2\right)} \qquad \ldots. \ 3.26$$

The function F is plotted against x to produce a universal curve as shown in figure III.4. Its minimum occurs at 2.5 mean free paths. Similarily, the corresponding minimum for dU/U for any Q or N_{OT} also occurs at this diameter. This is in good agreement with Grodzin [7] and Flannery [8] who have shown that the most sensitive diameter is between 2 and 3 mean free paths.

Equation 3.25 gives the minimum detectable fractional change in the linear attenuation coefficient when analyte is added to the matrix for any diameter. It is now required to find an expression for the corresponding minimum analyte concentration detectable.

93
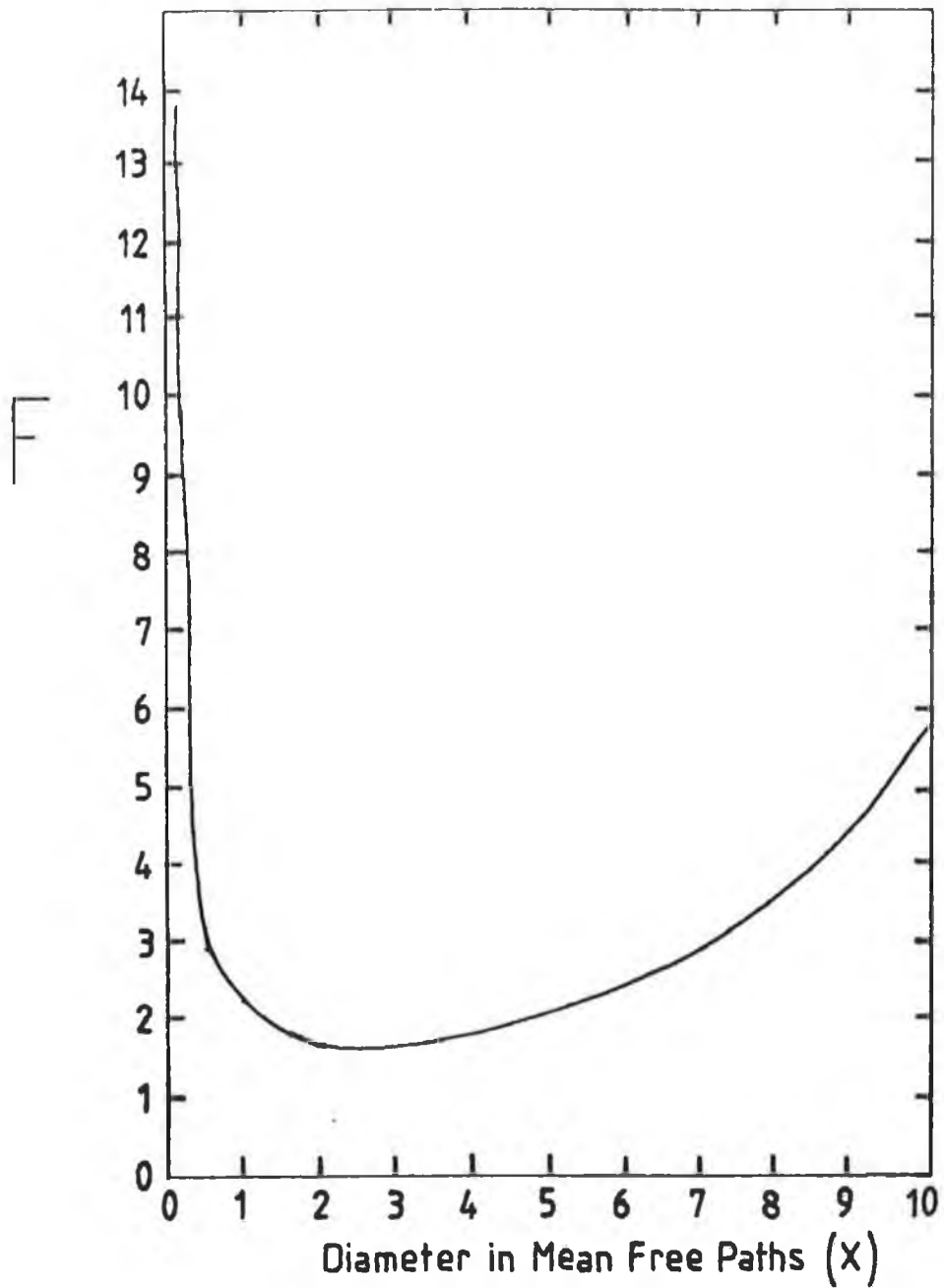
Fig. III.4
The function F, equation 3.25, plotted against the sample
diameter in mean free paths (x). This curve is a universal
curve and its minimum occurs at x = 2.5 where F = 1.54.

III.4.3 Minimum analyte concentration detectable when analyte can be added to the matrix.

Having determined an equation for the minimum fractional change in the linear attenuation coefficient detectable at any X-ray energy, when analyte can be added to the matrix, it is now possible to formulate an equation to calculate the corresponding minimum analyte concentration detectable. Then, by plotting the calculated analyte concentration against X-ray energy for a chosen matrix material, the most sensitive X-ray energy to the analyte element in that particular matrix can be determined.

Matrix Only   Matrix + Analyte
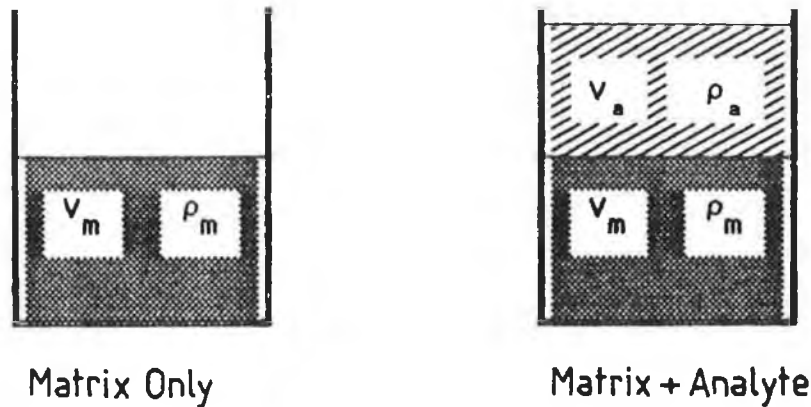
Fig. III.5
Diagrams of the matrix and matrix plus analyte samples for the case when analyte can be added to the matrix. Their volumes and densities are, V_m and V_a, and, p_m and p_a, respectively.

Consider the homogenous cylinder to have a volume V_m and a density p_m. To this is added a volume V_a of analyte mixture containing a density p_a of analyte. See figure III.5. The volume of this analyte and matrix mixture is V_a+V_m. The concentration of the analyte in this mixture is

$$C_a = \frac{(p_a V_a)}{(V_a+V_m)} \quad \dots \quad 3.27$$

while the concentration of the matrix in the same mixture is

$$C_m = \frac{(p_m V_m)}{(V_a+V_m)} \quad \dots \quad 3.28$$

Dividing equation 3.27 by equation 3.28 and then rearranging gives

$$C_a = \frac{(V_a p_a C_m)}{(V_m p_m)} \quad \dots \quad 3.29$$

which will be requred later in this discussion.

95

Now, the change in the linear attenuation due to analyte being added to the matrix can be defined as

$$dU = U_{a+m} - U_m \quad \ldots \ldots \ 3.30$$

where the subscript a+m refers to the analyte plus matrix mixture. The linear attenuation coefficient of an element can be defined as $U = uC$ where C is the element concentration and u is the element mass absorption coefficient. Therefore, replacing the linear attenuation coefficients on the right hand side of equation 3.30 with their concentrations and mass absorption coefficients gives

$$dU = (C_a u_a + C_m u_m) - p_m u_m \quad \ldots \ldots \ 3.31$$

where p_m is the density of the original matrix. Substituting for C_a and C_m in equation 3.31 with equations 3.27 and 3.28 it becomes

$$dU = p_a u_a \left(\frac{V_a}{V_a+V_m} \right) + p_m u_m \left(\frac{V_m}{V_a+V_m} \right) - p_m u_m. \quad \ldots \ldots \ 3.32$$

Collecting the $p_m u_m$ terms together gives

$$dU = p_a u_a \left(\frac{V_a}{V_a+V_m} \right) + p_m u_m \left(\frac{V_m}{V_a+V_m} - 1 \right) \quad \ldots \ldots \ 3.33$$

which can be rewritten as

$$dU = p_a u_a \left(\frac{V_a}{V_a+V_m} \right) + p_m u_m \left(\frac{V_m}{V_a+V_m} - \frac{V_a+V_m}{V_a+V_m} \right). \quad \ldots \ldots \ 3.34$$

Subtraction of the V_m terms on the right hand side of this equation and rearrangement of the remainder gives

$$dU = \left(\frac{V_a}{V_a+V_m} \right) \left(p_a u_a - p_m u_m \right). \quad \ldots \ldots \ 3.35$$

Since the original specimen was a homogenous matrix, dividing both sides of equation 3.35 by the matrix linear attenuation coefficient gives

$$\frac{dU}{U_m} = \frac{dU}{p_m U_m} = \left(\frac{V_a}{V_a+V_m} \right) \left(\left(\frac{p_a u_a}{p_m u_m} \right) - 1 \right). \quad \ldots \ldots \ 3.36$$

This equation can be rearranged to give the ratio of volumes as

$$\frac{V_a}{V_m} = \frac{\left(\dfrac{dU}{U_m} \right)}{\left(\left(\dfrac{p_a u_a}{p_m u_m} \right) - 1 - \left(\dfrac{dU}{U_m} \right) \right)} \quad \ldots \ldots \ 3.37$$

which can be substituted into equation 3.29 The resultant

substitution gives the equation

$$C_a = \frac{p_a\left(\dfrac{dU}{U_m}\right)}{\left(\left(\dfrac{p_a u_a}{p_m u_m}\right) - 1 - \left(\dfrac{dU}{U_m}\right)\right)}$$ 3.38

In equation 3.29, it was assumed that the change in the matrix concentration is negligible when the analyte is added so that $C_m = p_m$. If the term dU/U_m is taken to be the minimum detectable fractional change in the linear attenuation coefficient, as defined by equation 3.25, which is given by

$$\frac{dU}{U} = \frac{Q\ F}{N_{OT}^{1/2}}$$ 3.25

then equation 3.38 gives the minimum analyte concentration C_a, which is detectable in the resultant subtracted image when analyte is added to the matrix.

Close examination of equation 3.38 shows that C_a is dependent on several factors. These include the nature of the analyte and the nature of the matrix, i.e, their mass absorption coefficients and their densities. The densities are the elemental densities at S.T.P. The other factors include the specimen diameter in terms of matrix mean free paths, the total number of incident photons and the machine dependent factor Q. These last factors are included in the equation for dU/U.

In pratice, the specimen is scanned with a pencil beam of X-rays of energy E both before and after the analyte has been added. Then, after calculating the projection values, two images are reconstructed, one showing the spatial variation of the matrix linear attenuation coefficient, the other showing the spatial variation of the matrix plus analyte linear attenuation coefficient. When the first image is subtracted from the second, the resultant image shows the spatial variation of the analyte. In the next section, equation 3.38 is used to calculated the minimum analyte concentrations detectable above the noise in the resultant image when cadmium is added to a water matrix.

III.4.4 <u>Calculations of minimum detectable analyte concentrations</u>
<u>for cadmium in water and in silicon matrices.</u>

Figure III.6 shows the minimum detectable concentrations, calculated using equation 3.38 and figure III.4, plotted against X-ray energy with Q=1 for cadmium analyte in a water matrix of diameter 2.5 mean free paths using 10^7 incident photons. Using this graph, the minimum cadmium concentration detectable can easily be determined for any machine if the factor Q is known. Similarily, the analyte sensitivity at any other matrix diameter can be determined by multiplying the result at 2.5 mean free paths by the appropriate multiplying factor from figure III.7, which is a plot of $F_x/ F_{2.5}$ against diameter in mean free paths. Note, that the actual physical diameter changes with X-ray energy, as the linear attenuation coefficient changes with energy.

Figure III.8 shows C_a plotted against X-ray energy for cadmium in a water matrix with the machine factor Q≅38. Previously, Q was defined as $Q= \rho \ B \ K^{1/2}$. Normally ρ, the separation in standard deviations between the images is 3 and for a good algorithm B≅2 [41]. In this work K=40 since the step size is equal to the pixel size.

The calculations above show that the technique is most sensitive to cadmium in water just at the high energy side of the cadmium K-absorption edge. For the case of cadmium in silicon the maximum sensitivity occurs several keV above the cadmium K-edge. See figure III.9. Thus, it is important to note that the highest sensitivity does not necessarily occur at the high energy side of the K-edge of the analyte in all cases.

In III.4.2, it was shown that the technique is most sensitive to a matrix of diameter 2.5 mean free paths. In figure III.7 the sensitivity multiplying factor to determine the sensitivity at any other diameter, when the sensitivity at 2.5 mean free paths is known, is shown. Combining figures III.7 and III.8, the minimum cadmium concentration detectable in a water matrix is plotted for diameters .1 to 10 mean free paths and for all energies within the range, 4-60keV, for 10^7 incident photons. See figure III.10.
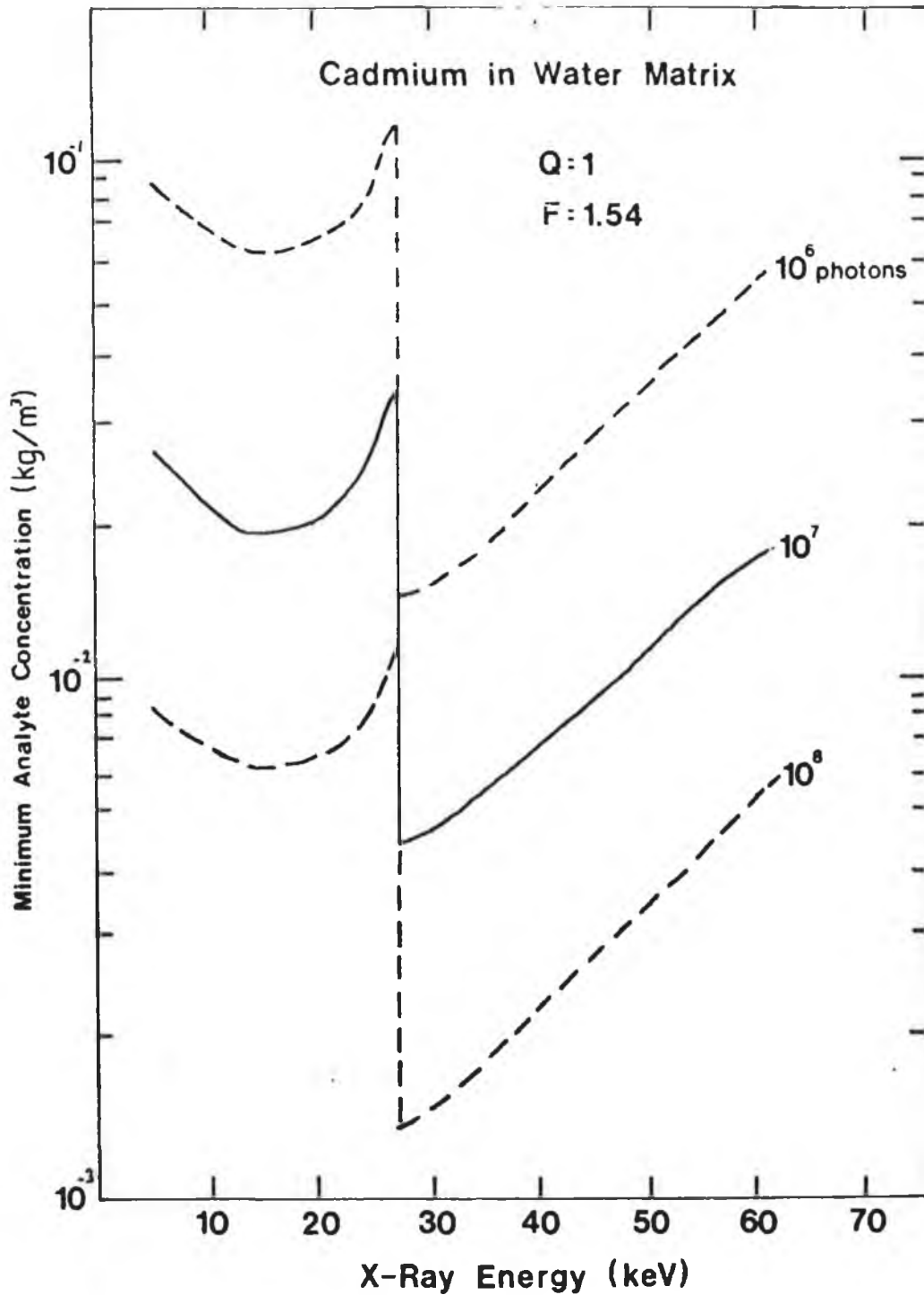
Fig. III.6
The minimum cadmium concentration detectable in a cylindrical
water matrix of diameter 2.5 mean free paths. This is for the
case when analyte can be added to the matrix. These values
were calculated using equation 3.38 and figure III.4 for the
machine factor Q-1. Knowing the machine factor for a machine,
the minimum cadmium concentration can be calculated.

DIAMETER IN MEAN FREE PATHS (X)

Fig. III.7
A plot of the concentration multiplying factor   Fx/F2.5
against matrix diameter for x=0.1 to 10. At x=2.5, Fx/F2.5=1.
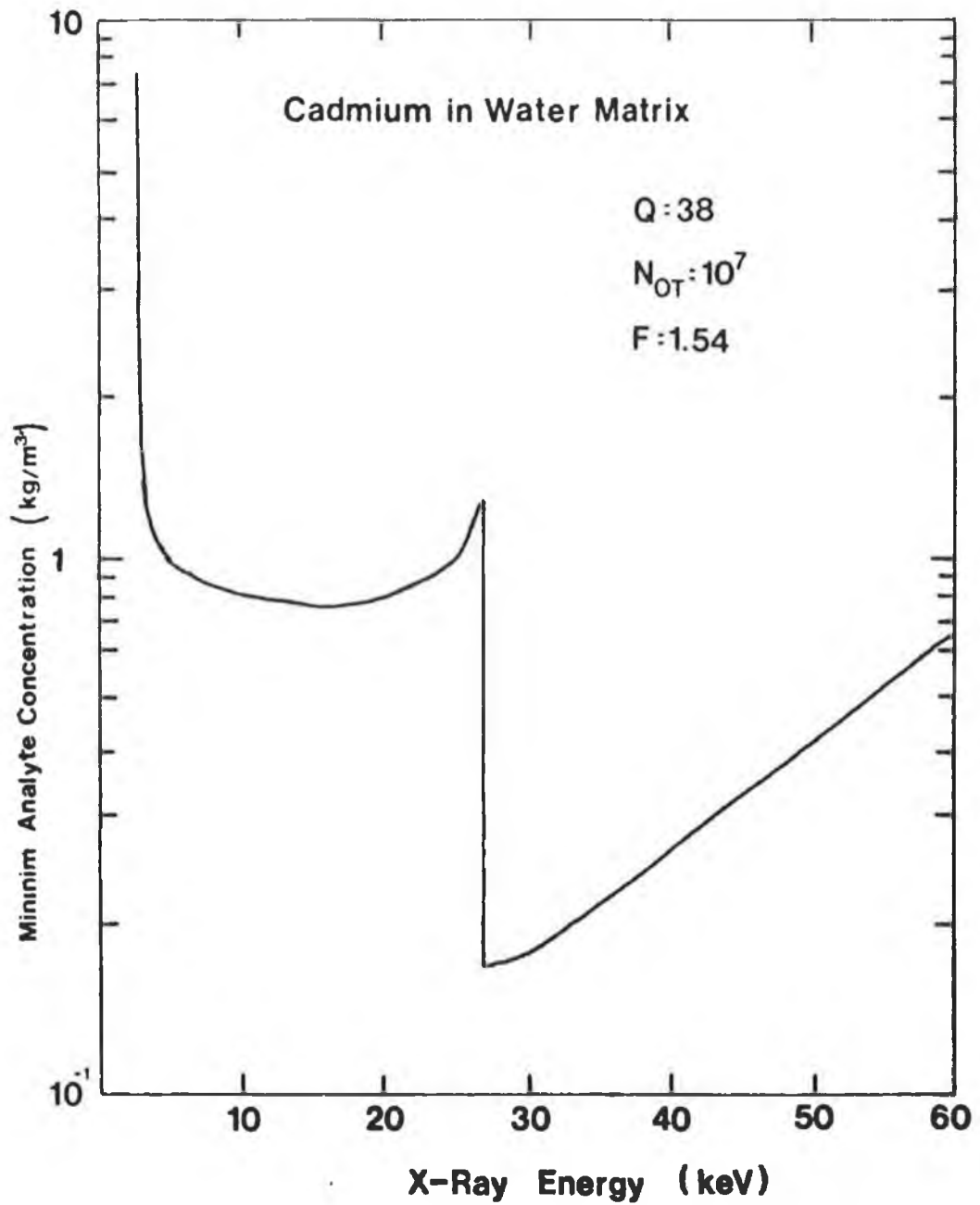
Fig. III.8
The minimum cadmium concentration detectable in a cylindrical
water matrix of diameter 2.5 mean free paths with machine
factor Q= 38 for the case when analyte can be added to the
matrix.

III.5

Calculation of the minimum analyte concentration detectable in a
homogenous matrix when analyte is already present in the matrix.

III.5.1 Introduction.

In this section, an equation to calculate the minimum analyte
concentration detectable in a homogenous specimen when the analyte
is already present in the specimen is formulated. For this case, it
is not possible to determine this concentration by scanning the
specimen at a single fixed X-ray energy. However, by scanning with
two or more X-ray beams, which are close in energy, the effect of
the matrix can be removed. It has been shown by J. Fryar, K.J.
McCarthy and A. Fenelon [28] that energies which straddle the
analyte attenuation edge are most effective for this purpose.

III.5.2 Calculation of the number of mean free paths in object
diameter.

Consider a specimen of diameter D being scanned by two X-ray
beams of energy E_l and E_h, where the subscripts l and h refer to
the low and high energy sides of the analyte K-absorption edge. The
diameter of the cylindrical object is defined, as in equation 3.11,
by

$$\text{diameter} = D = x_l L_l = x_h L_h \quad \dots \text{3.39}$$

where L is the mean free path for an X-ray beam of energy E and x
is the number of mean free paths in the diameter. Rearrangement of
equation 3.39 gives x_h in terms of x_l as

$$x_h = x_l \left(\frac{L_l}{L_h} \right) = x_l \left(\frac{U_h}{U_l} \right) \quad \dots \text{3.40}$$

where $L = 1/U$ by definition. The linear attenuation coefficient U
of the specimen can be seperated into its two parts, U_a and U_m,
which are the analyte and matrix linear attenuation coefficients
respectively. Substituting the U's into equation 3.40 gives

$$x_h = x_l \left(\frac{U_{ah} + U_{mh}}{U_{al} + U_{ml}} \right). \quad \dots \text{3.41}$$

Examining figure II.4, it is seen that at the analyte K-absorption
edge, $U_{ml} = U_{mh}$, which are now called U_m. Equation 3.41 now becomes

$$x_h = x_l \left(\frac{U_{ah} + U_m}{U_{al} + U_m} \right) \quad \dots \text{3.42.}$$
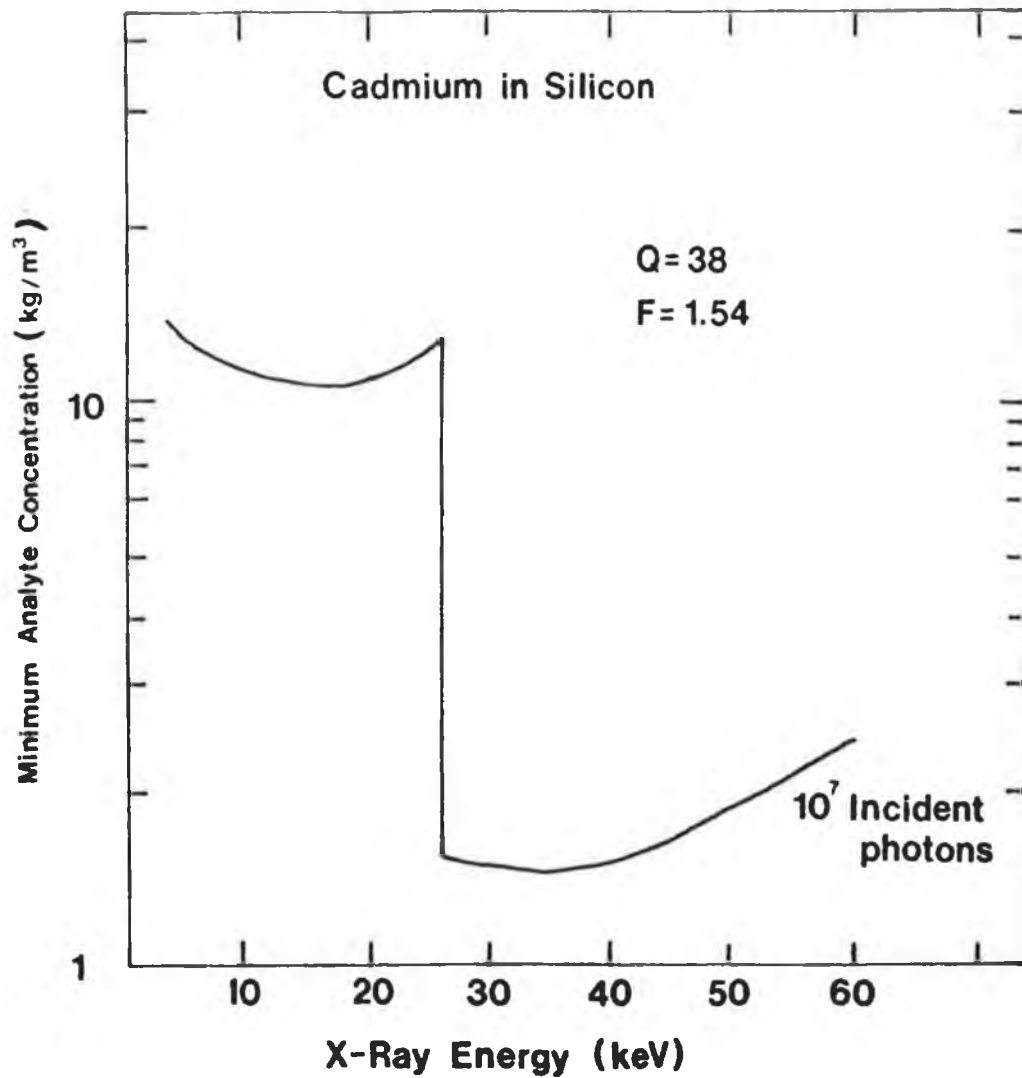
Fig. III.9
The minimum cadmium concentration detectable in a cylindrical
silicon matrix of dimeter 2.5 mean free paths plotted against
X-ray energy. The curve was plotted using equation 3.38 and
figure III.4. In this case Q - 38, N_{OT} - 10^7 and F - 1.54.

Cadmium in Water

$Q = 38$

$N_{OT} = 10^7$
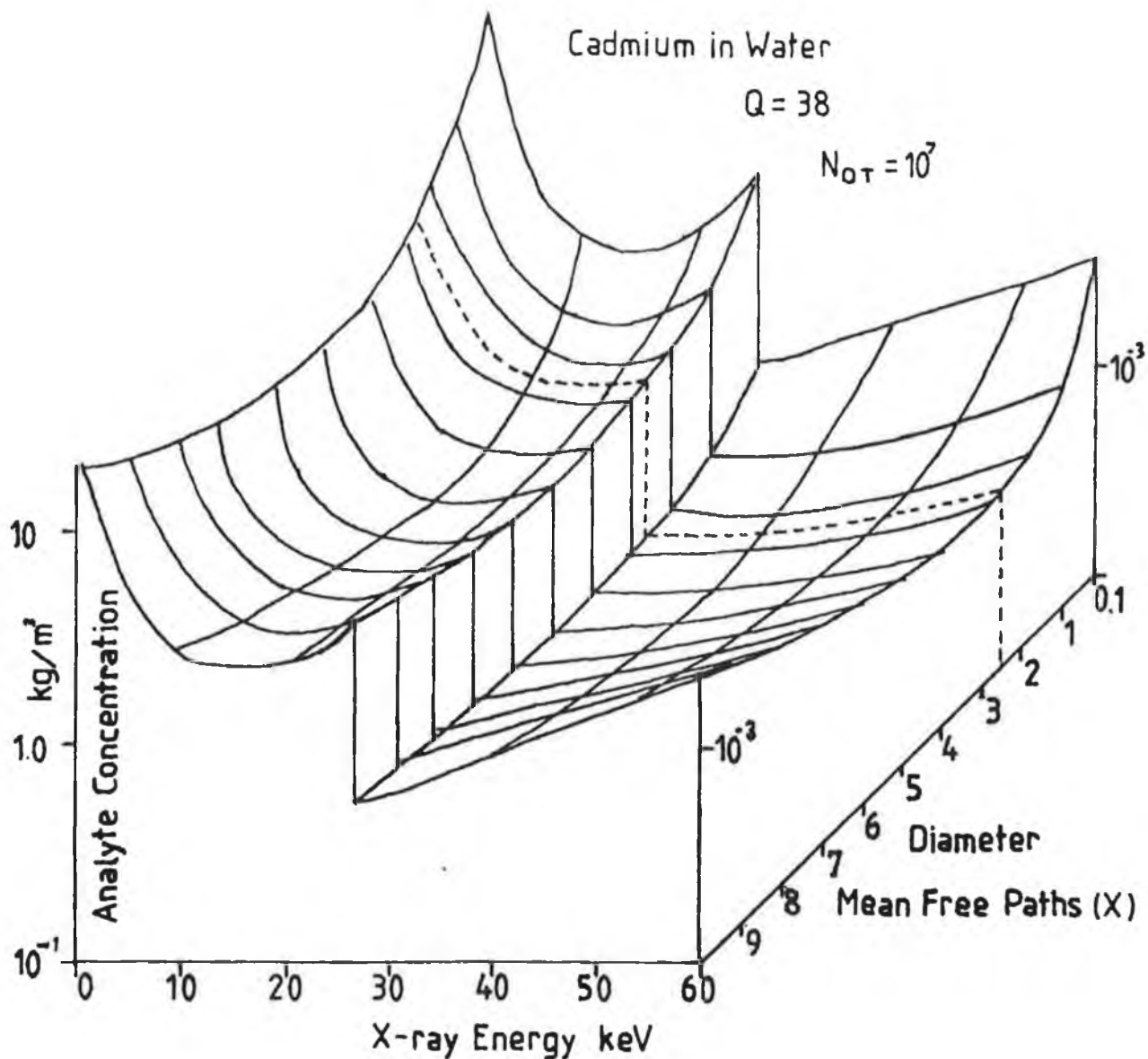
Fig. III.10
A three-dimensional plot showing the minimum cadmium concentration detectable in a cylindrical water matrix against X-ray energy and against diameter in mean free paths. The minumum concentration detectable occurs for all energies at 2.5 mean free paths. This is for the case when analyte can be added to the matrix.

Since $x_1 = (1/U_{a1}+U_m)$, addition of the term $x_1(U_{a1}-U_{a1}/U_{a1}+U_m)$ to the right hand side of equation 3.42 gives

$$x_h = x_1\left(\frac{U_{a1}+U_m+U_{ah}-U_{a1}}{U_{a1}+U_m}\right) \quad \cdots \quad 3.43$$

which can be rewritten as

$$x_h = x_1\left(1+\left(\frac{dU}{U_m+U_{a1}}\right)\right) \quad \cdots \quad 3.44$$

where $dU = U_{ah}-U_{a1}$, the change in the linear attenuation coefficient across the analyte K-absorption edge. Note that dU is due entirely to the analyte present in the specimen, i.e. $U_{m1}=U_{mh}$. Equation 3.44 gives the number of mean free paths of energy E_h in the specimen diameter in terms of the number of mean free path of energy E_1 in the same diameter. This is required further on in this discussion.

III.5.3 The minimum fractional change detectable in the linear attenuation coefficient for the case when analyte is present in the specimen.

The form of the arguement used in this case is similar to that used when the analyte is added to the matrix. Thus, it is first necessary to formulate an equation to determine the minimum fractional change in the linear attenuation coefficient that is detectable in the specimen. Since the specimen is cylindrical and homogenous, the total transmitted photon count for an X-ray beam scanning a homogenous cylindrical specimen is approximated, as in III.4.2, by

$$N_T = N_{OT}\exp\left\{-\left[0.0275+0.762x-0.0279x^2\right]\right\} \quad \cdots \quad 3.10$$

where x is the number of mean free patyhs in the diameter. Now, when the analyte plus matrix specimen is scanned by X-ray beams of energy E_1 and E_h, the total detected photon count is given by

$$N_{T1} = N_{OT1}\exp\left\{-\left[0.0275+0.762x_1-0.0279x_1^2\right]\right\} \quad \cdots \quad 3.45$$

and

$$N_{Th} = N_{OTh}\exp\left\{-\left[0.0275+0.762x_h-0.0279x_h^2\right]\right\} \quad \cdots \quad 3.46$$

respectively, where N_{OT1} and N_{OTh} are the total incident photon counts. Substituting for x_h in equation 3.46, with equation 3.44, gives

$$N_{Th} = N_{OTh} \exp\left\{-\left[0.0275 + 0.762 x_1\left(1 + \left(\frac{dU}{U}\right)\right)\right] - 0.0279 x_1^2 \left(1 + \left(\frac{dU}{U}\right)\right)^2\right\} \qquad 3.47$$

where $U = U_m + U_{al}$.

The presence of analyte in the specimen can be detected if the difference in the total counts for the two X-ray energies is greater than or equal to ρ standard deviations, where one standard deviation is $\sqrt{N_T}$. At the limit of analyte detection, this difference is given by

$$dN_T = N_{Tl} - N_{Th} \quad \ldots\ldots 3.48$$

and since N_{Tl} and N_{Th} are approximately equal, this difference can be given by

$$dN_T = \rho\left(N_{Tl}\right)^{1/2} \quad \ldots\ldots 3.49$$

However, because of the amplification of the statistical noise during reconstruction of the image, it is not possible to observe this change in the linear attenuation coefficient, due to this analyte concentration, in the image. Now, noting that on average, the number of photons of energy E_1 and E_h passing through a pixel in the image is N_{TL}/K and N_{TH}/K respectively, a criterion for observing analyte in the reconstructed image can be stated. It is, that the difference in the average number of photons passing through a pixel should be greater or equal to Q standard deviations. At the limit of detection this is given as

$$\frac{N_{TL}}{K} - \frac{N_{TH}}{K} = \rho\, B\sqrt{\frac{N_{TL}}{K}} \quad \ldots\ldots 3.50$$

or

$$N_{TL} - N_{TH} \geq \rho\, B\, K^{1/2}\, N_{TL}^{1/2} \quad \ldots\ldots 3.51$$

where $Q = \rho\, B\, K^{1/2}$ and one standard deviation is equal to $N_{TL}^{1/2}$, which is a measure of the Poisson noise. As before B is a factor introduced by the reconstruction algorithm, Chesler [41], and K is the number of the average number of pixels along a beam path. Substituting for N_{TL} and N_{Th} with equations 3.45 and 3.47 gives

$$Q(N_{OT})^{1/2} \exp\left\{-0.5\left[0.0275+0.762x_1-0.0279x_1^2\right]\right\} =$$

$$N_{OT}\left[\exp\left\{-\left[0.0275+0.762x_1-0.0279x_1^2\right]\right\}\right. \qquad \ldots. \ 3.52$$

$$\left. - \exp\left\{-\left[0.0275+0.762x_1\left(1+\frac{dU}{U}\right)-0.0279x_1^2\left(1+\frac{dU}{U}\right)^2\right]\right\}\right]$$

where it is assumed that $N_{OT1} = N_{OTh}$, which is now given by N_{OT}. Expansion and rearrangement of the terms on the right hand side of equation 3.52 gives

$$Q(N_{OT})^{1/2} \exp\left\{-0.5\left[0.0275+0.762x_1-0.0279x_1^2\right]\right\} =$$

$$N_{OT}\left[\exp\left\{-\left[0.0275+0.762x_1-0.0279x_1^2\right]\right\}\right. \qquad \ldots. \ 3.53$$

$$\left. \left(1-\exp\left\{-\left[0.762x_1\left(\frac{dU}{U}\right)-0.0558x_1^2\left(\frac{dU}{U}\right)-0.0279x_1^2\left(\frac{dU}{U}\right)^2\right]\right\}\right)\right]$$

Multiplying both sides of this equation by the term

$$-\exp\left\{\left[0.0275+0.762x_1-0.0279x_1^2\right]\right\} \qquad \ldots. \ 3.54$$

and then adding 1 to both sides, it becomes

$$\exp\left\{-\left[0.762x\left(\frac{dU}{U}\right)-0.0558x_1^2\left(\frac{dU}{U}\right)-0.0279x_1^2\left(\frac{dU}{U}\right)^2\right]\right\} =$$

$$\qquad \ldots. \ 3.55$$

$$1-Q\left[\exp\left\{0.5\left[0.0275+0.762x_1-0.0279x_1^2\right]\right\}\right]\Big/ N_{OT}^{1/2}$$

By taking the natural logarithm of both sides of equation 3.55, the term dU^2/U^2 becomes insignificant for small concentrations of analyte, i.e. $dU/U \gg dU^2/U^2$ when $dU \ll U$, and it disappears from the equation leaving

$$\left(0.0558x_1^2-0.762x_1\right)dU/U = \qquad \ldots. \ 3.56$$

$$\ln\left[1-Q\left[\exp\left\{0.5\left[0.0275+0.762x_1-0.0279x_1^2\right]\right\}\right]\right]\Big/ N_{OT}^{1/2}$$

Dividing both sides of this by the term $(0.0588x_1^2-0.762x_1)$ gives

$$\frac{dU}{U_m+U_{a1}} = \frac{\ln\left\{1-Q\left[\exp\left\{0.5\left[0.0275+0.762x_1-0.0279x_1^2\right]\right\}\right]\right/ N_{0T}^{1/2}\right\}}{\left(0.0558x_1^2-0.762x_1\right)} \qquad \ldots\ldots 3.57$$

where U, the linear attenuation coefficient has been replaced by U_m+U_{a1}, its matrix and analyte components. This equation can be simplified by considering the term ln[1-Z] which can be approximated by -Z when the term Z is small. In equation 3.57 the term inside the [] brackets is small provided both $N_{0T} > 10^6$ and $0.1 < x_1 < 10$. Thus equation 3.57 can be simplified to

$$\frac{dU}{U_m+U_{a1}} \cong \frac{Q\ F}{(N_{0T})^{1/2}} \qquad \ldots\ldots 3.58$$

where the function F is given by

$$F = \frac{\left(\exp\left\{0.5\left[0.0275+0.762x_1-0.0279x_1^2\right]\right\}\right)}{\left(0.762x_1-0.0558x_1^2\right)} \qquad \ldots\ldots 3.59$$

Using equation 3.58 it should be possible to calculate the minimum change in the linear attenuation coefficient detectable in a specimen, containing both analyte and matrix, when scanned by two X-ray beams whose energies straddle the analyte K-absorption edge. However, in its present form it is not possible to evaluate equation 3.58. Since the analyte concentration is unknown, the analyte and matrix linear attenuation coefficients cannot be determined. For the same reason, the mean free path of an X-ray beam through the specimen cannot be found. Therefore, the number of mean free paths in the specimen diameter, x_1, for an X-ray beam of energy E_1, is unknown. However, by making two approximations [43], it is possible to overcome this problem. They are

i) U_m+U_{a1} is approximated by U_m

and

ii) x_1 is approximated by x_m.

The first approximation can be considered if the matrix and analyte linear attenuation coefficients in equation 3.58 are rewritten in terms of their concentrations, C_m and C_a, and their mass absorption coefficients, u_m and u_{a1}. The left-hand side of

108

equation 3.58 can be rewritten as

$$\frac{dU}{U_m + U_{al}} = \frac{dU}{C_m U_m + C_a U_{al}} \quad \ldots \ 3.60$$

For the purpose of this work it can be assumed that the minimum analyte concentration detectable is at least one hundred times less than the matrix concentration. This is reasonable as the analyte concentrations are small. When applied to equation 3.60, this assumption gives

$$\frac{dU}{U_m + U_{al}} = \frac{dU}{C_m(u_m + (u_{al}/100))}. \quad \ldots \ 3.61$$

A second assumption can also be made here. Examination of a plot of mass absorption coefficients against X-ray energy for all elements reveals that the mass absorption coefficient on the low energy side of an analyte K-edge, u_{al}, is at most 10 times greater than the mass absorption coefficient of any matrix at the same energy. This can be seen in figure II.3 and is true for all analyte and matrix elements. Applying this assumption to equation 3.61 when $u_{al} = 10u_m$, gives

$$\frac{dU}{U_m + U_{al}} = \frac{dU}{C_m(u_m(1+1/10))} \quad \ldots \ 3.62$$

The term $u_m(1+1/10)$ in this equation can be approximated to u_m which gives

$$\frac{dU}{U_m + U_{al}} = \frac{dU}{C_m U_m} = \frac{dU}{U_m}. \quad \ldots \ 3.63$$

In this way the specimen can be approximated to a homogenous matrix specimen. This is reasonable for analyte concentrations of the order kilogrammes/metre^3 or less, in matrices with densities of the order 10^3 kilogrammes/metre^3.

The second approximation, which is made to x_1, the number of mean free paths in the specimen diameter at the X-ray energy E_1, can now be described. The mean free path, L_1, is defined as the inverse of the linear absorption coefficient at that energy. It can be rewritten in terms of the mass absorption coefficients, u_m and u_{al}, and the concentrations, C_m and C_a, giving

$$L_1 = \frac{1}{U_m + U_{al}} = \frac{1}{C_m U_m + C_a U_{al}}. \quad \ldots \ 3.64$$

The two assumptions made previously can also be applied here, the first being that C_m is at least one hundred times greater than C_a,

i.e., $C_m \geq 100C_a$, the second that $u_{al} \leq 10um$. At the extremes, where $C_m = 100C_a$ and $u_{al} = 10um$, equation 3.64 becomes

$$L_1 = \frac{1}{C_m(u_m(1+1/10))} \quad \dots \ 3.65$$

which can be approximated to

$$L_1 = \frac{1}{C_m u_m}. \quad \dots \ 3.66$$

The right-hand side of this equation is the mean free path through the matrix, L_m. Thus the specimen containing matrix plus analyte can be approximated to a homogenous matrix specimen since L_1 can be approximated by L_m. In this way the number of mean free paths in the specimen diameter x_1 can be approximated by x_m.

The two approximations are applied to equation 3.58 to give

$$\boxed{\frac{dU}{U_m} \cong \frac{Q \ F}{(N_{OT})^{1/2}}} \quad \dots \ 3.67$$

were the function F is now given by

$$F = \frac{\left(\exp\left\{0.5\left[0.0275+0.762x_m-0.0279x_m^2\right]\right\}\right)}{\left(0.762x_m-0.0558x_m^2\right)} \quad \dots \ 3.68$$

When plotted against x_m, the function F has the same shape as in figure III.4. The minimum of the function occurs at 2.5 mean free paths. Equation 3.67 is also similar to equation 3.25, which holds for the case where analyte can be added to the matrix. However, there is a different interpretation. In the latter, dU is the minimum detectable difference in linear attenuation coefficients when the specimen is scanned by two X-ray beams which straddle the analyte absorption edge. Also, in the present case, the analyte is present in the specimen when the scan is started. In III.4.2, dU was the minimum change in the linear attenuation coefficient detectable when the the specimen is scanned at the same X-ray energy before and after analyte is added.

III.5.4 The minimum analyte concentration detectable when analyte is present in the matrix.

Knowing the minimum detectable difference in the linear attenuation coefficients it is now possible to formulate an

equation to calculate the minimum analyte concentration detectable in the speciemn. The difference in the linear attenuation coefficient for the two X-ray beams can be rewritten as

$$dU = U_h - U_l = U_{ah} + U_{mh} - (U_{al} + U_{ml}). \quad \dots \quad 3.69$$

At the analyte absorption edge the matrix linear attenuation terms cancel, i.e., $U_{mh} = U_{ml}$, leaving

$$dU = U_{ah} - U_{al} \quad \dots \quad 3.70$$

The analyte linear attenuation coefficients can be rewritten in terms of the analyte concentration and analyte mass absorption coefficient so that equation 3.70 becomes

$$dU = C_a(u_{ah} - u_{al}). \quad \dots \quad 3.71$$

Dividing both sides of this equation by the matrix linear attenuattion coefficient U_m and rearranging the resultant gives

$$C_a = \left(\frac{p_m U_m}{u_{ah} - u_{al}} \right) \left(\frac{dU}{U_m} \right) \quad \dots \quad 3.72$$

where $U_m = p_m u_m$ and the term dU/U_m is given by

$$\frac{dU}{U_m} = \frac{Q \; F}{(N_{OT})^{1/2}} \quad \dots \quad 3.67$$

Using equation 3.72, the minimum analyte concentration detectable in a cylindrical homogenous specimen when the analyte is alredy present can be calculated. This concentration is dependant on several factors. These include the nature of the matrix, i.e. its density and its mass and linear attenuation coefficients, the jump in the analyte absorption coefficient at its absorption edge. All these factors can be found in published data, [29] and [44]. The other factors include the number of mean free paths in the specimen diameter, the total number of incident photons and the machine dependent factor Q, which are all included in the dU/U_m term.

In the foregone discussion it was assumed that the two X-ray beam energies are very close in energy to the analyte absorption edge. In practice however, counts measured in two energy bands close to the analyte absorption edge are extrapolated to the edge to give N_{Tl} and N_{Th}. This introduces an extra error into the total detected photon count on both sides of the absorption edge as shown by McCarthy and Fryar [43].

111

By considering figure III.11, which shows a typical spacing of two energy bands, it can easily be shown how this increased error due to extrapolation can be determined. During the normal process of extrapolation, the counts are projected to the absorption edge. If the statistical variations of the counts are also extrapolated to the absorption edge, then it can easily be shown, as in figure III.11, that the standard deviation in the extrapolated value is approximately a factor f times the standard deviation in the counts in the band closest to the absorption edge. This factor f should be included in equation 3.67 as a multiplying factor, to account for extrapolation to the absorption edge. Equation 3.67 is now given by

$$\frac{dU}{U_m} = \frac{Q \, f \, F}{(N_{OT})^{1/2}} \qquad \dots \ 3.73$$

where $Q = \rho \, B \, K^{1/2}$. Substituting this equation into equation 3.72 gives

$$C_a = \left(\frac{p_m U_m}{U_{ah} - U_{al}} \right) \left(\frac{Q \, f \, F}{N_{OT}^{1/2}} \right) \qquad \dots \ 3.74$$

which can be used to calculate the minimum analyte concentration detectable in a reconstructed image using the differential X-ray absorptiometry technique described in section II.3.2.

III.5.5 <u>Discussion.</u>

In order to illustrate equation 3.74, values for C_a for analyte elements in the range Z=20 to Z=80, where Z is atomic number, were calculated for a water matrix of diameter 2.5 mean free paths. This diameter was shown in figure III.4 to be the optimum diameter for greatest sensitivity to analyte elements in a homogenous cylindrical matrix, i.e. (F = 1.54). The separation in standard deviations was taken to be three, so ρ=3. Again, B≅2 [41] for the algorithm used and K was taken to be 40. The term f, to account for extrapolation to the absorption edge, was 3 [43]. Figure III.12 shows the calculated C_a values for 10^7 incident photons plotted against atomic number.

Using 10^7 photons, it is possible to detect from 6 kg/m^3, (6X 10^{-3}g/cm^3), at Z=20 down to approximately 0.5 kg/m^3, (5X10^{-4}g/cm^3)

Count Probability

Counts

A

B

E_{L_1} E_{L_2} E_k

X-ray Energy
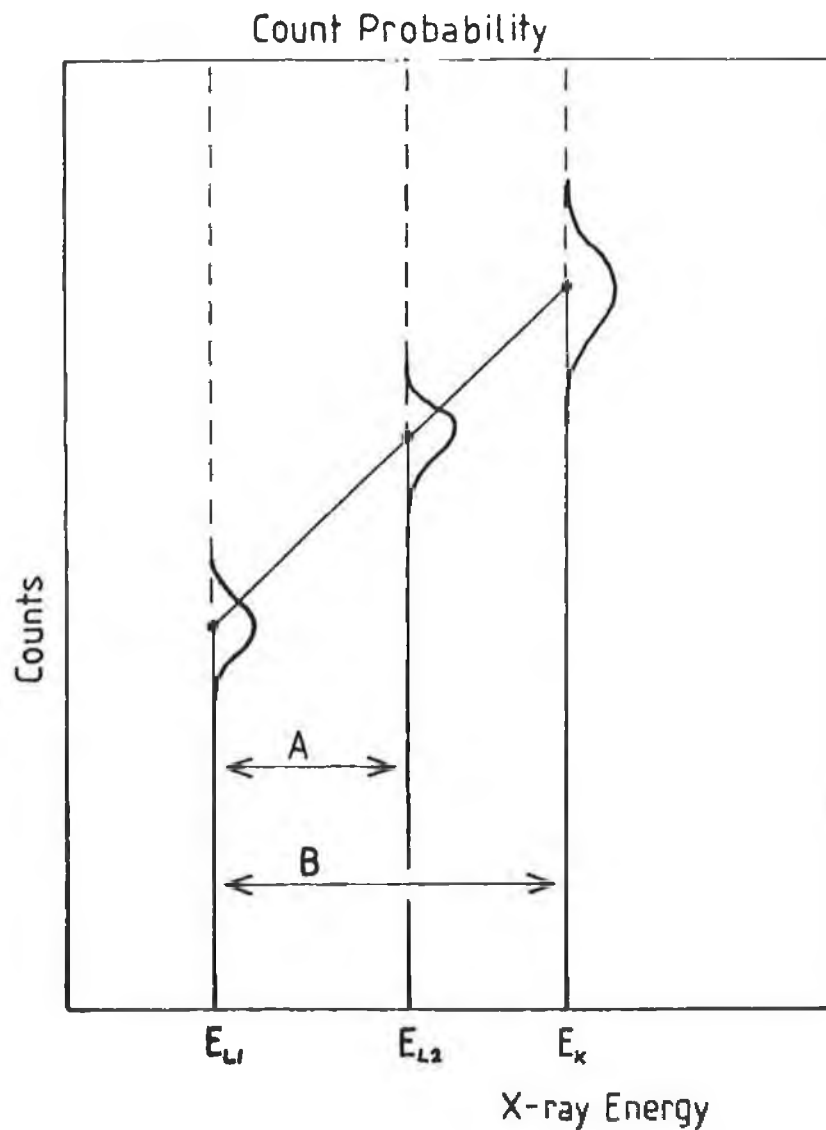
Fig. III.11

Extrapolation of the statistical variation in the photon counts in the two narrow energy bands, E_{L_1} and E_{L_2}, to the analyte edge E_k. The counts are shown as dots. The standard deviation in the extrapolated value is a factor f times the standard deviation in the narrow energy bands. The factor f is given by the ratio B/A.

between Z=40 to 55. The sensitivity falls to about 2 kg/m^3 at Z=80. The sensitivity for any other specimen diameter can be found by multiplying Ca at 2.5 mean free paths by the appropriate factor determined from figure III.7. Figure III.7 is a plot of $F_x/F_{x=2.5}$ against the specimen diameter in mean free paths. Note also, there is a factor of 10 increase in element sensitivity for all elements for a factor of 100 increase in the incident photon count.

Examination of equation 3.74 would suggest that the sensitivity to an analyte element decreases as the density and linear attenuation coefficient of the matrix increases. This can be seen in figure III.13, where the minimum analyte concentration detectable in water, silicon and iron matrices are shown. In each case the matrix diameter is 2.5 mean free paths, ρ=3 and the total incident photon count is 10^7. For the elements below Z=50 there is a factor of 10 decrease in sensitivity in a silicon matrix as compared to a water matrix. Above Z=50 the decrease in sensitivity in a silicon matrix is not so great. In an iron matrix, the sensitivity to analyte elements above Z=26 has deteriorated by a further order of magnitude. Below Z=26 the decrease in sensitivity is only a factor of five compared to a silicon matrix. This is because these analyte elements have their K-absorption edge energies below the iron K-absorption edge at 7.11keV. The reduced iron mass absorption coefficient below 7.11keV increases the sensitivity to these elements.

Grodzin [7] has produced some similar graphs, see figure I.9, which show the minimum fraction of critical atoms in water, silicon and iron matrices for all elements between Z=10 and Z=90. Although it is difficult to relate these curves directly to analyte concentrations, the relative decreases in sensitivity for a given analyte element in going from a water matrix to a silicon matrix and from an silicon matrix to an iron matrix are similar. Also, note, that in both figures III.13 and I.9 the maximum sensitivity occur at approximatly Z=50.

III.6.1 Example calculation.

As a worked example, it is required to determine the minimum cadmium concentrations detectable in a water matrix for the case
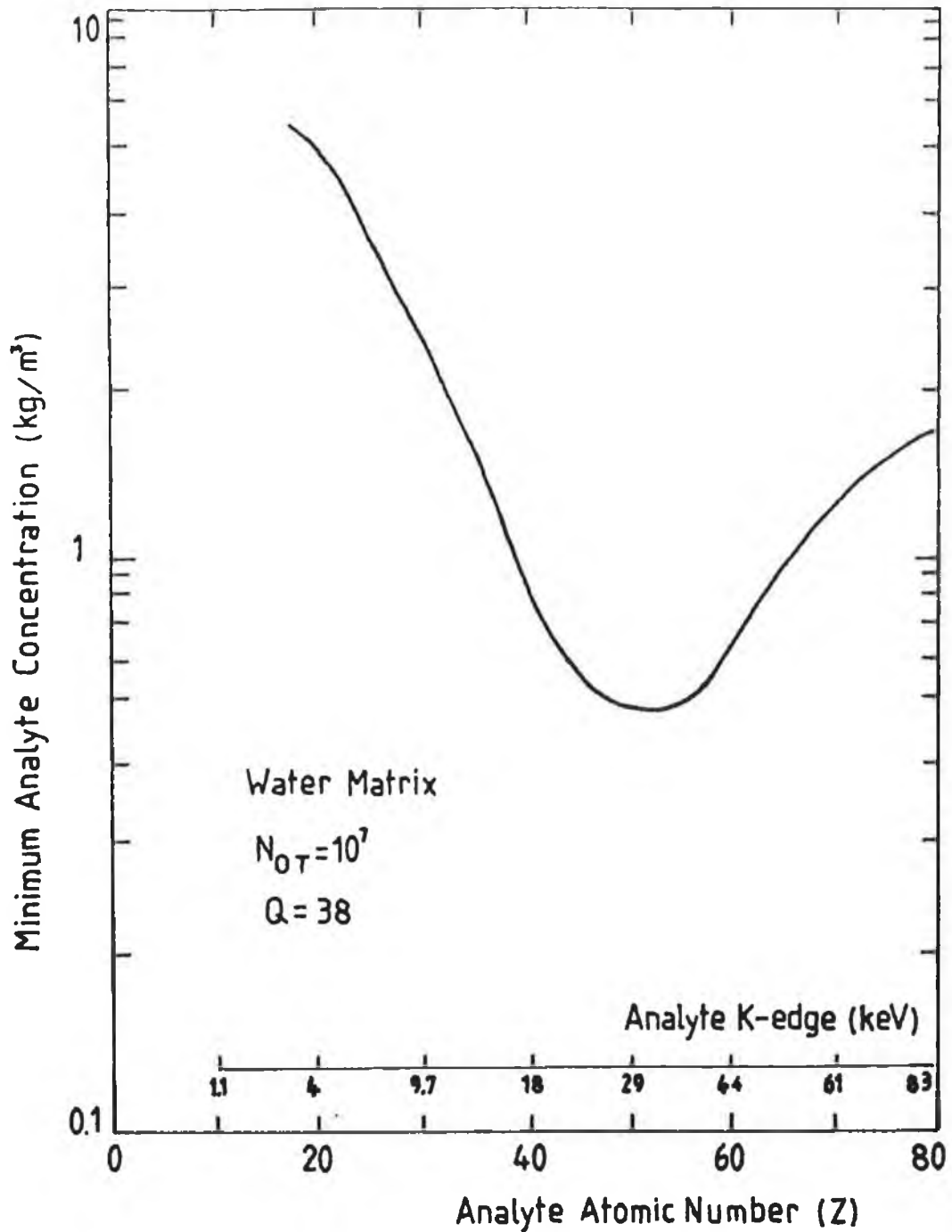
Fig. III.12
The minimum analyte concentration detectable in a cylindrical water matrix of diameter 2.5 mean free paths plotted against X-ray energy. The curve is drawn for Q = 38, f = 3 and N_{OT} = 10^7. This is for the case when the analyte is already present in the matrix.
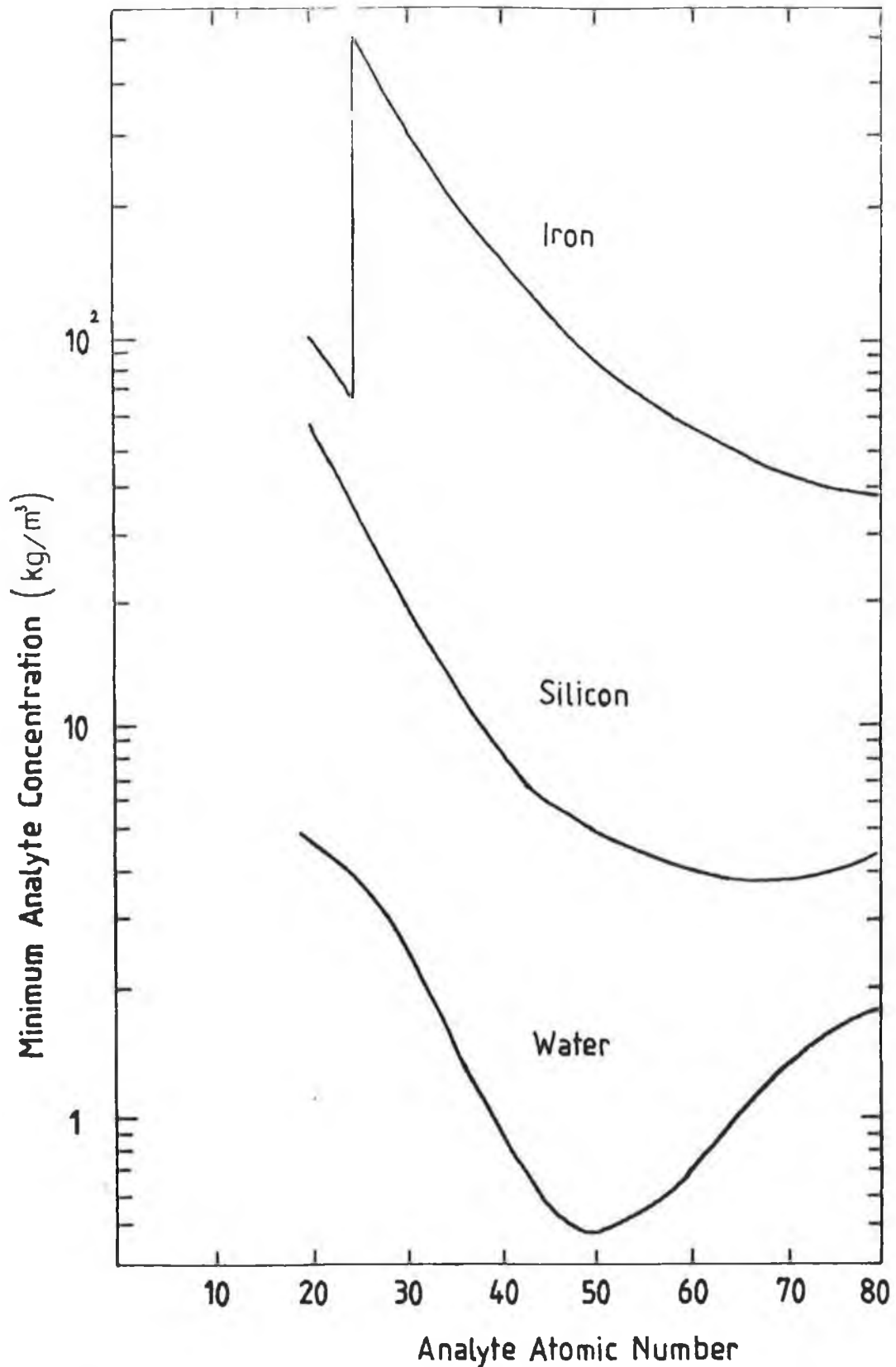
Fig. III.13
The minimum analyte concentration detectable in cylindrical water, silicon and iron matrices of diameter 2.5 mean free paths plotted against analyte atomic number. The X-ray energies required are dependant on the analyte K-edge. The curve is drawn for Q= 38, f =3 and N$_{OT}$= 10^7 for each case.

when cadmium analyte is added to a water matrix and for the case when cadmium analyte is already present in the water matrix. In both cases the water matrix diameter is 0.03 metres, there are 10^7 incident photons and the factor $Q \cong 38$, i.e. $\rho=3$, $B=2$ and $K=40$.

Example 1.

In this case, where cadmium is added to the water matrix, the specimen is scanned at 30keV before and after the cadmium is added. This X-ray energy was chosen because, as can be seen in figure III.8, the sensitivity to cadmium in a water matrix is highest at energies just above the cadmium K-absorption edge. The cadmium K-absorption edge occurs at 26.73keV [44]. It is first necessary to calculate the minimum cadimum concentration detectable in the subtracted image for a matrix diameter of 2.5 mean free paths. In order to calculate this concentration, the minimum change in the linear absorption coefficient detectable is required. Using equation 3.25 which is given by

$$\frac{dU}{U} = \frac{Q \; F}{N_{OT}^{1/2}} \qquad \ldots \ldots \; 3.25$$

where F=1.54 from figure III.4 for a diameter of 2.5 mean free paths, Q=38 for the machine used and $N_{OT}=10^7$, dU/U is calculated as

$$\frac{dU}{U} = 1.8 \times 10^{-2}.$$

Using equation 3.38, which is given by

$$C_a = \frac{p_a \left(\frac{dU}{U_m} \right)}{\left(\left(\frac{p_a U_a}{p_m U_m} \right) - 1 - \left(\frac{dU}{U_m} \right) \right)} \qquad \ldots \ldots \; 3.38$$

and the values for mass absorption coefficient and density in table 3.1 the calculated minimum cadmium concentration detectable for 2.5 mean free paths is

$$C_{a_{2.5}} = 1.8 \times 10^{-1} \; kg/ \; m^3$$

	Mass Absorption Coefficient at 30keV	Density
Water	3.72×10^{-2} m^2/kg	10^3 kg/m^3
Cadmium	3.74 m^2/kg	8.65×10^3 kg/m^3

Table 3a

Values for Mass Absorption Coefficient at 30keV
and elemental density for water and cadmium.

A simple multiplication factor from the graph of $F_x/F_{2.5}$ is all that is now needed to determine the minimum cadmium concetration detectable. The specimen diameter is 0.03 metres and at 30keV in water, one mean free path is 0.027 metres, where $L=1/U$. Thus, there are 1.11 mean free paths in the matrix diameter. The multiplying factor from figure III.7 is 1.29. Multiplying C_a for 2.5 mean free paths by 1.29, the resultant minimum cadmium concentration detectable, in the subtracted image, when cadmium can be added to the water matrix is

$$C_a = 2.4 \times 10^{-1} \text{ kg/ m}^3$$

or

$$C_a = 2.4 \times 10^{-4} \text{ g/cm}^3.$$

Example 2.

In this second example the cadmium analyte is already present in the water matrix. In theory, the specimen should be scanned at two energies which are close to the analyte absorption edge and also straddle it. In practice, the specimen is scanned at two X-ray energies above and below the cadmium K-absorption edge and the projection data is then extrapolated to the absorption edge. This introduces the factor f due to amplification of the noise due to extrapolation. In this case f is approximately equal to three. Again, as in example 1, the specimen diameter is 0.03 metres and the specimen is considered a water matrix when determining the mean free path.

In order to determine the analyte concentration, it is first necessary to determine the minimum linear attenuation coefficient detectable using equation 3.73 which is given by

$$\frac{dU}{U_m} = \frac{Q f F}{(N_{OT})^{1/2}} \quad \ldots \ldots \quad 3.73$$

As in example 1, F=1.54 for 2.5 mean free paths, $Q = 38$ and $N_{OT} = 10^7$. Putting these values in the equation gives

$$\frac{dU}{U_m} = 5.5 \times 10^{-2}$$

Using equation 3.74, which is given by,

$$C_a = \left(\frac{p_m U_m}{U_{ah} - U_{al}} \right) \left(\frac{dU}{U_m} \right) \quad \ldots . 3.74$$

the minimum cadmium concentration detectable in a specimen of 2.5 mean free paths is

$$C_{a_{2.5}} = 5.5 \times 10^{-1} \text{ kg/ m}^3$$

At the cadmium K-absorption edge, the mean free path for X-rays of energy 26.73keV is 0.025metres. Thus there are 1.2 mean free paths in the specimen diameter. The multiplying factor, from figure III.7, is 1.25 so the minimum cadmium concentration detectable in a water matrix of diameter 0.03 metres when the analyte is already present in the water is

$$C_a = 0.69 \text{ kg/ m}^3$$

or

$$C_a = 6.9 \times 10^{-4} \text{ g/cm}^3.$$

In the next chapter, experiments are carried out to determine the minimum cadmium concentrations detectable for both examples and a comparison is made between these predictions and experiment.

Chapter IV.

IV.1 Introduction.

In order to produce element specific images using differential X-ray absorptiometry, as described in chapter II, it was necessary to build working CAT systems. Previous researchers, [8] and [9], had produced element specific CAT images using synchrotron sources but in both cases, only one element could be imaged in a single scan. Also, quantitative element specific images were not produced in either work. In this chapter, the CAT systems built, the experiments undertaken and the results obtained are described.

In this work, two systems were built, one using radioisotope sources, the other using an X-ray tube source. In the first of these, quantitative element specific CAT images of specimens were produced for cases where the analyte could be added to the matrix. This was based on the theory developed in section II.3.1. The second system built, using an X-ray tube source, was the first CAT system built which could produce multiple element specific images in a single scan. It was also the first system which could image adjacent atomic elements [30]. The theory for this was derived in section II.3.2. For both systems, some experimental images were produced before the theory for sensitivity in chapter III was developed. In these cases, the analyte concentrations used in the specimens were based on sensitivities that could be detected according to the work done on sensitivity by Grodzin [7].

The sensitivity of the techniques developed was also investigated experimentally using this second system. In section III.6.1, the minimum cadmium concentrations detectable in a water matrix were calculated for the cases when the analyte element was added to the matrix and when the analyte was already present in the

matrix. In this chapter, these calculated concentrations are compared with experimentally determined values to verify the theory developed in chapter III.

IV.2. A brief overview of the apparatus.

The CAT system developed can be divided into three sections. The first was the data collection system. This consisted of an X-ray detector, an X-ray source, pulse shaping and counting apparatus, a scan table and a microcomputer, which stored and saved the data, and also controlled the whole system. See figure IV.1. The second section was a mini computer, the VAX 11/785, which sorted the data and generated the reconstructed images. It was necessary to use the VAX 11/758 due to the large number of computations involved in reconstructions. Finally, the third section was the display section, which consisted of a BBC microcomputer and VDU, and a printer to produce hard copies. Also, as in conventional CAT displays, regions of interest in an image could be enhanced.

IV.2.1 Si(Li) Detector.

The X-ray detector used was an energy dispersive Si(Li) detector, model SLP-06180 by EG+G Ortec, which has a quoted resolution of better than 200eV at 5.9keV. By using an energy dispersive detector, the required energy bands for several elements could be defined and their fluxes measured simultaneously as shown by J. Fryar, K.J. McCarthy and A. Fenelon [30]. Figure IV.2 shows the detector efficency against X-ray energy. The detector has 50% or greater efficency for photons with energies between 1.5 and 35keV. Thus the detector is most suited for imaging elements between ^{13}Al and ^{55}Cs using analyte K-edges and elements above ^{55}Cs using L-edges.

The Si(Li) detector was biased at -1.5kV by an EG+G model 459 bias supply. The detector and its pre-amplifier were kept at liquid nitrogeon temperature (77K) to minimise the electronic noise in the pre-amplifier output signal. It is because of the liquid nitrogen dewar required, that it was not possible to rotate the detector about the specimen as is normal in CAT scanners. The output signals from the pre-amplifier were amplified and shaped by an amplifier.

IV.2.2 The X-ray sources.

In section II.3, it was noted that X-ray energies which straddle
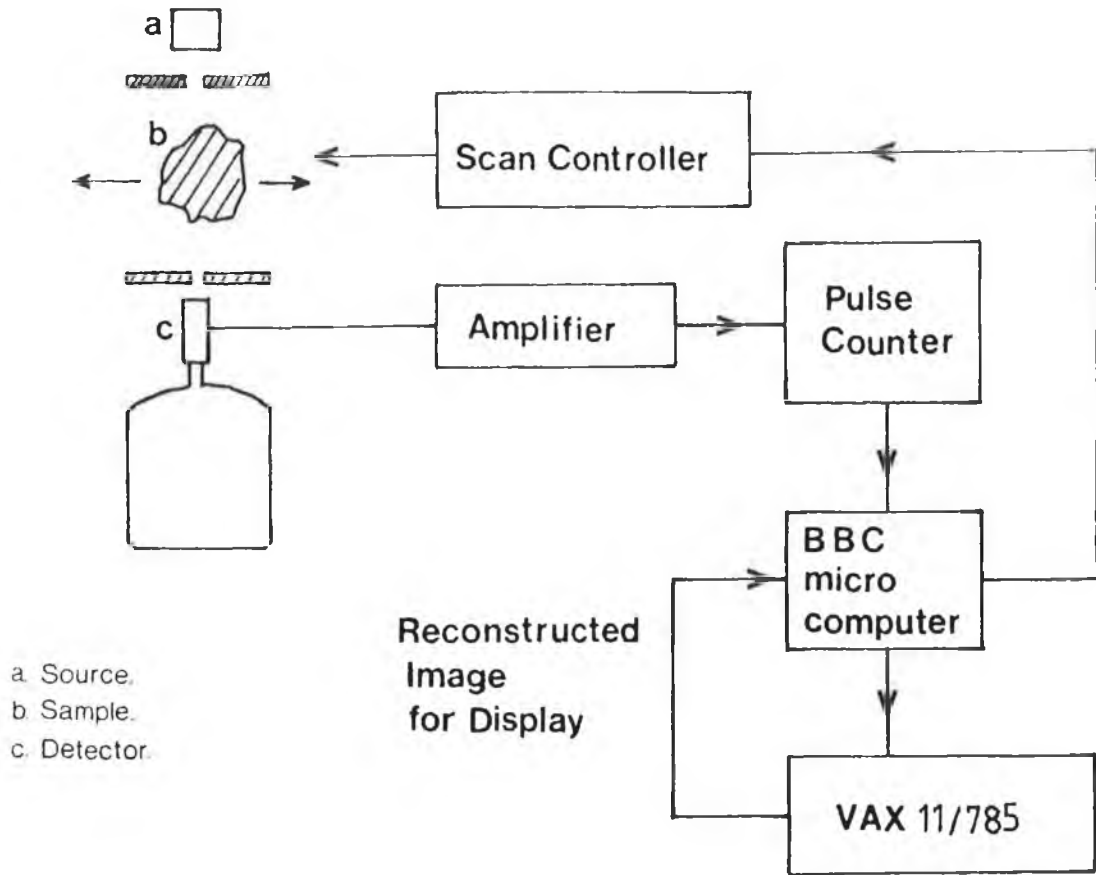
Fig. IV.1
Schematic diagram of the CAT apparatus.

a. Source.
b. Sample.
c. Detector.
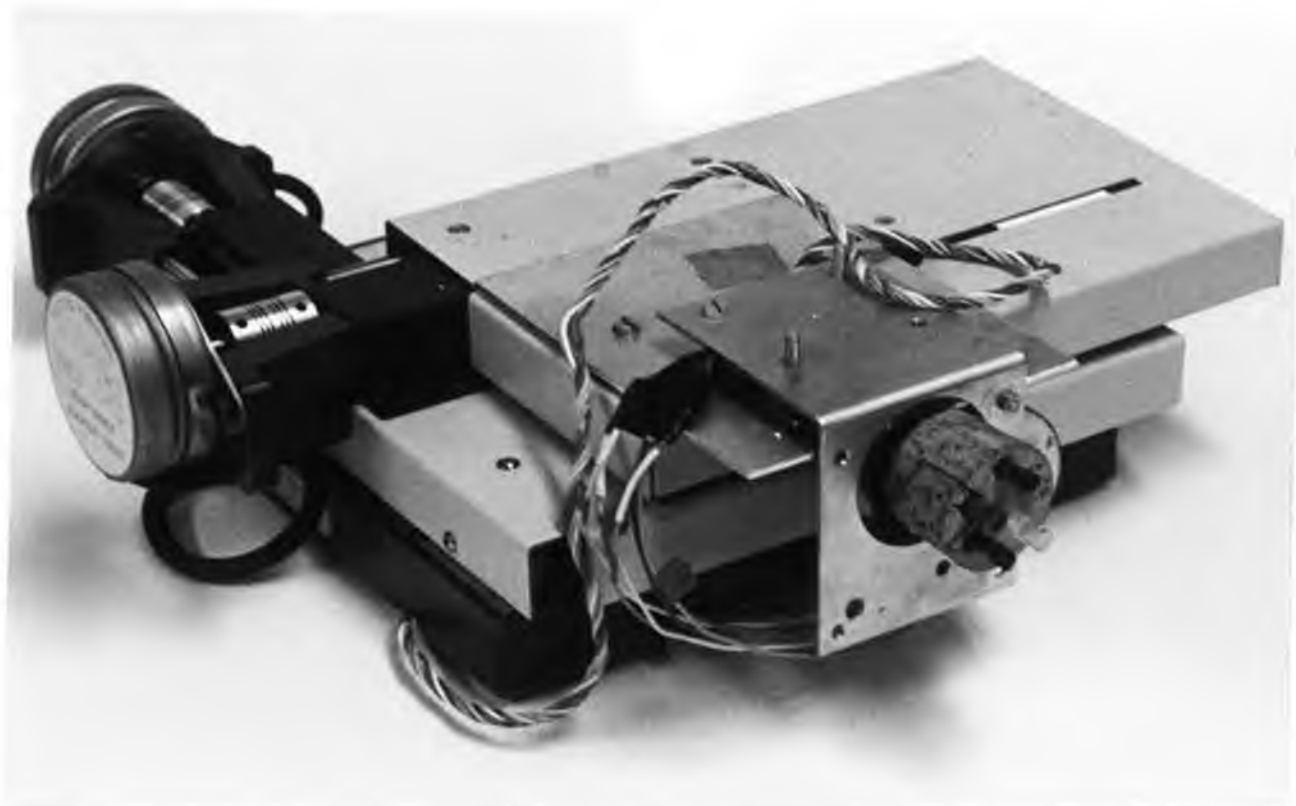
Plate 4.1   The scan table and the stepper motors.
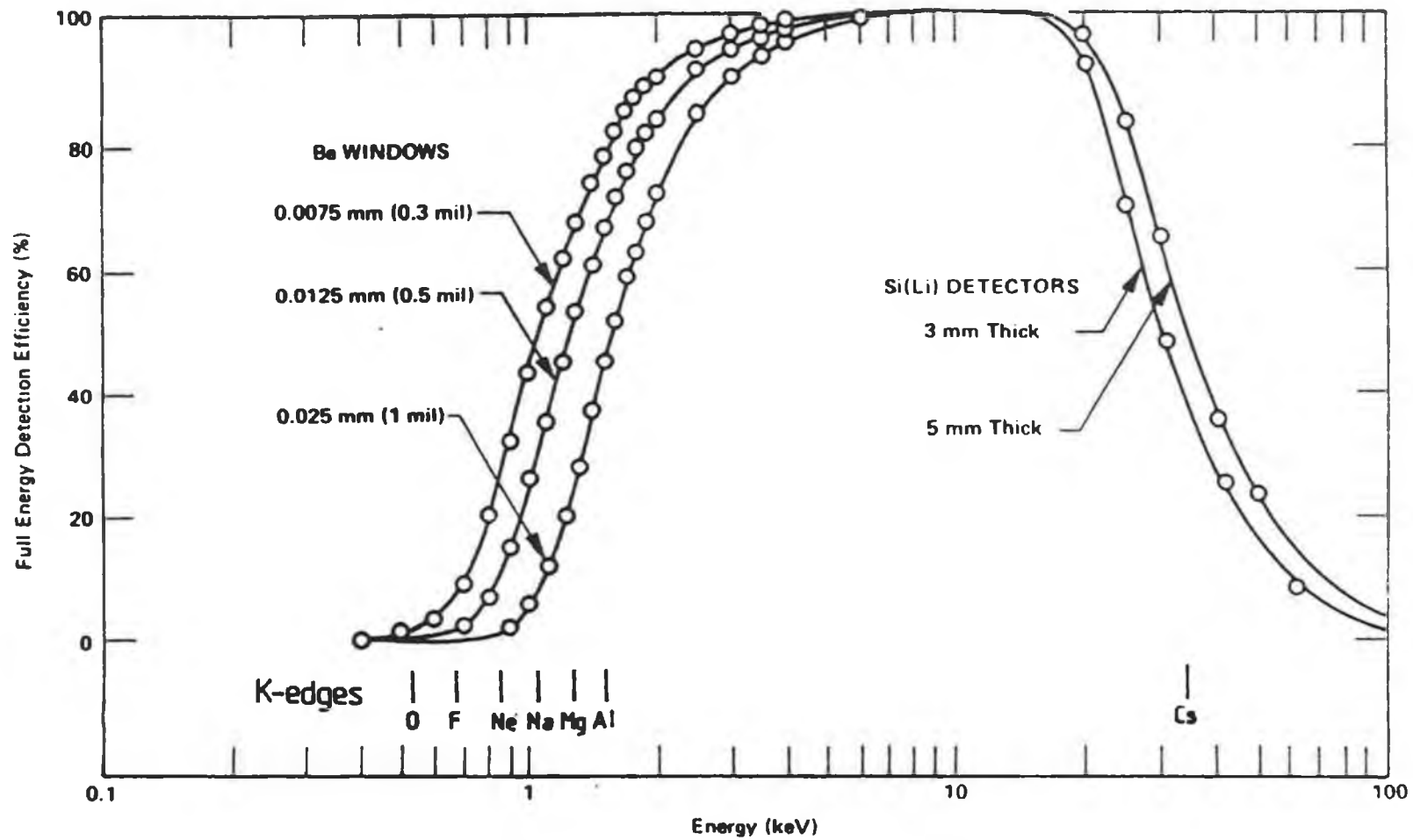
Fig. IV.2
Detector efficency against X-ray energy for Si(Li) detector.
Note: The detector has a 0.0127mm thick Be window and a
sensitive depth of 5.47mm.

the analyte absorption edge are required for differential X-ray absorptiometry. Several possible sources of X-rays are available. One possible source is to fluoresce a suitable target with a primary beam in order to produce the target's characteristic lines. In many cases, these lines straddle the absorption edge of an analyte element. It is also possible to obtain the desired monochromatic lines from a radioactive source. For instance, some radioisotopes emit the characteristic K-lines of an element of lower atomic number after decaying by electron capture. These lines may be suitable if they straddle the K-absorption edge of the analyte element, as shown by J. Fryar, K.J. McCarthy and A. Fenelon [28]. Another possible source is the monochromatic lines from crystal diffraction of a primary continuum of an X-ray tube [28]. A synchrotron which produces a very high photon flux and which is tunable, using a crystal spectrometer [45], has also proved to be a suitable source. The advantage of these methods is that a clean spectrum can be obtained. Alternatively, the primary beam of an X-ray tube can be filtered to give a narrow continum of X-rays. By choosing a suitable filter it is possible to image several elements simultaneously. This has been done by J. Fryar, K.J. McCarthy and A. Fenelon [30] and J. Fryar and K.J. McCarthy [43].

In this work three sets of experiments are described. X-ray radiation derived by fluorescence and directly from radioisotopes is used in the first set of experiments. In the second and third sets of experiments the filtered primary X-ray beam of an X-ray tube is used. The sources used are described later.

IV.2.3 Pulse shaping and counting apparatus.

The pulses from the pre-amplifier in the detector required amplification and shaping before being counted. The pulse shaping was done using NIM modules by EG+G Ortec. The modules used in each of the experiments are described later as are the pulse counting apparatus. In the first set of experiments a scaler ratemeter was used while a multi-channel analyser was used for the second and third sets of experiments.

IV.2.4 The specimen scan system.

The scanning system used was a converted Feedback CNC932 computer controlled drilling machine. See plate 4.1. It allowed

linear and rotational motion as required. A typical scan consisted of stepping the specimen through the X-ray beam and then rotating the specimen before moving the specimen back through the X-ray beam. See figure IV.3. This scan method is similar to the scan pattern used in first generation CAT scanners. In these scanners, the X-ray source and the X-ray detector are rotated about the patient. However, due to the detector's liquid nitrogen dewar, it was easier to move the specimen. This technique of scanning has been used by several experimenters, most frequently by those using a synchrotron, [9]. The scan results obtained in this way are the same as when the specimen is stationary and no corrections are needed. A similar scan method in which the specimen was rotated through all the rotation step positions at each step position was also used. This method was used for the final set of experiments.

IV.3 Experiments.

IV.3.1 Introduction to Experiments.

In this work, three sets of experiments were completed. The object of the experiments was to produce cross-sectional images, showing the analyte element distribution in a thin slice of the specimen. This section is divided into three sub-sections corresponding to the three sets of experiments. In each set of experiments there are two separate experiments and these are listed here.

i) Experiments using radioisotope source(s) to produce element specific images
   a) Experiment to image a single analyte element in a specimen. See IV.3.2.3.
   b) Experiment to image two analyte elements in a specimen. See IV.3.2.5.

ii) Experiments using an X-ray tube source to produce element specific images.
   a) Experiment to image three analyte elements simultaneously. See IV.3.3.4.
   b) Experiment to image two analyte elements in a specimen containing a mixture of both elements. See IV.3.3.7.

iii) Experiments to determine the sensitivity to analyte elements
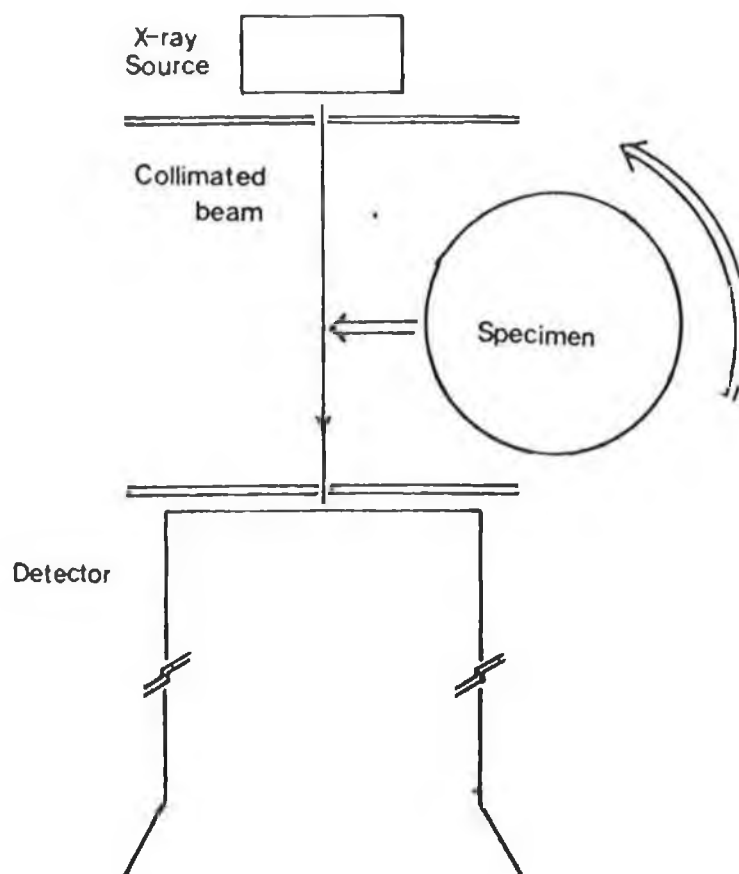
Fig. IV.3
The source, the specimen and the detector.

of Differential X-ray Absorptiometry when applied to CAT.

a) Experiment to determine sensitivty when analyte can be added to the matrix. See IV.3.4.3.

b) Experiment to determine the sensitivity when analyte is already present in the specimen. See IV.3.4.4.

In each case, the sources used and the elements imaged are detailed. The set-up of the apparatus is also described and the resultant images are analysed.

IV.3.2 Experiments to image analyte elements using radioisotopes.

Examination of the absorption edge energies and the characteristic X-ray lines of the elements shows that the absorption edges of many elements are straddled by the characteristic lines of elements which are slightly higher in atomic number. See appendix K. This makes the X-rays spectral lines of such elements, produced by fluorescence or by K- or L-orbital electron capture, very suitable for differential X-ray absorptiometry. However, using the spectral lines from a single radioisotope, it is only possible to image one analyte element at a time. In section II.3, it was required that these lines should be as close to the analyte absorption edge as possible in order to reduce the matrix effect. Since the X-ray spectral line energies may be several keV from the absorption edge it is therefore necessary to remove the resultant matrix effects. To do this, the matrix only is scanned first and then the matrix plus analyte. The theory to determine analyte equivalent thickness along a beam path and to remove the matrix effect was derived in section II.3.

IV.3.2.1 Radioisotopes.

The analyte elements imaged in these experiments were palladium and caesium. Palladium, with its K-edge at 24.36keV, was imaged using silver Kα and Kβ X-ray lines at 21.99-22.31keV and 24.71-25.46keV respectively. These silver X-ray lines were obtained from 3mCi(111MBq) of cadmium-109 (by Amersham International ref. no. CUC.13053) which emits silver X-rays after electron capture.

Caesium, with its K-edge at 35.96keV, was imaged using barium Kα and Kβ X-ray lines at 31.73-32.44keV and 36.12-36.63keV

respectively. The barium lines were derived by fluorescence, the fluorescence being excited by primary radiation from 10mCi(370MBq) of americum-241. The source was a variable energy source by Amersham International (ref. no. AMC.2084). Figures IV.4 and IV.5 show the X-ray energy spectra for both sources and the positions of the K-edges.

In both cases the lines are several keV from the K-edges. For example, the barium $K\alpha$ line is 3.8keV below the caesium K-edge. This would have given rise to a matrix effect which is not negligible when compared to the analyte equivalent thickness, unless as described in II.3, two scans were made, one of the matrix only and a second with the analyte added.

IV.3.2.2 Apparatus to image elements using radioisotope sources.

Two experiments to image elements were completed using radioisotope source and these are described in the next sections. A diagram of the apparatus used is shown in figure IV.6. The radioisotope source was positioned about 10cm above a lead collimator which was placed on the Si(Li) detector. During a scan the specimen was stepped through the X-ray beam using the converted Feedback CNC932 computer controlled drilling machine. The scan table of the drilling machine was driven by stepper motors which were controlled via an interface by a BBC microcomputer. See Appendix G. Pulses from the BBC "User Port" controlled the direction and motion of the stepper motors. Specimens were mounted onto the axle of the rotation stepper motor which was positioned on top of the drive table.

The pulses from the Si(Li) detector preamplifier were amplified using a delay line amplifier, model 460 by EG+G Ortec. See figure IV.7a. The pulse counters used were the logic pulse counters of a Nuclear Instruments scaler ratemeter SR7. The SR7 has two logic pulse counters, so that photon pulses from two energy regions could be counted at the same time. The regions of interest for the narrow energy bands were defined by the windows of two timing single channel analysers (TSCA) model 551 by EG+G Ortec. One TSCA was set to allow the $K\alpha$ pulses to pass, the other to pass the $K\beta$ X-ray photon pulses.

Timing NIM modules were not essential but they allowed quick

128
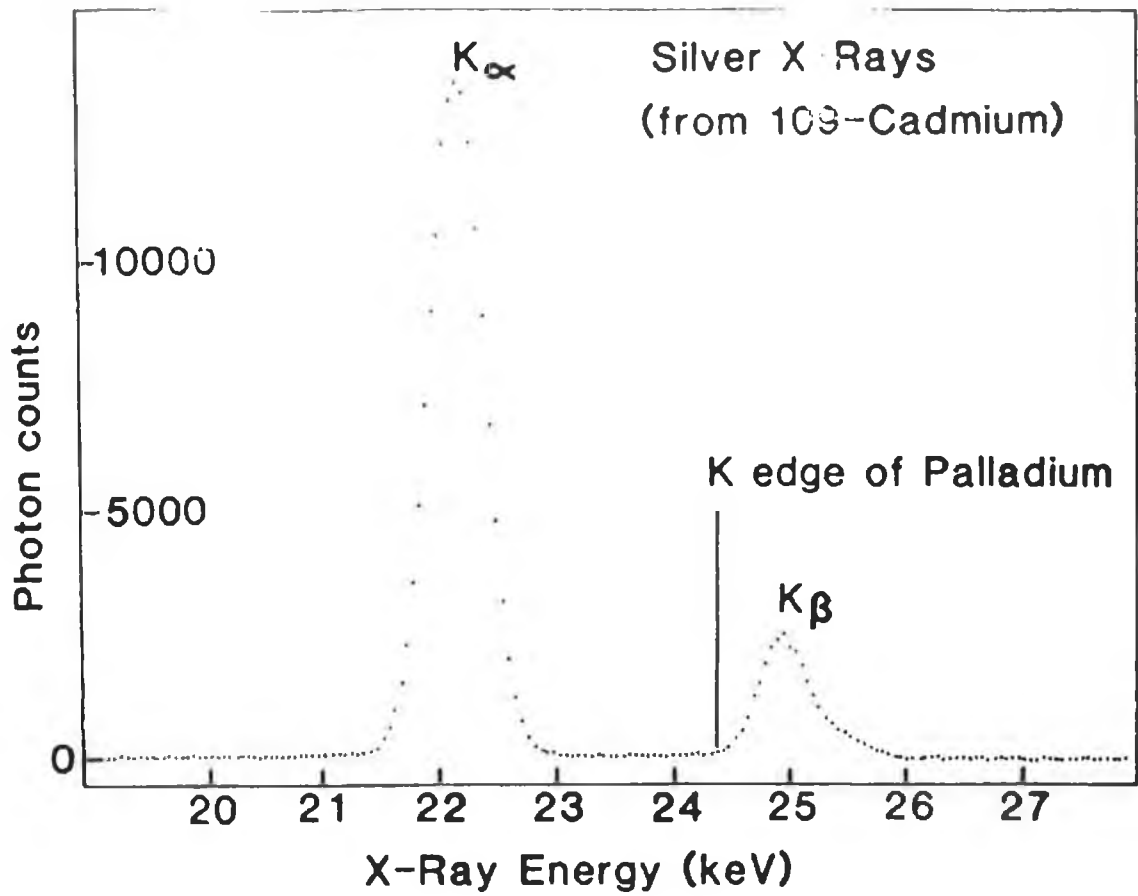
Fig. IV.4
The Silver K X-rays and the palladium K-edge.
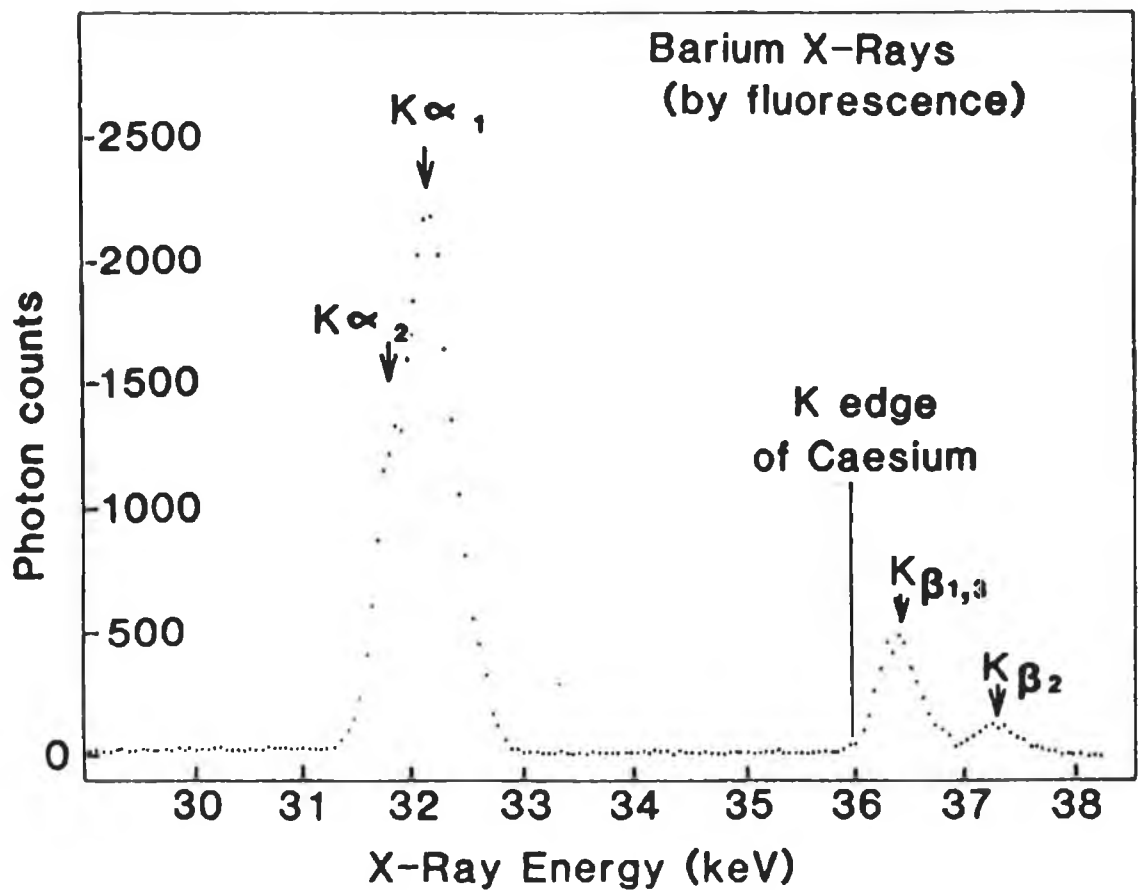
Fig. IV.5
The Barium K X-rays and the caesium K-edge.
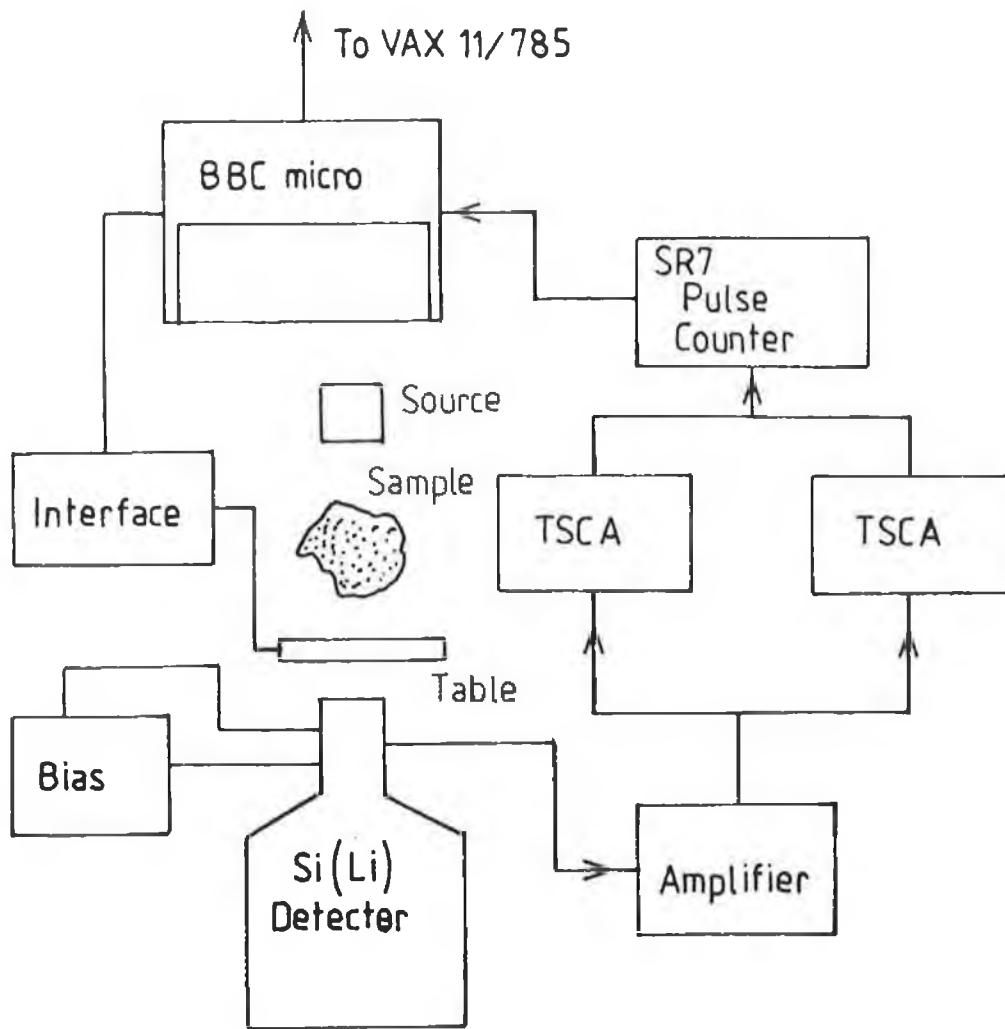
Fig. IV.6
The complete apparatus.

setting of the TSCAs' windows and threshold levels. This was done prior to starting a scan by using a model 427A delay amplifier in parallel with a TSCA. See figure IV.7b. Pulses from the delay amplifier were compared with logic pulses from the TSCA for coincidence by a multi-channel analyser (MCA). Only when the pulses were coincident would a pulse height analysis of the photon pulses be made and the pulses would appear on the MCA display.

At each step position during the specimen scan, after a preset counting period, the data in the SR7's counters was transferred in serial bit form to the RS423 serial port of the BBC microcomputer. A computer program in the BBC interpreted the ASCII code and then stored these photon counts. See appendix G. The SR7 reset its logic pulse counters and after a short pause, while the scan table was moved, it began counting again. At the end of each scan, the data stored in the BBC memory was copied onto a floppy disc. The process was repeated until the end of the scan.

IV.3.2.3 Experiment to image a single analyte element.

This was the first attempt to produce an element specific image of a slice through an object. The analyte element chosen was caesium. A quantity of caesium hydroxide, dissolved in water, with a concentration of several tens of kg/m^3 was soaked onto papers, which were then placed into hollows in a 3cm diameter cork bung. At the time of the experiment, the sensitivity of the method to element concentration was unknown. This is why a high concentration was used.

The caesium, with its K-edge at 35.97keV was imaged using the $K\alpha$ and $K\beta$ lines of barium, at 31.73-32.44keV and 36.12-36.63keV respectively. The energy spectrum is shown in figure IV.5. These lines were obtained by fluorescence excited by primary radiation from 370MBq of americium-241.

The complete scan of the cork bung consisted of twenty 2mm linear steps and twenty rotations of 9 degrees each about the horizontal axis. A lead sheet, 2mm thick, with a 2mm aperture was used to collimate the beam. See figure IV.3 and plate 4.2. The resultant collimated beam had a flux of 2×10^2 photons/sec. Pulses from the detector were amplified and passed through two single channel analysers. The pulses were counted by the logic counters of
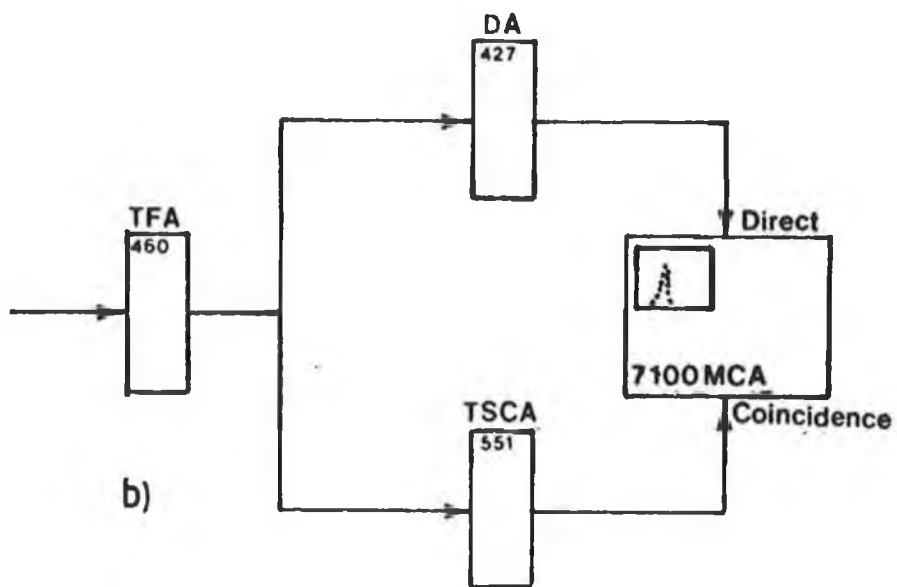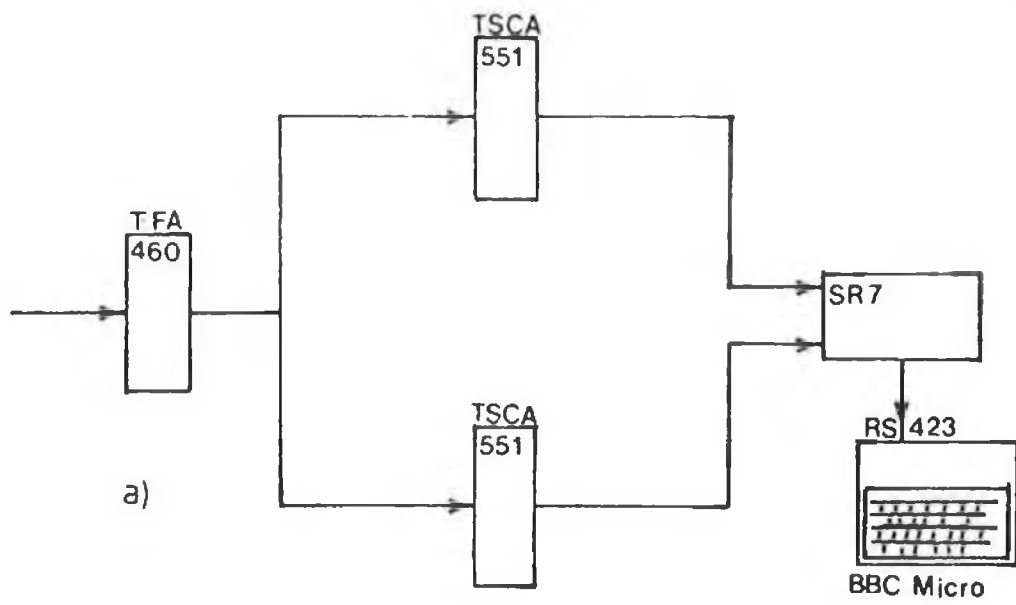
Fig. IV.7
a) Timing Single Channel Analysers and Pulse Counters.
b) Timing Single Channel Analyser, Delay Amplifier and
   Multi-channel Analyser.

the SR7. See figure IV.7a. The count data was stored on floppy disk and used to produce the element specific images.

V.3.2.4 Analysis of experimental results.

In this case, only one scan was made of the analyte plus matrix, no scan was made of the matrix only. The analyte equivalent thicknesses were calculated using equation 2.10 which is given by

$$t_a = \ln\left[\frac{N_l}{N_h}\frac{N_{oh}}{N_{ol}}\right] / (u_{ah} - u_{al}) \quad \dots \quad 2.10$$

where N_o and N are the incident and transmitted photon counts and l and h refer to X-ray energies below and above the analyte K-absorption edge. Figure IV.8 shows caesium equivalent thicknesses for a projection scan. No corrections were made for the matrix effects, because at the time of doing this experiment, a technique to remove the matrix effects had not yet been developed. Also, the low photon counts, (there were 2×10^6 detected $K\alpha$ photons and 3×10^5 detected $K\beta$ photons), resulted in large statistical fluctuations. For example, along beam paths with high caesium concentration, the errors due to statistical fluctuations were higher than 10%.

The images were reconstructed using the ART reconstruction algorithm described in chapter II, for twenty steps at each of twenty rotation positions. In this case, the relaxation constant τ was set to one, ie. $\tau=1$, and only one iteration was completed. The reconstructed image showing the caesium distribution is shown in figure IV.9. When compared with the diagram of the cross-section of the specimen they are compatible. The positions and shapes of the caesium in the reconstructed image is in good agreement with the positions and shapes of the caesium hydroxide papers.

This experiment was a test run to determine the feasibility of the technique. When the matrix correction technique in section II.3 had been developed the next experiment was completed.

V.3.2.5 Experiment to image two analyte elements.

In this second experiment using radioisotope sources, element specific images for two analyte elements were produced. The analyte elements chosen were palladium and caesium. As previously noted, it is not possible to image these elements using spectral lines from the same radioisotope. This is because their K-edges are 11.61keV
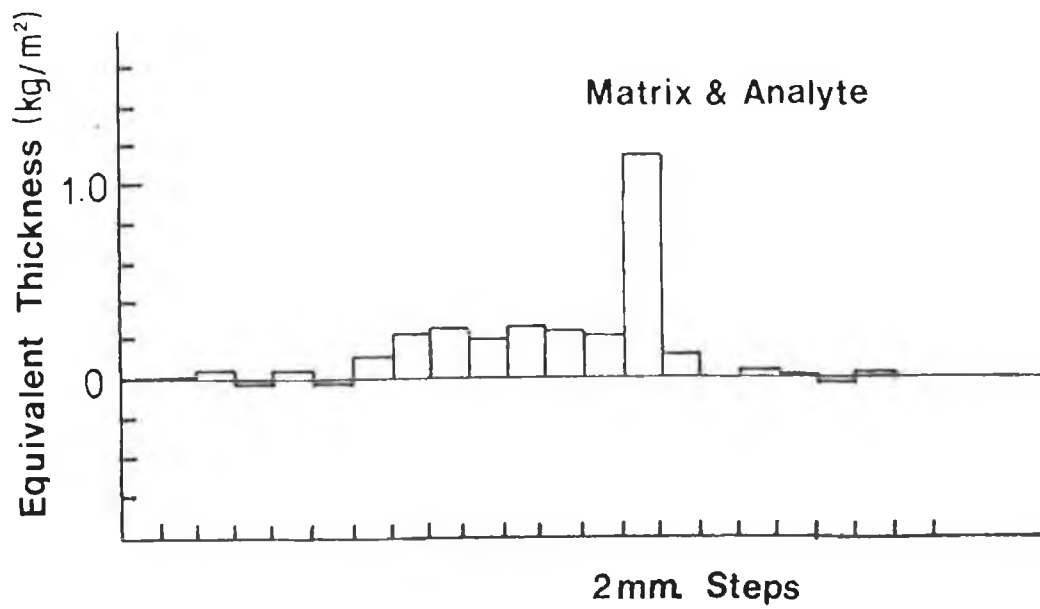
Fig. IV.8
An example of the equivalent thickness projection data
obtained by scanning the specimen with barium fluorescence
X-rays.
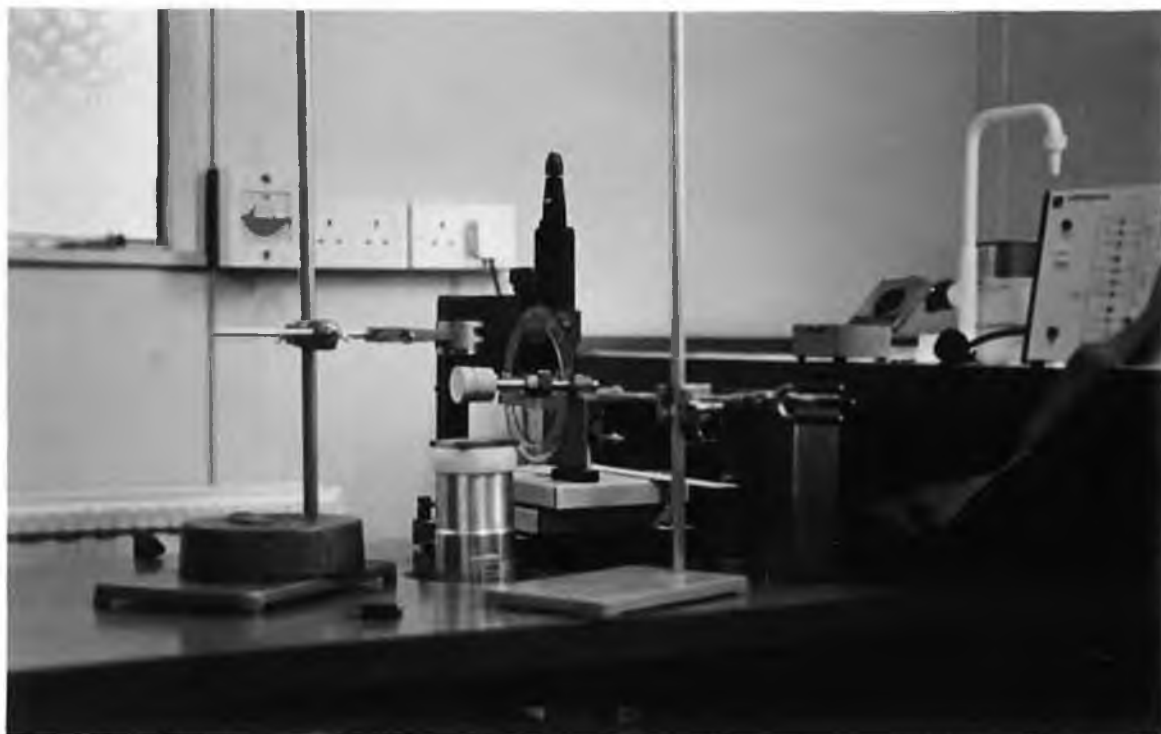
Plate 4.2
Experimental apparatus for imaging with radioisotopes.

apart. Instead, two sets of scans were made using two different radioisotopes. Also, since matrix effects were present, due to the spectral lines being several keV from the K-edges, two scans were needed for each radioisotope. The first in each case was of the matrix only, the second of the matrix plus analyte. The theory is detailed in section II.3.1.

The specimen consisted of three epoxy rods, 5mm in diameter, inserted into a cork bung, 3cm in diameter. See plate 4.3. The epoxy was made with 5 parts Araldite epoxy resin MY753 to 1 part Araldite hardener HY956. Palladium, in the form of 5% palladium metal in charcoal, was added to two of the rods while caesium, in the form caesium hydroxide, was added to the third rod. In all cases the concentrations were several kg/m^3.

In the first scans the palladium was imaged using the Kα and Kβ lines of silver, which were obtained from 111MBq of cadmium-109. During these scans the caesium was considered as a matrix element. The scan was repeated with epoxy rods containing no palladium.

In the second scan the caesium was imaged using the K-lines of barium. These were produced by fluorescence of a barium target by the primary radiation from 370MBq of americium-241. For this scan, the palladium was considered as a matrix element. Table 4a shows the energies of the K-lines and the K-edges for both cases and the regions of interest defined by the TSCAs.

Analyte Element	Analyte K-edge keV	Kα keV	Kα ROI keV	Kβ keV	Kβ ROI keV
Palladium	24.36	22.16	21.99-22.31	24.94	24.71-25.46
Caesium	35.97	32.19	31.73-32.44	36.38	36.12-36.63

Table 4a.
The regions of interest defined by the SCA's for the Ka and Kb lines. The lines are broadened because of the energy resolution of the Si(Li) detector. Its resolution is quoted as 200eV at 5.9keV.

A complete scan consisted of twenty linear steps of 2mm and twenty four rotation steps of 7.5 degrees. Before starting a scan,

135
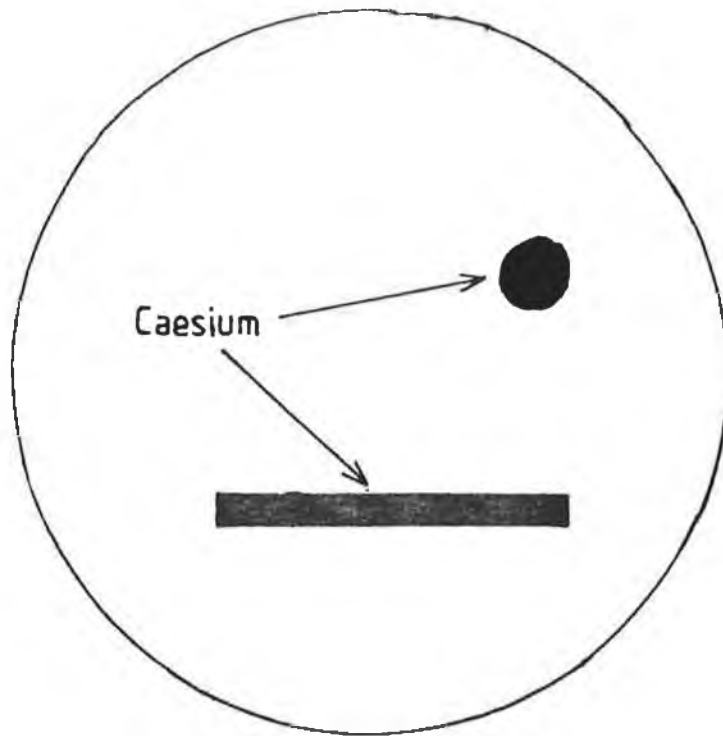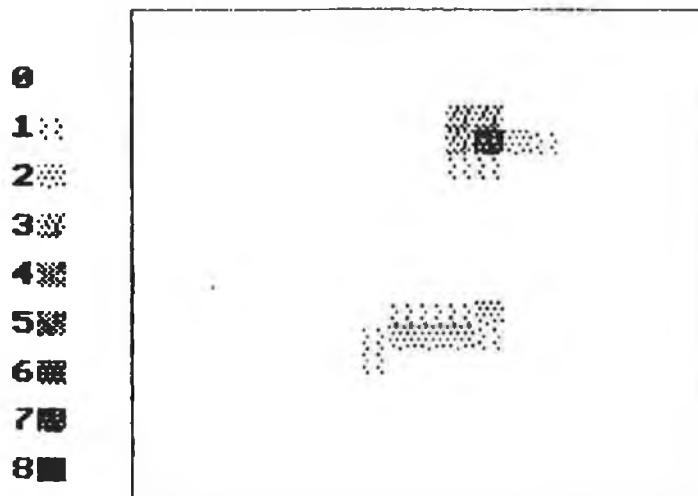
Fig. IV.9
  a) Diagram of the cross-section of the specimen.
     Note the position and the shape of the caesium analyte in
     the cork bung.
  b) The image of the caesium distribution which was
     reconstructed from caesium equivalent thicknesss.

the rotation axle centre was centered with respect to the beam. This was done to avoid ring artifacts. Also while scanning, allowances were made for backlash in the scanning table. The computer program written for the BBC microcomputer to control the scan table, the data collection and the data storage is shown in appendix G.

IV.3.2.6 Generation of scan profiles.

When all scans had been completed, the stored count data was sorted into a few large computer files and transferred to the VAX11/785. It was then decided to generate normal CAT images, as well as uncorrected and corrected element specific images. Conventional CAT images were reconstructed from the attenuation along the beam path. These were calculated using the equation

$$\ln\left\{\frac{N_0}{N}\right\} = \int U(y)\, dy \quad \ldots \quad 1.4$$

where U is linear attenuation coefficient and dy is a small path length. The uncorrected equivalent thicknesses were calculated using equation 2.10, derived in section II.2.2. It is given by

$$t_a = \ln\left[\frac{N_1}{N_h}\frac{N_{0h}}{N_{0l}}\right]\Big/(U_{ah}-U_{al}). \quad \ldots \quad 2.10$$

Finally, the corrected analyte equivalent thicknesses were calculated using equation 2.21, which is given by

$$t_a = \ln\left[\frac{N_{l(a+m)}}{N_{h(a+m)}}\frac{N_{hm}}{N_{lm}}\right]\Big/(U_{ah}-U_{al}). \quad \ldots \quad 2.21$$

This equation was derived in section II.3.1. The $N_{(a+m)}$ terms are the detected photons counts for the specimen containing both matrix and analyte while the N_m terms are for the matrix only specimen.

Figure IV.10 shows scan profiles of palladium equivalent thicknesses for three different cases. The first, see figure IV.10a, shows the equivalent thicknesses for the scan of the matrix only, i.e. the cork and epoxy rods. The equivalent thickness values, calculated using equation 2.10, are negative as predicted in section II.3. Figure IV.10b shows the uncorrected equivalent thicknesses when palladium and caesium were added to the matrix. No corrections were made for the matrix effects and so the caesium

137

appears as a negative peak. When corrected equivalent thickness values were calculated using equation 2.21, see figure IV.10c, the base line of the profile was restored to zero except where the caesium occurs. This was because the caesium was not present during the scan of the matrix. Note also, the palladium equivalent thicknesses have increased with correction, as expected.

For the second case, when imaging the caesium using lines from fluorescence of barium, only one scan, with palladium and caesium in the rods, was completed. No scan was made of the matrix alone because of the low photon counts. In figure IV.11, the caesium gives a positive peak while palladium produces negative peaks. No corrections for the matrix effect were made.

IV.3.2.7 Image reconstruction and analysis.

When all the scan profiles had been calculated the next step was to reconstruct the images. A computer program based on the ART reconstruction algorithm was used. See appendix F2. The VAX11/785 computer was required because of the large amount of memory space needed, mainly for the pixel overlap areas, and the large number of computations involved. The resultant images consisted of twenty by twenty pixels. Each pixel contained either the average attenuation or concentration in the corresponding voxel. The first images are conventional CAT images at energies both above and below the analyte K-edge. In these images, the effect of the absorption edge is clearly visible. The other images show the uncorrected and corrected element specific images.

The first two images in figure IV.12, show conventional CAT images of the matrix specimen. Figure IV.12a was reconstructed from projection data calculated using equation 1.4 for the silver $K\alpha$ count data only. The $K\beta$ projection data was used to produce the image in figure IV.12b. In both images all three rods and the cork bung are visible and they are similar as might be expected, i.e. if palladium were present there would be a noticeable difference in the attenuations of such rods. In the next two images, figures IV.12c and IV.12d, palladium and caesium have been added to the rods. The differential absorption of the palladium is clearly visible here. In the lower energy $K\alpha$ image, the caesium rod is dominant, since it is the heavier element. In the higher energy $K\beta$
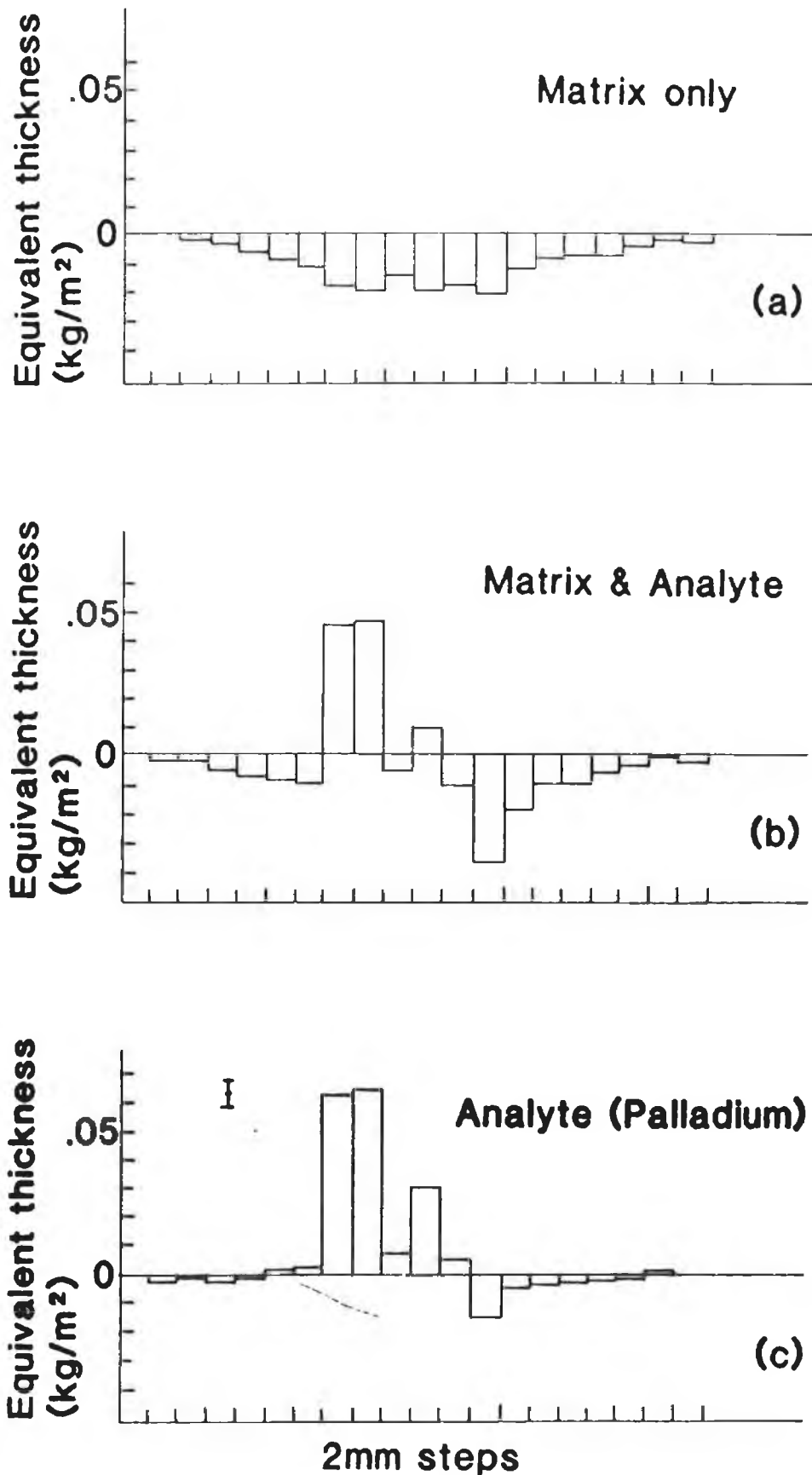
Fig. IV.10
Examples of the equivalent thickness projection data obtained by scanning the specimen with silver K X-rays from [109]Cd.
 a) No palladium was present.
 b) Palladium and caesium have been added to the matrix.
 c) The data in a) has beeen used to correct for the matrix background in b).
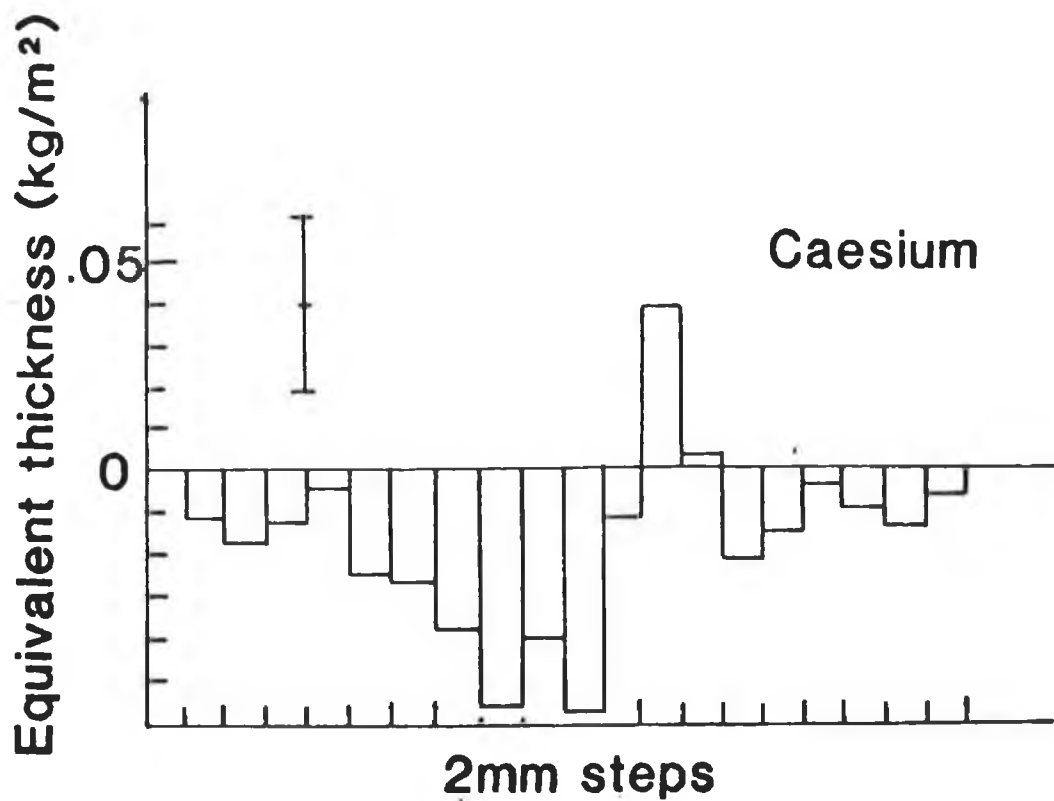
Fig. IV.11
An example of equivalent projection data obtained by
scanning the specimen with barium fluorescence X-rays.

Plate 4.3
Three epoxy rods in cork bung. The black rods contain
palladium and the light rod contains caesium.

image, the palladium becomes dominant because of the jump in mass absorption coefficient at its absorption edge.

Finally, figures IV.12e and IV.12f show palladium specific images. Figure IV.12e is reconstructed from the uncorrected equivalent thicknesses so that its concentration values are lower than in figure IV.12f, which was reconstructed from corrected equivalent thickness values.

The reconstructed image showing the caesium rod is shown in figure IV.13. The caesium is clearly seen above the general background. However, the background is much higher because of the poorer statistics due to the lower photon counts. No corrections were made for the matrix effects.

The final concentration values obtained in the reconstructed images depended on two factors in the reconstruction algorithm. The first was the number of iterations completed, the second the value of the relaxation constant τ. If $\tau=1$, the maximum concentration value oscillated to the final value of 18.4 kg/m^3. As lower values of τ were chosen the concentration rose monotonically to a lower value. See figure IV.14. With $\tau= 0.1$ the final palladium concentration was 16 kg/m^3. However, more iterations were required. See table 4b.

Relaxation constant τ	Final iteration number	Maximum Palladium concentration (kg/m^3)
1	5	18.4
0.4	8	17.7
0.2	11	16.9
0.1	17	16.0

Table 4b. [28]
The variation of the maximum palladium concentration with the relaxation constant t. The final iteration is the iteration as determined by equation II.56.

A comparison of the analyte concentrations and equivalent thicknesses was made to determine the accuracy of the results. In order to make the comparison, measurements were made on the rods, with and without the analyte being present, by conventional differential X-ray absorptiometry. In table 4c, concentrations from the element specific images are compared with concentrations
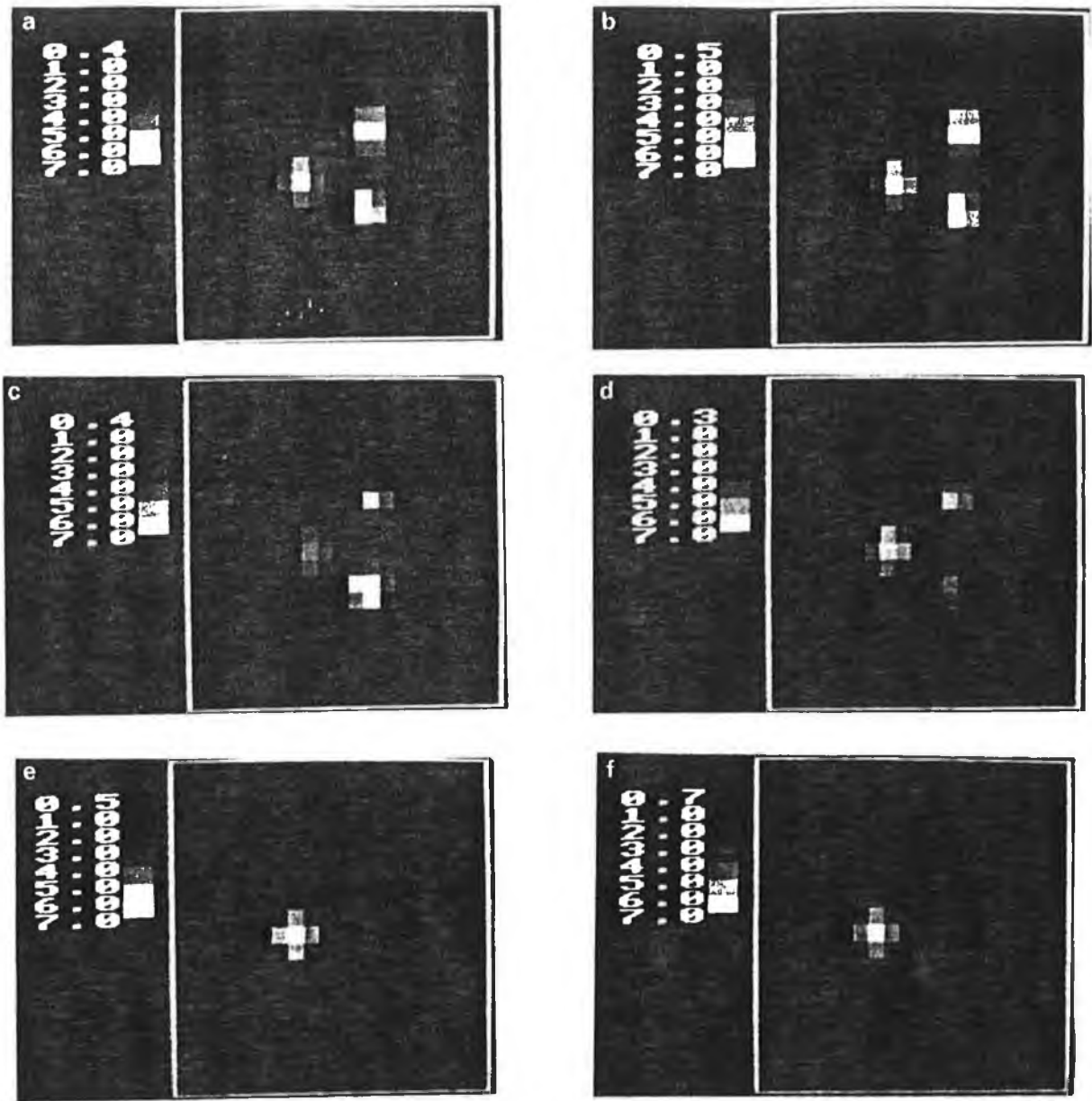
Fig. IV.12

A sequence of reconstructed images which show steps in the imaging of palladium. (a) and (b): Reconstructed images derived from absorption data for Ag K_a (a) and K_β (b) X-rays. Palladium and caesium have not been added. (c) and (d): Reconstructed images derived from absorption data for Ag K_a (c) and K_β (d) X-rays. Palladium and caesium have been added. Note the change in emphasis is from caesium to palladium on going from the lower energy K_a to the higher energy K_β X-rays. (e) and (f): Reconstructed images of palladium. (e) has not been corrected for matrix effects (maximum concentration: 14.1 kg/m³). (f) has been corrected (maximum concentration: 16 kg/m³).
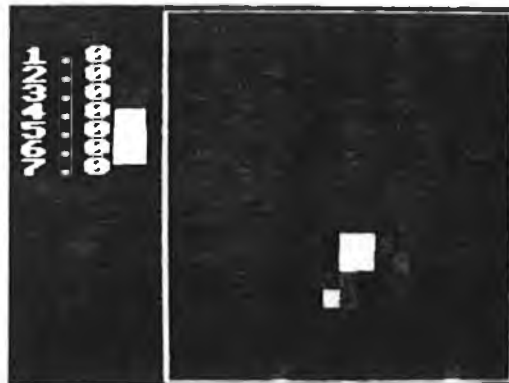
Fig. IV.13
A reconstructed image of rod containing the caesium. No correction has been made for matrix effects (maximum concentration: 9kg/m³).

142

determined by differential X-ray absorption. A second comparision is also made in table 4c between projection scan equivalent thicknesses and those obtained by differential X-ray absorption. The errors in the equivalent thicknesses were determined from statistical variations in the X-ray counts. In the case of the palladium, both the concentrations and the equivalent thicknesses are in good agreement. However, the agreement for the caesium was not so good. This was due to the poorer counting statistics. In the case of palladium the total number of $K\beta$ photons used was 10^7 while 10^6 $K\beta$ photons were used for caesium.

Rod	Concentration (kg/m^3)	
	by differential absorption	from reconstructed image
Palladium	15 ± 0.6	16
Palldaium	7 ± 0.6	8
Caesium	5 ± 2.5	9
	Equivalent Thickness (10^{-2} kg/m^2)	
Palladium	6.2 ± 0.3	6 ± 0.5
Palladium	3.2 ± 0.3	3 ± 0.5
Caesium	2.5 ± 1.2	3.8 ± 2

Table 4c. [28]

Comparison of the equivalent thickness and concentrations obtained in static differential absorption measurements and from the scan data.

IV.3.3 Experiments to image analyte elements using an X-ray tube.

In the previous experiments using radioisotopes, it was only possible to image one analyte element at a time. In these experiments, using an X-ray tube, several elements with adjacent atomic numbers are imaged simultaneously. For each element, the analyte equivalent thicknesses along the beam paths were determined by extrapolation of the photon counts in narrow energy bands to the low and high energy sides of the analyte absorption edge. The theory for this work and the equation required were derived in section II.3. The equation to calculate the analyte equivalent thickness from the extrapolated values Y_h and Y_l is given by

$$t_a = \left[\frac{Y_h - Y_l}{u_{ah} - u_{al}} \right] \quad \ldots \ 2.35$$

In section II.3, it was described how adjacent elements can be imaged simultaneously by extrapolating the photon counts in the

143
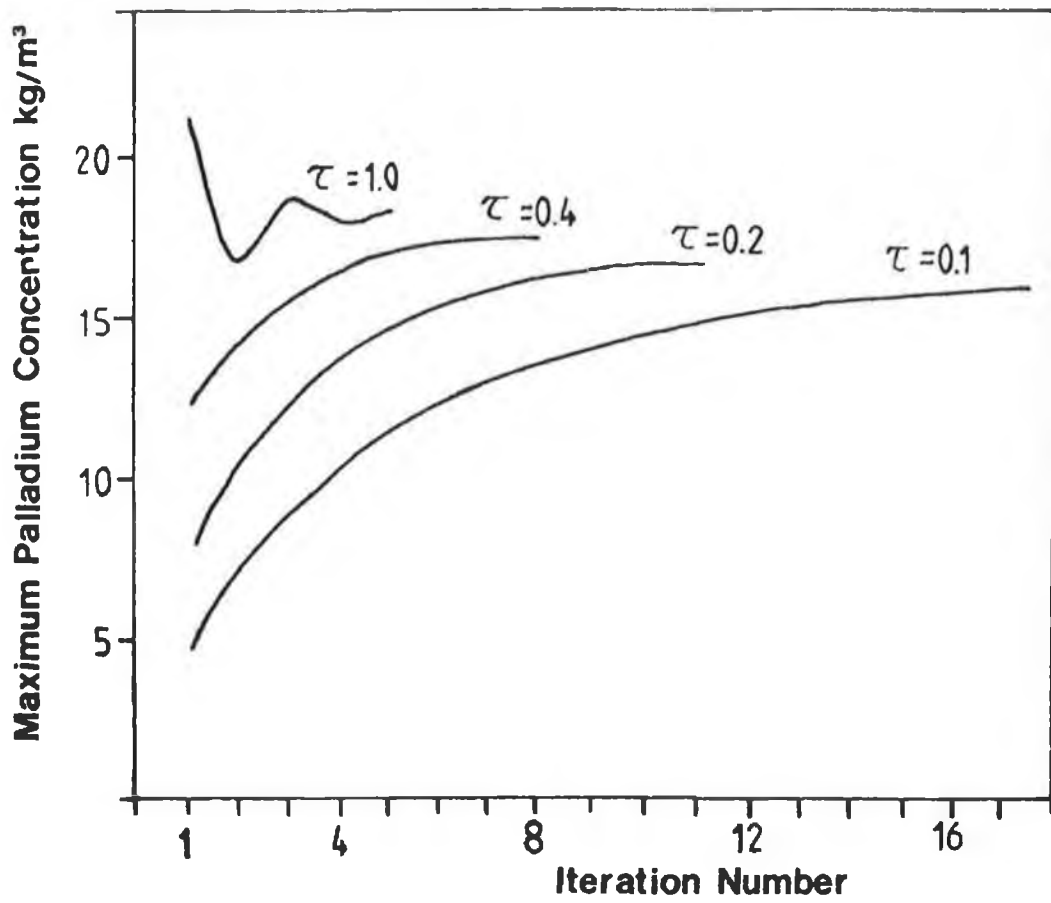
Fig. IV.14
The variation in the maximum palladium concentration
with iteration number and relaxation constant τ.

narrow energy bands to both the high energy side of one element's absorption edge and to the low energy side of the absorption edge of the next highest element.

In order to provide the required X-ray energies, an X-ray spectrometer unit was converted to provide a broad continuum X-ray beam. Filtering of this beam was required to remove unwanted photons and shielding was installed to provide protection. The pulse shaping and counting apparatus differed from that used in the first experiments. See figure IV.15 and plate 4.4. In these experiments a multi-channel analyser was used. The scan system used was the same as before as was the scan method. These are now described in more detail.

IV.3.3.1a The X-ray tube.

The second source of X-rays was the primary beam from an X-ray tube. This had the advantages of a high flux density, which reduced the specimen scan times, and also of a broad X-ray spectrum, which allowed the analyte equivalent thicknesses of several elements to be determined simultaneously. However, since high photon fluxes would saturate the photon counting apparatus, it was necessary to filter the primary beam. Also, since most of the primary photons were superfluous they could be removed with a suitable filter. This resulted in a X-ray beam with a low flux and a narrow energy spectrum. Here, the X-ray system, the X-ray tube and the shielding required are described first. Then the filter used and the resultant spectra are described.

The X-ray tube system used was part of a modified Philips PW 1270 automatic simultaneous X-ray spectrometer. The modified system consisted of the original X-ray tube, the H.T. power supply, the water cooling system and the power supply cabinet. See figure IV.16 and plate 4.5. A lead cabinet with an internal mild steel box was built around the X-ray tube to reduce the external exposure to radiation and also to hold the scan table and beam filters. The X-ray detector was placed below the lead cabinet.

The X-ray tube was a Philips type PW2184/00 with a tungsten target and a 1mm thick beryllium window. The filament current and the target potential were provided by the high tension power

supply. The tube potential could be stepped from 20 to 60kV, in 10kV steps. The filament current had settings at 5mA and at 10mA intervals between 20mA and 80mA inclusively. The X-ray energy spectrum was determined by the tube voltage while the beam flux was determined by the tube current. The maximum operating tube power to avoid damage due to overheating was 3kW.

IV.3.3.1b Shielding for the X-ray tube.

In order to minimize the radiation risk to persons working with the X-ray system and to prevent accidental exposures, the X-ray tube was shielded with mild steel and lead surroundings and interlocks were fitted to prevent the machine from working if any of the shielding doors were not fitted or locked properly. With this in mind, the radiation outside the machine was calculated.

At the maximum operating voltage of 60kV, the tube output at constant potential is 10^2 Gray/A.min at 1m from the target, [46]. Thus, the tube output for 0.05A (50mA) is given by

$$0.05 \times 10^2 \times 60 = 3 \times 10^2 \text{ Gray hr.}^{-1} \text{ at 1m.}$$

The conversion factor from flux density to exposure rate for 60keV gamma rays is 1.2×10^{-13} Gray hr.$^{-1}$ per Photon m^{-2}sec.$^{-1}$, [47]. This is the maxiumum numbers of photons possible as the conversion factor curve is a minimum at 60keV. Using this conversion factor the calculated beam flux density at 1m below the tube is

$$\frac{3 \times 10^2}{1.2 \times 10^{-13}} = 2.5 \times 10^{15} \text{ photons m}^{-2} \text{ sec.}^{-1}$$

The floor of the mild steel box is 0.18m below the tube. See figure IV.17 and plate 4.6. The beam flux density at that point can be calculated using the inverse square law and is calculated as

$$\frac{1^2}{0.18^2} \times 2.5 \times 10^{15} = 8 \times 10^{16} \text{ photons m}^{-2} \text{ sec.}^{-1}$$

The transmission for 50kV constant potential X-rays through the 3×10^{-3}m mild steel plate which lies on the floor of the mild steel box is 10^{-5}, [48]. The resultant transmitted beam flux density through this plate is calculated to be

$$8 \times 10^{16} \times 10^{-5} = 8 \times 10^{11} \text{ photons m}^{-2} \text{ sec.}^{-1}$$

Below this plate, a 2×10^{-3}m diameter hole was drilled in the 10^{-2}m

146

To VAX 11/785

BBC micro

RS 423

Serial Port

Tube

Sample

Table

Interface

MCA

Bias

Si(Li) Detector

AMPLIFIER
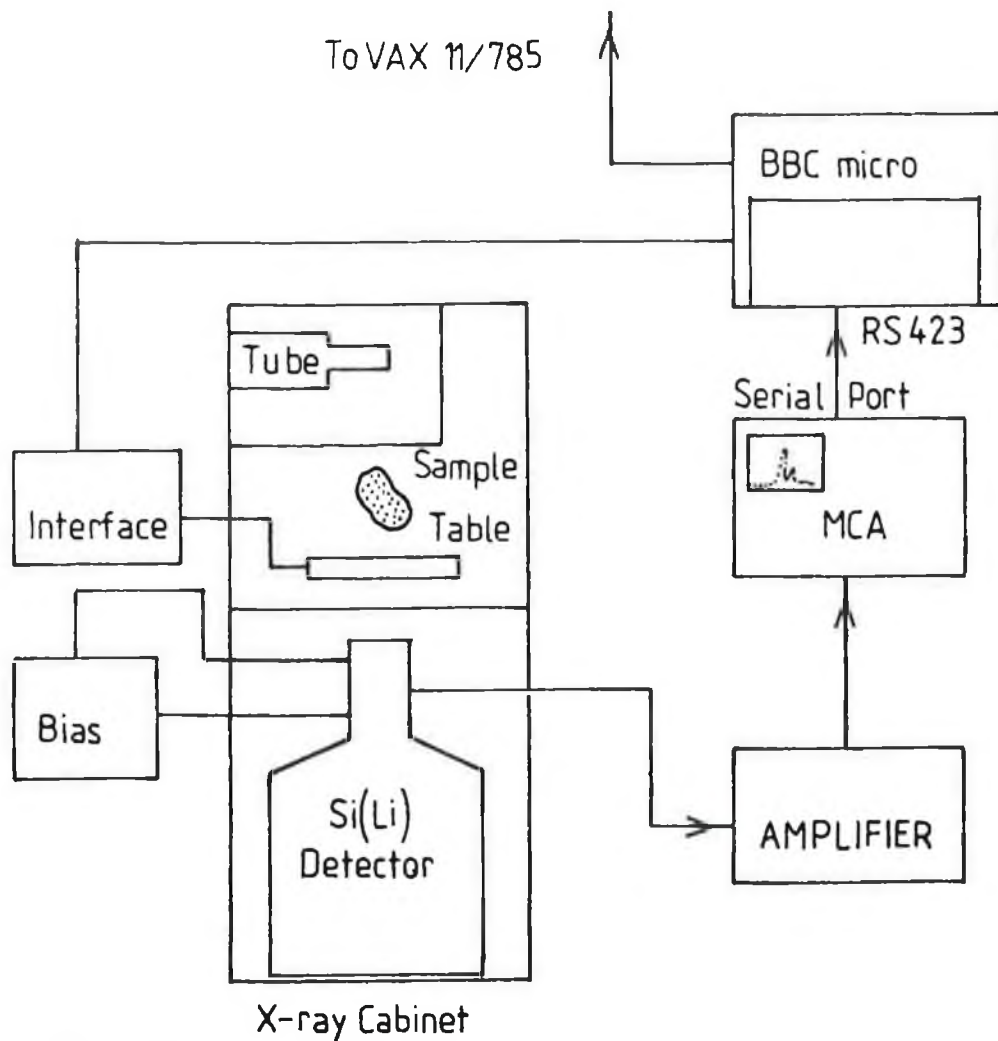
X-ray Cabinet

Fig. IV.15
Diagram of the apparatus used to produce images using
the X-ray tube source.

Plate 4.4
The X-ray machine and the pulse counting apparatus.
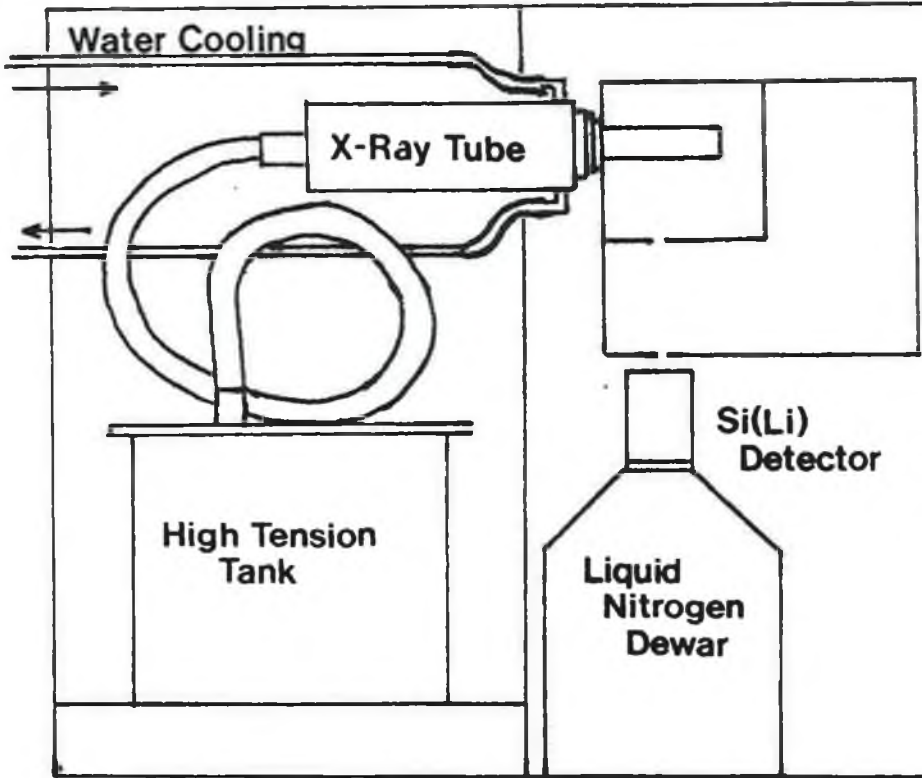
Fig. IV.16
Diagram of the X-ray tube cabinet.

Plate 4.5
The X-ray tube and the high tension power supply.

thick floor of the mild steel box. The transmission for 50kV constant potential X-rays through 10^{-2}m of mild steel is 10^{-8} [48] and so the transmitted flux through the mild steel floor is 10^{-8} X 8×10^{11}photons m^{-2} sec.$^{-1}$ This is small compared to the calculated beam flux through the 2 millimetre diameter hole which is

$$\Pi \times (10^{-3})^2 \times 8 \times 10^{11} = 2.5 \times 10^6 \text{photons sec.}^{-1}$$

and so can be neglected.

A 10^{-2}m diameter hole was made in the 3×10^{-3}m thick floor of the lead box which is 0.2m directly below the aperture in the mild steel box. The transmission through 3×10^{-3}m of lead for 50kV constant potential X-rays is 6×10^{-12}, [49]. Since the 2mm aperture in the mild steel box resulted in a narrow diverging beam, it is reasonable to assume, since the transmission through the lead is so small, i.e. 6×10^{-12} X 2.5×10^6, that the beam flux through the 10^{-2}m aperture in the lead box can be approximated as

$$2.5 \times 10^6 \text{photons sec.}^{-1}$$

This is equivalent to an exposure rate of 2.5×10^{-2} Gray hr.$^{-1}$

When X-ray radiation impinges upon any material, radiation is scattered in all directions. In the lower cabinet, the pencil beam is scattered to the walls of the cabinet. This scattered radiation has a much lower exposure rate and it can be calculated using equation (1) of [50]. For a 45°/45° scatter angle, there is a maximum of 0.05% of the incident beam scattered to 1m per 100cm^2 irradiated area, [51]. Using the equation referred to in [50], the maximum exposure-rate of the scattered beam on the inside of the lead shield of the cabinet door is

$$2.5 \times 10^{-2} \text{ X } \frac{\Pi \times (0.1)^2}{100} \text{ X } 5 \times 10^{-4} \cong 3.9 \times 10^{-9} \text{ Gray hr.}^{-1}$$

The walls of the lower cabinet were lined by 1.5×10^{-3}m thick lead shielding. Transmission through the 1.5×10^{-3}m lead for 50kV constant potential X-rays is 3×10^{-7}, [49]. The maximum calculated exposure rate of the scattered beam outside the door of the cabinet is

$$3.9 \times 10^{-9} \text{ X } 3 \times 10^{-7} = 1.2 \times 10^{-15} \text{ Gray hr.}^{-1}$$

In this way the radiation outside the X-ray cabinet is kept extremely low. The machine was passed for operation by the Nuclear Energy Board.
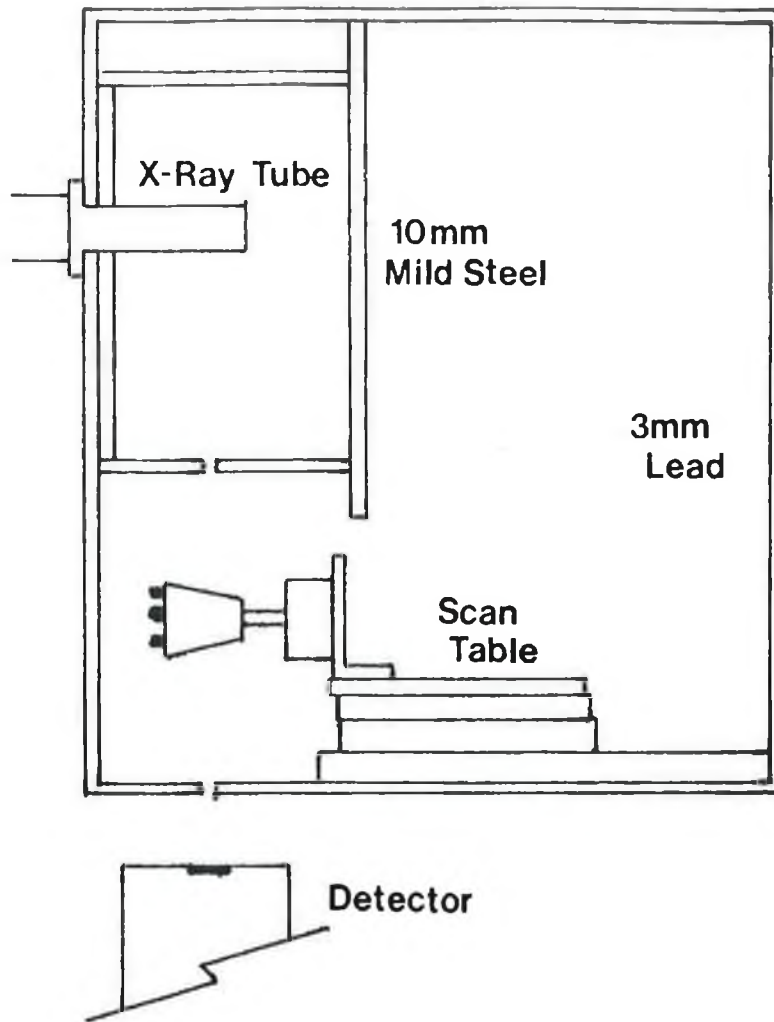
Fig. IV.17
Diagram of the lead and mild steel cabinets.
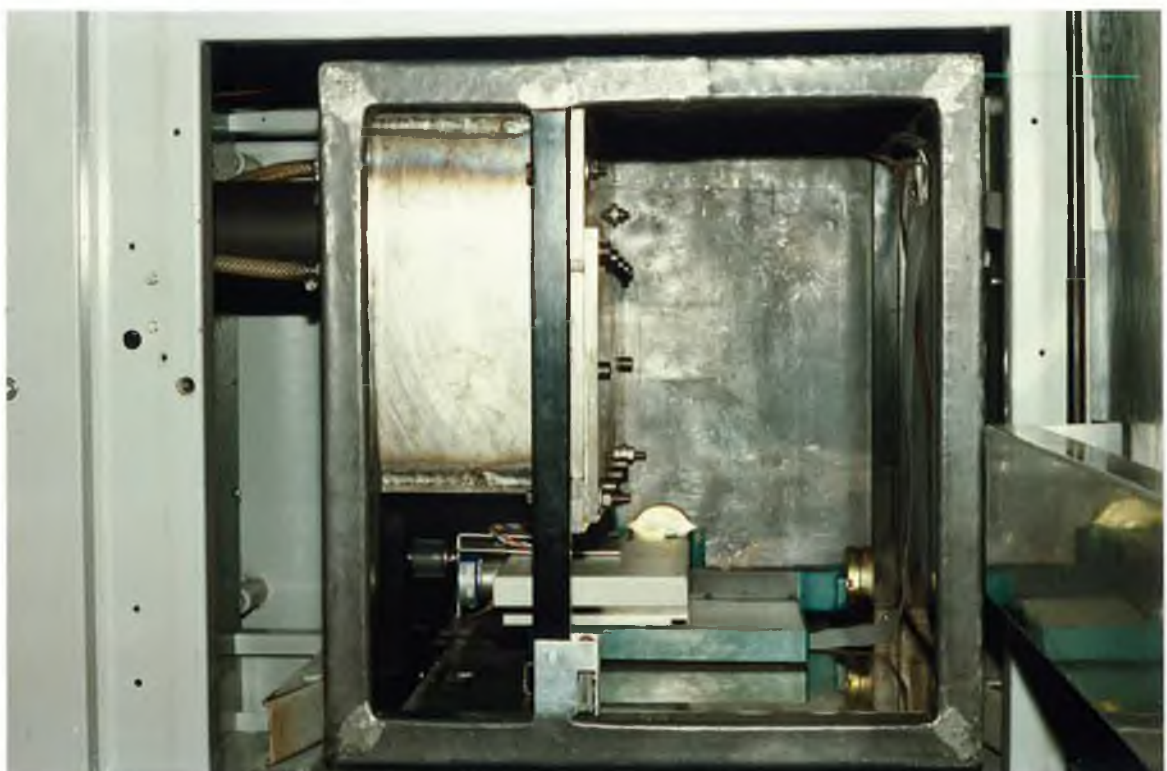
Plate 4.6
The lead and mild steel chambers and the scan table.

IV.3.3.1c Filtering the X-ray beam.

For the purpose of differential absorptiometry, many of the photon energies produced by the X-ray tube were superfluous and added to the dead-time in the detector and in the pulse counting equipment. In the second and third set of experiments, elements close in atomic number were imaged. For this, only a narrow energy band of photons, which straddled the analyte K-absorption edges, were required. By filtering the X-ray beam with a suitable absorber the unwanted photon energies were removed. This had the added advantage of reducing the beam flux, thus reducing dead-times.

In order to find a suitable filter, a computer program was written to calculate the filtered spectrum of the primary spectrum for possible filters. This program, see appendix J, is based on Beer's law for a pencil beam of X-rays which is given by

$$N(E) = N_0(E) \exp\left\{ U(E) \ P \right\} \ldots . \ 4.1$$

where N_0 and N are the incident and transmitted beam fluxes at energy E, U is linear attenuation coefficient and P is absorber thickness. The program calculated the transmitted flux at each energy, knowing the incident fluxes and linear attenuation coefficients at that energy. This was repeated for several different filter materials and thicknesses. Then, having produced many spectra, a suitable one was chosen.

For example, in the second set of experiments the analyte elements of interest were palladium $_{46}$Pd, K-edge at 24.36keV, silver $_{47}$Ag, K-edge at 25.53keV, and cadmium $_{48}$Cd, K-edge at 26.73keV. The X-ray energy spectrum most suited for imaging these elements was one with low flux for energies both below 25keV and above 29keV.

It was found, using the computer program in appendix J, that tin $_{50}$Sn produces a suitable profile for the desired energy range. Figure IV.19a, shows the unattenuated spectrum for a tube voltage of 40kV, [52]. Figure IV.19b shows the calculated spectrum for a 0.5mm Sn filter. Note the sudden drop in the photon count above 29.2keV. This is due to the sharp increase in the tin mass absorption coefficent at this energy, see figure IV.18. The program

calculated a drop of 4×10^{-2} in the measured beam flux. When a 0.29mm tin sheet was placed in a slide below the 2mm aperture in the mild steel box the resultant energy spectrum, when corrected for detector efficency, was in good agreement with the calculated energy spectrum. See figure IV.19. This filter was used for the second and third sets of experiments.

IV.3.3.2   The Multi-Channel Analyser (MCA).

It was required to image several elements in these experiments. In order to count the photon pulses, either eight single channel analysers or a multi-channel analyser was needed. A model 7100 MCA by EG+G Ortec was available and was thus used. A schematic diagram of the apparatus used, which was the same for both experiments, is shown in figure IV.15. A serial remote control interface board had been inserted into the MCA so that it could be controlled by the BBC microcomputer. In this way the complete scan system was controlled by the BBC microcomputer.

During a scan, the output pulses from the energy dispersive Si(Li) detector, which were amplified by a spectroscopy amplifier, model 575 by EG+G Ortec, were firstly fed to the MCA. In the MCA, a pulse height analysis was performed. This involved measuring and sorting the pulse heights, according to height, into a histogram of photon energy versus photon count. After a preset counting period, the pulse counts in each of the regions of interest, which had been defined prior to starting the scan, were summed. The summation values were then transferred via the serial port as ASCII code to the RS423 serial port of the BBC. In the BBC, the ASCII code was interpreted by a computer program and the count data was stored in BBC memory. At the end of every second linear scan the data was sorted and stored on floppy disc.

As in the first set of experiments, the scan table consisted of a converted feedback CNC932 computer controlled drilling machine. Again, the scan stepper motors were controlled via an interface by the BBC microcomputer. A typical scan consisted of 40 X 1mm linear steps and 40 X 4.5 degree rotation steps. The BASIC computer program which controlled the data collection and the scan system is shown in appendix H.

153
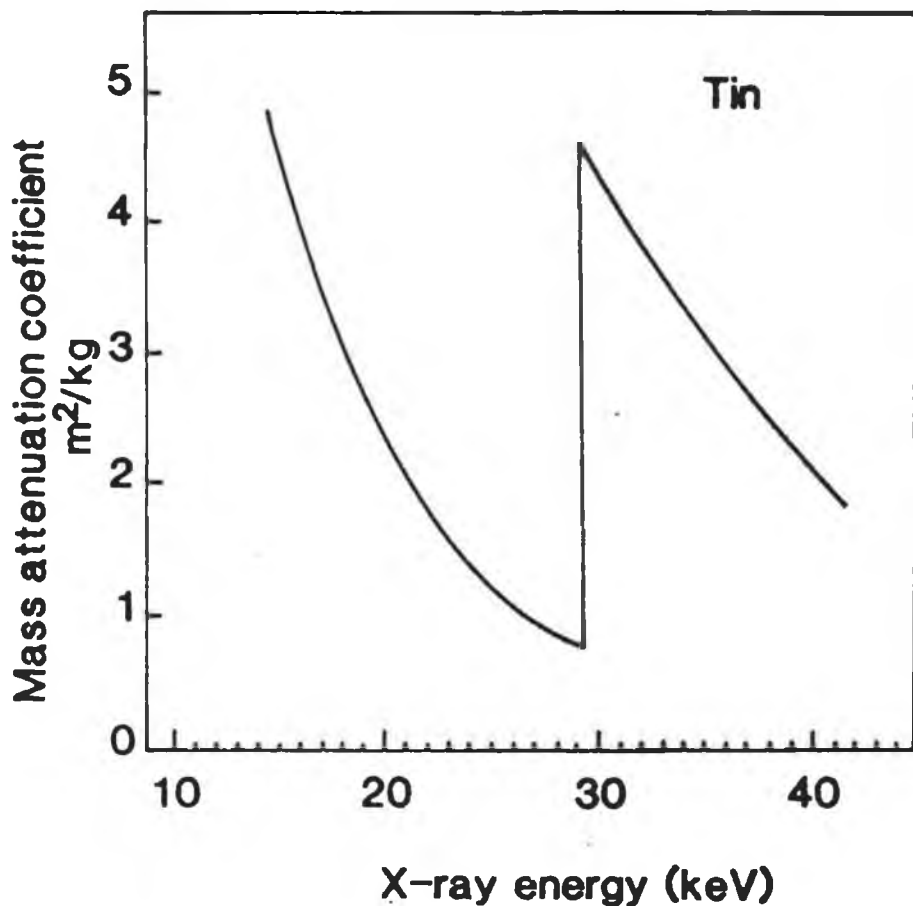
Fig. IV.18
The variation in mass attenuation coefficient for tin in the vicinity of the tin K-edge.
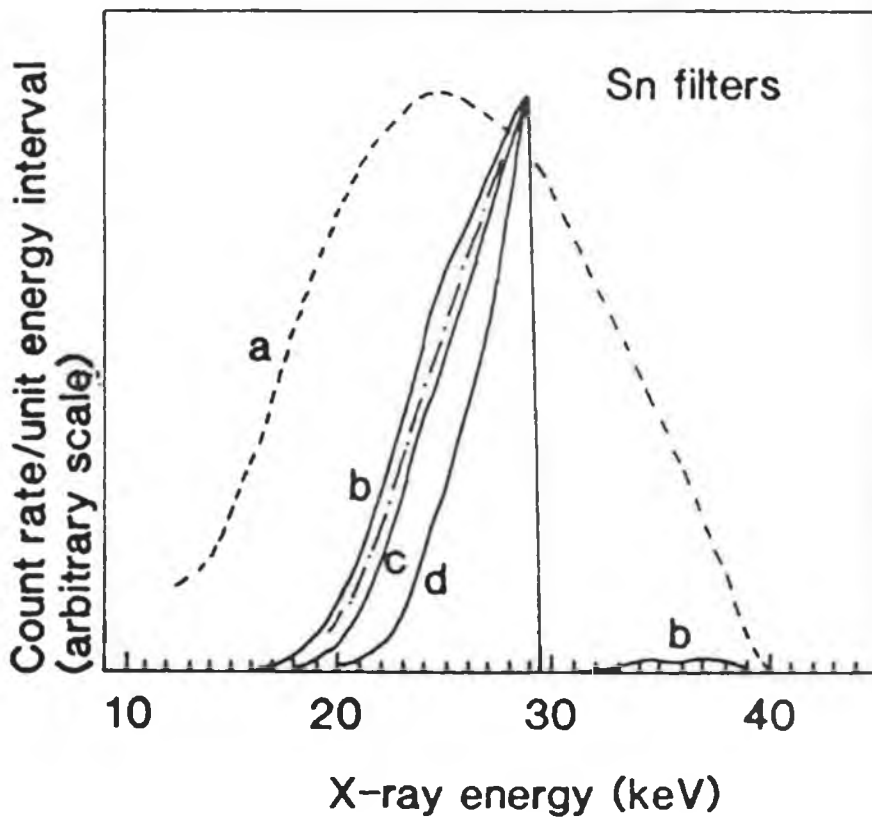
Fig. IV.19
 The calculated effect of a tin filter on an X-ray tube
spectrum (for each case,the first number gives the filter
thickness, the second the calculated transmission)
        a) none, 1
        b) 0.2mm, 9×10^{-2}
        c) 0.3mm, 4×10^{-2}
        d) 0.5mm, 8.4×10^{-3}
The dashed line is the measured X-ray spectrum for 0.29mm tin.

The advantage of using a MCA for these experiments was that it allowed many regions of interest to be defined simultaneously. This meant that several elements could be imaged in one scan. However, a disadvantage of the MCA was that scan times were long, as the dead-time in the MCA was high. For example, the dead-time was 22% for 10,000 pulses/sec but this could be reduced to 14% by increasing the level of the low level discriminator of the MCA. No corrections for dead-times were necessary, as described in section II.3.2.

IV.3.3.3 Method to centre rotation axle.

Before starting a scan, it was first necessary to align the scan apparatus so that the centre of rotation of the scan coincided with the centre of the rotation stepper motor axle. It was not possible to do this manually as the scan system was enclosed in the lead box which surrounded the X-ray tube. Incorrect centring would have resulted in ring artifacts in the images as described in chapter I. A computer program was written for the BBC microcomputer to find the centre of the rotation stepper motor axle and then, having found it, to position the motor at the scan starting position. See appendix I.

In order to find the centre of rotation the scan system was firstly driven forward towards the X-ray beam in the Z-direction until the rotation motor axle was in line with the X-ray beam. The rotation axle was then stepped through the X-ray beam in 0.1mm steps and the X-ray flux at each postion was measured. As the rotation axle passed through the beam the photon flux fell and then rose again as it passed out of the beam. The computer program recognised this fall and rise in the beam flux. The change in flux was not sudden, it was in fact a gradual change. See figure IV.20. From the intercept of the slopes the position of the centre of the axle relative to the scan starting position was found. The scan system was then moved to the starting position and the specimen was moved into line with the X-ray beam. In this way the rotation centre was found to within 0.1mm.

IV.3.3.4 Experiment to image three analytes in a matrix.

In this experiment the three analyte elements were palladium $_{46}$Pd, silver $_{47}$Ag and cadmium $_{48}$Cd. Their K-edges are at 24.36keV, 25.53keV and 26.73keV respectively, [44]. The specimen consisted of

six epoxy rods in glass test tubes, with outside diameter 6mm, inserted into a cork bung, 36mm in diameter. To two of these rods was added, 5% palladium metal in charcoal. Silver, in the form silver nitrate, was added to two more rods, while cadmium, in the form cadmium sulphate, was added to the final two rods. The analyte concentration in each case was several kg/m^3. A diagram of the cross section of the specimen is shown in figure IV.21.

The X-ray tube potential for the scan was set at 40kV and the filament current at 5mA. The X-ray beam was collimated to give a 1mm diameter pencil beam. The beam was filtered with a 0.29mm thick sheet of tin. Tin was a suitable filter since its K-edge occurs at 29.21keV. The resultant transmitted spectrum is shown in figure IV.19. Prior to scanning, eight regions of interest were defined on the multi-channel analyser, two on each side of the analyte K-absorption edges. Their energy ranges are shown in table 4d.

Region of Interest	Lower Energy keV	Higher Energy keV	Centre Point keV
1	23.20	23.50	23.36
2	23.90	24.20	24.04
3	24.54	24.70	24.70
4	25.40	25.20	25.20
5	25.72	25.88	25.88
6	26.24	26.38	26.38
7	26.94	27.10	27.10
8	27.44	27.60	27.60

Table 4d.
The regions of interest defined on the MCA.
Their centres were used to extrapolate to the
analyte absorption edges.

A complete scan took 40 hours to complete. It consisted of forty 1mm steps at forty rotation positions, 4.5 degrees apart. The computer program used to control the scanning and to store the data is described in appendix H.

IV.3.3.5 Scan Profiles.

When the scan was completed, the data stored on floppy disc was transferred to the VAX11/785. This data consisted of the counts at each step position for each region of interest on the MCA. Figure IV.22 shows a typical X-ray absorption spectrum in which the effect of the palladium, silver and cadmium present in the beam path is
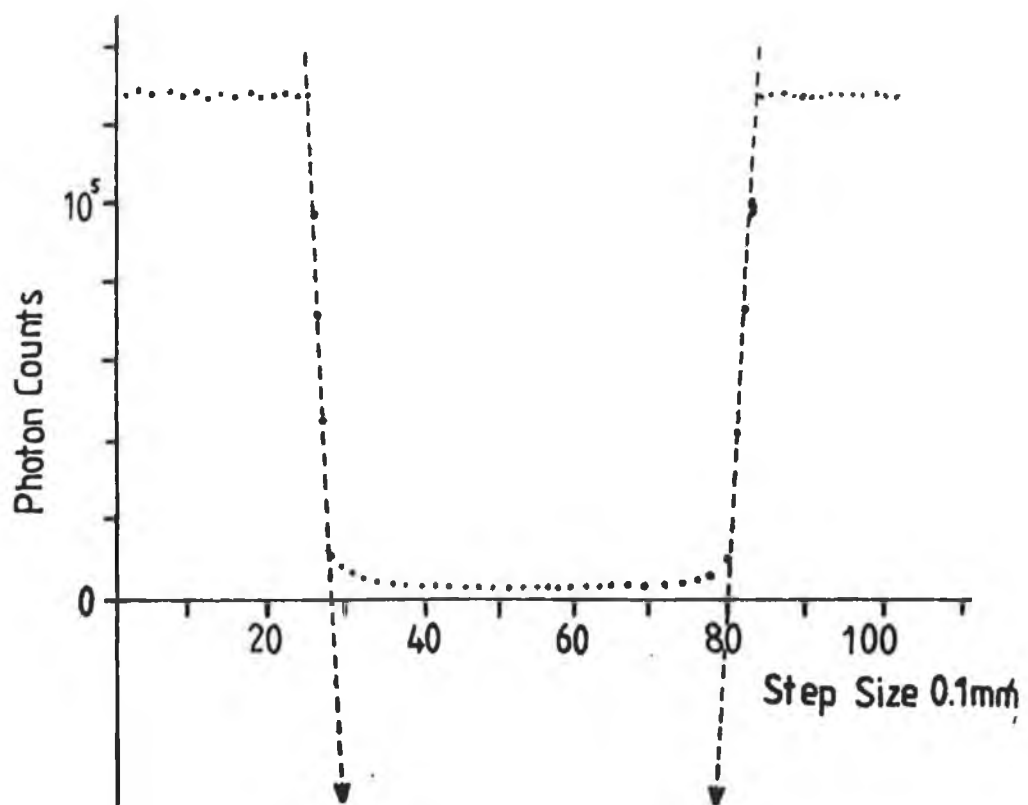
Fig IV.20
The variation in the measured photon count as the rotation stepper motor axle is stepped through the collimated X-ray beam. The dotted lines represent the extrapolation of the slopes.From the extrapolated lines the mid-point of the axle is determined.

clearly seen. Using the extraoplation method described in section
II.3, the analyte equivalent thicknesses for each of the three
elements were calculated. See figure IV.23. Here, scan profiles and
reconstructed images are described and analysed.

In order to generate conventional CAT images, scan profiles
were generated on the VAX11/785 using the count data from a single
ROI. The projections, as shown in figure IV.24a for a typical scan,
are due to all elements present, both matrix and analyte. These
were calculated using equation 2.1. There is no elemental
discrimintion, unlike in the projection scan in figure IV.24b. This
shows palladium equivalent thicknesses calculated, using equation
2.10, with the counts from regions of interest 2 and 3 only. In
this case there is no extrapolation so the palladium peaks sit on a
negative background. In the same figure, the negative background
due to the matrix has been removed by the extrapolation method.
Note, for this case, the the other elements, silver and cadmium,
are considered to be part of the matrix.

IV.3.3.6 Image reconstruction and analysis.

Two methods of image reconstruction were used, the first being
the filtered back-projection method, the second being the iterative
ART method. The filtered back-projection method was used to
reconstruct images from projections for a single ROI as it was fast
to implement and the absolute pixel were not critical. On the other
hand, the ART method was much slower, several minutes CPU time per
iteration compared to 30 seconds CPU time in total for filtered
back-projection. Several iterations were required for ART before a
final image was produced which satisfied the criteria for
convergence as defined in section II.4.5. However, the elemental
concentrations are close to the expected values. See table 4e. This
is because of the use of fractional overlap ares to 2% accuracy.

The first image reconstructed was a conventional CAT image
showing the spatial variation in attenuation through the slice at
24.04keV, the average energy of region of interest 2. Plate 4.7a
shows the six test tubes in the cork. However, it is not possible
to say which element is present, nor tell its concentration, in
each of the test tubes. On the other hand, it is possible to say
that the two tubes on the left have higher densities. Overall, this
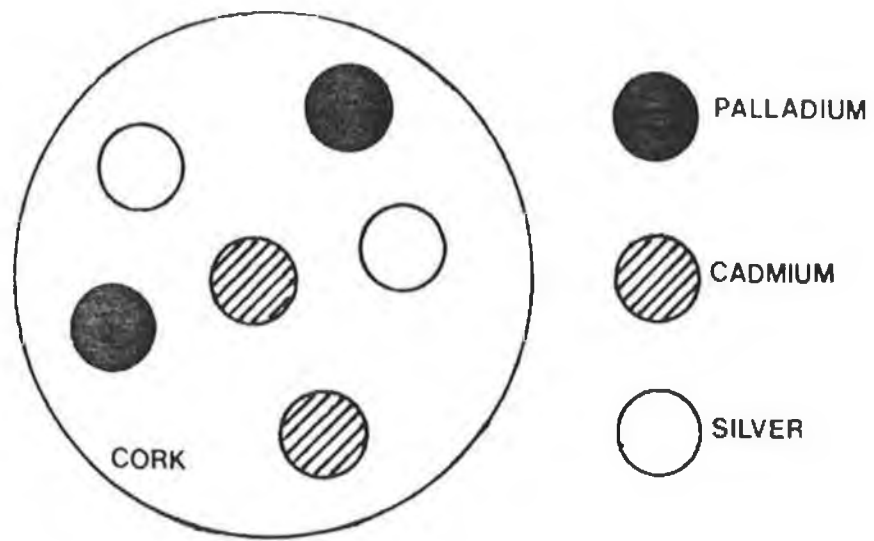
Fig. IV.21
Diagram of a cross-section through the specimen showing
the relative positions of the test tubes in the cork.

type of image is useful in seeing the spatial relationships within the specimen but no element information is present.

The CAT images reconstructed using analyte equivalent thicknesses show the variation in concentration of each analyte element through the slice. In plates 4.7b, 4.7c and 4.7d, there are three images which show the spatial distribution of the palladium, silver and cadmium respectively. When compared to plate 4.7a and figure IV.21, it is possible to tell what element is in each test tube. In these images, the display colour for each pixel is determined by the pixel concentration. By placing the screen cursor on a pixel, the display program printed the concentration in that pixel. Having found the maximum elemental concentrations in this way, a comparison was made with the expected concentrations in Table 4e. The differences may be due to uneven mixing, especially in the case of the silver nitrate in the epoxy. However, the test tubes with low and high concentrations are correctly identified. Overall, this experiment shows that it is possible, using this technique, to produce in a single CAT scan, element specific images of several adjacent elements showing the elemental distribution and concentration in a slice through a specimen. These were the first multiple element specific CAT images produced using a tube source of X-rays. In previous methods, by Van Riet et al. [4] and Riederer and Mistretta [5], only one element could be image in a single scan and the methods failed when another element, close in atomic number to the element of interest, was present.

Element	Concentration $[kg/m^3]$	
	Maximum from Image	Expected from amounts added
Pd	21	15
Pd	10	7
Ag	17	25.4
Ag	12	12.7
Cd	15	22
Cd	10	11

Table 4e. [30]
A comparison of the average concentration of
Pd, Ag and Cd in each rod with those obtained
by Differential X-ray Absorptiometry CAT.

A total of 10^7 photons were detected during the complete scan.
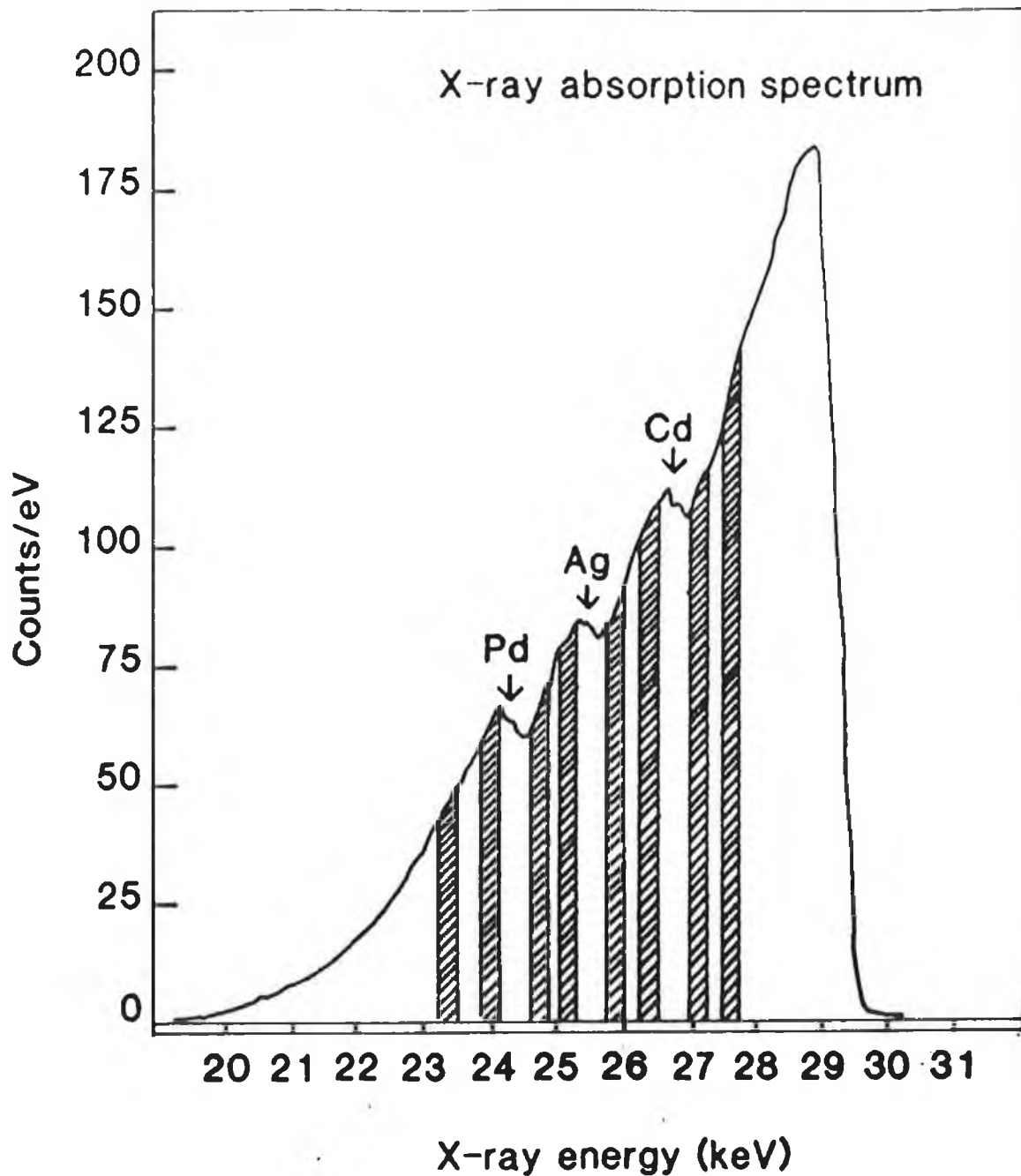
Fig. IV.22
An example of the filtered spectrum after transmission through the specimen. The dips are due to the increased absorption near the Pd, Ag and Cd K-edges. These edges are marked by arrows. The regions of interest are given in table 4e.
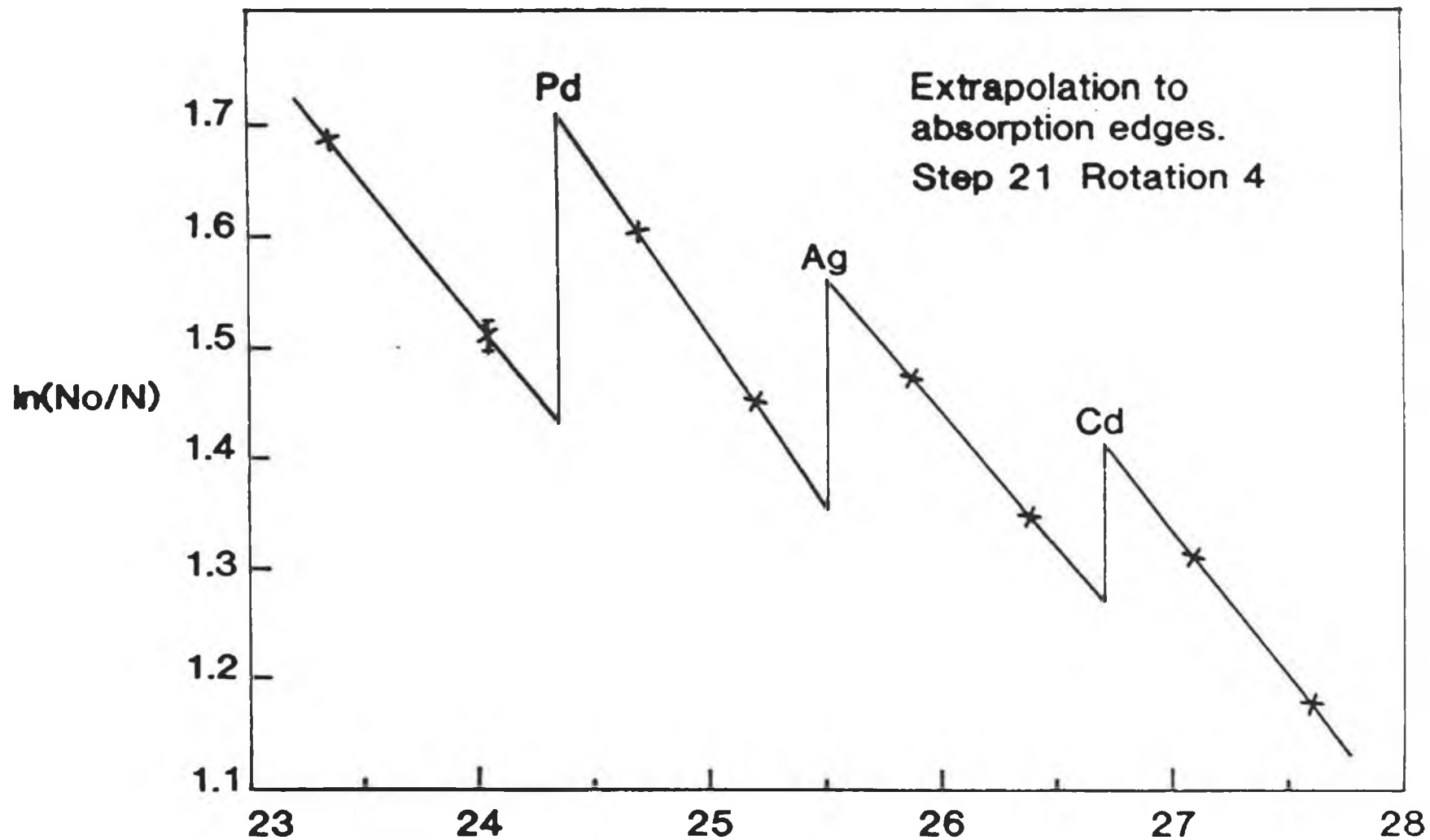
Fig. IV.23
The variation in ln(No/N) as a function of X-ray energy near the Pd, Ag, and Cd K-edges for a typical transmitted beam. The extrapolated values values are used in equation 2.21 to determine the equivalent thickness of each analyte element for this particular beam direction.

161
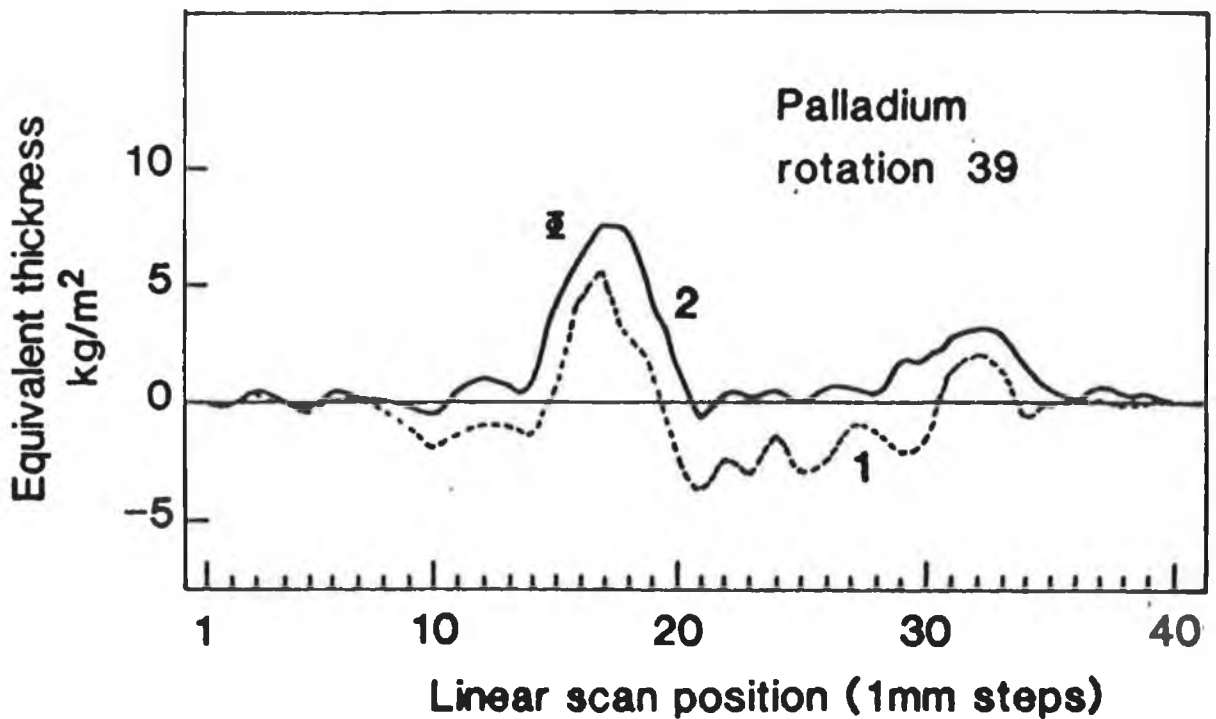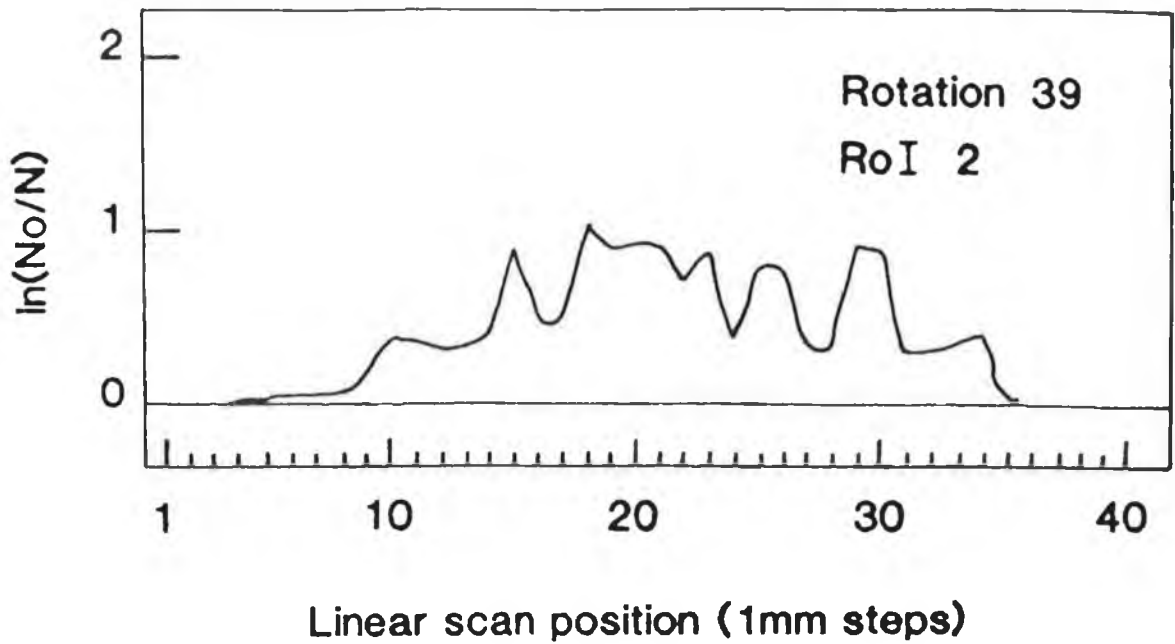
Fig. IV.24
a) Projection data obtained using equation 2.1 from the counts in region of interest 2 of table 4e. These are conventional CAT projection data but for a narrow energy band.

b) 1) A typical scan profile showing the variation in palladium equivalent thickness. The data was generated using equation 2.11 for regions of interest 2 and 3. No corrections were made for matrix effects hence the negative background.

   2) As in 1) but obtained using equation 2.21 which was extrapolated data. The negative background has been effectively removed.

Using equation 3.74 in section III.5, for a water like matrix of similar diameter and the same range of energies, the sensitivity to these elements is of the order of kg/m^3 for differential X-ray absorption CAT. This is in agreement with the pixel to pixel variation in the images.

IV.3.3.7 Experiment to image analyte elements in a mixture.

In all the experiments so far described, the analyte elements have been separated into test tubes containing only one analyte. There has been no mixing of the analytes. In this experiment, two analyte compounds are mixed nonuniformly together in a silicon rubber mould. In order to visually distinguish between the two compounds, fluorescent dyes were added to the mixture. The sample was scanned using the X-ray tube source and the resultant images were compared with the distribution of the dyes in the slice.

The two analyte elements chosen were cadmium and indium which are one atomic number apart. Cadmium has its K-edge at 26.73keV while indium's K-edge occurs at 27.95keV, [44]. Prior to mixing, two separate mixtures were made. The first consisted of cadmium sulphate and fluorol green gold dye in silicon rubber while the second consisted of indium(III)-chloride and pyrenebutyric acid in the silicon rubber. In both cases, the concentration of the analyte element was several kg/m^3. The two mixtures were mixed together in a cylindrical mould, 3cm in diameter, and then left to solidify. When solid, the sample was mounted onto the axle of the rotation stepper motor.

The tube filament current was set to 20mA, due to the higher attenuation of the silicon rubber while the tube potential was set to 40kV. The tin filter, 0.29mm thick, which was used in the previous experiment was also suitable for imaging these two analyte elements. The shape of the resultant filtered spectrum is shown in figure IV.19. Six regions of interest were defined on the MCA prior to scanning. They are shown in Table 4f. The apparatus used and the procedures followed were the same as in the previous experiment. Again, the scan consisted of forty 1mm steps at forty rotation positions.
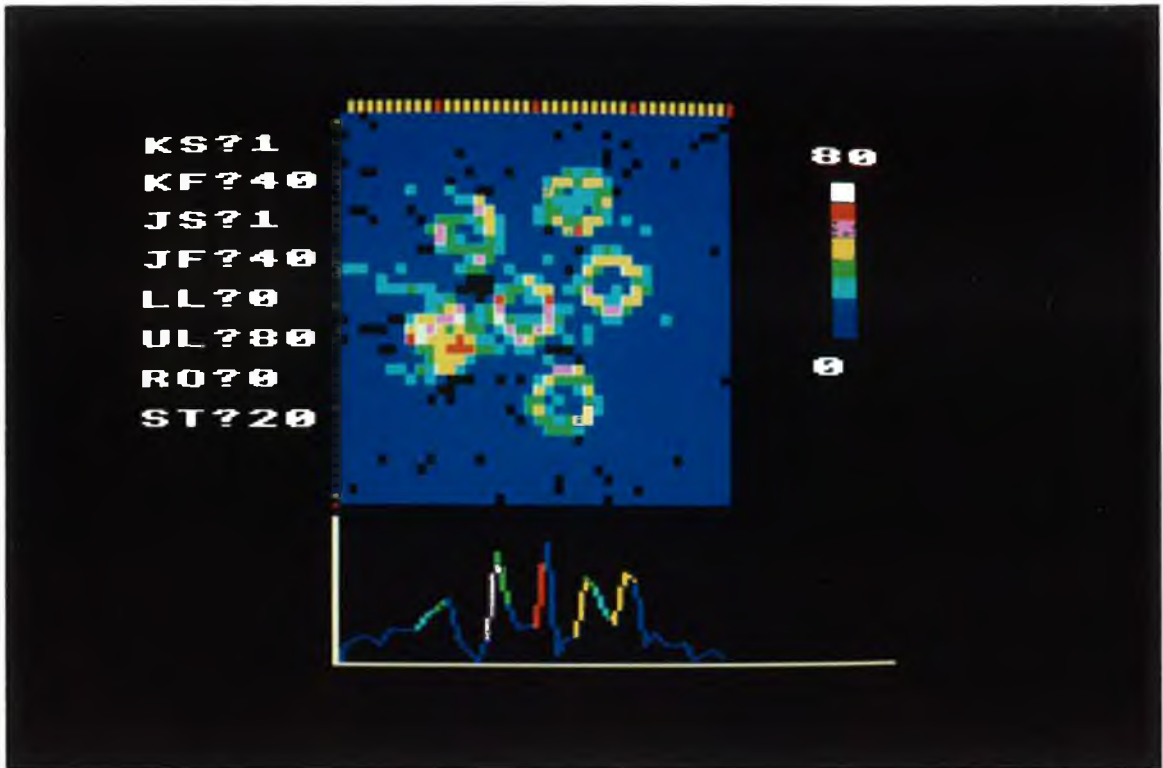
Plate 4.7a
Reconstructed image showing the six test tubes.
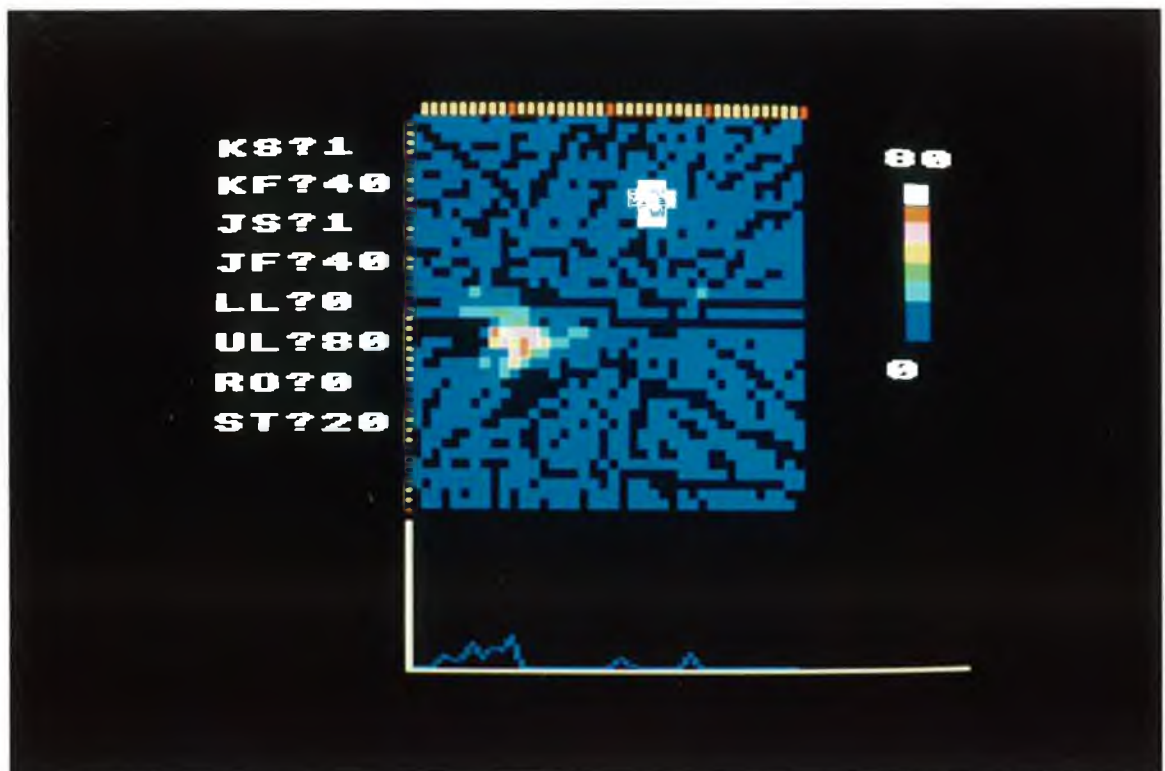
Plate 4.7b
Palladium specific image.
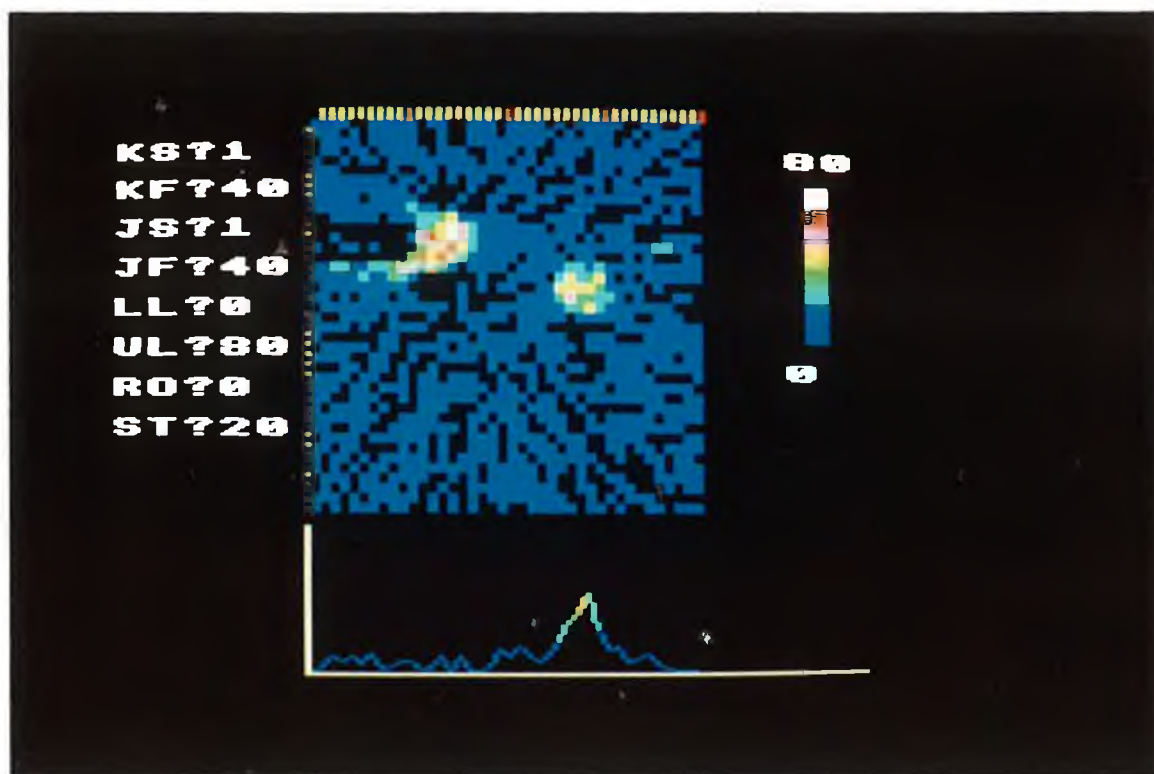
Plate 4.7c
Silver specific image.
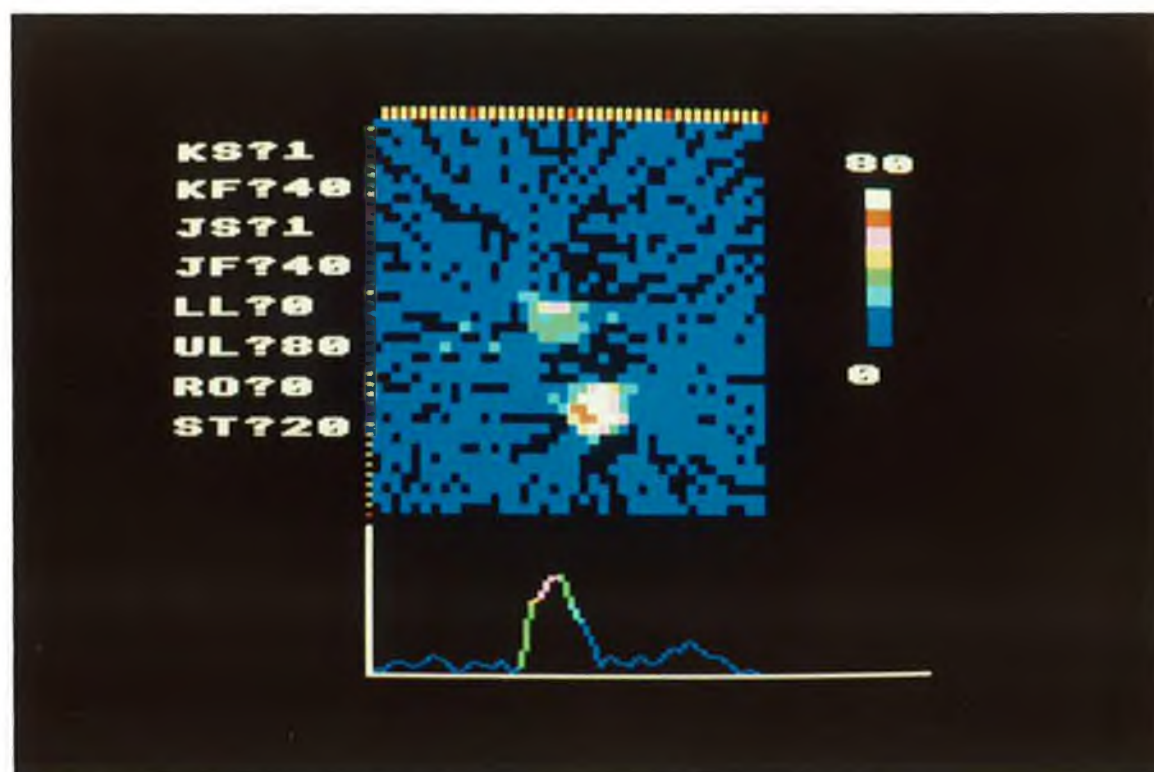
Plate 4.7d
Cadmium specific image.

Region of Interest	Lower Energy keV	Higher Energy keV	Centre Point keV
1	25.72	26.02	25.87
2	26.25	26.54	26.40
3	26.94	27.24	26.09
4	27.44	27.74	27.59
5	28.14	29.44	27.29
6	28.64	28.94	26.79

Table 4f

The regions of interest as defined on the MCA. Their centres were used when extraploating to the analyte absorption edges.

IV.3.3.8   Image reconstruction and analysis of results.

One scan of the specimen was made. When completed, the data was transferred to the VAX11/785 for reconstruction. Prior to reconstructing the images, the scan projections and equivalent thicknesses were calculated. Figures IV.25a and IV.25b show the equivalent thicknesses of the cadmium and indium respectively which were calculated using the extrapolation method. In both profiles, the matrix effects have been removed by the extrapolation. The filtered back-projection reconstruction method was used in this case as it was faster and the concentration values were not required. The first images were reconstructed using the projection data from region of interest 2. The image to the right in plate 4.8 shows density variations across the slice but there is no elemental discrimination.

Element specific images of the object were reconstructed from extrapolated equivalent thicknesses. The first is on the left in plate 4.9 and shows cadmium. Note the "scottie dog" in the left hand side of this image. The second on the right of figure 4.9 shows indium. If these two images are overlapped the match is very good. Note that there is some mixing of the two elements in the top right hand corners. When these images were compared with the original specimen the match was excellent. Unlike the previous experiments, the elements were mixed unevenly in the specimen so no comparisons of concentrations could be made. However, this experiment showed that the technique can image separately two unevenly distributed and adjacent elements in a single scan of the specimen.

IV.3.4 Experiments to determine the sensitivity of CAT to elemental imaging.

IV.3.4.1 Introduction.

Equations to determine the sensitivity of CAT to an analyte element in a uniform matrix were derived in chapter III for two common situations. The first, using equations 3.25 and 3.38, was for the case when analyte can be added to the matrix and the second, using equations 3.73 and 3.74, was for when analyte is already present in the matrix. Then, using the calculated examples which were from section III.6, the theoretically determined sensitivities are compared with sensitivities which were determined experimentally. In this way, it was hoped to verify the theory for sensitivity to analyte elements derived in chapter III.

The experiments involved scanning in turn, specimens which contained successively lower concentrations of analyte. Then, from the reconstructed images of the specimens, the minimum detectable analyte concentration in the matrix could be determined. Note, in order to reduce the number of scans required, only one set of scans was made. One scan of each specimen was sufficient as the same count data could be used for both situations.

IV.3.4.2 Description of specimen and apparatus.

Water was chosen as the matrix for the experimental work while cadmium, $_{48}$Cd, in the form cadmium sulphte was chosen as the analyte. Solutions of cadmium sulphate dissolved in distilled water were made having cadmium concentrations of 10, 1, 0.1 and 0.01 kg/m^3. A matrix sample containing distilled water only was also made. The samples were sealed with a layer of paraffin wax in a light plastic cylindrical container. The container had an outside diameter of 3.2cm with walls 0.1cm thick. Plastic was chosen as the container material because it's attenuation coefficients are similar to those of water for energies near the cadmium K-absorption edge at 26.73keV. The linear attenuation coefficients of water and polyethylene at 26.73kev are 44m^{-1} and 30m^{-1} respectively [29].

The apparatus is the same as that used in the second set of experiments. Again, the X-ray tube was the source used. In order to
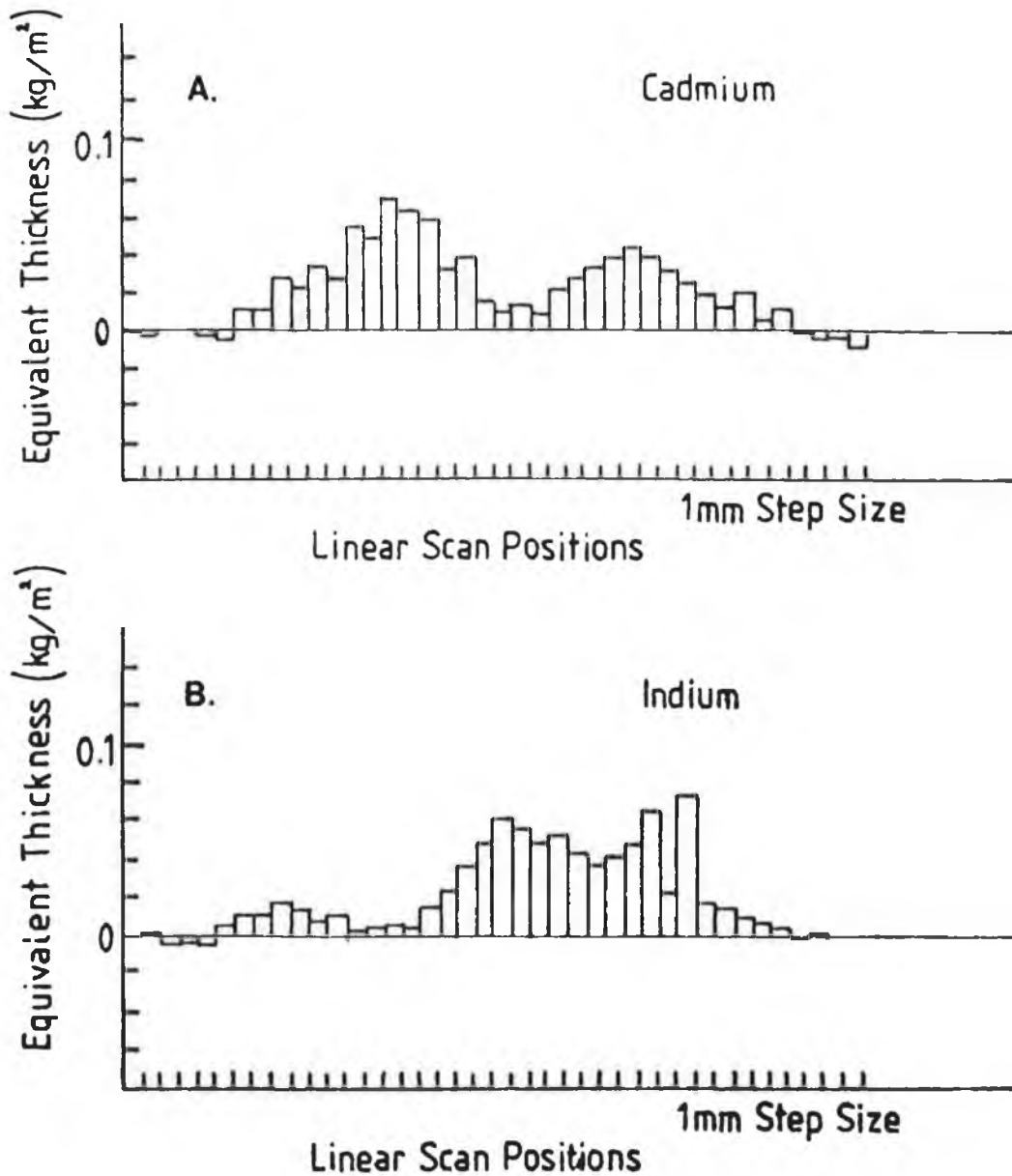
Fig. IV. 25
 a) A typical scan profile showing the variation in cadmium equivalent thickness. The data was obtained from the extrapolated ln(No/N) values.
 b) The corresponding scan profile showing the variation in the indium equivalent thickness.
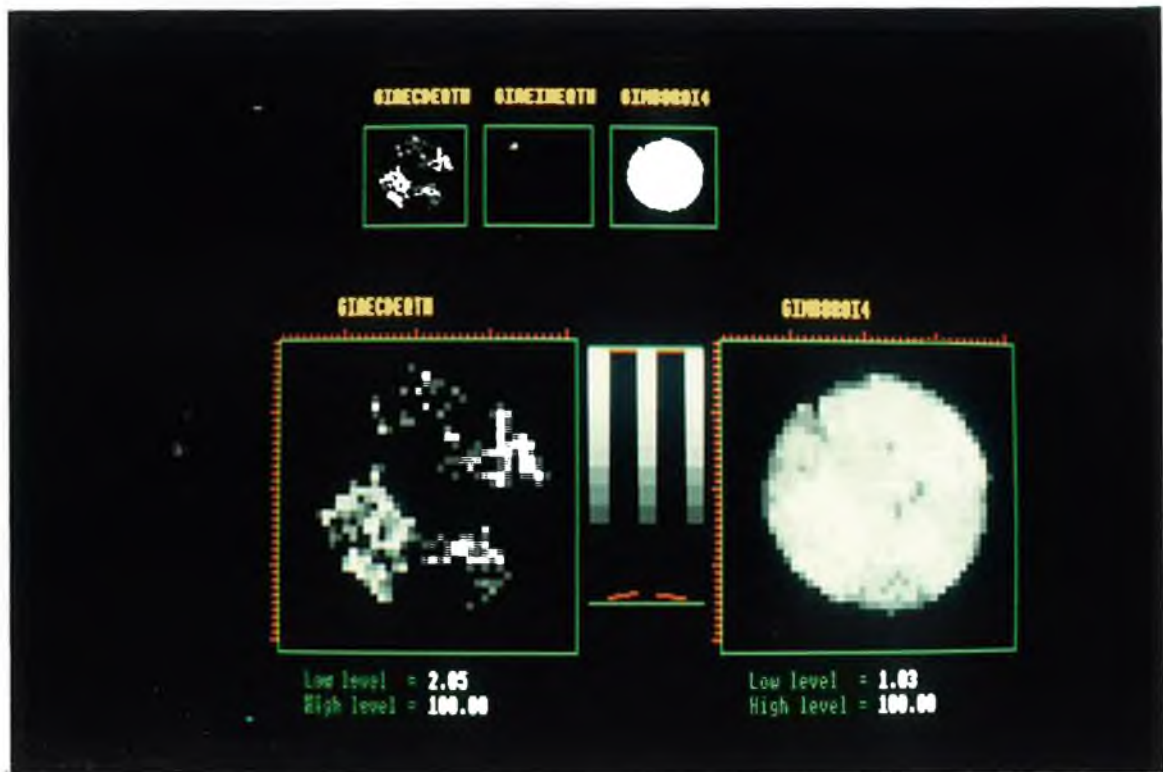
Plate 4.8
Reconstructed images of silicon rubber specimen. The bottom
left shows cadmium while the bottom right is a conventional image.
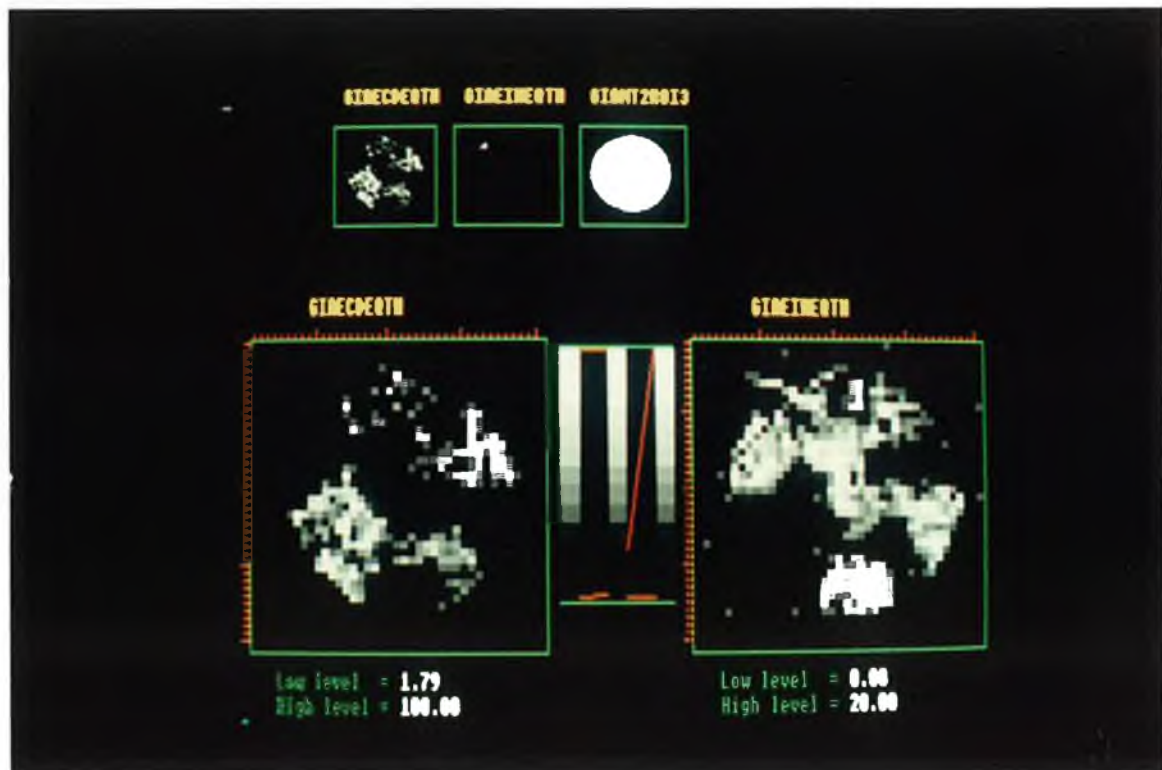
Plate 4.9
Element specific CAT images showing cadmium (bottom left) and
indium (bottom right). The top images are similar.

image cadmium, X-ray energies which straddled the cadmium K-edge at 26.73keV were required. The 0.29mm thick filter tin filter was used to remove unwanted photons. The filtered spectrum is shown in figure IV.19. The tube voltage and filament current were set at 40kV and at 20mA respectively. Prior to scanning, two regions of interest on both sides of the cadmium K-edge energy were defined on the multi-channel analyser. See table 4g. The 1mm diameter pencil beam of X-rays was obtained by using 1mm diameter apertures in 0.01m thick lead sheets which were placed on the floors of the steel box and lead cabinet.

Region of Interest	Lower Energy keV	Higher Energy keV	Centre Point keV
1	25.72	26.02	25.87
2	26.25	26.54	26.40
3	26.94	27.24	26.09
4	27.44	27.74	27.59

Table 4g

The regions of interest as defined on the MCA.
Their centres were used when extrapolating to
analyte absorption edges.

Scans of the specimens consisted of forty 1mm linear steps and forty 4.5 degree rotations. The specimens were mounted onto rotation the axle. In order to ensure the reproduciblity of the scans, the scan start position was found by using the centre of rotation program described in section IV.3.3.3 and appendix I. It was important to be able to reproduce the scans exactly as images were subtracted when determining the sensitivity. Incorrect positioning would result in artifacts in the subtracted images and might lead to incorrect determination of the sensitivity.

IV.3.4.3 Experiment to determine the elemental sensitivity when analyte can be added to the matrix.

In section III.6, example 1, it was predicted by calculation that the sensitivity to cadmium analyte in a water matrix of diameter 0.03m, using 10^7 incident photons of energy 30keV and with a machine factor Q=38 is 0.24kg/m^3. It would therefore be expected that for a similar water matrix using a similar number of X-ray photons of an energy which is just above the cadmium K-edge energy,

that the experimentally determined sensitivity would be close to this calculated sensitivity. This comparison is made here by considering the scan data for region of interest 3. This region of interest encompasses photons of energies 26.94keV to 27.24keV and for each scan the estimated incident photon count was approximately 8.5×10^6 photons. Thus using region of interest 3, it would be expected that the experimentally determined sensitivity should be in good agreement with the calculated sensitivity.

In figure IV.26, scan profiles of ln[No/N] are shown for typical scans of the sample for each cadmium concentration. Images of the slices through the specimens were reconstructed using the computer program in appendix B which is based on the Ram-Lak. filtered back-projection method. In order to show the density distribution of the cadmium analyte only for each scan, the image of the water matrix was subtracted in turn from each of the water plus cadmium images. The resultant images, see the top of plate 4.10, show the resultant cadmium density distribution through the slice. The cresent shaped artifact is due to imperfect matching of the water and water plus cadmium images. Also, the unevenness in the images is due to amplification of the statistical noise in the count data. However, because of the noise in the images and the small concentration of cadmium, the cadmium is not visible in the subtracted images for 0.1 and $0.01kg/m^3$. On the other hand, the cadmium is quite visible in the subtracted images for 10 and $1kg/m^3$. See plate 4.10.

Subsequently, a scan was made of a specimen with a cadmium concentration of $0.25kg/m^3$. In the resultant subtracted image, the cadmium is just distinguishible above the background. See bottonm left image of plate 4.10. This is in fact in good agreement with the previously calculated cadmium sensitivity of $0.24kg/m^3$ and so it is a good verification of the theory developed for sensitivity when analyte can be added to a matrix.

IV.3.4.4 Experiment to determine elemental sensitivity when the analyte is already present in the matrix.

In this second situation, when the analyte is already present in the matrix, the count data from all four regions of interest was required to compensate for the lack of matrix data. Although a
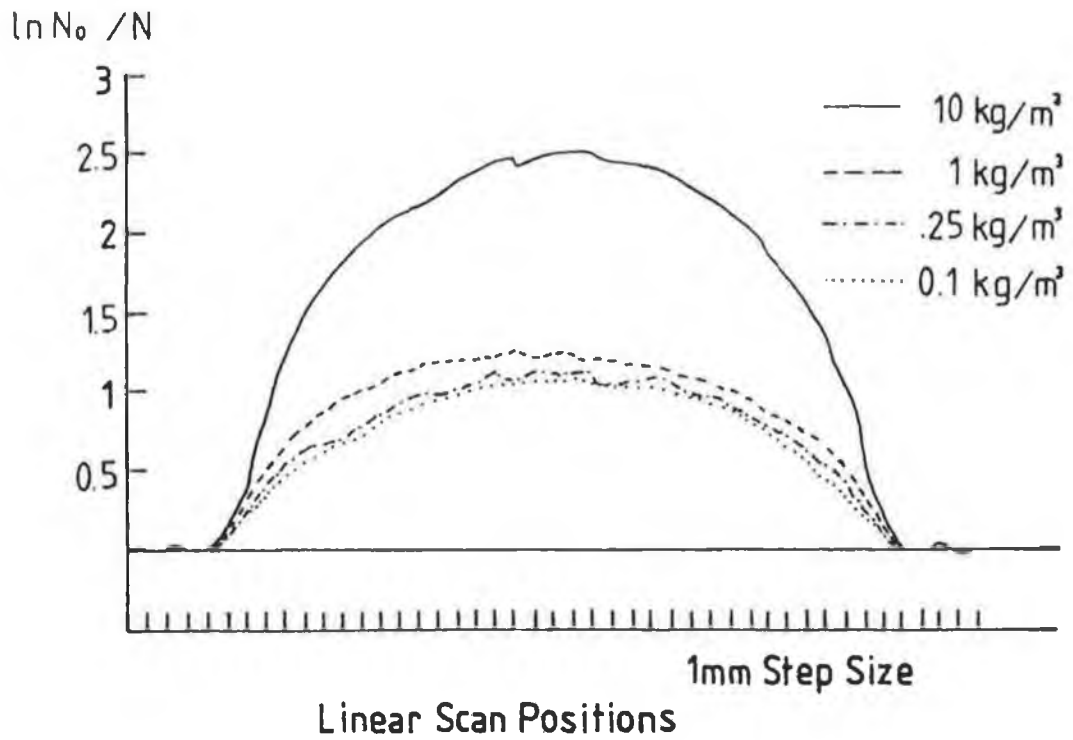
Fig. IV.26
Projection data obtained using equation 2.1 from the counts in table 4g for water and cadmium. The data obtained for cadmium concentrations of 10, 1, 0.25 and 0.1 kg/m³ are shown.

Plate 4.10
Resultant images when water images are subtracted from water plus cadmium images. The top images are for 10, 1 . 0.25, 0.1 and 0.01 kg/m^3. The bottom left shows the subtracted image for 0.25 kg/m^3 and the bottom right shows the subtracted image for 0.1 kg/m^3.
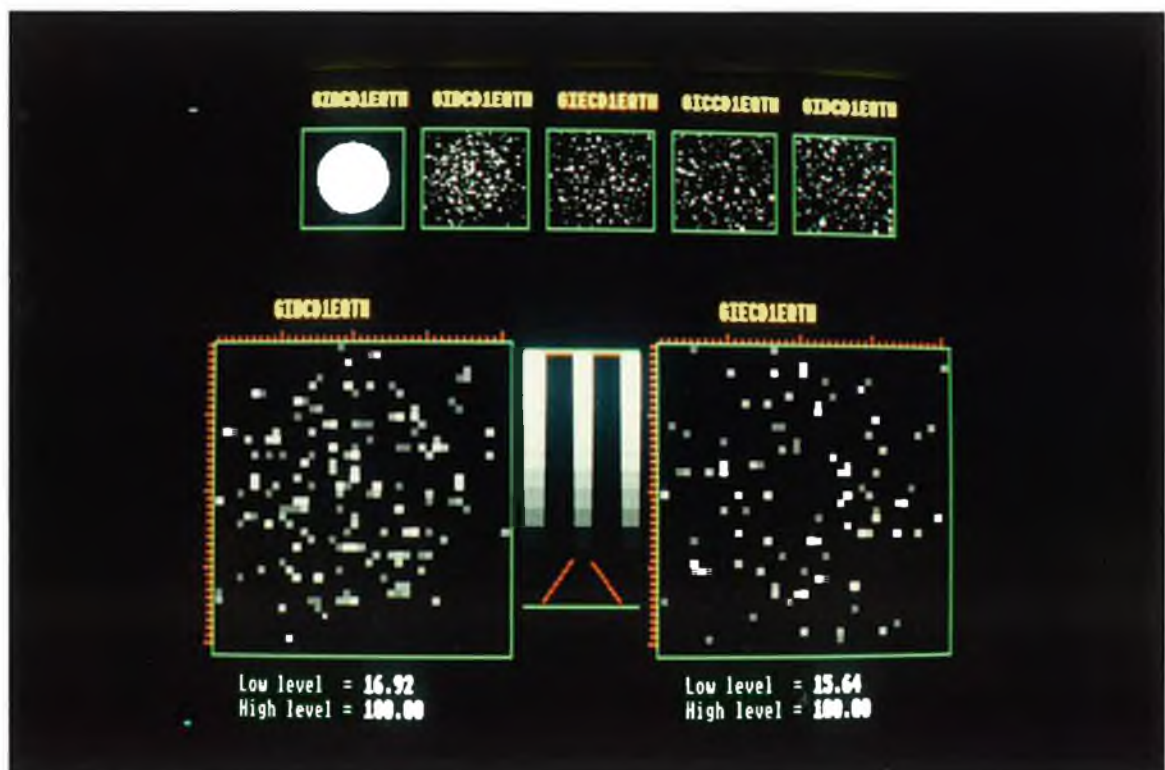
Plate 4.11
The images for extraploation to cadmium K-edge. The top images are 10, 1, 0.25, 0.1 and 0.01 kg/m^3. The bottom left is for 1 kg/m^3 and the bottom right is for 0.25 kg/m^3.The cadmium is just visible in the bottom left image but not in the bottom right.

matrix sample was available for this experiment, it was not used in order to simulate a situation where a matrix specimen would not be available. Instead, the count data in the regions of interest were extrapolated to both sides of the analyte K-edge to remove the effect of the matrix. Thus, there was no need for image subtraction and the analyte was said to be detectable if it was visible above the background in the image. In example 2 of section III.6 it was calculated, that the sensitivity to cadmium in a 3.2cm diameter water matrix using 10^7 photons is $0.69kg/m^3$. Included in this calculation was a machine factor Q=38 and a factor f=3 to account for the noise amplification due to extrapolation.

In the experiment the scan data collected in all four regions of interest was considered. Only the matrix scan data was disregarded. The cadmium equivalent thicknesses were calculated using equation 2.21 which is given by

$$ t_a = \left[\frac{Y_h - Y_l}{U_{ah} - U_{al}} \right] \quad \ldots\ldots \quad 2.21 $$

where the terms Y_h and Y_l were obtained by extrapolation of the counts to the cadmium K-absorption edge. The cadmium absorption edge jump $(U_{ah}-U_{al})$ is $3.6m^2/kg$ [29]. The images of the slice through the specimen were reconstructed using the cadmium equivalent thicknesses by the Ram-Lak filtered back-projection method. See the top images of plate 4.11. The cadmium is cleary visible in the $10kg/m^3$ image and it is still visible in the $1kg/m^3$ image, (see bottom left image of plate 4.11). In the 0.25, (see bottom left image of plate 4.11), 0.1 and $0.01kg/m^3$ images it is not possible to distinguish the cadmium above the background. Thus, it is obvious that the sensitivity must lie between 1 and $0.25kg/m^3$. It would be difficult to determine an exact value of the sensitivity, as it is subjective, and depends on the visual perception of the viewer. However, it can still be said that the experimentally determined sensitivity is in good agreement with the calculated sensitivity of $0.69kg/m^3$.

Summary.

In the course of this thesis, the application of differential
X-ray absorptiometry to computerised axial tomography to produce
element specific images of the distribution and concentration of
atomic elements in non-living specimens was investigated both
theoretically and experimentally. The sensitivity of the techniques
developed, in terms of the minimum analyte concentration detectible
in a reconstructed image of the specimen was also investigated.
Finally, the equations derived to calculate the minimum analyte
concentrations detectible in a cylindrical matrix were compared
with experimentally obtained values. In this summary, the
theoretical and experimental work undertaken is summarized and the
main observation noted are outlined briefly.

In the theory developed in chapter II, equations based on
differential X-ray absorptiometry were derived and applied to
computerised axial tomography in order to produce element specific
images. The theory derived and outlined in chapter II was centred
on two situations. This included the situation where the atomic
element of interest, i.e. the analyte element, could be added to or
removed from the specimen, i.e. the matrix, and the situation where
the analyte element was already present in the matrix. For both
situations, equations were derived, see equations 2.21 and 2.35, to
calculate the analyte equivalent thickness (kg m^{-2}) along a path
length through the specimen from the measured incident and
transmitted photon counts. Using such calculated equivalent
thicknesses, it was then possible to produce element specific
images which were completly free from matrix effects and beam
hardening effects. For the first case, where the analyte was added
to the matrix, two scans were required. The first was a scan of the
matrix only while the second was a scan of the matrix plus analyte.
Two scans were necessary since the X-ray energies which straddled

the analyte absorption edge were typically several keV from the analyte absorption edge. In the second case, where the analyte element was already present in the matrix, only one scan was required. Only one scan was required because the incident and transmitted photon counts were monitored at several narrow energy bands on both sides of each analyte absorption and the effect of the matrix was removed by extrapolation of the projection values to the analyte absorption edge. Using this technique, several elements could be imaged simulateously in a single scan. This was possible by extrapolating the projection values in the narrow energy bands, which lay between two analyte absorption edges, to both analyte absorption edges.

In order to produce reconstructed images of a cross-sectional slice through a specimen, reconstruction programs were written on the VAX11/785. These programs were based on well established reconstruction algorithms which are normally used to reconstruct conventional CAT images. Using these reconstruction algorithms, images showing analyte concentration (kg m^{-3}) through a cross-section were reconstructed from analyte equivalent thickness data. The first algorithm used was the additive algebraic reconstruction technique (ART) [15]. Using ART, it was found that the resultant analyte concentration values were in good agreement with the expected values to within 5% error [28]. However, this method was very slow. It required 35 minutes of CPU time per iteration for a 40X40 pixel image on the VAX11/785 and many iterations were normally needed to obtain a satisfactory image. Also, a large amount of computer memory was needed to store the beam path and pixel overlap areas. The second reconstruction technique adopted was a modified version of the Ram-Lak filtered back-projection reconstruction technique [36]. Again, a computer program was written on the VAX11/785. It was found that the filtered back-projection reconstruction technique was much faster to implement than the ART reconstruction technique. It took less than 1 minute CPU time to reconstruct a 40X40 pixel image. However, the resultant and expected analyte concentration values were not in such good agreement as with ART. Conventional CAT images, which were used as reference images for the element specific images were also produced using the filtered back-projection reconstruction method from conventional projection data.

In chapter III, the sensitivity in terms of the minimum analyte concentration detectible in a cylindrical uniform matrix was investigated. Grodzin [7] had previously investigated the sensitivity to critical atoms for differential X-ray absorptiometry applied to CAT using synchrotron radiation. However, Grodzin [7] did not derive equations to calculate the minimum analyte concentration detectible in a chosen matrix. In this chapter, equations to calculate sensitivity were derived for the two situations. The first equations, equations 3.25 and 3.38, were derived for the case where analyte can be added to the matrix. For this case, the minimum analyte concentration detectible in a matrix was investigated as a function of X-ray energy for cadmium analyte in water, silicon and iron matrices. It was found that the sensitivity was a maximum at energies above the cadmium K-absorption edge for all matrices. The second set of equations, equations 3.59 and 3.74, were derived for the case when the analyte is already present in the matrix. For this second case, the sensitivities of all analyte elements between atomic number Z=20 and Z=90 were calculated for water, silicon and iron matrices. The calculations showed that the sensitivity decreased as the atomic number of the analyte decreased, except for analytes which were lower in atomic number than the matrix where there was a sudden increase in sensitivity. For both the former and latter cases, it was found that the minimum concentration detectible in a specimen was dependent on several factors. These included the specimen diameter, in terms of mean free paths, the total number of incident photons, the separation in standard deviations between images with and without analyte, the number of steps per linear scan across the matrix diameter and the matrix and analyte densities and mass absorption coefficients. It should be noted that, for all total incident photon counts greater than 10^6 photons and for any number of linear steps greater than twenty per linear scan, the sensitivity to any analyte in any matrix is a maximum when the specimen diameter is equal to 2.5 mean free paths. A further factor f was included for the case when the analyte is present in the matrix. This was to account for the projection of the Poisson distribution of the photon counts during the process of extrapolation. In order to test these equations, example calculations were made for cadmium in a water matrix. These proved to be in good agreement with the experimentally obtained values in

section IV.3.4.

In the experiments undertaken to produce element specific images, the use of a high resolution energy dispersive Si(Li) detector was the key which allowed such images to be produced. It was because of the high resolution of this detector, that it was possible to define narrow energy bands close to and straddling the analyte absorption edge. The scan principles used to collect the data were based on the scan principles used in the first generation CAT scanners [3]. However, since the Si(Li) detector was mounted in a liquid nitrogen dewar, the specimen was stepped and rotated. This was completly analogous to stepping and rotating the source and detector. In the experiments, the spatial resolution of the images was limited by the diameter of the X-ray beam collimators which were 1mm in diameter. In addition, the use of timing single channel analysers allowed one analyte element to be imaged while the use of a multi-channel analyser made it possible to image several analyte elements simultaneously. The multi-channel analyser was not suited to coping with high photon fluxes and hence producing element specific images in short scan times. This would have required pulse counting apparatus with high count capabilities.

The experiments undertaken in chapter IV were based on the theory developed in chapter II. In the first set of experiments, the analyte equivalent thicknesses were calculated, using equation 2.21, from the scan data which was collected when using radioisotope sources. When using the radioisotope sources, the specimens were scanned both before and after the palladium and caesium analytes were added. Two scans were required in order to remove the matrix effect. Since the output photon flux from the radioisotopes was low, long scan times were required. Also, the number of analyte elements that could be imaged was limited by the availability of radioisotopes which could provide the required X-ray energies.

The tube source used in experiments ii) and iii) of chapter IV was part of a converted Philips PW 1270 automatic simultaneous X-ray spectrometer which had been modified by A.G.R. Fenelon. However, because of the high output photon flux from the tube and the low count capabilities of the multi-channel analyser, it was found necessary to filter the X-ray beam. Filtering the X-ray beam

had the effect of both reducing the photon count as well as removing superfluous photon energies. Even with filteration of the X-ray beam, large dead-times were recorded in the multi-channel analyser. The calculated analyte equivalent thicknesses were unaffected by the MCA dead-time. A computer program was written to help choose a suitable filter and filter thickness. It was found using this program that a tin filter, which is the next highest element above indium in the perodic table, was most suitable when imaging palladium, silver, cadmium or indium. Several experiments were carried out and element specific images of adjacent elements were produced both when the analyte elements were seperated into test tubes and mixed together. In all cases the analyte concentrations were several kg/m^3. Experiments were also carried out which verified the theory developed on the sensitivity to analyte for both situations. It was found that the minimum cadmium concentration that could be imaged in a 3 centimetre diameter water matrix using 10^7 photons was 0.25 kg/m^3 for the case where the analyte could be added to the matrix. Similarily, it was found that the minimum cadmium concentration that could be imaged when the analyte was already present in the water matrix was 1 kg/m^3 under the same conditions.

Conclusion.

In the research undertaken for this thesis, differential X-ray absorptiometry was applied to computerised axial tomography to produce element specific images, showing analyte concentration, using both radioisotope and X-ray tube sources. In the experiments undertaken using these sources, element specific images showing analyte concentration were obtained for analyte elements, even in the presence of other elements close in atomic number, which were free from matrix effects and beam hardening effects. These problems had been present in images which had been produced in previous work by Van Riet [4] and Riederer and Mistretta [5]. Images without these artifacts had only previously been obtained using synchrotrons, i.e. by Flannery et al. [8] and by Thompson et al. [9]. However, neither of these authors discussed the ability of the technique to measure the concentration of the analyte element. Finally, the sensitivity of the technique was investigated and equations were derived and verifed experimentally to calculate the minimum concentration of an element that is detectible in an image.

The images obtained using the X-ray tube source were the first element specific images of adjacent atomic elements obtained in a single scan. Despite the low output photon fluxes of the radioisotopes and X-ray tube, as compared to a synchrotron source, it is interesting to note that a factor of two increase in the total number of photons only results in a factor of one increase in the sensitivity. Even though only five different analyte elements were imaged, namely palladium, silver, cadmium, indium and caesium, the work in this thesis has shown that it is possible to image a wide range of analyte elements using suitable radioisotope and X-ray tube sources in a variety of low atomic number matrices.

Future Developments.

The new elemental imaging techniques developed and the experimental findings reported herein have been the basis for several new CAT elemental imaging techniques which are currently under investigation. The equations derived for element sensitivity have also been of assistance in these projects. A dedicated system, which is portable, could also be designed and built using the principles decribed in chapter II. There is also still much work that could be done to examine possible applications of the techniques developed.

The spatial resolution of the apparatus described in chapter IV was of the order of 1 millimetre which is compatible with modern conventional CAT scanners. Presently, element specific images with better spatial resolution can only be produced using synchrotron sources, [8], [9]. A CAT scanner, using a tube source of X-rays and designed to produce element specific images with submillimetre resolution, is currrently being assembled and investigated by N. O'Hare. With this apparatus, it is hoped to image low atomic number elements, in objects of diameter less than 4 millimetre, using the element imaging techniques developed in chapter II. Although the spatial resolution will not be as great as with synchrotrons CAT systems, which have spatial resolutions of the order of micrometres [8], the system will be portable.

A second system, which is currently being investigated by C.E. Markham, involves the possibility of producing element specific CAT images using low resolution energy dispersive detectors and a tube source of X-rays. It is hoped that by sweeping the tube voltage across the analyte K-absorption edge, while measuring the transmitted photon flux using a low resolution energy dispersive detector in conjunction with a scaler whose low level discriminator

181

is set at a fixed position behind the tube potential, data may be collected in the form of photon counts within an energy band. By deconvolution of this data, monochromatic spectral information should be obtained. This spectral information could then be used to produce element specific images. Some sensitivity would be lost, as compared to the present technique, but it should still be possible to image a few kilogrammes per cubic metre using similar total photon counts.

It might be also possible, using an element as a contrast agent, to diagnose damage to the muscle in the wall of the heart. It is known that the uptake of certain atomic elements in damaged heart muscle is different from that in normal muscle. Thus by using a suitable contrast agent in conjunction with element specific imaging it might be possible to recognise the damaged muscle. At the moment the sensitivity to different elements in a chest phantom, using the technique described in section III.4, is being examined by J. Fryar, N. O'Hare and C.E. Markham to find a suitable element. Preliminary measurements have shown that the measured and calculated sensitivities are in good agreement for potassium iodide. However, it is expected that better sensitivity could be achieved using gadolinium as the contrast agent. This has yet to be investigated.

It was stated in chapter IV that the scan times were long when using the multi-channel analyser with the tube source. This was because of the large dead-time for relatively low count rates i.e. greater than $2X10^4$ counts per second. A dedicated pulse counting system, using single channel analysers and individual pulse counters might reduce such dead times and hence decrease the scan times. It might also be possible to reduce the time to generate reconstructed images. In the apparatus used for the research in this thesis, the count data was transferred to the VAX 11/785 on completion of the whole scan. If instead, the data was transferred to a microcomputer such as an Acorn Archimedes at the end of each linear scan, the reconstruction process could run in parallel to the data collection. However only filtered back-projection algorithms could be used since the ART reconstruction process requires that all data is collected before beginning a reconstruction [15]. In addition, the present system is too heavy and too bulky to be portable. However, a purpose built portable

machine, based on the Hewlett Packard Faxitron X-ray photography machine, could be built. The Faxitron can generate X-rays up to 120keV at a maximum tube current of 3mA. This would allow imaging of the heavier elements. If scan times were reduced considerably, three-dimensional element specific images might become a reality. Such a machine would be a very useful non-destructive testing tool.

There is much work yet that could be done to study possible applications of the techniques of differential X-ray computerised tomography developed. These could include medical and non-medical applications. Medical applications might include the detection of lead (K-edge 88.01keV) in bones, the distribution and concentration of calcium (4.03 keV) or strontium (16.11 keV) also in bones or the accumulation of iodine(33.17 keV) in the thyroid gland. For medical application however, a fast scan time system would be required. Also the high absorption of low energy X-rays could be a problem.

References.

[1] E.M. Bocage, Patent No. 536,464, Paris, France, (Quoted in "History of Tomography" by J. Massiot, Medica Mundi, vol. 19 (3), pp. 106-115, 1974)

[2] A.M Cormack, "Representation of a function by its line integrals, with some radiological applications", J. App. Phys, vol. 34, pp. 2722, 1963.

[3] G. N. Hounsfield, "Computerised transverse axial scanning (tomography): Part 1. Descrpition of system", British Journal of Radiology, vol. 46, pp. 1016-1022, 1973.

[4] B. Van Riet, R. Luypaert and L. Cools, "Basic methods in Quantitative CT", J. Belge. Radiol, vol 69, pp. 423-30, 1986.

[5] S.J. Riederer and C.A Mistretta, "Selective iodine imaging using K-edge energies in computerised X-ray tomography", Med. Phys, vol. 4, pp. 474-481, 1977.

[6] L. Grodzin, "Optimum energies for X-ray transmission tomography of small samples", Nucl. Instr. and Meth, vol.206, pp. 541-545, 1983.

[7] L. Grodzin, "Critical absorption tomography of small samples", Nucl. Instr. and Meth, vol. 206, pp. 547-552, 1983.

[8] B.P. Flannery, H.W. Deckman, W.G. Roberge and K.L D'Amico, "Three-dimensional X-ray microtomography", Science, vol. 237, pp. 1439-44, 1987.

[9] A.C. Thompson and J. Llacer, L. Campbell Finman, E.B. Hughes, J.N. Otis, S. Wilson, H.D. Zeman, "Computed tomography using synchrotron radiation", Nucl. Instr. and Meth, vol. 222, pp. 319-323, 1984.

[10] W.B. Gilboy, "X- and γ-Ray tomography in NDE applications", Nucl. Instr. and Meth, vol. 221, pp. 193-200, 1984.

[11] J.H. Kinney, Q.C. Johnson, U. Bonse, M.C. Nichols, R.A Saroyan, R. Nusshardt, R. Pahl and J.M. Brase, "Three-dimensional X-ray computed tomography in materials science", MRS Bulletin, pp. 13-17, January 1988.

[12] R.G. Waggener, J.G. Kereiakes and R.J. Shalek, "Handbook of medical physics, volume II", CRC Press, Florida, pp. 37-80, 1984.

[13] T. Taylor and L.R Lupton, "Resolution, artifacts and the design of computed tomography systems", Nucl. Instr. and Meth, vol A242, pp. 603-609, 1986.

[14] T.H. Newton and D. Gordon Potts, "Radiology of the skull and brain", The C.V. Mosby Company, St. Louis, Toronto and New York, The Company, vol. 5, ch. 109, pp. 3853-3876, 1981.

[15] H. Barrett and W. Swindell, "Radiological imaging, vol. II", Academic Press, New York, London, Paris, San Diego, San Francisco, São Paulo, Sydney, Tokyo and Toronto, ch. 7, pp. 377-407, 1981.

[16] A.R. Spowart, "Neutron radiography", J. Phys. E., vol. 5(6), pp. 497-510, 1972.

[17] G. Pfister and P. Maier, "A neutron tomography scanner for application in non destructive testing", Materialpruefung, vol.29 (1-2), pp. 8-12, 1987.

[18] G. Matsumoto and S. Krata, "The neutron computer tomography", Proc. of the first World Conference, San Diego, California, part 12, pp. 899-906, Dec 7-10, 1981.

[19] R. Stuart Mackay, "Medical images and displays", John Wiley & Sons, New York, Chichester, Brisbane, Toronto and Singapore, ch. 7, pp. 138-165, 1984.

[20] G. Holland, P. Bottomely and W. Hinshaw, "Fluorine-19 magnetic resonance imaging", J. Magn. Reson, vol. 28, pp. 133-136, 1977.

[21] J. De Layre, J. Ingewall and C. Malloy, "Gated sodium-23 NMR images of an isolated perfused working rat heart", Science, vol. 212, pp. 935-936, 1981.

[22] J. Haselgrove, H. Subramanian, J. Leigh, L. Gyulai and B. Chance, "In vivo one-dimensional imaging of phosphorus metabolites by phosphorus-31 by NMR", Science, vol. 220, pp. 1170-1173, 1983.

[23] W.C. Röentgen, "On a new kind of rays", Ann. Phys. Chem., vol 64, pp 12-17, 1898.

[24] C.G. Barkla, and C.A. Sadler, "Absorption of Röentgen rays", Phil. Mag. [6], vol 17, pp. 739-60, 1909.

[25] R. Glocker, W. Frohnmeyer, "Röentgen-Spectroscopic determination of the quantity of an element in mixtures", Ann. Phys, vol. 76, pp. 369-95, 1925.

[26] E.P. Bertin, "Principles and Practices of X-ray Spectrometric Analysis", Plenum Press, New York-London, Chapter 20, pp. 879-881, 1979.

[27] E.P. Bertin, R.J. Longobucco and R.J. Carver, "Simplified routine method for X-Ray absorption-edge spectrometric analysis", Anal. Chem., vol. 36, pp. 641-55, 1964.

[28] J. Fryar, K.J. McCarthy and A. Fenelon, "Differential X-ray

absorptiometry applied to computerised X-ray tomography"
Nucl. Instr. and Meth, vol. A259, pp. 557-565, 1987.

[29] J. H. Hubbel, "Photon mass attenuation and energy-absorption
coefficients from 1keV to 20MeV", Int. J. Appl. Radiat. Isot,
vol. 33, pp. 1269 to 1290, 1982.

[30] J. Fryar, K. J. McCarthy and A. Fenelon, "Multielement imaging
in computerised X-ray tomography", Nucl. Instr. and Meth,
vol. A271, pp. 671-677, 1988.

[31] R. A. Crowther, D. J. De Rosier and A. Klug, "The reconstruction
of a three dimensional structure from projections and its
application to electron microscopy", Proceedings Royal
Society London, vol. A317, pp. 319-340, 1970.

[32] R. N. Bracewell and A. C. Riddle, "Inversion of fan beam scans
in Radio-astronomy", Astrophysics Journal, vol. 150, pp.
427-435, 1967.

[33] R. Gordon, R. Bender and G. T. Herman, "Algebraic reconstruction
technique for three dimensional electron microscopy and X-ray
photography", Journal of Theoretical Biology, vol. 29, pp.
471-481, 1970.

[34] G. T. Herman, "Radiology of the skull and brain", The C. V.
Mosby Company, St. Louis, Toronto and New York, The Company,
vol. 5, ch. 110, pp. 3888-3903, 1981.

[35] L. A. Shepp and B. F. Logan, "The Fourier reconstruction of a head
section", IEEE Trans. Nucl. Sci, vol. NS-21, pp. 21-43, 1974.

[36] G. N. Ramachandran and A. V. Lakshminarayanan, "Three dimensional
reconstruction from radiographs and electron micrographs:
application of convolutions instead of Fourier Transforms",
Proc. Nat. Acad. Sci. US, vol. 68, pp. 2236-2240, 1971.

[37] J. Radon, "Über die Bestimmung von Funktionen durch ihre
Integralwerte längs gewisser Mannigfaltigkeiten", Berichte
Sächsische Akademie der Wissenschaften Leipzig, Math.-Phys.
Kl., vol. 69, pp. 262-267, 1917.

[38] H. E. Johns and J. R. Cunningham, "The physics of radiology",
Charles C. Thomas·Publisher, Springfield, Illinois, USA, ch.
16, pp. 633-645, 1983

[39] S. Webb, "Reconstruction of cross sections from transmission
projections - A short review and comparison of performance of
reconstruction algorithms", Physical Aspects of Medical
Imaging, J. Wiley & Sons, Chichester, New York, Brisbane,

Toronto and Singapore, Chapter 6, pp. 303-318, 1981.

[40] G.T. Herman and S.W.Roland, "Three methods for reconstructing objects form X-rays: a comparative study", Computer Graphics and Image Processing, vol. 2, pp. 151-178, 1973.

[41] D.A. Chesler, S.J. Riederer and N.J. Pelc, "Noise due to photon statistics in computed X-ray tomography", J. Compt. Asstd. Tomo., vol. 1(1), pp. 64-74, 1977.

[42] B.P. Flannery and W.G. Roberge, "Observational strategies for three-dimensional synchrotron microtomography" J. Appl. Phys, vol. 62(12), pp. 4668-4674, 1987.

[43] J. Fryar and K.J. McCarthy, "Multi-element imaging in CT using a tube source of X-rays", IEEE Transitions on Nuclear Science, vol. 36, no. 1, Feb. 1989.

[44] G.W.C.Kaye and T.H. Laby, "Tables of physical and chemical constants", Longman, pp. 271-278, 1986.

[45] Y.Suzuki, K.Usami, K.Sakamoto, H.Kozaka, T.Hirano, H.Shiono, and H.Kohno, "X-ray computerized tomography using monochromated synchrotron radiation", Jap. J. Appl. Phys., vol. 27(3), pp. L461-L464, 1988.

[46] "X-ray output 50kV to 200kV constant potential", British Standard 4094: Part 2: pp. 13, 1971.

[47] "Conversion from gamma flux density to exposure rate", British Standard 4094: Part 1: pp. 48, 1966.

[48] "Transmission of 10kV to 50kV constant potential X-rays through mild steel", British Standard: 4094: Part 2, pp. 22, 1971.

[49] "Transmission of 50kV to 200kV constant potential X-rays through lead", British Standard 4094: Part 2, pp. 35, 1971.

[50] "Scattered Radiation", British Standard 4094: Part 2, pp. 49, 1971.

[51] "Variation of percentage scatter with energy for metals", British Standard: 4094: Part 2, pp. 56, 1971.

[52] T.A. Littlefield and N. Thorley, "Atomic and Nuclear Physics: An Introduction", Van Nostrand Reinhold, New York, Cincinnati, Toronto, London and Melbourne, ch. 6, pp. 69-84, 1979.

Appendices

Appendix

A: Details of the convolution function and Hilbert transfrom which
    were outlined in section II.4.

B: Program to filter the projection data using the Ram-Lak filter
    function and to reconstruct an image using back-projection.

C: Program to calculate analyte equivalent thicknesses by
    extrapolation to the analyte absorption edge for the VAX11/785.

D: Program to display a reconstructed image using either grey or
    false colour shades for the BBC microcomputer.

E: Program to calculate dummy data for a phantom consisting of two
    small cylindrical objects 3X3 pixels in size on the VAX 11/785.

F1: Program to calculate the X-ray beam and pixel overlap areas for
    a 40X40 pixel reconstruction grid on the VAX 11/785.

F2: Program to reconstruct the images using the Algebraic
    Reconstruction Technique for 40X40 pixels on the VAX 11/785.

G: Program to control the scan table motions and to collect and
    store the photon counts when using the SR7 scaler ratemeter
    and radioisotope sources for the BBC micro-computer.

H: Program to control the scan table stepper motors and the data
    collection and storage when using the Multi-Channel Analyser
    and X-ray tube source for the BBC micro-computer.

I: Program to find the stepper motor axle centre and to find the
    scan start position for the BBC micro-computer.

J: Program to calculate and display filtered spectra for X-ray
    tube source.

K: Tables of X-ray K-absorption edges, characteristic X-ray lines
    fluorescence yields.

189

In section II.4.4.3, it was stated that the Radon transform associates a function [Rf] of two variables with a function f of two polar variables. Furthermore, it was stated that the operator R^{-1}, called the inverse transform associates the function f with the function [Rf]. It was shown that if such an operator exists, then for any function of two polar variables, $[R^{-1}Rf]$ equals f for all point (r,ϕ) such that

$$[R^{-1}Rf](r,\phi) = f(r,\phi) \quad \ldots \quad 2.44$$

The operator R^{-1} can expressed as a sequence of simple operators,

$$R^{-1} = -\frac{1}{2\pi} B \ Hz \ Dz$$

where

1) Dz is the partial derivative of $p(\mathit{l},\theta)$, where $p = Rf$, with respect to its first variable to obtain the function $q(\mathit{l}',\theta)$ and it is given by

$$[Dz \ p](\mathit{l},\theta) = \lim_{d\mathit{l}\to0} \frac{p(\mathit{l}+d\mathit{l},\theta) - p(\mathit{l},\theta)}{d\mathit{l}} \ ,$$

2) Hz is a Hilbert transform of the function $q(\mathit{l}',\theta)$ with respect to its first variable to obtain the function $t(\mathit{l}',\theta)$. It is given by

$$[Hzq](\mathit{l}',\theta) = -\frac{1}{\pi} \int_{-\infty}^{\infty} \frac{q(\mathit{l},\theta)}{\mathit{l}'-\mathit{l}} \ d\mathit{l}$$

This is an improper integral, since its integrand diverges at $\mathit{l}=\mathit{l}'$. It is instead evaluated in the Cauchy principle value sense, that is

$$[Hzq](\mathit{l}',\theta) = -\frac{1}{\pi} \lim_{E\to0} \left[\int_{-\infty}^{\mathit{l}'-E} \frac{q(\mathit{l},\theta)}{\mathit{l}'-\mathit{l}} \ d\mathit{l} + \int_{\mathit{l}'+E}^{\infty} \frac{q(\mathit{l},\theta)}{\mathit{l}'-\mathit{l}} \ d\mathit{l} \right]$$

and

3) where Bt is the back projection operator. It is a function of two polar variables whose value at any point (r,ϕ) is defined by

$$[Bt](r,\phi) = \int_{0}^{\pi} t\left(r \ \cos\left(\theta - \phi\right), \ \theta\right) d\theta$$

From figure II.11, it can be seen that the value at any point (r,ϕ), the back-projection of a function t can be obtained by integrating t on a segment (from t=0 to t=π) of the curve described

in that figure.

Combining all the equations, one gets that for a function p of two variables and for any point (r,ϕ)

$$[BHzDzp](r,\phi) = -\frac{1}{\pi} \int_0^\pi \int_{-\infty}^\infty \frac{p_1(l,\theta)}{r\cos(\theta-\phi) - l} \, dl \, d\theta$$

$$[BHzDzp](r,\phi) = -\frac{1}{\pi} \int_0^\pi \int_{-\infty}^\infty \frac{p_1(l,\theta)}{r\cos(\theta-\phi) - l} \, dl \, d\theta$$

```
10 ** .................................... **
10 **                                      **
20 **              APPENDIX B              **
40 **                                      **
50 ** PROGRAM T  FILTER PROJECTION         **
60 ** DATA USING RAM-LAK FILTER            **
70 ** AND BACK-PROJECT FOR 40X40 GRID**    **
80 **                                      **
90 **************************************
100 ** APPLICATION OF RAM_LAK FILTER **
110 big1=-1000
120 big2=-1000
130 small=100
140 input"NAME OF DATA STORAGE FILE",name1
150 input"FILE NAME FOR DATA STORAGE",name2$
160 open name1 for input as file #1
170 dim stp(2100), correct(2110)
180 for r=0 to 39
190 for t=(r*50)+1 to (r*50)+5
200 stp(t)=0
210 next t
220 for t=(r*50)+46 to (r*50)+50
230 stp(t)=0
240 next t
250 for t=(r*50)+6 to (r*50)+45
260 input#1,stp(t)
270 stp(t)=-log(((10-stp(T))/10)
280 if stp(t) big1 then big1=stp(t)
290 next t
300 next r
310 close#1
320 for r= 0 to 39
330 for k=(r*50)+6 to (r*50)+45
340 corrct(k)=stp(k)*.25-((stp(k-1)*.101)+(stp(l+1)*.101))-((stp(k-3)*.0112)
350 next k
360 next r
370 open name2$ for output as file#2
380 for j%=0 to 39
390 forn%=(j%*50)+6 to (j%*50)+45
400 print#2,corrct(n%)
410 next n%
420 next j%
430 close#2
440 ** BACK-PROJECTION PROGRAM FOR 40X40 PIXELS **
450 input "DATA FILE NAME",name$
460 input "RECONSTRUCTED IMAGE FILE NAME",name2$
470 dim lambda(40,40), f(80,80),a(80)
480 big=0
490 small=100
500 open name$ for input as file#1
510 for  r%= 0 to 39
520 for s%=1 to 40
530 input #1,lambda(s%,r%)
540 next s%
550 next r%
560 close#1
570 theta=pi/40
580 for r%=0 to 39
590 phi=r%*theta
600 cosphi=cos(phi)
610 tanphi=tan(phi)
620 if r%=20 then gosub 500
630 if r%=20 then goto 340
640 range=abs(0.5/cosphi)
650 if range>40 then range=40
660 for s=1 to 80
670 cept=(40.5-s)/cosphi
680 for x=-39.5 to 39.5
690 y=(x*tanphi)+cept
700 k%=41+int(x)
710 jc=41-y
720 if jc>87 or jc<-7 then goto 320
730 for j%=jc-range to jc+range
740 if j%<=0 or j% 80 then goto 310
750 s%=int((s+1)/2)
760 f(k%,J%)=f(k%,J%)+lambda(s%,r%)
770 if f(k%,J%) big then big=f(k%,J%)
780 if f(k%,J%) small then small=f(k%,J%)
790 next j%
800 next x
810 next s
820 print r%
830 next r%
840 open name2$ for output as file #2
850 for K%= 1 to 80
860 for j%= 1 to 80
870 print#2,f(k%,j%)
880 next j%
890 next k%
900 close#2
910 goto 700
920 for s= 1 to 80
930 k%=s
940 for j%= 1 to 80
950 s%=int((s+1)/2)
960 f(k%,J%)=f(k%,J%)+lambda(s%,r%)
970 if f(k%,J%)>big then big=f(k%,J%)
980 if f(k%,J%)<small then small=f(k%,J%)
990 next j%
1000 next s
1010 return
```

```
10 **********************************************
20 **                                          **
30 **              APPENDIX C                   **
40 **                                          **
50 **     PROGRAM TO CALCULATE ANALYTE         **
60 **      EQUIVALENT THICKNESSES BY           **
70 **    EXTRAPOLATION TO THE ANALYTE          **
80 **           ABSORPTION EDGE                **
90 **                                          **
100 **********************************************
110 dim a(1600),b(1600),c(1600),d(1600),e(1600)
120 mxm1=0\mxm2=0\mxm3=0\mxm4=0
130 input "input data file name$", name$
140 input "output data file name$", name1$
150 for nm=1 to 4
160name$=name$+str$(nm)+".dat"
170 open name$ for input as file#1
180 for t=1 to 1600
190 input#1,ct
200 if nm=1 then a(t)=ct
210 if nm=2 then b(t)=ct
220 if nm=3 then c(t)=ct
230 if nm=4 then d(t)=ct
240 if a(t)>mxm1 then mxm1=a(t)
250 if b(t)>mxm2 then mxm2=b(t)
260 if c(t)>mxm3 then mxm3=c(t)
270 if d(t)>mxm4 then mxm4=d(t)
280 next t
290 close#1
300 next nm
310 for an=1 to 1600
320 !calculate the projection value for each ROI.
330 lm1=log(mxm1/a(an))
340 lm2=log(mxm2/b(an))
350 lm3=log(mxm3/c(an))
360 lm4=log(mxm4/c(an))
370 ! calculate the slopes
380 slope1=(lm2-lm1)/.5
390 slope2=(lm4-lm3)/.5
400 !calculate the lower and higher extrapolation values.
410 yl=(slope*-.35)+lm2
420 yh=(slope2*.37)+lm3
430 !calculate the analyte equivalent thicknesses.
440 e(an)=(yh-yl)/4.9
450 print e(an),yh,yl
460 next an
470 !save analyte equivalent thicknesses
480 open name1$+".dat" for output as file#1
490 for t=1 to 1600
500 print#1,e(t)
510 next t
520 close#1
```

193

```
  10 ***********************************
  20 **                              **
  30 ** DISPLAYS RECONSTRUCTED IMAGE **
  40 ** IN COLOUR OR IN GREY SCALE   **
  50 ** FOR RANDOM ACCESS FILES      **
  60 ***********************************
  70 REM *in colour or or grey scale. *
  80 REM *For Random Access Files*
  90 REM Define grey shades
 100 *SHADOW
 110 DIM A(40,40):MAX=255:PIXEL=0.002
 120 STP%=16::S%=1::F%=40:JS%=1:JF%=40:LL%=0:JL%=80
 130 VDU23,248,255,255,255,255,255,255,255,255
 140 MODE7
 150 PRINTTAB(6,10 "COLOUR";CHR$(131);"C";CHR$ (35 ;" OR B/W";CHR$(131);"B";CHR$
 135 ;:0$=GET$
 160 IF Q$<>"C" AND Q$<>"B" THEN 140
 170 IF Q$="C" THEN CODE=0 ELSE CODE=1
 180 MODE7
 190 *.
 200 MAX=255:RESTORE
 210 INPUT'FILE NAME (*. Catalog: ",NAME$
 220 IF NAME$="*." THEN GOTO 300
 230 *.
 240 GOTO 210
 250 PRINTTAB(8)CHR$(130);"**********";CHR$(135)
 260 INPUT"HEADING1 ",HEAD1$
 270 IF LEN(HEAD1$) 11 THEN 260
 280 INPUT"HEADING2",HEAD2$
 290 IF LEN(HEAD2$) 11 THEN 280
 300 CLS
 310 VDU23;8202;0;0;0;
 320 PRINTTAB(0,10)CHR$(136);CHR$(131);CHR$(157);CHR$(132);"    LOADING FILE "
;NAME$
 330 ** INPUT IMAGE DATA  **
 340 X=OPENIN NAME$
 350 INPUT#X,max
 360 FOR J%=1 TO 40
 370 FOR K%=1 TO 40
 380 NUM=BGET#X
 390 A(K%,J%)=NUM
 400 NEXT K%
 410 NEXT J%
 420 CLOSE#X
 430 ** PROCESS IMAGE DATA **
 440 PRINTTAB(0,10)CHR$(136);CHR$(132);CHR$(157);CHR$(131);"  PROCESSING DATA"
 450 Factor=80/MAX
 460 FOR J%=1 TO 40
 470 FOR K%=1 TO 40
 480 A(K%,J%)=A(K%,J%)*Factor-.001
 490 NEXT K%
 500 NEXT J%
 510 MODE2:PRINTTAB(1,5)
 520  VDU23;8202;0;0;0;
 530 VDU5
 540 ** DETERMINE PIXEL DISPLAY COLOUR **
 550 PROCSHOWCODE
 560 PROCSCALES
 570 PROCINFO
 580 FOR J%=JS% TO JF%
 590 FOR K%=KS% TO KF%
 600 PROCGETA
 610 IF CODE=0 THEN PROCSELECTCOL(A) ELSE PROCSELECTSHADE(A)
 620 GCOL 0,HUE
 630 MOVE((K%-KS%)*STP%)+352,900-((J%-JS%)*STP%):PRINT CHR$(248)
 640 NEXT K%
 650 GCOL0,0:MOVE((K%-KS%)*STP%)+352,900-((J%-JS%)*STP%):PRINT CHR$(248)
 660 VDU13
 670 NEXT J%
 680 GCOL0,0
 690 FOR K%=KS% TO KF%
 700 MOVE((K%-KS%)*STP%)+352,900-((J%-JS%)*STP%):PRINT CHR$(248)
 710 NEXT K%
 720 GCOL0,7
 730 VDU4
 740 KSO%=KS%:COLOUR12:PRINTTAB(3,5)STR$(KS%):COLOUR7:INPUTTAB(0,5)"KS",KS$:KS%
=VAL(KS$):IF KS%=0 THEN KS%=KSO%
 750 PRINTTAB(3,5)STR$(KS%);:IF KS%<10 THEN PRINT" "
 760 IF KS$="N" THEN 180
 770 KFO%=KF%:COLOUR12:PRINTTAB(3,7)STR$(KF%):COLOUR7:INPUTTAB(0,7)"KF",KF$:KF%
=VAL(KF$):IF KF%=0 THEN KF%=KFO%
 780 IF KF$="N" THEN 180
 790 PRINTTAB(3,7)STR$(KF%);:IF KF%<10 THEN PRINT" "
 800 IF KF$="N" THEN 180
 810 JSO%=JS%:COLOUR12:PRINTTAB(3,9)STR$(JS%):COLOUR7:INPUTTAB(0,9)"JS",JS$:JS%
=VAL(JS$):IF JS%=0 THEN JS%=JSO%
 820 PRINTTAB(3,9)STR$(JS%);:IF JS%<10 THEN PRINT" "
 830 IF JS$="N" THEN 180
 840 JFO%=JF%:COLOUR12:PRINTTAB(3,11)STR$(JF%):COLOUR7:INPUTTAB(0,11)"JF",JF$:J
F%=VAL(JF$):IF JF%=0 THEN JF%=JFO%
 850 PRINTTAB(3,11)STR$(JF%);:IF JF%<10 THEN PRINT" "
 860 IF JF$="N" THEN 180
 870 IF KF%-KS%>20 OR JF%-JS% 20 THEN STP%=16 ELSE STP%=32
```

```
 880 COLOUR1:GCOL0,3:PRINTTAB(7,13)STR$(LL%):COLOUR7:INPUTTAB(0,13)"LL",LL$:
     IF LL$="" THEN LL%=LL% ELSE LL%=VAL(LL$)
 890 PRINTTAB(7,13)STR$(LL%);:IF LL%<10 THEN PRINT
 900   IF LL$="N" THEN 180
 910 ULO%=UL%:COLOUR1:PRINTTAB(7,15)STR$(UL%):COLOUR7:INPUTTAB(0,15)"UL",UL$:I
 FUL$="" THEN UL%=ULO% ELSE UL%=VAL(UL$)
 920 PRINTTAB(7,15)STR$(UL%);;:IF UL%<10 THEN PRINT" "
 930   IF UL$="N" THEN 180
 940 GOTO 510
 950 END
 960 ** DEFINE DISPLAY HUES **
 970 DEF PROCSELECTCOL(CLR)
 980   IF CLR<=80 AND CLR>70 THEN HUE=7
 990   IF CLR<=70 AND CLR>60 THEN HUE=1
1000   IF CLR<=60 AND CLR>50 THEN HUE=5
1010   IF CLR<=50 AND CLR>40 THEN HUE=3
1020   IF CLR<=40 AND CLR>30 THEN HUE=2
1030   IF CLR<=30 AND CLR>20 THEN HUE=6
1040   IF CLR<=20 AND CLR>0 THEN HUE=4
1050   IF CLR<0 OR CLR>80 THEN HUE=0
1060 ENDPROC
1070 **  DEFINE DISPLAY PIXEL SHADES **
1080 DEF PROCSELECTSHADE(CLR)
1090   IF CLR<=80 AND CLR>70 THEN HUE=7
1100   IF CLR<=70 AND CLR>60 THEN HUE=3
1110   IF CLR<=60 AND CLR>50 THEN HUE=6
1120   IF CLR<=50 AND CLR>40 THEN HUE=2
1130   IF CLR<=40 AND CLR>30 THEN HUE=5
1140   IF CLR<=30 AND CLR>20 THEN HUE=1
1150   IF CLR<=20 AND CLR>0 THEN HUE=4
1160 IF CLR<0 OR CLR>80 THEN HUE=0
1170 ENDPROC
1180 DEF PROCGETA
1190 FACTOR2=80/(UL%-LL%)
1200 A=(A(K%,J%)-LL%)*FACTOR2
1210 ENDPROC
1220 DEF PROCSHOWCODE
1230 FOR V%=5 TO 75 STEP 10
1240 IF CODE=0 THEN PROCSELECTCOL(V%) ELSE PROCSELECTSHADE(V%)
1250 GCOL0,HUE
1260 MOVE1168,800-V%*32/10:PRINTCHR$(248):GCOL0,0:MOVE1208,800-V%*32/10:PRINTCH
R$(248)
1270 NEXT V%
1280 GCOL0,7
1290 MOVE1130,850:PRINTSTR$(LL%):MOVE1130,500:PRINTSTR$(UL%)
1300 ENDPROC
1310 DEF PROCENDLINE
1320 IF KT%=0 THEN 1340
1330 PRINTCHR$(248);CHR$(248)
1340 ENDPROC
1350 DEF PROCSCALES
1360 FOR J%=JS% TO JF%
1370 IF J%/10=INT(J%/10) THEN GCOL0,1 ELSE GCOL0,3
1380 MOVE340,900-((J%-JS%+1)*STP%):DRAW345,900-((J%-JS%+1)*STP%)
1390 NEXTJ%
1400 FOR K%=KS% TO KF%
1410 IF K%/10=INT(K%/10) THEN GCOL0,1 ELSE GCOL0,3
1420 MOVE((K%-KS%+1)*STP%)+352,905:DRAW((K%-KS%+1)*STP%)+352,920
1430 NEXT K%
1440 ENDPROC
1450 ** CHOOSE SECTION OF IMAGE FOR DISPLAY **
1460 DEF PROCINFO
1470 GCOL 0,7
1480 VDU4
1490 PRINTTAB(0,5)"KS?";KS%
1500 PRINTTAB(0,7)"KF?";KF%
1510 PRINTTAB(0,9)"JS?";JS%
1520 PRINTTAB(0,11)"JF?";JF%
1530 PRINTTAB(0,13)"LL?";LL%
1540 PRINTTAB(0,15)"UL?";UL%
1550 COLOUR 3:PRINTTAB(0,18)"NEW N"
1560 VDU5
1570 ENDPROC
```

```
   10 *******************************************
   20 **              APPENDIX E                **
   70 **                                        **
   40 ** PROGRAM TO CALCULATE DUMMY DATA **
   50 **      FOR TWO SMALL CYLINDRICAL         **
   60 **              PHANTOMS                   **
   70 **                                        **
   80 *******************************************
   90 DIM teqth(40,40)
  100 ** PHANTOMS ARE 3X3 PIXELS AND ARE CENTRED AT F=15,J=8 AND F=33,J=29 IN 1
E RECONSTRUCTION GRID **
  110 ** THE SCAN PROFILES ARE CREATED BY DETERMINING WHICH BEAM PATHS OVERLAF
HE OBJECT PIXELS. **
  120 ** THIS PROGRAM IS BASED ON BACK-PROJECTION **
  130 FO=15\JO=8
  140 FOO=33\JOO=29
  150 A%=0
  160 ** THE SAME PROCESS IS REPEATED FOR ROTATIONS GREATER THAN 90DEGREES **
  170 FOR W%=0 TO 1
  180 FOR R%=0 TO 19
  190 if W%=0 then RR%=R%
  200 if W%=1 then RR%=R%+20
  210 THETA=PI*R%/40
  220 FOR S%= 1 TO 40
  230 TOTH=0
  240 SLOPE1=TAN(THETA)
  250 IF SLOPE1<0 THEN SLOPE1=-SLOPE1
  260 CEPTA=(21-S)/COS(THETA)
  270 IF COS(THETA)<0 THEN CEPTA=-CEPTA
  280 CEPTB=(20-S%)/COS(THETA)
  290 IF COS(THETA)<0 THEN CEPTB=-CEPTB
  300 FOR K%=1 TO 40
  310 FOR J%=1 TO 40
  320 if W%=0 then KK%=K%
  330 if W%=1 then KK%=J%
  340 if W%=0 then JJ%=J%
  350 if W%=1 then JJ%=41-K%
  360 XP=(K%-21)
  370 YP=(20-J%)
  380 IF YP>SLOPE1*XP+CEPTA AND YP>SLOPE1*(XP+1)+CEPTA THEN GOTO 820
  390 IF YP+1<SLOPE1*XP+CEPTB AND YP+1<SLOPE1*(XP+1)+CEPTB THEN GOTO 820
  400 AREA=0
  410 FOR X=XP+0.01 TO XP+0.99 STEP 0.02
  420 CORTOP=0
  430 CORBOT=0
  440 YA=SLOPE1*X+CEPTA
  450 YB=SLOPE1*X+CEPTB
  460 IF YA>YP+1 AND YB<YP+1 THEN CORTOP =0
  470 IF YA<=YP+1 AND YA>=YP THEN CORTOP=(YP+1-YA)*0.02
  480 IF YB>=YP AND YB<=YP+1 THEN CORBOT=(YB-YP)*0.02
  490 IF YB<YP AND YA>YP THEN CORBOT=0
  500 SLICEAREA=0.02-CORTOP-CORBOT
  510 IF YB>YP+1 THEN SLICEAREA=0
  520 IF YA<YP THEN SLICEAREA=0
  530 AREA=AREA+SLICEAREA
  540 SLICEAREA=0
  550 NEXT X
  560 IF AREA=0 THEN GOTO 820
  570 conc=0
  580 ** THE OBJECTS HAVE CONCENTRATION EQUAL TO ONE, THE BACKGROUND HAS CONCENT
RATION EQUAL TO ZERO **
  590 if KK%=KO-1 and JJ%=JO then conc=1
  600 if KK%=KO-1 and JJ%=JO-1 then conc=1
  610 if KK%=KO-1 and JJ%=JO+1 then conc=1
  620 if KK%=KO and JJ%=JO-1 then conc=1
  630 if KK%=KO and JJ%=JO then conc=1
  640 if KK%=KO and JJ%=JO+1 then conc=1
  650 if KK%=KO+1 and JJ%=JO-1 then conc=1
  660 if KK%=KO+1 and JJ%=JO then conc=1
  670 if KK%=KO+1 and JJ%=JO+1 then conc=1
  680 if KK%=KOO-1 and JJ%=JOO-1 then conc=1
  690 if KK%=KOO-1 and JJ%=JOO then conc=1
  700 if KK%=KOO-1 and JJ%=JOO+1 then conc=1
  710 if KK%=KOO and JJ%=JOO-1 then conc=1
  720 if KK%=KOO and JJ%=JOO then conc=1
  730 if KK%=KOO and JJ%=JOO+1 then conc=1
  740 if KK%=KOO+1 and JJ%=JOO+1 then conc=1
  750 if KK%=KOO+1 and JJ%=JOO then conc=1
```

```
760 if FF%=FOO+1 and JJ%=JOO-1 then conc=1
770 PRINT conc
780 OTH=AREA*conc
790 conc=0
800 TDOTH=TDOTH+OTH
810 OTH=0
820 NEXT J%
830 NEXT K%
840 teqth(S%,RR%)=TDOTH
850 rem IF teqth(S%,RR%)=0 THEN teqth(S%,RR%)=1
860 print S%,RR%,teqth(S%,RR%)
870 TDOTH=0
880 OTH=0\AREA=0\conc=0
890 NEXT S%
900 PRINT R%
910 NEXT R%
920 NEXT W%
930 'Save Areas to File
940 OPEN "point40.DAT" FOR OUTPUT AS FILE #1
950 FOR R%=0 to 39
960 for S%=1 to 40
970 PRINT #1,teqth(S%,R%)
980 NEXT S%
990 NEXT R%
1000 CLOSE #1
1010 END
```

197

```
10 ****************************************
20 **                                   **
30 **          APPENDIX F1              **
40 **                                   **
50 **     PROGRAM TO CALCULATE THE      **
60 **  X-RAY BEAM AND PIXEL OVERLAP     **
70 **  AREAS FOR 40x40 PIXEL GRID       **
80 **                                   **
90 ****************************************
100 OPEN "AREA40.DAT" FOR OUTPUT AS FILE #1
110 ** FOR EACH BEAM THE SLOPE WITH RESPERCT TO THE FIRST BEAM IS CALCULATED *
*
120 A%=0
130 FOR W%=0 TO 1
140 FOR R%=0 TO 19
150 THETA=PI*R%/40
160 FOR S%= 1 TO 40
170 SLOPE=TAN(THETA)
180 IF SLOPE 0 THEN SLOPE=-SLOPE
190 CEPTA=(21-S%)/COS(THETA)
200 IF COS(THETA)<0 THEN CEPTA=-CEPTA
210 CEPTB=(20-S%)/COS(THETA)
220 IF COS(THETA)<0 THEN CEPTB=-CEPTB
230 FOR K%=1 TO 40
240 FOR J%=1 TO 40
250 XP=(K%-21)
260 YP=(20-J%)
270 IF YP>SLOPE*XP+CEPTA AND YP SLOPE*(XP+1)+CEPTA THEN GOTO 520
280 IF YP+1 SLOPE*XP+CEPTB AND YP+1 SLOPE*(XP+1)+CEPTB THEN GOTO 520
290 AREA=0
300 FOR X=XP+0.01 TO XP+0.99 STEP 0.02
310 ** EACH PIXEL IS DIVIDED INTO 50 SLICES **
320 CORTOP=0
330 CORBOT=0
340 YA=SLOPE*X+CEPTA
350 YB=SLOPE*X+CEPTB
360 IF YA>YP+1 AND YB<YP+1 THEN CORTOP =0
370 IF YA<=YP+1 AND YA>=YP THEN CORTOP=(YP+1-YA)*0.02
380 IF YB>=YP AND YB<=YP+1 THEN CORBOT=(YB-YP)*0.02
390 IF YB<YP AND YA>YP THEN CORBOT=0
400 SLICEAREA=0.02-CORTOP-CORBOT
410 IF YB>YP+1 THEN SLICEAREA=0
420 IF YA<YP THEN SLICEAREA=0
430 ** THE OVERLAPPED SLICES ARE SUMMED **
440 AREA=AREA+SLICEAREA
450 NEXT X
460 IF AREA =0 THEN GOTO 520
470 ** THE PROCESS IS SIMILAR FOR SLOPES GREATER THAN 90 DEGREES **
480 IF W%=0 THEN AREA$=STR$(AREA)+","+STR$(K%)+","+STR$(J%)+","+STR$(S%)+","+S
TR
490 IF W%=1 THEN AREA$=STR$(AREA)+","+STR$(J%)+","+STR$(41-K%)+","+STR$(S%)+",
"+
500 PRINT #1,AREA$
510 A%=A%+1
520 NEXT J%
530 NEXT K%
540 NEXT S%
550 PRINT R%
560 NEXT R%
570 NEXT W%
580 PRINT #1,"100,1,1,1,1"
590 CLOSE #1
600 END
```

198

```
10 ******************************************
20 **                                      **
30 **            APPENDIX F2               **
40 **                                      **
50 **      PROGRAM ON VAX11 75 TO          **
60 **    RECONSTRUCT IMAGES USING THE      **
70 **      ALGEBRAIC RECONSTRUCTION        **
80 **    TECHNIQUE FOR 40X40 PIXELS        **
90 **                                      **
100 ******************************************
110 dim area$(160),f(40,40),lambda(40,40)
120 all=0
130 open name1$ for input as file #1
140 print 'opening file'
150 for r=0 to 39
160 for s=1 to 40
170 input#1,x
180 lambda(s,r)=x
190 all=all+x
200 next s
210 next r
220 close #1
230 all=all/64000\print"average=",all
240 for j=1 to 40
250 for k=1 to 40
260 f(k,j)=all
270 next k
280 next j
290 times=1\ t1=20
300 until times=t1
310 a=0 s1=1\r1=0\sum1=0\sum2=0
320 open"area40.dat" for input as file #1
330 input #1,v,k,j,s,r
340 a$=str$(v)+","+str$(k)+","+str$(j)+","+str$(s)+","+str$(r)
350 if s=s1 and r=r1 then gosub 400 else gosub 450
360 if a$>"100,1,1,1,1" then goto 330 else gosub 580
370 times=times+1
380 next
390 stop
400 gosub 620
410 gosub 800
420 area$(a)=a$
430 a=a+1
440 return
450 c$=a$
460 gosub 840
470 for a=0 to 160
480 area$(a)=" "
490 next a
500 a$=c$
510 gosub 620\ !decode a$
520 if a$="100,1,1,1,1" then return
530 s1=s\r1=r\a=0\sum1=0\sum2=0
540 gosub 800
550 area(a$)=a$
560 a=a+1
570 return
580 close #1
590 gosub 1020
600 gosub 910
610 return
620 !DECODE AREAS
630 p1com=0\p2com=0\p3com=0\p4com=0\h=0
640 for i=1 to len(a$)
650 b$=mid$(a$,i,1)
660 if b$="," then gosub 740
670 next i
680 k=val(mid$(a$,p1com+1,p2com-p1com-1))
690 j=val(mid$(a$,p2com+1,p3com-p2com-1))
700 s=val(mid$(a$,p3com+1,p4com-p3com-1))
710 r=val(mid$(a$,p4com+1,len(a$)-p4com))
720 w=val(mid$(a$,1,p1com-1))
730 return
740 if h=1 then p1com=i
750 if h=2 then p2com=i
760 if h=3 then p3com=i
770 if h=4 then p4com=i
780 h=h+1
790 return
800 'sum the concentrations
810 if a$<"100,1,1,1,1" then sum1=sum1+(w*f(k,j))
820 if a$<"100,1,1,1,1" then sum2=sum1+(w 2)
830 return
840 'correct the f values
850 for z =0 to a-1
860 a$=area$(z)
870 gosub 620 \!decode areas
880 f(k,j)=f(k,j)+0.2*w*(lambda(s1,r1)-sum1)/sum2
890 next z
900 return
```

199

```
910 'save the image to file
920 name$="imageFILENAME"+str$(titres)+".dat"
930 open name$ for output as file #1
940 for j=1 to 40
950 for i=1 to 40
960 print #1,f(i,j)
970 next i
980 next j
990 print#1,"sigma=",standev
995 close #1
1010 return
1020 mean=0
1030 for i=1 to 40
1040 for j=1 to 40
1050 mean=mean+f(i,j)
1060 next j
1070 next i
1080 mean=mean/1600
1090 diff=0
1100 for k=1 to 40
1110 for j=1 to 40
1120 diff=diff+(f(k,j)-mean)^2
1130 next j
1140 next k
1150 standev=sqr(diff/40
1160 if abs(oldstandev-standev)>oldstanev/100 then stop
1190 return
```

200

```
10 *********************************
20 **          APPENDIX 3           **
30 **                               **
40 ** PROGRAM TO CONTROL SCAN TABLE **
50 ** AND TO COLLECT PHOTON COUNTS  **
60 **    WHEN USING THE SR7 AND      **
70 **     RADIOISOTOPE SOURCES       **
80 **                               **
90 *********************************
100 *FX7,4
110 ** PROGRAM CONTROL PROCEDURES    **
120 PROCCENTRESTEPPER
130 PROCCENTREANGLE
140 PROCQUESTIONS
150 PROCSETZERO
160 PROCDEFINE
170 PROCASSEMB
180 PROCPOINTERS
190 REPEAT
200 SCANNUM%=0
210 REPEAT
220 JUMP%=0
230 PROCSCAN1
240 FAN= RESULT%(1):KBN=RESULT%(3)
250 PROCCONCENTRATIONS
260 PROCSCAN
270 PROCSAVEDATA
280 PROCRETURN
290 SCANNUM%=SCANNUM%+1
300 UNTIL SCANNUM%=24
310 END
320 ** INPUT AND DEFINE CONTROL VARIABLES **
330 DEF PROCDEFINE
340 OSBYTE=&FFF4
350 M=22405:NUMCHR=M-1:STORE=M-2:BREAK=M-3:?BREAK=0:?NUMCHR=&79:SCANNUM%=0
360 DIM REG%(7):DIM WHERE%(5):DIM HOWMANY%(5):DIM RESULT%(4):DIM EQUIVTHICK(SC
ANSIZE%)
370 DIM AA$(7):DIM SCA(23):DIM SCB(23)
380 ENDPROC
390 ** ASSEMBLY PROGRAM TO INTERPRET COUNT DATA FROM SR7 **
400 DEF PROCASSEMB
410 FOR N=0 TO 2 STEP 2
420 P%=22255
430[OPT N
440 .RS423    LDA#00
450           STA BREAK
460           STA STORE
470 .INIT     LDX #01
480           LDA #02
490           JSR OSBYTE
500 .LOOP     LDA#145
510           LDX #0
520           LDY #00
530           JSR OSBYTE
540           CPY #83
550           BEQ ESC
560           LDX #254
570           LDA #128
580           JSR OSBYTE
590           CPX #00
600           BEQ LOOP
610           LDX #01
620           LDA #145
630           JSR OSBYTE
640           LDX STORE
650           TYA
660           STA M,X
670           INX
680           STX STORE
690           CPX NUMCHR
700           BEQ QUIT
710           JMP INIT
720 .ESC      LDA #01
730           STA BREAK
740 .QUIT     LDX #00
750           LDA #02
760           JSR OSBYTE
770           RTS
780]
790 NEXT N
800 ENDPROC
810 ** PROCEDURE TO CENTRE STEPPER MOTOR **
820 DEF PROCCENTRESTEPPER
830 *FX4,1
840 CLS
850 PRINT "USE EDIT KEYS TO POSITION SCAN"
860 PRINT "SMALL STEP FORWARD",  CHR$(93)
870 PRINT"SMALL STEP BACKWARDS",  CHR$(91)
880 PRINT "          (QUIT)",     "Q"
890 Q$=GET$
900 IF Q$<>CHR$(&88) AND Q$<>CHR$(&89) AND Q$<>"Q" THEN GOTO 840
910 IF Q$="Q" THEN GOTO 960
920 IF Q$=CHR$(&89) THEN DIR=0 ELSE DIR=2
930 PROCSTEPPER(5)
940 *FX21,0
```

```
950 GOTO 840
960 *FX4,0
970 ENDPROC
980 ** PROCEDURE TO SET ROTATION STEPPER MOTOR AT START POSITION **
990 DEF PROCCENTREANGLE
1000 *FX4,1
1010 CLS
1020 PRINT "USE EDIT KEYS TO ROTATE MOTOR"
1030 PRINT "CLOCKWISE ROTATION",CHR$(9)
1040 PRINT "ANTICLOCKWISE ROTATION",CHR$(9)
1050 PRINT "           (QUIT)  ",   "Q"
1060 Q$=GET$
1070 IF Q$ <> CHR$(&8B) AND Q$ <> CHR$(&89) AND Q$ <> "Q" THEN GOTO 1010
1080 IF Q$="Q" THEN GOTO 1130
1090 IF Q$=CHR$(&89) THEN DIR=0 ELSE DIR=2
1100 PROCANGLE(0)
1110 *FX21,0
1120 GOTO 1010
1130 *FX 4,0
1140 ENDPROC
1150 DEF PROCPOINTERS
1160 RESTORE 1210
1170 FOR I%= 0 TO 4
1180 READ WHERE%(I%),HOWMANY%(I%)
1190 NEXT I%
1200 ENDPROC
1210 DATA 39,6,58,7,71,10,91,7,104,10
1220 ** STEP CONTROL PROCEDURE **
1230 DEFPROCSTEPPER(S)
1240 PROCINITIALISE
1250 PROCSTEP(S)
1260 ENDPROC
1270 ** ROTATION CONTROL PROCEDURE **
1280 DEFPROCANGLE(S)
1290 PROCINITIALISE
1300 PROCROTATE(S)
1310 ENDPROC
1320 DEF PROCINITIALISE
1330 PA=64704:AC=PA+1:PB=PA+2:BC=PA+3
1340 ?AC=0:?BC=0:?PA=207:?PB=255
1350 ?AC=4:?BC=4:?PA=0:?PB=0
1360 ENDPROC
1370 DEFPROCROTATE(S)
1380 ?PA=1
1390 FOR I%= 0 TO S
1400 ?PB=1+(DIR*3/2):?PB=0+DIR
1410 FOR DELAY=0 TO 50:NEXT DELAY
1420 NEXT I%
1430 ?PA=0
1440 ENDPROC
1450 , ** STEP PROCEDURE **
1460 DEF PROCSTEP(S)
1470 ?PA=2
1480 FOR F%= 0 TO S
1490 ?PB=4+(DIR*2):?PB=0+DIR
1500 FOR DELAY = 0 TO 50:NEXT DELAY
1510 NEXT F%
1520 ?PA=0
1530 ENDPROC
1540 DEF PROCQUESTIONS
1550 CLS:INPUT"HOW MANY SCAN STEPS",SCANSIZE%
1560 ENDPROC
1570 DEFPROCSETZERO
1580 CLS:PRINT "SCAN MOVING TO STARTING POSITION"
1590 S=47 :DIR=0
1600 FOR J=0 TO SCANSIZE%+1
1610 PROCSTEPPER(S)
1620 NEXT J
1630 S=47:DIR=2
1640 FOR K=0 TO 2
1650 PROCSTEPPER(S)
1660 NEXT K
1670 ENDPROC
1680 DEF PROCSCAN
1690 IF SCANSIZE%=1 THEN  GOTO 1790
1700 S=95:DIR=2
1710 FOR L= 2 TO SCANSIZE%
1720 PROCSTEPPER(S)
1730 PRINT "START DATA TRANSFER"
1740 PROCCOUNT
1750 JUMP%=JUMP%+1
1760 PROCCONCENTRATIONS
1770 FOR G%= 1 TO 1000:NEXT G%
1780 NEXT L
1790 ENDPROC
1800 DEF PROCRETURN
1810 S=95:DIR=0
1820 FOR V= 1  TO SCANSIZE%+1
1830 PROCSTEPPER(S)
1840 NEXT V
1850 S=95:DIR=2
1860 FOR N=1 TO 2
1870 PROCSTEPPER(S)
1880 NEXT N
```

202

```
1890 DIM=...PROCANGLE 0
1900 ENDPROC
1910 DEF PROCSCAN1
1920 CLS :PRINT "START SR-7 COUNTER
1930 IF TIME 17000 THEN GOTO 1930
1940 PROCCOUNT
1950 ENDPROC
1960 DEF PROCCOUNT
1970 PRINT "TRANSFER ...
1980 CALL RS423
1990 K%=0
2000 FOR I%=0 TO 4
2010 A$=""
2020 FOR J%= 0 TO HOWMANY%...
2030 A$=A$+CHR$(...M=WHERE%...J%...
2040 NEXT J%
2050 IF I%=0 THEN CTT=VAL A$
2060 RESULT%(I%)=VAL A$
2070 K%=K%+1
2080 NEXT I%
2090 ENDPROC
2100 DEF PROCCONCENTRATIONS
2110 KAC=RESULT%(1):KBC=RESULT%(3)
2120 SCA(JUMP%)=RESULT% 1 :SCB(JUMP%)=RESULT%(3)
2130 PRINT"Step number= ";JUMP%
2140 PRINT"Scan Angle= ";SCANNUM%*7.5"degrees"
2150 PRINT "KAC=";KAC,    "KBC=";KBC
2160 HI=5.9:LO=1.3
2170 EQUIVTHICK(JUMP%)=(LN((KAC*BN)/(KBC*KAN)))/(HI-LO)
2180 PRINT "Equivalent Thickness =";EQUIVTHICK(JUMP%;"g/square metre"
2190 FOR T=1 TO 2000:NEXT T
2200 ENDPROC
2210 DEFPROCSAVEDATA
2220 TIME=0
2230 NAMES$= "DATA"+STR$(SCANNUM%)
2240 X=OPENOUT NAME$
2250 FOR G%=0 TO SCANSIZE%-1
2260 PRINT #X,EQUIVTHICK(G%)
2270 NEXT G%
2280 FOR E%=0 TO SCANSIZE%-1
2290 PRINT #X,SCA(E%)
2300 NEXT E%
2310 FOR D%=0 TO SCANSIZE%-1
2320 PRINT #X,SCB(D%)
2330 NEXT D%
2340 CLOSE#X
2350 ENDPROC
```

```
1.' *********************************
10 **          APPENDIX H            **
20 **                                **
40 ** PROGRAM TO CONTROL THE SCAN    **
50 ** TABLE AND THE DATA COLLECTION  **
60 ** WHEN USING THE MULTI-CHANNEL   **
70 ** ANALYSER AND X-RAY TUBE.       **
80 **                                **
90 *********************************
100 CLEAR:CLS
110 ** CONTROL PROCEDURE **
120 PROCLOADDATA
130 DIM COUNT1(5,2,NUMSTEPS):DIM STORE(8,NUMSTEPS):REF=-1
140 PROCVARIABLES
150 PROCASSEMB
160 PROCsetup
170 PROCSETPHA
180 PROCSETIO
190 VDU3
200 PROCSCAN
210 PROCRETURN
220 CHAIN "REARR"
230 END
240 ** INPUT CONTROL PARAMETERS  **
250 DEF PROCLOADDATA
260 X=OPENIN"NUMBERS"
270 INPUT #X,Z,NUMSTEPS,NUMROTS,SIZESTEP,EMAX,TT%
280 PRINTZ,NUMSTEPS,NUMROTS,SIZESTEP,EMAX,TT%
290 CLOSE#X
300 ENDPROC
310 ** SCAN CONTROL PROCEDURE **
320 DEF PROCSCAN
330 GH=0
340 FOR stp%=0 TO NUMSTEPS-1
350 CLS
360 PRINT"STEP NO",stp%
370 D=124:R=108
380 dir=0
390 FOR ROTAT=0 TO NUMROTS-1
400 PRINT"ROTATION No.",ROTAT
410 S=600/NUMROTS
420 PROCCOUNT
430 PROCTRANSFER
440 PROCINTERPRET
450 PROCROTATE
460 NEXT ROTAT
470  IF GH=1 THEN PROCSAVEDATAX
480 GH=GH+1
490 S=(SIZESTEP*48):D=124:R=108
500 PROCSTEP(S)
510 PROCROTATEBACK
520 NEXT stp%
530 ENDPROC
540 ** PULSE SEQUENCES FOR STEPPER MOTORS   **
550 DEF PROCSTEP(S)
560 B=&FE60
570 ?(B+2)=255
580 FOR X=1 TO S
590 ?B=D
600 Q=TIME+5
610 REPEAT
620 UNTIL TIME>=Q
630 ?B=R
640 Q=TIME+5
650 REPEAT
660 UNTIL TIME>=Q
670 NEXT X
680 ENDPROC
690 ** DATA COLLECTION AND STEP PROCEDURE **
700 DEF PROCSTEPX
710 CLS
720 PRINT TAB(4,2)"angle=";scan%*180/NUMROTS"degrees"
730 PRINT TAB(7,3)"step"
740 PRINT TAB(15,3)"COUNT"
750 FOR step%=1 TO NUMSTEPS
760 S=SIZESTEP*48
770 IF step%=1 AND dir=0 THEN S=(SIZESTEP*48)+1
780 PROCCOUNT
790 PROCSTEP(S)
800 NEXT step%
810 ENDPROC
820 ** DATA STORE AND SORT PROCEDURE **
830 DEF PROCSAVEDATAX
840 REF=REF+1
850 NAME$="DATA"+STR$(stp%-REF)
860 X=OPENOUT NAME$
870 FOR GH=0 TO 1
880 FOR G%=0 TO NUMROTS-1
890 FOR F%=1 TO 5
900 PRINT #X,COUNT1(F%,GH,G%)
910 PRINT COUNT1(F%,GH,G%)
920 NEXT F%
930 NEXT G%
940 NEXT GH
950 CLOSE#X
960 GH=0
970 GOTO 490
```

```
 980 ENDPROC
 990 ** SAMPLE ROTATION PROCEDURE **
1000 DEF PROCROTATE
1010 D=14:R=12
1020 PROCSTEP(S)
1030 ENDPROC
1040 ** DATA SORT PROCEDURE **
1050 DEF PROCINVERT
1060 IF dir=0 THEN 1180
1070 FOR R%= 1 TO NUMSTEPS
1080 FOR OO%=1 TO 5
1090 STORE(OO%,NUMSTEPS-R%+1)=COUNT1(OO%,1,R%)
1100 NEXT OO%
1110 NEXT R%
1120 FOR W%= 1 TO NUMSTEPS
1130 FOR OO%=1 TO 5
1140 COUNT1(OO%,1,W%)=STORE(OO%,W%)
1150 PRINTCOUNT1(OO%,1,W%)
1160 NEXT OO%
1170 NEXT W%
1180 ENDPROC
1190 ** RETURN SCAN TABLE TO SCAN START POSITION **
1200 DEF PROCRETURN
1210 S=500+(±00/NUMROWS)
1220 PROCSTEP(S)
1230 CLS:PRINTTAB(2,12) "Scan Finished and Rotor Angle=0degrees"
1240 ENDPROC
1250 ** MULTI-CHANNEL ANALYSER CONTROL PROCEDURE **
1260 DEF PROCCOUNT
1270 PROCsetup
1280 PROCclear
1290 PROCstartpha
1300 VDU7
1310 TIME=0
1320 REPEAT
1330 UNTIL TIME=1700
1340 ENDPROC
1350 ** TRANSMIT AND INTERPRET DATA FROM MAC **
1360 DEF PROCTRANSFER
1370 PROCsetup
1380 PROCrunio
1390 CALL INIT
1400 ?MEMLOC=00:?(MEMLOC+1)=&48:?STORE=255
1410 VDU3
1420 ENDPROC
1430 DEF PROCsetup
1440 *FX5,2
1450 *FX8,6
1460 *FX7,6
1470 VDU2
1480 VDU1,7
1490 ENDPROC
1500 ** CODES TO CONTROL MAC **
1510 DEF PROCSETPHA
1520 VDU1,67:FOR tt=1 TO 1000:NEXT tt
1530 VDU1,83:FOR tt=1 TO 1000:NEXT tt
1540 VDU1,80:FOR tt=1 TO 1000:NEXT tt
1550 VDU1,78:FOR tt=1 TO 1000:NEXT tt
1560 VDU1,64:FOR tt=1 TO 1000:NEXT tt
1570 VDU1,43:FOR tt=1 TO 1000:NEXT tt
1580 VDU1,78:FOR tt=1 TO 1000:NEXT tt
1590 VDU1,65:FOR tt=1 TO 1000:NEXT tt
1600 VDU1,78:FOR tt=1 TO 1000:NEXT tt
1610 VDU1,90:FOR tt=1 TO 1000:NEXT tt
1620 VDU1,49:FOR tt=1 TO 1000:NEXT tt
1630 VDU1,50:FOR tt=1 TO 1000:NEXT tt
1640 VDU1,78:FOR tt=1 TO 1000:NEXT tt
1650 ENDPROC
1660 DEFPROCSETID
1670 VDU1,67:FOR tt=1 TO 1000:NEXT tt
1680 VDU1,83:FOR tt=1 TO 1000:NEXT tt
1690 VDU1,73:FOR tt=1 TO 1000:NEXT tt
1700 VDU1,78:FOR tt=1 TO 1000:NEXT tt
1710 VDU1,64:FOR tt=1 TO 1000:NEXT tt
1720 VDU1,88:FOR tt=1 TO 1000:NEXT tt
1730 VDU1,78:FOR tt=1 TO 1000:NEXT tt
1740 VDU1,64:FOR tt=1 TO 1000:NEXT tt
1750 VDU1,49:FOR tt=1 TO 1000:NEXT tt
1760 VDU1,78:FOR tt=1 TO 1000:NEXT tt
1770 VDU1,64:FOR tt=1 TO 1000:NEXT tt
1780 VDU1,85:FOR tt=1 TO 1000:NEXT tt
1790 VDU1,78:FOR tt=1 TO 1000:NEXT tt
1800 VDU1,64:FOR tt=1 TO 1000:NEXT tt
1810 VDU1,71:FOR tt=1 TO 1000:NEXT tt
1820 VDU1,78:FOR tt=1 TO 1000:NEXT tt
1830 ENDPROC
1840 DEF PROCclear
1850 VDU1,67:FOR tt=1 TO 1000:NEXT tt
1860 VDU1,48:FOR tt=1 TO 1000:NEXT tt
1870 VDU1,62:FOR tt=1 TO 1000:NEXT tt
1880 VDU1,65:FOR tt=1 TO 1000:NEXT tt
1890 ENDPROC
1900 DEF PROCstartpha
```

```
1910 .DU1,67:FOR tt=1 TO 1000:NEXT tt
1920 VDU1,82:FOR tt=1 TO 1000:NEXT tt
1930 VDU1,80:FOR tt=1 TO 1000:NEXT tt
1940 ENDPROC
1950 DEF PROCrun1a
1960 VDU1,67:FOR tt=1 TO 1000:NEXT tt
1970 VDU1,82:FOR tt=1 TO 1000:NEXT tt
1980 VDU1, run1a tt=1 TO 1000:NEXT tt
1990 VDU3
2000 ENDPROC
2010 DEF PROCINTERPRET
2020 MEM=18705
2030 FOR NUM=1 TO 5
2040 FOR mem=MEM TO MEM+12
2050 IF ?(mem).=48 AND ?(mem).=57 THEN 2060 ELSE 2140
2060 A$=A$+CHR$(?(mem))
2070 NEXT mem
2080 COUNT1(NUM,GH,ROTAT)=VAL(A$)
2090 A$=" "
2100 PRINT COUNT1(NUM,GH,ROTAT),NUM,ROTAT,stp%
2110 MEM=MEM+31
2120 NEXT NUM
2130 GOTO 2260
2140 IF ?(mem)=69 OR ?(mem)=43 OR ?(mem)=46 OR ?(mem)=32 THEN 2060 ELSE 2160
2150 GOTO 2260
2160 PROCclearMEM
2170 PROCsetup
2180 PROCclear
2190 PROCstartpha
2200 VDU3
2210 TIME=0
2220 REPEAT
2230 UNTIL TIME=1700
2240 PROCTRANSFER
2250 GOTO 2020
2260 PROCclearMEM
2270 ENDPROC
2280 DEF PROCclearMEM
2290 MEM=18600
2300 REPEAT
2310 ?MEM=0
2320 MEM=MEM+1
2330 UNTIL MEM=19000
2340 ENDPROC
2350DEF PROCVARIABLES
2360CONREG=&FE0B:STATREG=&FE08:RECREG=&FE09
2370MEMLOC=&70:STORE=&72:NUMCHR=&73:COMPARE1=&74:COMPARE2=&75
2380?MEMLOC=00:?(MEMLOC+1)=&48:?STORE=255:?COMPARE1=&49:?COMPARE2=&9F
2390ENDPROC
2400 ** ASSEMBLY PROGRAM TO INTERPRET DATA FROM MCA **
2410DEF PROCASSEMB
2420FOR N=0 TO 2 STEP 2
2430P%=30000
2440[OPT N
2450.INIT    LDA #03
2460         STA CONREG
2470         LDA #&12
2480         STA CONREG
2490.LOOP     LDY #00
2500          LDA #01
2510          BIT STATREG
2520          BEQ LOOP
2530          LDA RECREG
2540          CMP #22
2550          BEQ LOOP
2560          CMP #23
2570          BEQ LOOP
2580          CMP #13
2590          BEQ LOOP
2600          CMP #0
2610          BEQ LOOP
2620          CMP #10
2630          BEQ LOOP
2640          BEQ LOOP
2650          CMP #25
2660          BEQ LOOP
2670          LDY STORE
2680          STA (MEMLOC),Y
2690          CMP #04
2700          BEQ QUIT
2710          INY
2720          STY STORE
2730          CPY NUMCHR
2740          BEQ LOOP2
2750          JMP COMP
2760          JMP INIT
2770.LOOP2    INC (MEMLOC +1)
2780          JMP INIT
2790.COMP     LDX (MEMLOC +1)
2800          CPX COMPARE1
2810          BEQ CONP
2820          JMP INIT
2830.CONP     LDX STORE
2840          CPX COMPARE2
2850          BEQ QUIT
```

206

```
2660          JMP INIT
2870.OUIJ     RTS
2880J
2890NEXT N
2900ENDPROC
2910DEFPROCMEMORY
2920 CLS:PRINT"DO YOU WANT PRINTOUT" Y N":C$=GET$
2930 IF O$= Y  THEN GOTO 2960
2940 IF O$= N  THEN GOTO 3050
2950 GOTO 2920
2960DIM A$(1):INPUT SAMPLE NAME/NO",A$(1)
2970PRINT "SAMPLE NAME NO",A$(1)
2980PRINT "CHANNEL NO.                COUNTS"
2990MEM=1846I: I=0
3000REPEAT
3010X=?(MEM+I)
3020IF ?(MEM+I)  22 AND ?(MEM +I)  0 THEN PRINT CHR$(X):ELSE PRINT" ";
3030I=I+1
3040UNTIL I=480
3050VDU 3
3060 ** RETURN ROTATION STEPPER MOTOR TO START POSITION **
3070 DEF PROCROTATEBACK
3080 S=600:D=14:R=12
3090 PROCSTEP(S)
3100 ENDPROC
```

```
  10 ******************************
  20 ***          INTENCE  1        **
  30 ** PROGRAM TO FIND STEPPER MOTOR**
  40 **          AXLE CENTRE          **
  45 **                               **
  50 ******************************
  60 PROCQUESTIONS
  70 PROCSAVEDATA
  80  PROCZFORWARDDRIVE
  90 CLS:PRINT TAB(2,12) "Do You Want a Hard Copy r N":Q$=GET$
 100 IF Q$= "Y" AND Q$ "N" THEN 90
 110 IF Q$="Y" THEN 120 ELSE 130
 120 VDU2
 130 PROCX5mmDRIVE
 140 PROCFINDMIN
 150 VDU3
 160 PROCFINDSTART
 170 PROCZBACKDRIVE
 180 VDU3
 190 CLS:PRINT TAB(1,12) "DO YOU WANT TO CHAIN COUNTER PROG Y/N";Q$=GET$
 200 IF Q$  "Y" AND Q$  "N" THEN 190
 210 IF Q$="Y" THEN 220 ELSE END
 220 CHAIN"COUNTER"
 230 END
 240 REM *** PROCEDURE TO INPUT PARAMETERS ***
 250 DEF PROCQUESTIONS
 260 CLS
 270 INPUT TAB(1,12) "Z Position mm from end of axle  MAX 75 mm)",Z
 280 IF Z 75 GOTO 260
 290 CLS
 300  INPUT TAB(4,12) 'Number of steps/scan (20 OR 40)",NUMSTEPS
 310 IF NUMSTEPS  20 AND NUMSTEPS  40 THEN 290
 320 CLS
 330 INPUT TAB(4,12) "STEP SIZE (MAX 2mm)",SIZESTEP
 340 IF SIZESTEP 2 GOTO 320
 350 CLS
 360 INPUT TAB(8,12) "Maximum X-ray Energy(keV)",EMAX
 370 CLS
 380 INPUT TAB(4,12) "TIME FOR EACH STEP",TT%
 390 CLS
 400 INPUT TAB(2,12) "Number of Rotations (24 or 40)",NUMROTS
 410 IF NUMROTS<>24 AND NUMROTS<>40 THEN 390
 420  CLS:INPUT TAB(4,12) "BOTTOM LIMIT SET ",limit
 430 ENDPROC
 435 ** SAVE DATA **
 440 DEF PROCSAVEDATA
 450 X=OPENOUT "NUMBERS"
 460 PRINT #X,Z,NUMSTEPS,NUMROTS,SIZESTEP,EMAX,TT%
 470 CLOSE#X
 480 ENDPROC
 490 DEF PROCZFORWARDDRIVE
 500 CLS: PRINT TAB(1,12) "Do You Want Z Forward Drive Y/N";Q$=GET$
 510 IF Q$<>"Y" AND Q$ <>"N" THEN 500
 520 IF Q$="Y" THEN 530 ELSE 560
 530 CLS:PRINT"PROCZFORWARDDRIVE"
 540 S=Z*48:D=6:R=4
 550 PROCSTEP(S)
 560 ENDPROC
 565 ** DRIVE AXLE INTO BEAM PATH **
 570 DEF PROCZBACKDRIVE
 580 S=Z*48:D=14:R=12
 590 PROCSTEP(S)
 600 CLS:PRINT TAB(1,12) "Change Plug on Stepper Interface and Hit any Key";Q$=
GET$ - - - - - - - - - - - - - - - - - - - - - - - - - - - - - - -
 610 ENDPROC
 615 ** MOVE TO SCAN START **
 620 DEF PROCX5mmDRIVE
 630 CLS:PRINT"PROCX5mmDRIVE"
 640 S=5*48:D=112:R=96
 650 PROCSTEP(S)
 660 S=8:D=48:R=32
 670  PROCSTEP(S)
 680 ENDPROC
 685 ** PULSE SEQUENCE TO DRIVE MOTORS **
 690 DEF PROCSTEP(S)
 700 B=&FE60
 710 ?(B+2)=255
 720 FOR X= 1 TO S
 730 ?B=D
 740 Q=TIME+5
 750 REPEAT
 760 UNTIL TIME>=Q
 770 ?B=R
 780 Q=TIME+5
 790 REPEAT
 800 UNTIL TIME>=Q
 810 NEXT X
 820 ENDPROC
 825 ** FIND THE MINIMUM PHOTON COUNT **
 830 DEF PROCFINDMIN
 840 PROCCOUNT
 850 NUMsteps=NUMSTEPS*8
 860 DIM Step(NUMsteps):A%=0
 870 PRINT "PROCFINDMIN"
 880 PROCFIRST3
```

208

```
 890 PROCCOMPAREDOWNSLOPE:IF A%=1 THEN GOTO 910
 900 PROCCONTINUE>
 910 PROCFINDUP
 920 PROC5MORESTEPS
 930 PROCAVERAGETOP
 940 PROCAVERAGEBOTTOM
 950 PROCSETSTDBOTTOM
 960 PROCSETLIMITS
 970 PROCFINDPOINTS
 980 PROCCHECK
 990 PROCSLOPES
1000 ENDPROC
1010  DEF PROCCOMPAREDOWNSLOPE
1020 PRES=0:PAST1=0:PAST2=0:A%=0:AVERPRES=0
1030 PRES=Step(T-1):PAST1=Step(T-2):PAST2=Step(T-3)
1040 AVERPRES=(PRES+PAST1+PAST2)/3:PRINT"AVERAGE=",AVERPRES
1050 IF AVERPRES>AVERPAST-(10*SQR(AVERPRES)) THEN 1060 ELSE 1080
1060 POSITION1=T-3:SLOPE0=PAST2:SLOPE1=PAST1:A%=1
1070 PRINTPOSITION1,    SLOPE0 ,SLOPE1
1080 AVERPAST=AVERPRES
1090 ENDPROC
1100 DEF PROCCOUNT
1110 PROCsetup
1120 PROCtimeset
1130 PROCcheck
1140 ENDPROC
1150 DEF PROCsetup
1160 A=&FCC0
1170 '&70=0 : '&74=0
1180 A?2=&00
1190 A?3=&00
1200 A?12=&CE
1210 A?12=&CC
1220 A?13=&FF
1230 A?14=&00
1240 ENDPROC
1250 DEF PROCtimeset
1260 A=&FCC0
1270 RR%=TT%*(10)
1280 A?11=&E0
1290 A?6=&50
1300 A?5=&C3
1310 A?8=RR%MOD 256
1320 A?9=RR%DIV 256
1330 ENDPROC
1340 DEF PROCcheck
1350 DIM CHK 100
1360 FOR I%=0 TO 2 STEP 2 :P%=CHK
1370 [ OPT I%
1380 .check    LDX#&00
1390           LDY#&00
1400           LDA#&EC
1410           STA&FCCC
1420           LDA#&80
1430           STA&FCC2
1440 .start    LDA&FCCD
1450           AND#&02
1460           BNE increm1
1470 .counter2 LDA&FCCD
1480           AND#&10
1490     •     BNE increm2
1500 .timechk  LDA&FCCD
1510           AND#&20
1520           BNE next
1530           JMP start
1540 .increm1  LDA#&02
1550           STA&FCCD
1560           INX
1570           BNE counter2
1580           INC&72
1590           JMP counter2
1600 .increm2  LDA#&10
1610           STA&FCCD
1620           INY
1630           BNE timechk
1640           INC&76
1650           JMP timechk
1660 .next     LDA#&CC
1670           STA&FCCC
1680           LDA#&00
1690           STA&FCCB
1700           STX&71
1710           STY&75
1720           RTS :] NEXT I%
1730 CALL check
1740 AA%=A?1 :?&70=AA%
1750 ?&FCC2=&00
1760 BB%=A?0 :?&74=BB%
1770 CC%=A?13 - ---
1780 IF (CC% AND 2)=2 THEN DD%=256 ELSE DD%=0
1790 IF (CC% AND 16)=16 THEN EE%=256 ELSE EE%=0
1800 COUNTER1%=('&70)+DD%-2
1810 COUNTER2%=('&74)+EE%-2
1820 ENDPROC
```

```
1830 DEF PROCFIRST
1840 T=1:S=3:D=48:R=32
1850 REPEAT
1860 PROCCOUNT:PRINT COUNTER1%,T
1870 Step T:=COUNTER1%
1880 PROCSTEP S:
1890 T=T+1
1900 UNTIL T 3
1910 AVERPAST=0:AVERPAST=(Step T-1)+step( T-2 )/2)/2
1920 PRINT AVERPAST=",AVERPAST
1930 ENDPROC
1940 DEF PROCFINDSTART
1950 REM TO FIND NO OF STEPS TO START
1960 PRINT "FINDING START"
1970 S=((NUMSTEPS-1)*SIZESTEP*24)-((T-Midpoint)*3)+142
1980 PRINT"No Pulses to Start="S
1990 D=48:R=32
2000 PROCSTEP(S)
2010 S=144:D=112:R=96
2020 PROCSTEP(S)
2030 CLS:PRINT TAB(6,12) "Scan at Starting Position'
2040 ENDPROC
2050 DEF PROCCONTINUEX
2060 S=3:D=48:R=32
2070 REPEAT
2080 PROCCOUNT:PRINT COUNTER1%,T
2090 Step(T)=COUNTER1%
2100 T=T+1
2110 PROCCOMPAREDOWNSLOPE
2120 PROCSTEP(S)
2130 UNTIL A%=1
2140 ENDPROC
2150 DEF PROCFINDUP
2160 S=3:D=48:R=32
2170 REPEAT
2180 PROCCOUNT:PRINT COUNTER1%,T
2190 Step(T)=COUNTER1%
2200 T=T+1
2210 PROCCOMPAREUPSLOPE
2220 PROCSTEP(S)
2230 UNTIL B%=1
2240 ENDPROC
2250 DEF PROCCOMPAREUPSLOPE
2260 PRES=0:PAST1=0:PAST2=0:PAST3=0:B%=0
2270 PRES=Step(T-1):PAST1=Step(T-2):PAST2=Step(T-3):PAST3=Step(T-4)
2280 IF PRES<PAST1+(3*SQR(PAST1)) AND PRES>PAST1-(12*SQR(PAST1)) AND PAST2<PAST
1-(3*SQR(PAST1)) AND PAST3<PAST2-(3*SQR(PAST2)) AND PRES>Step(1)/2 THEN 2290 ELS
E 2310
2290 POSITION2=T-2:SLOPEUP0=PAST2:SLOPEUP1=PAST1:B%=1
2300 PRINT POSITION2    ,SLOPEUP0 ,SLOPEUP1
2310 ENDPROC
2320 DEF PROC5MORESTEPS
2330 FOR MORE= 1 TO 5
2340 S=3:D=48:R=32
2350 REPEAT
2360 PROCCOUNT
2370 PRINTCOUNTER1% ,T
2380 Step(T)=COUNTER1%
2390 T=T+1
2400 PROCSTEP(S)
2410 NEXT MORE
2420 ENDPROC
2430 DEF PROCAVERAGETOP
2440 SUMTOPL=0:SUMTOPR=0
2450 FOR TPL= 1 TO POSITION1
2460 SUMTOPL=SUMTOPL+Step(TPL)
2470 NEXT TPL
2480 FOR TPR= POSITION2 TO (T-1)
2490 SUMTOPR=SUMTOPR+Step(TPR)
2500 NEXT TPR
2510 AVERAGE=(SUMTOPL+SUMTOPR)/(TPL+((T-1)-POSITION2))
2520 PRINT "TOP AVERAGE=";AVERAGE
2530 ENDPROC
2540 DEF PROCAVERAGEBOTTOM
2550 min=1000000
2560 FOR val= 1 TO (T-1)
2570 IF Step(val)<min THEN min =Step(val)
2580 NEXT val
2590 PRINT "min ",min
2600 ENDPROC
2610 DEF PROCSETSTDBOTTOM
2620 DIM AV(T)
2630 SDB1=min+(5*SQR(min))
2640 SDB2=min-(5*SQR(min))
2650 IF SDB2<0 THEN SDB2=0
2660 C=0
2670 FOR P= 1 TO (T-1)
2680 IF Step(P)<SDB1 AND Step(P)>SDB2 THEN  2700 ELSE AV(P)=0
2690 GOTO 2710
2700 AV(P)=Step(P):C=C+1
2710 NEXT P
```

```
2720 SUMAV=0
2730 FOR P=1 TO (T-1)
2740 SUMAV=SUMAV+AV(P)
2750 NEXT P
2760 AVBOTTOM=SUMAV/C
2770 PRINT"BOTTOM AVERAGE=";AVBOTTOM
2780 ENDPROC
2790 DEF PROCSETLIMITS
2800 ratio=AVERAGE/AVBOTTOM
2810 TopLIMIT=AVERAGE-(ratio*SQR(AVERAGE))
2820 BOTTOMLIMIT=AVBOTTOM+(ratio*limit*SQR(AVBOTTOM))
2830 PRINT"TOPLIMIT",TopLIMIT,"BOTTOMLIMIT",BOTTOMLIMIT
2840 ENDPROC
2850 DEF PROCFINDPOINTS
2860 NoPTS=1:Nopts=1
2870 DIM DWNPTS(T/2):DIM UPPTS(T,2):DWNPTS(0)=1000000
2880 FOR PTS=2 TO (T-1)
2890 IF Step(PTS)<TopLIMIT AND Step(PTS)>BOTTOMLIMIT AND Step(PTS)<Step(PTS-1)
AND Step(PTS)<DWNPTS(NoPTS-1) THEN 2930
2900 IF Step(PTS)<TopLIMIT AND Step(PTS)>BOTTOMLIMIT AND Step(PTS)>Step(PTS-1)
THEN 2950
2910 NEXT PTS
2920 GOTO 2980
2930 DWNPTS(NoPTS)=Step(PTS):PRINT"DOWNPTS",DWNPTS(NoPTS);NoPTS=NoPTS+1:t=PTS
-(NoPTS-1)
2940 GOTO 2900
2950 UPPTS(Nopts)=Step(PTS):Nopts=Nopts+1:tt=PTS-Nopts+1
2960 PRINT"UPPTS",UPPTS(Nopts-1)
2970 GOTO 2910
2980 ENDPROC
2990 DEF PROCCHECK
3000 IF NoPTS=Nopts THEN GOTO 3070
3010 IF NoPTS<Nopts THEN GOTO 3060
3020 IF NoPTS>Nopts THEN GOTO 3030
3030 FOR I= 1 TO NoPTS
3040 UPPTS(I)=UPPTS(I+1):PRINTUPPTS(I)
3050 NEXT I:tt=tt+(Nopts-NoPTS):Nopts=NoPTS:GOTO 3070
3060 NoPTS=Nopts
3070 ENDPROC
3080 DEF PROCSLOPES
3090 PROCDownIntercept
3100 PROCUpIntercept
3110 Intercept1=Intercept1+t
3120 Intercept2=Intercept2+tt
3130 PRINT"Intercept1= ",Intercept1,"Intercept2= ",Intercept2
3140 PROCLINEIntercept
3150 ENDPROC
3160 DEF PROCDownIntercept
3170 a=0:b=0:c=0:d=0:e=0
3180 FOR h= 1 TO (NoPTS-1)
3190 a=a+DWNPTS(h)
3200 b=b+h
3210 c=c+(h*DWNPTS(h))
3220 d=d+(DWNPTS(h)^2)
3230 NEXT h
3240 h=h-1
3250 a=a/h:b=b/h:c=c/h:d=d/h:e=a*a
3260 slope1=((a*b)-c)/(e-d)
3270 Intercept1=-((d*b)-(a*c))/(e-d)
3280 PRINT "Intercept1= ",Intercept1
3290 PRINT "slope1= ",slope1
3300 ENDPROC
3310 DEF PROCUpIntercept
3320 a=0:b=0:c=0:d=0:e=0
3330 FOR g= 1 TO (Nopts-1)
3340 a=a+UPPTS(g)
3350 b=b+g
3360 c=c+(g*UPPTS(g))
3370 d=d+(UPPTS(g)^2)
3380 NEXT g
3390 g=g-1
3400 a=a/g:b=b/g:c=c/g:d=d/g:e=a*a
3410 slope2=((a*b)-c)/(e-d)
3420 Intercept2=-((d*b)-(a*c))/(e-d)
3430 PRINT "Intercept2= ",Intercept2
3440 PRINT "slope2= ",slope2
3450 ENDPROC
3460 DEF PROCLINEIntercept
3470 Midpoint=(Intercept1+((Intercept2-Intercept1)/2))
3480 PRINT"Midpoint=",Midpoint
3490 ENDPROC
3500 DEF PROCInput
3510 INPUT #Y,COUNTER1%
3520 ENDPROC
```

```
10 REM ***********************************
20 REM **                              **
30 REM **           APPENDIX 3          **
40 REM **                              **
50 REM **     PROGRAM TO CALCULATE AND   **
60 REM **   DISPLAY FILTERED SPECTRA FOR **
70 REM **      THE X-RAY TUBE SOURCE    **
80 REM **                              **
90 REM ***********************************
100 REM INPUT X-RAY TUBE SPECTRUM
110 CLEAR:DIM SPECT(40):DIM MAC(40):DIM FILTERD(40):DIM ENERGY%(40)
120 X=OPENIN"SPECTRM"
130 FOR A= 1 TO 39
140 PRINT "INTENSITY AT LAMBDA=";11+A
150 INPUT #X,SPECT(A)
160 PRINTSPECT(A)
170 NEXT A
180 CLOSE#X
190 CLS
200 REM CALCULATE FILTERED SPECTRUM
210 PRINT "To Calculate Equiv. Thick. Input Filter Density and Thickness"
220 PRINT
230 INPUT "FILTER DENSITY g/cubic cm",F
240 PRINT
250 INPUT "FILTER THICKNESS  cm",T
260 TH=F*T
270 CLS
280 PRINT"Do you Want to Type in Data or Take from File D/F?";Q$=GET$
290 IF Q$="D" THEN GOTO 310
300 IF Q$="F" THEN GOTO 460 ELSE GOTO 280
310 REM MASS ABSORPTION COEFFICENTS
320 FOR B= 1 TO 39
330 PRINT "INPUT M.A.C. AT LAMBDA=",.15+(.05*B)
340 INPUT MAC(B)
350 NEXT B
360 CLS:PRINT "Do you Want to Save Mass Absorption Coeffs? Y/N";Q$=GET$
370 IF Q$="Y" THEN GOTO 400
380 IF Q$="N" THEN GOTO 540 ELSE GOTO 360
390 REM SAVE FILTERED SPECTRUM
400 INPUT"FILE NAME",NAME$
410 X=OPENOUT NAME$
420 FOR C= 1 TO 39
430 PRINT #X,MAC(C)
440 PRINT MAC(C):NEXT C
450 CLOSE#X :GOTO 540
460 CLS
470 INPUT"Name of File with M.A.Cs.";NAMES$
480 X=OPENIN NAMES$
490 FOR D=1 TO 39
500 INPUT #X,MAC(D)
510 PRINT MAC(D)
520 NEXT D
530 CLOSE#X
540 REM CALCULATION OF INTENSIY DROP
550 FOR E=1 TO 39
560 FILTERD(E)=SPECT(E)*EXP(-TH*MAC(E))
570 PRINT FILTERD(E)
580 NEXT E
590 REM SAVE FILTERED SPECTRUM TO DISC
600 PRINT" Do you want to save Filtered Spectrum on Disc Y/N ";Q$=GET$
610 IF Q$="Y" THEN GOTO 630
620 IF Q$="N" THEN GOTO 690 ELSE GOTO 600
630 INPUT "FILTERED SPECTRUM FILE NAME";NME$
640 X=OPENOUT NME$
650 FOR F=1 TO 39
660 PRINT #X,FILTERD(F)
670 NEXT F
680 CLOSE#X
690 CLS:PRINT"Do you want a printout of Energies and intensities Y/N  ?";Q$=GET
T$
700 IF Q$="Y" THEN GOTO 720
710 IF Q$="N" THEN GOTO 790 ELSE GOTO 690
720 MODE 0:VDU2
730 PRINT "ENERGY (kev)          WAVELENGHT (A)          Io          I
"
740 FOR G=1 TO 39
750 ENERGY%(G)=11+G
760 PRINT ENERGY%(G)," ",(12.396/(11+G))," ",SPECT(G)," ",FILTERD(G)
770 NEXT G
780 VDU3:MODE7
790 PRINT "DO YOU WANT TO GRAPH? Y/N";Q$=GET$
800 IF Q$="Y" THEN GOTO 830
810 IF Q$="N" THEN GOTO 110 ELSE GOTO 790
820 REM DISPLAY PROGRAM FOR GRAPHS
830 DIM A$(70)
840 INPUT"Graph Scale",MAG
850 MODE4
860 INPUT "Input Heading for Graph",HEAD$
870 FOR I= 1 TO LEN(HEAD$)
880 A$(I)=MID$(HEAD$,I,1)
890 NEXT I
900 I=25:IF LEN(HEAD$)<=25 THEN GOTO 970
910 REPEAT
920 X$=A$(I)
930 I=I-1
940 UNTIL X$=" "
950 FIRST$=LEFT$(HEAD$,I)
960 SECLN$=RIGHT$(HEAD$,LEN(HEAD$)-I-1):GOTO 990
```

```
 ... FIRST#####
 830 SECLN$=""
 990 CLS
1000 .DULB,0,29,24,28
1010 VDU24,0;150;1279;10.;
1020 DIM EQUIVTHICK(39)
1030 PRINT "ENERGY OR WAVELENGHT PLOT (E/W)":O$=GET$
1040 IF O$< "E" AND O$<  "W" THEN GOTO 1030
1050 INPUT "FILE NAME",NAME$
1060 X=OPENIN NAME$
1070 FOR J%=1 TO 39
1080 INPUT#X,EQUIVTHICK(J%)
1090 NEXT J%
1100 CLOSE#X
1110 VDU5
1120 MOVE0,150:DRAW 1200,150
1130 MOVE 0,100:DRAW 0,1000
1140 FOR I%=0 TO 900 STEP 60
1150 MOVE 0,I%+200:DRAW 10,I%+200
1160 NEXT I%
1170 MOVE 0,740:DRAW20,740
1180 IF O$="E" THEN GOTO 1200
1190 IF O$="W" THEN GOTO 1320 ELSE GOTO 1030
1200 REM PLOT OF INTENSITY vs. ENERGY
1210 MOVE 340,900:PRINT"Intensity vs. Energy(Kev)"
1220 FOR J%=39 TO 1 STEP-1
1230 G=11+J%
1240 MOVE((G*22)-200),150:DRAW((G*22)-200),160
1250 NEXT J%
1260 MOVE48,150+EQUIVTHICK(39)*MAG
1270 FOR J%=39 TO 1 STEP-1
1280 G=11+J%
1290 DRAW((G*.. .. .. .. .. .. .. .. ...  #IHN
1300 NEXT J%
1310 GOTO 1410
1320 REM PLOTTING INTENSITY vs. WAVELENGHT
1330 MOVE 340,900:PRINT" Intensity vs. Wavelenght"
1340 FOR J%=17 TO 1 STEP -1
1350 MOVE J%*50,150:DRAWJ%*50,160
1360 NEXT J%
1370 MOVE17*50,150+EQUIVTHICK(17)*50
1380 FOR J%=17 TO 1 STEP -1
1390 DRAWJ%*50,150+EQUIVTHICK(J%)*50
1400 NEXT J%
1410 MOVE450,800:PRINT FIRST$
1420 MOVE550,750:PRINT SECLN$
1430 VDU4
1440 CLS:PRINT"HARD COPY H,NEW SPEC N OR MORE SPECTRA M";:O$=GET$
1450 IF O$< "H"AND O$< "N"AND O$< "M"THEN GOTO 1440
1460 CLS:IF O$="H" THEN PROCDUMP
1470 CLS:IF O$="N" THEN GOTO 810
1480 CLS
1490 GOTO 1030
1500 DEF PROCASSEMB
1510 M=22405:STORE1=M-10:STORE2=M-20:MEMST=&70:OSWORD=&FFF1
1520 FOR N=0 TO 2 STEP 2
1530 P%=M-150
1540 [OPT N
1550 .PLT        LDA #00
1560             TAY
1570 .LOOP1      LDA #00
1580             TAX
1590 .LOOP3      ROR STORE1,X
1600             ROL A
1610             INX
1620             CPX #08
1630             BMI LOOP3
1640             STA STORE2,Y
1650             INY
1660             CPY #08
1670             BMI LOOP1
1680             RTS
1690 ]
1700 NEXT N
1710 ENDPROC
1720 DEFPROCDUMP
1730 PROCASSEMB
1740 VDU2,1,27,1,65,8
1750 X%=M-30:Y%=X%DIV256
1760 FORYY%=0TO9920STEP 320
1770 VDU1,27,1,75,1,63,1,1
1780 FORXX%=0TO312 STEP8
1790 MEMST=(22528+XX%+YY%)
1800 FOR J%=0 TO 7
1810 STORE1?J%=FNREADIO(MEMST+J%)
1820 NEXT J%
1830 CALL PLT
1840 FORZ%=7TO0STEP -1
1850 VDU1,?(STORE2+Z%)
1860 NEXTZ%
1870 NEXTXX%
1880 VDU1,13
1890 NEXTYY%
1900 VDU3
1910 ENDPROC
1920 DEF FNREADIO(addr):Y%=X%DIV256:!X%=addr:A%=5:CALL OSWORD
1930 =X%?4
```

213

Atomic number and element	K-series					
	K edge	KN_III	KM_III	KM_II	KL_III	KL_II
		Kβ₂	Kβ₁	Kβ₃	Kα₁	Kα₂
Intensity	—	~5	~30	~12	100	~50
4 Be	0.115					0.109
5 B	0.188					0.183
6 C	0.282					0.277
7 N	0.397					0.393
8 O	0.533					0.525
9 F	0.692					0.677
10 Ne	0.874		0.858			0.848
11 Na	1.080		1.071			1.041
12 Mg	1.309		1.302			1.253
13 Al	1.562		1.557		1.487	1.486
14 Si	1.840		1.836		1.740	1.739
15 P	2.143		2.139		2.014	2.013
16 S	2.471		2.464		2.308	2.307
17 Cl	2.824		2.816		2.622	2.620
18 Ar	3.203		3.190		2.958	2.956
19 K	3.607		3.590		3.314	3.311
20 Ca	4.034		4.013		3.692	3.688
21 Sc	4.486		4.461		4.090	4.086
22 Ti	4.965		4.932		4.511	4.505
23 V	5.463		5.427		4.952	4.944
24 Cr	5.987		5.947		5.415	5.405
25 Mn	6.537		6.490		5.899	5.888
26 Fe	7.112		7.058		6.404	6.391
27 Co	7.712		7.649		6.930	6.915
28 Ni	8.339		8.265		7.478	7.461
29 Cu	8.993		8.905	8.903	8.048	8.028
30 Zn	9.673	9.658	9.572	9.567	8.639	8.616
31 Ga	10.386	10.366	10.271	10.261	9.252	9.231
32 Ge	11.115	11.101	10.983	10.978	9.887	9.856
33 As	11.877	11.864	11.727	11.721	10.544	10.509
34 Se	12.666	12.652	12.496	12.489	11.222	11.181
35 Br	13.483	13.470	13.292	13.285	11.924	11.878
36 Kr	14.330	14.315	14.113	14.105	12.650	12.598
37 Rb	15.202	15.185	14.962	14.952	13.396	13.336
38 Sr	16.106	16.085	15.836	15.826	14.166	14.098
39 Y	17.037	17.015	16.737	16.725	14.958	14.882
40 Zr	17.997	17.963	17.662	17.649	15.770	15.692

Atomic number and element	K-series					
	K edge	KN_III	KM_III	KM_II	KL_III	KL_II
		Kβ₂	Kβ₁	Kβ₃	Kα₁	Kα₂
Intensity	—	~5	~30	~12	100	~50
41 Nb	18.985	18.947	18.623	18.606	16.615	16.521
42 Mo	20.002	19.960	19.608	19.590	17.479	17.374
43 Tc	21.048	21.002	20.619	20.599	18.367	18.251
44 Ru	22.123	22.072	21.656	21.637	19.279	19.150
45 Rh	23.229	23.173	22.723	22.698	20.216	20.073
46 Pd	24.365	24.303	23.819	23.792	21.178	21.021
47 Ag	25.531	25.465	24.943	24.912	22.163	21.991
48 Cd	26.727	26.653	26.095	26.061	23.173	22.985
49 In	27.953	27.872	27.275	27.237	24.209	24.002
50 Sn	29.211	29.122	28.491	28.439	25.272	25.044
51 Sb	30.499	30.402	29.725	29.677	26.359	26.110
52 Te	31.817	31.712	30.995	30.944	27.472	27.201
53 I	33.168	33.054	32.295	32.239	28.612	28.317
54 Xe	34.551	34.428	33.625	33.562	29.779	29.459
55 Cs	35.966	35.833	34.985	34.918	30.973	30.625
56 Ba	37.414	37.270	36.378	36.303	32.194	31.817
57 La	38.894	38.739	37.802	37.721	33.442	33.034
58 Ce	40.410	40.243	39.258	39.170	34.720	34.279
59 Pr	41.958	41.778	40.748	40.653	36.026	35.550
60 Nd	43.558	43.345	42.272	42.166	37.361	36.847
61 Pm	45.152	44.947	43.825	43.713	38.725	38.171
62 Sm	46.801	46.584	45.413	45.289	40.118	39.523
63 Eu	48.486	48.256	47.036	46.902	41.542	40.902
64 Gd	50.207	49.964	48.696	48.554	42.996	42.309
65 Tb	51.965	51.709	50.382	50.228	44.481	43.744
66 Dy	53.761	53.491	52.119	51.956	45.999	45.208
67 Ho	55.593	55.308	53.878	53.707	47.547	46.699
68 Er	57.464	57.164	55.681	55.491	49.128	48.221
69 Tm	59.374	59.059	57.513	57.303	50.742	49.773
70 Yb	61.322	60.991	59.374	59.157	52.389	51.354
71 Lu	63.311	62.960	61.286	61.049	54.070	52.965
72 Hf	65.345	64.973	63.236	62.979	55.790	54.611
73 Ta	67.405	67.011	65.221	64.946	57.533	56.277
74 W	69.517	69.100	67.244	66.951	59.318	57.982
75 Re	71.670	71.230	69.309	68.994	61.140	59.718
76 Os	73.869	73.404	71.416	71.077	63.001	61.487
77 Ir	76.111	75.620	73.560	73.203	64.896	63.287
78 Pt	78.400	77.883	75.751	75.364	66.832	65.123
79 Au	80.729	80.182	77.985	77.580	68.804	66.990
80 Hg	83.109	82.532	80.261	79.822	70.819	68.894

Atomic number and element	K-series					
	K edge	KN_III	KM_III	KM_II	KL_III	KL_II
		Kβ₂	Kβ₁	Kβ₃	Kα₁	Kα₂
Intensity	—	~5	~30	~12	100	~50
81 Tl	85.532	84.924	82.575	82.384	72.872	70.832
82 Pb	88.008	87.367	84.936	84.450	74.969	72.804
83 Bi	90.540	89.866	87.354	86.831	77.118	74.815
84 Po	93.113	92.403	89.801	89.250	79.301	76.863
85 At	95.730	94.983	92.302	91.722	81.523	78.943
86 Rn	98.402	97.617	94.866	94.246	83.793	81.065
87 Fr	101.131	100.306	97.477	96.807	86.114	83.231
88 Ra	103.909	103.099	100.130	99.432	88.476	85.434
89 Ac	106.738	105.837	102.846	102.101	90.884	87.675
90 Th	109.641	108.690	105.611	104.831	93.358	89.952
91 Pa	112.599	111.606	108.435	107.606	95.883	92.287
92 U	115.606	114.561	111.303	110.424	98.440	94.659
93 Np	118.678	117.591	114.243	113.312	101.068	97.077
94 Pu	121.818	120.703	117.261	116.277	103.761	99.552
95 Am	125.027	123.891	120.360	119.317	106.523	102.085
96 Cm	128.220	127.066	123.423	122.325	109.290	104.441
97 Bk	131.590	130.355	126.663	125.443	112.138	107.205
98 Cf	135.960	134.681	130.851	129.601	116.030	110.710
99 Es	139.490	138.169	134.238	132.916	119.080	113.470
100 Fm	143.090	141.724	137.693	136.347	122.190	116.280
101 Md	146.780	145.370	141.234	139.761	125.390	119.170
102 No	150.540	149.092	144.852	143.295	128.660	122.100
103 Lw	154.380	152.900	148.670	146.920	132.020	125.100